

A Thesis Submitted for the Degree of PhD at the University of Warwick

Permanent WRAP URL:

<http://wrap.warwick.ac.uk/135004>

Copyright and reuse:

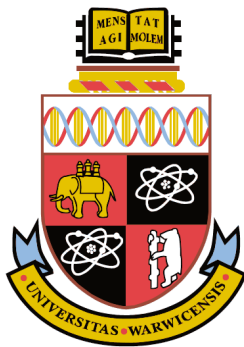
This thesis is made available online and is protected by original copyright.

Please scroll down to view the document itself.

Please refer to the repository record for this item for information to help you to cite it.

Our policy information is available from the repository home page.

For more information, please contact the WRAP Team at: wrap@warwick.ac.uk



NMR CRYSTALLOGRAPHY OF PHARMACEUTICAL SOLIDS

by

Gemma Marie Candy

Supervisor: Steven P. Brown

A thesis submitted to
The University of Warwick
for the degree of
DOCTOR OF PHILOSOPHY

Department of Physics
The University of Warwick
December 2018



Abstract

High resolution ^1H Magic Angle Spinning (MAS) NMR is a sensitive probe of hydrogen chemistry, in particular hydrogen bonds, which often govern packing arrangements of crystalline systems of organic solids. This thesis uses experimental solid-state NMR together with DFT-based GIPAW (Gauge-Including Projector Augmented Wave) calculations in an approach referred to as NMR crystallography to study pharmaceutical salts and cocrystals.

A study of nitrogen sites in two salt/cocrystal systems, first: isonicotinamide/ 2,4,6- trihydroxybenzoate salt ($1\text{-NH}^+ : 2\text{-COO}^-$) and isonicotinamide/4-hydroxy-3-nitrobenzoic acid co-crystal ($1\text{-N} : 3\text{-COOH}$) and second: 4,4'-bipyridine5-sulfosalicylic acid ($4\text{-NH}^+ : 5\text{-SO}_3^-$) and 4,4'-bipyridine/phthalic acid ($4\text{-N} : 6\text{-COOH}$) is presented, whereby NMR crystallography was used to identify protonation. NMR crystallography is also applied to cocrystals and a salt where citric acid is present to gain a greater understanding of the hydrogen bonding interactions that govern packing arrangements notably for the carboxylic acid groups.

Specifically, 1D ^1H MAS NMR and ^1H - ^1H Double-Quantum (DQ) MAS NMR solid-state NMR experiments were used alongside 2D ^{14}N - ^1H HMQC (Heteronuclear Multiple Quantum Coherence) experiments. The ^{14}N shift in the 2D ^{14}N - ^1H HMQC experiment was shown to change significantly upon protonation of the nitrogen site, and changes in shift of magnitude of hundreds of ppm were observed. Further evidence of protonation was provided by the variation of the recoupling time in 2D ^{14}N - ^1H HMQC experiments to enable the observation of longer range ^{14}N - ^1H proximities.

The experimental data is complemented by data obtained from GIPAW calculations of NMR chemical shielding and quadrupolar interactions which show that the combined experimental and calculation approach is viable in determining the presence of a salt or co-crystal form. Specifically, the trend in P_Q values of the chosen nitrogen site becoming higher upon protonation is observed. Isolated molecule to crystal GIPAW chemical shift calculations were also performed that give further insight into hydrogen bonding strength.



Contents

Contents	i
List of Abbreviations	1
List of Figures	5
List of Tables	9
Acknowledgements	11
Declarations	13
1 Thesis Overview	15
1.1 Overview	15
2 Pharmaceutical Solid-State Forms	19
2.1 Overview	19
2.2 Pharmaceutical Drug Products	19
2.2.1 Pharmaceutical Salts	20
2.2.2 Pharmaceutical Co-crystals	20
2.2.3 Amorphous dispersions	21
2.2.4 Pharmaceutical Drug Products: The Potential of Cocrystals	22

2.2.5	APIs and their Identification Using Solid-State NMR	23
2.2.6	Excipients	24
2.3	Hydrogen Bonding Interactions	25
3	NMR Crystallography of Pharmaceutical Solids	31
3.1	Introduction	31
3.2	Diffraction	31
3.3	The Gauge Including Projector Augmented Wave Method (GIPAW)	33
3.3.1	Isolated Molecule Calculations	34
3.4	^1H MAS NMR	35
3.4.1	^1H Spin Diffusion NMR Experiments	36
3.5	^{13}C CPMAS NMR	37
3.6	^{15}N in Solid-State NMR Experiments	42
3.7	Quadrupolar Nuclei	44
4	NMR theory	47
4.1	Spin Angular Momentum	47
4.2	The NMR Experiment	48
4.2.1	The Vector Model	48
4.2.2	Net Magnetisation and Thermal Equilibrium	49
4.2.3	Larmor Precession	50
4.2.4	Detection of the NMR Signal	51
4.2.5	Pulses and the Rotating Frame of Reference	53
4.2.6	The Time and Frequency Domain Signals	55
4.2.7	Absorption and Dispersive Lineshapes	57
4.3	Quantum Mechanical Description of NMR	58
4.4	The Density Operator	61
4.5	Product Operators	62
4.5.1	Isolated Spin	63
4.5.2	Coupled Spins	65
4.5.3	Multiple Quantum Coherences	67
4.6	Hamiltonians and Interactions	67
4.6.1	The Radiofrequency Hamiltonian	68
4.6.2	Evolution Under an Offset	70
4.7	Frame Rotations and Tensors	71
4.8	Internal Interactions	73

4.8.1	Chemical Shielding	73
4.8.2	Dipolar Coupling	77
4.8.3	Magic Angle Spinning	79
4.8.4	<i>J</i> -Coupling	81
4.8.5	Quadrupolar Coupling	82
4.9	Summary	90
5	Experimental Techniques	91
5.1	Introduction	91
5.2	¹ H Decoupling	92
5.3	¹ H- ¹³ C CPMAS	93
5.4	2D NMR	98
5.5	Phase Cycling	101
5.6	Recoupling	102
5.7	¹ H DQ MAS	102
5.8	Heteronuclear Multiple Quantum Coherence Spectroscopy	103
5.9	NMR Crystallography	108
6	Experimental Techniques and Computational Details	115
6.1	Introduction	115
6.2	Experimental Details	115
6.2.1	Sample Preparation	115
6.2.2	Solid-State NMR Experiments	116
6.3	PXRD	117
6.3.1	PXRD of citric acid monohydrate	117
6.3.2	PXRD for Isonicotinamide Salt and Cocrystal	118
6.4	Computational Details	120
7	Protonation in Pharmaceutical Compounds: Isonicotinamide Salt and Co-crystal	127
7.1	Introduction	127
7.2	One-dimensional ¹ H MAS NMR Spectra	128
7.3	¹ H- ¹ H DQ MAS NMR Spectra	132
7.4	¹⁴ N- ¹ H HMQC MAS NMR spectra	137
7.5	Conclusion	145

8	Protonation in Pharmaceutical Compounds: Bipyridine Salt and Co-crystal	149
8.1	Introduction	149
8.2	One-dimensional ^1H MAS NMR Spectra	149
8.3	^1H - ^1H DQ MAS NMR Spectra	153
8.4	^{14}N - ^1H HMQC MAS NMR Spectra	159
8.5	Conclusion	167
9	Citric acid, co-crystals and a citrate salt	169
9.1	Introduction	169
9.2	Solid-State NMR of Citric Acid	170
9.2.1	Experimental and GIPAW Calculated ^1H Chemical Shifts	170
9.2.2	^1H - ^1H DQ-SQ NMR	172
9.2.3	^{13}C CPMAS NMR	172
9.3	NMR Crystallography of Citric Acid and Citric Acid Cocrystals	176
9.4	Caffeine-Citric Acid Cocrystal	182
9.5	Sildenafil Citrate	187
9.6	Outlook	196
9.7	Conclusion	196
10	Trends in Experimental & Calculated NMR Parameters for Hydrogen Bonds	199
10.1	Overview	199
10.2	^1H Chemical Shifts	201
10.2.1	Hydrogen Bonds and $\Delta\delta_{C-M}$ From Literature	201
10.2.2	Difference in $\Delta\delta_{C-M}$ Values Between Salt and Cocrystal Forms	202
10.2.3	C-H...O Weak Hydrogen Bonding	203
10.3	^{14}N Quadrupolar Parameters	203
10.4	Conclusion	207
11	Thesis Summary	209
11.1	Research Aim	209
11.2	Key Findings	209
11.3	The Future of NMR Crystallography	211
	Bibliography	215



List of Abbreviations

2Q-HORROR	Double-Quantum H _O monuclear R _O tary Resonance
ANDA	Abbreviated New Drug Application
API	Active Pharmaceutical Ingredient
BABA	BAck-to-BAck
CASTEP	CAmbridge Serial Total Energy Package
CP	Cross Polarisation
CPMD	Car-Parrinello Molecular Dynamics
CRAMPS	Combined Rotation And Multiple Pulse Spectroscopy
CSA	Chemical Shift Anisotropy
CSD	Cambridge Structural Database
CW	Continuous Wave
DFT	Density Functional Theory
DNP	Dynamic Nuclear Polarisation
DQ/DQC	Double-Quantum Coherence

DRAMA	Dipolar Recoupling At the Magic Angle
DUMBO	Decoupling Under Mind Boggling Optimisation
EFG	Electric Field Gradient
EMA	the European Medicines Agency
FDA	the Food and Drug Administration
FID	Free Induction Decay
FSLG	Frequency Switched Lee-Goldburg
FT	Fourier Transform
FT-IR	Fourier Transform Infrared Spectroscopy
GGA	Generalised Gradient Approximation
GIPAW	Gauge-Including Projector Augmented Wave
HETCOR	Heteronuclear Correlation
HF	Hartree Fock
HMQC	Heteronuclear Multiple-Quantum Coherence
INADEQUATE	Incredible Natural Abundance Double Quantum Transfer Experiment
INEPT	Insensitive Nuclei Enhanced by Polarisation Transfer
IP	Intellectual Property
IUPAC	The International Union of Pure and Applied Chemistry
LG	Lee Goldberg
MAGRES	Magnetic Resonance
MAS	Magic Angle Spinning
MQC	Multiple-Quantum Coherence
NMR	Nuclear Magnetic Resonance

PAS	Principal Axis System
PAW	The projector augmented wave method
PBE	Perdew-Burke-Ernzerhof (functional)
PMLG	Phase Modulated Lee-Goldburg
POST-C7	Permutationally Offset STabilised-C7
ppm	Parts Per Million
PXRD	Powder X-Ray Diffraction
R3	Rotary Resonance Recoupling
RCPL	Recoupling
rf	RadioFrequency
SCXRD	Single Crystal X-Ray Diffraction
SDG	Solvent Drop Grinding
SPINAL	Small Phase INcremental ALternation
SQ/SQC	Single-Quantum Coherence
T	Tesla
TDSE	Time Dependent Schrodinger Equation
TISE	Time Independent Schrodinger Equation
TOSS	TOfal Supression of Spinning sidebands
TPPI	Two Pulse Phase Increment
TPPM	Two Pulse Phase Modulated
XPS	X-ray Photoelectron Spectroscopy
ZQ	Zero-Quantum

List of Figures

2.1	Schematic representations of different solid-state forms	21
3.1	Experimental powder pattern for polymorph 1 of dG(C ₁₀)	33
3.2	¹ H- ¹⁵ N CPMAS solid-state NMR spectra	44
3.3	¹⁴ N- ¹ H HMQC experiment for a cocrystal	45
4.1	Precession of the Magnetisation Vector	51
4.2	Larmor frequency	52
4.3	The Magnetisation Vector when tilted by angle β	53
4.4	X and Y components of magnetisation	54
4.5	B_{eff} in the rotation field	55
4.6	The Absorption and Dispersive Lineshapes	57
4.7	Vector model showing the product operators I_x , I_y and I_z for an isolated spin $\frac{1}{2}$ nucleus.	63
4.8	Representation of the transformation of the product operators of an isolated spin $\frac{1}{2}$ nucleus	64
4.9	Product operators for a single spin $\frac{1}{2}$ nucleus: (a) schematic spectra, (b) energy level diagrams.	65
4.10	Representation of a selection of product operators.	66
4.11	Energy level diagrams which represent the transitions which can take place between the different energy states	67

LIST OF FIGURES

4.12	Euler angles defined in a Cartesian co-ordinate system	72
4.13	A representation of the shielding field (B_S) and the applied field (B_0) in an isotropic and anisotropic case.	74
4.14	The shielding tensor, σ	76
4.15	Representation of two magnetic dipoles which interact through space.	77
4.16	Pake Doublet pattern for a pair of isolated heteronuclear nuclei in a powdered sample.	80
4.17	Spectra for a polycrystalline sample	86
4.18	Simulated second order MAS quadrupolar powder patterns	87
5.1	A pulse sequence showing a Cross Polarisation experiment between the abundant spin I and the dilute spin S	94
5.2	The signal to noise ratio (normalised) for the CH_3 peak, CH peak and the COO^- peak in L -alanine varies as a function of contact time (μs) in a ^1H - ^{13}C CP MAS experiment	96
5.3	^{13}C CP MAS spectra of L -alanine showing the effect of changing the TPPM proton decoupling pulse length.	99
5.4	General sequence for a 2D NMR experiment	100
5.5	A ^1H - ^1H DQ-SQ spectrum with skyline projections of L -alanine	104
5.6	A ^1H DQ MAS experiment using a BABA pulse sequence, shown alongside its coherence transfer pathway.	105
5.7	Pulse sequence and coherence transfer pathway for a ^{14}N - ^1H HMQC experiment.	107
6.1	PXRD data of of citric acid monohydrate	118
6.2	PXRD of isonicotinamide/4-hydroxy-3-nitrobenzoic acid co-crystal (1-N:3-COOH)	119
6.3	PXRD of isonicotinamide/4-hydroxy-3-nitrobenzoic acid co-crystal (1-N:3-COOH)	120
6.4	The reference shieldings for the nicotinamdie and bipyridine systems.	124
7.1	Molecular structure for isonicotinamide/ 2,4,6- trihydroxybenzoate salt (1- $\text{NH}^+:$ 2- COO^-), isonicotinamide/4-hydroxy-3-nitrobenzoic acid co-crystal (1-N:3-COOH).	128
7.2	Isonicotinamide/ 2,4,6- trihydroxybenzoate salt (1- $\text{NH}^+:$ 2- COO^-)	129

7.3	^1H one-pulse MAS NMR spectra of (a) $1\text{-NH}^+2\text{-COO}^-$ and (b) 1-N:3-COOH compared to stick representations of calculated (GIPAW) ^1H chemical shifts	130
7.4	O-H...O hydrogen bonds in $1\text{-NH}^+2\text{-COO}^-$	133
7.5	C-H...O hydrogen bonds in $1\text{-NH}^+2\text{-COO}^-$	134
7.6	^1H - ^1H DQ-SQ MAS NMR spectra with skyline projections of (a) $1\text{-NH}^+2\text{-COO}^-$ and (b) 1-N:3-COOH	135
7.7	^{14}N - ^1H (600 MHz) - HMQC MAS spectra for (a) the $1\text{-NH}^+2\text{-COO}^-$ and (b, c) the 1-N:3-COOH	142
8.1	Molecular structure for 4,4-bipyridine5-sulfosalicylic acid ($4\text{-NH}^+5\text{-SO}_3^-$) and 4,4'-bipyridine/phthalic acid (4-N:6-COOH).	150
8.2	Molecular packing for 4,4-bipyridine5-sulfosalicylic acid ($4\text{-NH}^+5\text{-SO}_3^-$)	151
8.3	^1H one-pulse MAS (60kHz) NMR spectra of (a) $4\text{-NH}^+5\text{-COO}^-$ and (b) 4-N:6-COOH compared to stick representations of calculated (GIPAW) ^1H chemical shifts for the full crystal structure	152
8.4	A representation of the crystal structure of 4-N:6-COOH showing the mirror symmetry of the phthalic acid and bipyridine molecules	154
8.5	C-H...O weak hydrogen bonding interactions for $4\text{-NH}^+5\text{-COO}^-$	156
8.6	^1H - ^1H DQ-SQ MAS spectra with skyline projections of (a) $4\text{-NH}^+5\text{-COO}^-$ and (b) 4-N:6-COOH	157
8.7	^{14}N - ^1H - HMQC MAS (60 kHz) NMR spectra for (a,b) the $4\text{-NH}^+5\text{-COO}^-$ and (c) the 4-N:6-COOH	163
8.8	^{14}N - ^1H - HMQC MAS (60 kHz) spectra for the $4\text{-NH}^+5\text{-COO}^-$	164
9.1	The chemical structure of citric acid.	170
9.2	Citric acid.	170
9.3	One-Pulse ^1H MAS spectrum of citric Acid	171
9.4	^1H - ^1H DQ-SQ MAS NMR spectrum with skyline projections of citric acid	172
9.5	^1H (500 MHz) - ^{13}C CP MAS NMR spectrum of citric acid monohydrate	173
9.6	^1H (500 MHz) - ^{13}C CP MAS NMR spectrum of citric acid monohydrate	174
9.7	^1H (500 MHz) - ^{13}C CP MAS NMR spectrum of citric acid monohydrate	175
9.8	The structures of betaine, Caffeine, nicotinamide, nitrofurantoin, paracetamol and theophylline which form cocrystals with citric acid.	176
9.9	The hydrogen bond between H31 (H5 with citric acid labelling) and the N6 of the nicotinamide aromatic ring.	181

LIST OF FIGURES

9.10	Trend between isotropic chemical shift (δ_{ISO}) and $d(X...Y)$	184
9.11	The hydrogen bonding interactions of the carboxylic acid groups in the cocrystal of nicotinamide citric acid.	185
9.12	PXRD of Caffeine citric acid cocrystal	186
9.13	Molecular structure for the caffeine citric acid cocrystal	187
9.14	Spectra of (a) A ^1H one-pulse MAS NMR spectrum of a caffeine citric acid cocrystal and (b) a ^{13}C CPMAS NMR spectrum of a caffeine citric acid cocrystal.	188
9.15	Sildenafil Citrate Monohydrate	189
9.16	A ^1H one-pulse MAS NMR spectrum of sildenafil citrate monohydrate. . .	190
9.17	sildenafil citrate monohydrate obtained using GIPAW and viewed via MagresView.	190
9.18	Sildenafil citrate monohydrate	191
9.19	Sildenafil citrate monohydrate	192
9.20	^1H - ^1H DQ-SQ MAS NMR spectrum with skyline projections of sildenafil citrate monohydrate	193
9.21	A ^{14}N - ^1H - HMQC MAS (60 kHz) NMR spectrum for sildenafil citrate monohydrate	193
9.22	Sildenafil Citrate Monohydrate: highlighting the nitrogen atoms.	194

List of Tables

4.1	Comparison of absorptive and dispersive lineshapes	58
6.1	Computational details of the results which are presented in this thesis . .	122
6.2	Reference shielding	125
7.1	Experimental and GIPAW calculated ^1H chemical shifts for 1-NH $^+$:2-COO $^-$ and 1-N:3-COOH.	131
7.2	Hydrogen-bond distances and geometry	132
7.3	^1H - ^1H distances	138
7.3	Continuation of table 7.3	139
7.4	^1H - ^1H distances for the geometry-optimised (CASTEP) crystal structure of 1-N:3-COOH.	140
7.5	N-H distances (2.5 Å) and ^{14}N and ^1H NMR shifts for 1-NH $^+$:2-COO $^-$ and 1-N:3-COOH	141
7.6	A comparison of experimental and GIPAW calculated ^{15}N isotropic chemical shifts and ^{14}N quadrupolar parameters and shifts for 1-NH $^+$:COO $^-$ and 1-N:3-COOH.	144
8.1	Hydrogen-bond distances and geometry	153
8.2	^1H chemical shifts for 4-NH $^+$:5-COO $^-$ and 4-N:6-COOH.	155

LIST OF TABLES

8.3	^1H - ^1H distances ^a and SQ and DQ ^1H chemical shifts for the geometry-optimised crystal structure of 4-NH ⁺ :5-COO ⁻	160
8.3	^1H - ^1H distances ^a and SQ and DQ ^1H chemical shifts for the geometry-optimised crystal structure of 4-NH ⁺ :5-COO ⁻	161
8.4	^1H - ^1H distances and SQ and DQ ^1H chemical shifts for the geometry-optimised (GIPAW) crystal structure of 4-N:6-COOH.	162
8.5	N-H distances and ^{14}N and ^1H NMR shifts for 4-NH ⁺ :5-COO ⁻ & 4-N:6-COOH.	165
8.6	A comparison of experimental and GIPAW calculated ^{15}N isotropic chemical shifts and ^{14}N quadrupolar parameters and shifts for 4-NH ⁺ :5-COO ⁻ and 4-N:6-COOH.	166
9.1	Experimental and GIPAW calculated isotropic (full crystal and isolated molecule) chemical shifts.	171
9.2	H-H distances in citric acid corresponding to ^1H - ^1H DQ peaks in figure 9.4	173
9.3	Experimental and calculated ^{13}C chemical shifts for citric acid monohydrate.	174
9.4	Calculated shieldings, σ_{XX} , σ_{YY} , σ_{ZZ} , σ_{ISO} and $\delta_{ISO} = -[\sigma_{ISO} - \sigma_{ref}]$ for all of the hydrogen atoms within citric acid and the comparative hydrogens when the citric acid is in a cocrystal form with betaine, caffeine, nicotinamide, nitrofurantoin, paracetamol and theophylline. [†]	177
9.4	Continuation of table 9.4	178
9.5	Calculated (with geometry optimisation), calculated (without geometry optimisation) ^1H isotropic chemical shift and $\Delta\delta(^1\text{H})_{calc} - \delta(^1\text{H})_{nogeoopt}$ for the theophylline citric acid, piracetam-citric acid and betaine citric acid cocrystals.	180
9.6	Hydrogen bond parameters after geometry optimisation for carboxylic acid groups.	183
9.7	GIPAW calculated ^{15}N isotropic chemical shifts and ^{14}N quadrupolar parameters and shifts for sildenafil citrate monohydrate	194
10.1	Hydrogen bonds from literature and current research	200
10.2	GIPAW calculated ^{14}N quadrupolar parameters for nitrogen containing hydrogen bonds.	205
10.2	Continuation of Table 10.2.	206



Acknowledgements

First of all I would like to thank Prof Steven Brown for giving me the opportunity to complete a PhD at the University of Warwick, for which I will always be grateful.

I would also like to thank GSK for part-funding my PhD as Industrial CASE studentship as well as contributing to this research through regular conference calls and for providing me with an invaluable industry experience by allowing me to spend an extended period at one of their sites. In particular I would like to thank Dr Tran Pham for supporting and contributing to this research.

I'd like to thank my colleagues past and present for their support, help and friendship Manju, Ann, Aiden, Anjali, Trent and Emily.

I would also like to say thank you to all of the Warwick NMR group for their friendship, support and cake.

A special thank you to Steven for proof reading my thesis.

A special mention to my Mum, Dad, and my brothers Richard and Martin.

Finally, to Mathis, Stewart and Adalie, for their love, support and understanding.

LIST OF TABLES



Declarations

The work presented in this thesis is a result of my own original research carried out between January 2014 and December 2018, under the supervision of Professor Steven P. Brown at the University of Warwick. Where contributions of others are included, these are indicated within the text. This work has not been submitted as part of another degree.

LIST OF TABLES

Thesis Overview

1.1 Overview

This thesis will explore the use of solid-state NMR experiments, and the calculation of NMR parameters linking to X-ray Diffraction in order to characterise pharmaceuticals. Particular emphasis is given to studying the hydrogen bonding interactions which occur in pharmaceutical drug products to gain a greater understanding of the relationship between the ^1H isotropic chemical shift and ^{14}N quadrupolar parameters and the strength of different hydrogen bonds.

Chapter 2 provides an overview of current drug delivery forms and how co-crystals have the potential to be an alternative drug delivery method. Definitions of the different forms will be outlined along with their advantages and disadvantages. Specifically, co-crystals will be covered with reference to their impact in the pharmaceutical industry. The last section of this chapter gives an overview of what hydrogen bonds are, in which molecules they are normally found and their corresponding strength in different molecules.

Chapter 3 provides background information on how the different techniques used in this thesis have made a contribution to the field of NMR crystallography. Teachings of how past research has influenced the research that has been conducted in this thesis are presented, in respect to the NMR crystallography of pharmaceutical solids, namely pharmaceutical salts and cocrystals. An overview of diffraction is provided along with the advantages of using the GIPAW method of calculating NMR parameters and how the use of isolated molecule calculations has allowed greater insight into hydrogen bonding

CHAPTER 1. THESIS OVERVIEW

interactions. Furthermore, the advantages of using different solid-state NMR experiments involving a variety of nuclei namely ^1H , ^{13}C and $^{14}\text{N}/^{15}\text{N}$ is provided with reference to key areas of research in this area. Information on how co-crystals can be characterised is provided along with a discussion of how solid-state NMR can be used together with NMR calculations to aid this process.

Chapter 4 outlines the basic theory behind NMR; with key concepts and terminology explained. The classical model of NMR and the quantum mechanical approach is presented with the Hamiltonians of the key interactions. Specifically, the Internal Hamiltonians of chemical shielding, dipolar coupling, J -coupling and Quadrupolar coupling are detailed with particular focus on the Dipolar coupling and Quadrupolar coupling as they are important concepts in this thesis. Magic Angle Spinning and its role in solid-state NMR experiments is detailed and further details about NMR crystallography is provided.

Chapter 5 outlines the underlying experimental concepts explained in detail including: ^1H One-Pulse MAS, Cross Polarisation with Magic Angle Spinning (CP MAS), ^1H Double Quantum Magic Angle Spinning (DQ MAS), and HMQC experiments. The important concepts of phase cycling and dipolar decoupling and their importance in experiments is also provided. The final part of the chapter gives an overview of the NMR calculations used in this research. It covers why calculations are a useful tool and how they aid research in the area of solid-state NMR and in NMR crystallography. An overview of the foundations of the theory primarily Density Functional Theory (DFT) and Hartree-Fock Theory (HF), will be discussed. The exchange-correlation is introduced along with descriptions of the basis set and the use of pseudopotentials. The physical and computational approximations used in calculations are also presented and the importance of the GIPAW method in the ability to generate the NMR parameters. The section will end with an outlook on the potential of computational approaches with solid-state NMR. The theory behind XRD is outlined and a description of single crystal (SCXRD) and PXRD is provided with advantages and limitations of the techniques.

Chapter 6 is presenting experimental and computational details which are further utilised in the analysis of experiment results in chapters 7-9.

Chapter 7 and 8 presents research involving 1D ^1H MAS NMR and ^1H - ^1H DQ MAS NMR Solid-State NMR experiments used alongside 2D ^{14}N - ^1H HMQC experiments to determine protonation of a nitrogen site in a pharmaceutical salt. Experimental results are presented together with calculated NMR parameters determined using the GIPAW method in CASTEP (CAmbridge Serial Total Energy Package). This produces quantitative information which enables further insight into hydrogen bond interactions taking place within the molecules. Presented are two salt/co-crystal systems. The nicotinamide

system (in chapter 7); Isonicotinamide/ 2,4,6- trihydroxybenzoate salt ($\text{NH}^+:\text{COO}^-$), Isonicotinamide/4-hydroxy-3-nitrobenzoic acid co-crystal ($\text{N}:\text{COOH}$) with the bipyridine system (in chapter 8) comprising of: 4,4-Bipyridine5-Sulfosalicylic acid ($\text{NH}^+:\text{COO}^-$) and 4,4'-bipyridine/phthalic acid ($\text{N}:\text{COOH}$). For each system, results on the salt will be presented first followed by the cocrystal with results on experimental ^1H MAS NMR shown alongside GIPAW calculated ^1H resonances for the full crystal structure and isolated molecules. This is followed by ^1H - ^1H DQ MAS NMR experiments for each of the structures with key ^1H - ^1H distances noted. Finally, results for the ^{14}N - ^1H HMQC experiment are presented whereby the recoupling time is varied. The experimental results are viewed alongside calculated ^{14}N NMR parameters. Results show that the 2D ^{14}N - ^1H HMQC experiment allows a salt or co-crystal to be determined, furthermore a substantial change in the δ ^{14}N shift of 371 ppm in comparison to 68 ppm in ^{15}N Cross Polarisation (CP) MAS data (nicotinamide system) is also presented.

Chapter 9 presents research on co-crystals and a salt where citric acid is present. Research was conducted into the effect citric acid had on the various APIs in terms of hydrogen bonding inside the co-crystal and the salt. The research principally involved the calculation of NMR parameters. Results show the relationship between the ^1H isotropic chemical shift and the various hydrogen bond parameters.

The research presented in chapters 7 and 8 is developing a greater understanding of hydrogen bonding interactions in pharmaceutical salts and cocrystals. Chapter 10 gathers key concepts about hydrogen bonding interactions from 7 and 8 wherein a comparison between experimental and calculated hydrogen bonding parameters is presented in comparison with those from literature.

Pharmaceutical Solid-State Forms

2.1 Overview

This section will provide an overview of current drug delivery forms and how co-crystals have the potential to be an alternative drug delivery method for pharmaceuticals. Definitions of the different delivery forms, relevant to this thesis, will be outlined along with their advantages and limitations. Special focus will be given to pharmaceutical cocrystals with reference to their potential impact on the pharmaceutical industry. Information on how co-crystals can be characterised is provided along with a discussion of how solid-state NMR can be used together with calculated NMR parameters to aid this process. Finally, key hydrogen bonding information relevant to this research is presented.

2.2 Pharmaceutical Drug Products

A drug is a chemical substance that has been designed for the treatment, cure, prevention, or diagnosis of disease, or to enhance physical or mental well-being. A drug is manufactured into a drug product which is a finished dosage form, for example, a tablet, capsule or solution that contains an Active Pharmaceutical Ingredient (API). The API is the substance that directly acts in the cure, treatment, diagnosis or prevention of a disease. The API is normally administered in association with inactive ingredients known as coformers. Coformers can have a number of roles that enhance the pharmaceutical

product in some way, for example, delivery of the API [1–5], improving bio-availability and stability fillers, aiding taste and enhancing the effect of the API.

2.2.1 Pharmaceutical Salts

Currently pharmaceutical salts are the most common solid delivery method but they rely upon the API being ionisable in the drug product. This limits the number of potential API molecules and thus coformers molecules as they will also have to be ionisable. Pharmaceutical salts have a number of advantages which include improved stability, targeted drug delivery and improved taste. However, not all functional groups are ionisable which means preparation of a stable salt may not be possible for some drug products. A drug usually exists chemically as a weak acid or base. This is not always ideal for effective dissolution or absorption into the human body. Dissolution and absorption are important requirements of the drug to have an effect and it needs to be soluble in water. As a result, drugs are made into their salt forms (if possible) to enhance dissolution and aid absorption into the blood stream.

2.2.2 Pharmaceutical Co-crystals

Pharmaceutical co-crystals are crystalline materials which consist of an API and one or more crystal coformers bound together in a crystal lattice through a combination of non-covalent interactions. These non-covalent interactions can include hydrogen bonding [6] and π -stacking, thus negating the need for the API and coformer molecules to be ionisable opening up the possibility of utilising more chemical compounds to be researched in a cocrystal form or investigate whether cocrystals have a greater pharmaceutical impact than the salt form currently in use.

Solid-state polymorphic forms of an API can be classified as crystalline, amorphous, or solvate and hydrate forms. Co-crystals present a challenge for such a classification. Polymorphs normally contain only the API within the crystal lattice whereas co-crystals consist of an API with a neutral guest compound (a neutral molecule which is not a solvent), in the crystal lattice. Unlike salt forms, where the components in the crystal lattice are ionised, co-crystal components are in a neutral state and interact via non-ionic interactions. At the moment, there is no formal regulatory policy from The Food and Drug Administration (FDA) or The European Medicines Agency (EMA) which governs the classification of pharmaceutical co-crystals.

Co-crystals are classified as dissociable “API-excipient” molecular complexes (where the neutral guest is the coformer) and are thus treated as drug product intermediates. This

2.2. PHARMACEUTICAL DRUG PRODUCTS

has the effect of it not being regarded as a new API. Drug products that contain “API-excipient” co-crystals are not considered to contain a new API but rather a specifically designed component called a “co-crystal drug product intermediate”. While, to date, there are no co-crystal drug products on the market, there is considerable research and interest from pharmaceutical companies.

In general, in a salt $\Delta pK_a = pK_a(\text{base}) - pK_a(\text{acid}) \geq 1$. When this is the case there is usually substantial proton transfer which results in ionisation and subsequent formation of a salt form instead of a co-crystal. If $\Delta pK_a = pK_a(\text{base}) - pK_a(\text{acid}) < 1$, there is not expected to be substantial proton transfer. If this is the case, the API-excipient is classified as a co-crystal. However, these rules are only for guidance and other methods can be used to prove otherwise which is the basis for the investigation in this thesis.

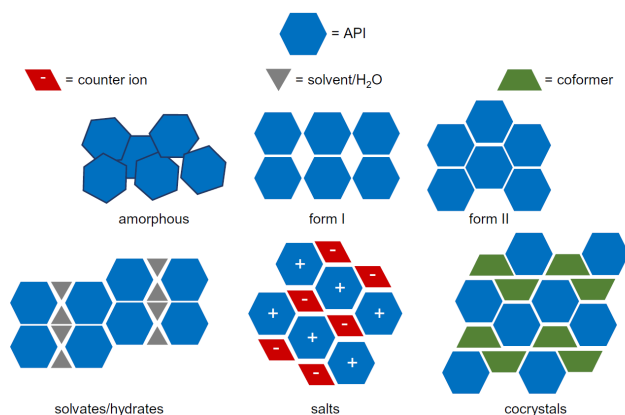


Figure 2.1: Schematic representations of different solid-state forms based on figure 1 in [7].

2.2.3 Amorphous dispersions

Amorphous forms are also an example of materials which have a high degree of solubility and bio-availability in drug products [8–10]. Amorphous materials are described as non-equilibrium materials, due to their lack of long range periodic order and the possession of disorder therefore they are considered unstable readily converting back to a crystalline state. Amorphous drug products are used in the pharmaceutical industry as they generally are more bio-available and soluble than their crystalline form [11]. Amorphous dispersions generally consist of a drug which is poorly soluble in water in a solid dispersion with a polymeric hydrophilic carrier. Solid dispersions of an amorphous solid with a highly water-soluble polymer can improve physical stability. Amorphous forms can be

identified using thermal methods such as differential scanning calorimetry but limitations exist when used in isolation. Access to the bulk properties is gained but access to the detailed structure is more difficult from thermal methods [12, 13]. XRD methods (which use long-range periodic order) will not be able to be used to provide detailed structural information whereas solid-state NMR is able to probe the atomic arrangement due to its non-reliance of periodicity.

2.2.4 Pharmaceutical Drug Products: The Potential of Cocrystals

As insoluble drug products are becoming more prevalent [14], this requires the need for new strategies and approaches which have the ability to modify physiochemical properties. Co-crystals, therefore, are attractive due to their possibilities in supramolecular design [15] which employs crystal engineering strategies. This allows the possibility of tailoring the physical and material properties for a specific drug product [16, 17]. Figure 2.1 shows the difference between a salt and a cocrystal.

Co-crystals are an attractive alternative to salt forms as increases in bioavailability [18] in poorly soluble drug molecules have been observed and there is further potential to enhance the properties of the API due to the huge variety of coformers. Other advantages presented in the review by Kumar et al [19] include:

1. API molecules are not limited to them being ionisable therefore all types of API molecules including those which are non-ionisable have the possibility to form co-crystals,
2. Cocrystals have intrinsic thermodynamic stability (unlike amorphous forms) and covalent bonds do not need to be altered,
3. An advantage particularly for pharmaceutical companies is that cocrystals provide an opportunity for pharmaceutical companies to increase Intellectual Property (IP) portfolios as the area of co-crystals provides a broad patent space due to the large availability of crystal coformers.

As a result, co-crystals have the potential to become more important in the development of pharmaceutical products in the future.

Whether salt or cocrystal, it is important to find the structure of the different delivery forms, as small changes in the molecular structure can have a significant impact upon the performance of the drug. This thesis will consider how solid-state NMR along with DFT calculations of NMR chemical shielding and quadrupolar interactions can distinguish between a pharmaceutical salt and a co-crystal.

2.2.5 APIs and their Identification Using Solid-State NMR

It is not uncommon that APIs exist in different solid forms: the most important difference being between the crystalline and amorphous forms. The amorphous API form lacks long range periodic order in contrast to the crystalline form which does possess long range periodic order of the unit cell. It is known that at least two different types of crystalline solids frequently occur: polymorphs and solvates. Related to solvates are desolvated solvates which are obtained when the solvent is removed from a solvate without altering the crystal structure.

Different solid forms of an API will have different chemical and physical properties (solubility, melting point, stability) meaning that they will have a different response to the processing and formulation of the drug product. This will also affect the properties of the final drug product so that the different forms will have different end properties for example bioavailability and stability. Therefore it is important to find the different solid forms of the drug product so that the presence of these solid forms does not impact on the final drug product and change its properties which could lead to a significant change in the performance of the drug product and affect patients safety. The importance of this is highlighted by the FDA providing guidance for (Abbreviated New Drug Application) ANDA which states that companies should have adequate knowledge about drug substance polymorphs [20]. Harris et al [21] have carried out structural determination studies of numerous APIs and some examples of APIs that have been investigated using solid-state NMR can be found in this reference. Polymorphs can result from differences in conformational properties of molecules or in their packing arrangements in the lattice [22], this means that the local environment of some of the nuclei will be different in different polymorphs thus resulting in the isotropic chemical shifts being different. It is possible to differentiate between the different polymorphs using solid-state NMR. Solvates can be determined by isotropic chemical shifts as the solvent causes a change in the local environment of some of the nuclei either directly or indirectly thus changing the properties of the lattice structure.

While studying APIs, NMR dynamic investigations focus on two areas: differences in the dynamic behaviour between different solid forms and in amorphous forms where it is important to find the relationship between stability and dynamics. As mentioned earlier, amorphous forms are important in the pharmaceutical industry due to them usually having an increase in solubility, dissolution rate and bioavailability. But amorphous forms are unstable so it is important to study them. Dynamics can be measured in NMR in two main ways: spectral features [23–28] which are able to study processes in the

slow-intermediate region (Hz-kHz), and by relaxation times [29–34] where processes are able to be studied in the intermediate-fast (kHz-MHz) region.

2.2.6 Excipients

The last section focused on the study of APIs however the most abundant part of a drug product is made up of excipients. excipients can be described as having two main roles in a solid dosage form (e.g. tablet). The first role is possessing properties for the processing or compression of the tablet which include binders, glidants and lubricants. The second role is when excipients add desirable characteristics to the tablet for example colours, sweeteners and taste modifiers. Particularly for excipients it is important to be able to characterise the physicochemical properties in the state the dosage form is administered i.e. in this thesis this is the solid-state. Most of the methods used for APIs can be applied to investigating excipients but there are other things to consider when dealing with excipients, one consideration is that they are usually much larger molecules than APIs. As they are larger this introduces greater complexity in determining structural and dynamical aspects. The majority of excipients are polymers, which means that they are very heterogeneous; the nuclei experiencing a range of different chemical environments. Due to the number of different chemical environments this can result in low resolution in the NMR spectrum. However small-mid sized molecules can be investigated by solid-state NMR techniques and progress is being made on being able to study larger sized molecules.

Four of the main physicochemical properties that are studied using solid-state NMR are:

1. Detecting different solids form of an excipient and detecting different excipients in a mixture. Pharmaceutically this is important as it can have an effect on the bioavailability of the drug and detecting amorphous forms has an effect on stability of the drug.
2. Determining what physical or chemical processes have an effect on the drug product which is important during storage of the product, these include exposure to temperature, humidity and pH.
3. Exploring new ways of administering a drug by subjecting the excipient to physical or chemical treatments which results in a modification of the excipient in the final drug product.
4. It is not just one excipient that can be present in a drug product there can be a mixture. Investigating the physical or chemical interactions that occur between

the excipients in the mixture is important as it can affect the final properties of the drug product, for example, bioavailability.

What is interesting is that polymorphism is known to occur in APIs but polymorphism in excipients is limited, three examples investigated using solid-state NMR are aspartame [35, 36], neotame [37, 38] and mannitol [39, 40].

2.3 Hydrogen Bonding Interactions

While a salt consists of an API and coformer joined through ionic interactions, a cocrystal consists of the API and coformer joined through non-covalent interactions such as hydrogen bonding. NMR is sensitive to hydrogen bond interactions and the relative strength of a hydrogen bond can be quantified. Results in this thesis look into firstly identifying hydrogen bonds and secondly look into determining the relative strength of the hydrogen bonds and seeing if there is a correlation which emerges as the strength of a hydrogen bond changes. This section gives an overview of what hydrogen bonds are, in which molecules they are normally found and their corresponding strength in different molecules. The discussion is based on that presented in reference [41].

A hydrogen bond is a donor-acceptor interaction involving hydrogen atoms. The letters A and B are used for the term donor and acceptor, respectively, because of the analogy with the Bronsted-Lewis acid which is a proton donor and the base which is a proton acceptor. They are formed when the electro-negativity of A relative to H in a A-H covalent bond acts to withdraw electrons and has the effect of leaving the proton deshielded. The acceptor B must have a lone-pair of electrons or polarisable π electrons for it to be able to interact with the donor A-H bond. There are a whole range of hydrogen bonds: strong hydrogen bonds behave like covalent bonds, whereas weak hydrogen bonds behave more like van der Waals forces. However, most hydrogen bonds are found between the classification of “strong” and “weak”.

Strong hydrogen bonds are formed by groups where there is a lack of electron density in the donor group, this also relates to an excess of electron density in the acceptor group. Intermediate hydrogen bonds are the most common and are generally formed by neutral donor and acceptor groups. Here, the donor atoms will be electronegative in comparison to the hydrogen atom and the acceptor group will have a lone pair of electrons. It is these hydrogen bonds which are important for biological molecules. The weak form of the hydrogen bond is formed when the hydrogen atom is covalently bonded to a slightly more electro-neutral atom such as C-H, Si-H or when the acceptor group has no lone-

pairs but has π electrons, such as $\text{C}\equiv\text{C}$ or an aromatic ring. The hydrogen bond therefore depends on the type of the donor and acceptor group.

Hydrogen bonds can be both intramolecular and intermolecular interactions. Intramolecular interactions occur when the donor and acceptor group are part of the same molecule and intermolecular interactions occur if the donor and acceptor group are on different molecules. Three important parameters are used to describe the geometry of a hydrogen bond and will be referred to throughout the results sections: A-H (covalent bond length), H-B (hydrogen bond length) and A-B (hydrogen bond distance). It is these parameters which define the hydrogen bond angle, which is represented by: $\angle\text{AHB}$. Only in very strong hydrogen bonds is this angle 180° . For other hydrogen bond interactions, the angle X-H...A often varies from the 180° .

There are a number of techniques which are used to characterise pharmaceutical samples, comprising PXRD, differential scanning calorimetry (DSC), and vibrational spectroscopies including Raman and IR. At the moment PXRD is the "go to" technique for identifying compounds however, challenges are faced when presented with mixtures of solid phases where the effects of preferred orientation have a large effect. If all crystal structures of possible solid phases in the mixture are known then Rietveld refinement can be used which takes into account effects of preferred orientation within the crystal. Research conducted by Li et al [42] showed that the error associated with DSC or PXRD was lower than that obtained by Raman spectroscopy. Vibrational spectroscopy methods are an alternative to PXRD as they are also able to obtain structural and polymorphic information.

In order to produce an x-ray diffraction pattern an x-ray is shined, for example, on a crystal, the x-rays are diffracted to produce a pattern which is characteristic of the structure. SCXRD is when the diffraction pattern is obtained from a single crystal and PXRD is when the diffraction pattern is obtained from a powder. The advantage of PXRD, as mentioned previously, is that single crystals do not have to be made thus making the technique accessible to a greater number of samples. As a result, the diffraction pattern will represent the bulk material of a crystalline solid. Most materials have a unique diffraction pattern and these patterns are stored on databases, such as the CSD. This allows a lot of samples to be easily identified using the databases. The purity of a sample can also be determined along with the generation and refinement of lattice parameters. Rietveld refinement is commonly used to generate a theoretical structure of the sample under investigation [43].

IR spectroscopy is the study of how IR interacts matter. The fundamental measurement obtained in IR spectroscopy is an IR spectrum, which is a plot of measured IR intensity

2.3. HYDROGEN BONDING INTERACTIONS

versus wavelength (or frequency) of light. When a molecule absorbs IR radiation, its chemical bonds vibrate. The bonds can stretch, contract, and bend. For a molecule to absorb IR a molecule must have a vibration where the change in dipole moment with respect to distance is non-zero. A lot of functional groups absorb IR radiation at around the same wavenumber, independent of what the rest of the structure consists of. For example, C-H stretching vibrations usually appear between 3200 and 2800 cm^{-1} and carbonyl(C=O) stretching vibrations usually appear between 1800 and 1600 cm^{-1} . These ranges are known as band markers/group frequencies and are used to identify the presence of different functional groups in a sample. As with all techniques IR has limitations: atoms or monatomic ions and homonuclear diatomic molecules do not have IR spectra plus complex mixture and aqueous solutions are challenging to analyse [44, 45]. In general, the width of IR bands for solid and liquid samples is determined by the number of chemical environments which is related to the strength of intermolecular interactions such as hydrogen bonding. If hydrogen bonds are present in a molecule the number and strength of intermolecular interactions will vary resulting in bands being broader. When intermolecular interactions are weak, the number of chemical environments is small, and narrower IR bands are observed.

The region of the IR spectrum from 1200 to 700 cm^{-1} is commonly known as the "fingerprint region". This is because a large number of IR bands are found there. Many different vibrations, including C-O, C-C and C-N single bond stretches, C-H bending vibrations, and some bands due to benzene rings are found in this region. Due to the presence of a high number of bands the fingerprint region is often the most challenging to analyse[46].

In comparison to the vibrational technique of IR, Raman spectroscopy can simplistically be described as the use of monochromatic light, such as from an argon-gas laser, passing through a sample, the light being scattered at right angles to the incident beam and analysed by an optical spectrometer. Spectra is produced when photons are "captured" by molecules in the sample and "gain" a small amount of energy due to changes in the molecular vibrational and rotational energies before the photon is emitted and scattered. The changes in the vibrational and rotational energies result in changes in wavelength of the incident light. The changes are detected as lines falling both above and below the wavelength of the incident light. The line positions in Raman spectra represented by wave numbers [47, 48].

Although changes in wavelength in Raman scattering correspond to absorption or emission of IR radiation, IR and Raman spectra are not identical. Valuable information about molecular symmetry may be obtained by comparing IR and Raman spectra. When a

bond is electrically symmetrical it does not absorb IR radiation and, for this reason, symmetrical diatomic molecules do not provide IR absorption spectra. However, excitation of symmetrical vibrations, such as in ethene, does occur in Raman scattering. Therefore, it is possible to deduce that a molecule has no important symmetry if all IR bands are the same as found in Raman scattering.

The advantages of Raman scattering are that it does not damage the sample, water produces very little signal, there is a large range which is beneficial for both organic and inorganic materials and it produces sharper peaks with less noise than IR. Limitations of the technique are that it can not be used for fluorescent materials, metals or metal alloys. Generally, Raman spectroscopy is more attractive than IR due the use of its smaller bandwidths.

There are a lot of experiments which can identify hydrogen bonds and each will have their own way of describing what a hydrogen bond actually is. Methods such as IR, Raman, and microwave spectroscopy define the hydrogen bond in terms of vibrational motions. Diffraction techniques measure bond length and bond angle while thermodynamic experiments measure hydrogen bond energies. In IR spectroscopy, the width of IR bands for solid and liquid samples is determined by the number of chemical environments which is related to the strength of intermolecular interactions such as hydrogen bonding. In any sample where hydrogen bonding occurs, the number and strength of intermolecular interactions varies greatly within the sample, causing the bands in these samples to be particularly broad.

Neutron diffraction can also be used to characterise molecules. Where x-rays are scattered by electronic density in atoms, neutrons are scattered by the nuclei. This makes neutron diffraction dependent on nuclear properties rather than atomic number as in techniques involving x-rays. This can result in greater accuracy in identifying unknown samples, especially between materials which are similar in composition as the interaction is with the nucleus of the atom rather than the outer electrons. Where identifying light atoms in x-ray diffraction is difficult neutron diffraction is able to locate both light and heavy atoms posing an alternative to x-ray analysis. In particular, the ability to locate proton positions is of importance for research involving hydrogen bonding. However, a disadvantage of neutron scattering is in the analysis of protons due to their large incoherent cross section. For simple molecules it would then be required to deuterate the sample but this would require considerable synthetic effort. Furthermore, if protons are substituted in a molecule with deuterons this would effect the bond lengths in a hydrogen bond possibly providing inaccurate results [49].

2.3. HYDROGEN BONDING INTERACTIONS

The intensity of the scattered neutrons will relate to the wavelength at which it was emitted. The arrangement of atoms in a material will result in coherently and/or incoherently scattered neutrons. Incoherent scattering is usually due to the isotopes and nuclear spins of the atoms. An advantage of the technique is the magnetic scattering of neutrons whereby neutrons which possess a magnetic moment are able to interact with the orbital or spin magnetic moment of atoms in the sample material (note that not all nuclear isotopes possess magnetic moments - only those which have unpaired electron spins) [50, 51].

A drawback of the technique is that a source of neutrons (made in a nuclear reactor) is required requiring a great deal of energy. In addition, relatively large crystals are needed ($\sim 1 \text{ mm}^3$ [52]). This may not always be possible especially in the area of pharmaceutical cocrystals. When comparing neutron diffraction with x-ray diffraction: neutrons better describe atomic level chemical interactions, whereas x-rays provide a better idea of the macromolecular structure of the sample being examined.

In solid-state NMR, the ^1H chemical shift of a hydrogen bonded proton is a sensitive indicator of the strength of a hydrogen bond [53]. The chemical shift is caused by the change in the electronic environment around the proton. Recently, solid-state NMR experiments have been combined with calculation of NMR parameters. This has allowed better interpretation of the effect hydrogen bonding has on the ^1H chemical shift. This has been shown in particular with the comparison of chemical shifts calculated for the full crystal structure and for the isolated molecule [54]. Such approaches are used in this thesis.

Due to the higher electro-negativity of oxygen atoms (3.4) compared to hydrogen atoms (2.2), intermolecular hydrogen bonds can form. Specifically, when a hydrogen atom in a molecule is hydrogen bonded, the electron density around it decreases, thus making it more deshielded than a hydrogen atom that is not taking part in an hydrogen bond interaction. This deshielding will increase the amount of magnetic field it experiences and therefore will have a higher ppm (or a higher chemical shift). The stronger the hydrogen bond, the more deshielded the hydrogen nucleus will be and thus the higher the chemical shift. As a result, hydrogen as part of a hydrogen bonding interaction can have chemical shifts of up to 20 ppm.

NMR Crystallography of Pharmaceutical Solids

3.1 Introduction

The first seminal accounts of NMR crystallography in the literature were by Harris [55] and Taulelle in 2004 [56], with a NMR Crystallography Handbook produced in 2009 [57]. These accounts detailed how the measurement of NMR parameters, in particular the chemical shift, obtained from MAS NMR spectra used with quantum mechanical computations is able to provide crystallographic information. Crystallographic information obtained using this methodology have included the determination of the number of molecules in the asymmetric unit cell and molecular symmetry in a solid-state environment, and the assignment of space group. Various examples have been provided to show the versatility of the methodology, for example, the probing of intermolecular hydrogen bonding in cortisone acetate polymorphs and solvates using chemical shift information (also measuring full tensor parameters [55]). As early as 2004, advances in solid-state NMR enabled Taulelle et al [56] to solve an inorganic crystal structure from NMR data alone.

3.2 Diffraction

Solid-state NMR can be used to aid the process of structure determination using PXRD. Solid-state NMR can verify a proposed structure from PXRD [58–65], for example, by supplying restraint information or and estimation of structures to aid with the structure

CHAPTER 3. NMR CRYSTALLOGRAPHY OF PHARMACEUTICAL SOLIDS

solution calculation that takes place during the PXRD process. The restraint information, for example, can be input into a computation algorithm to produce an estimate of a structure subsequently enabling crystal structures to be solved by Rietveld refinement. Common restraint information that is useful to solve the crystal structure encompasses specific internuclear distances, molecular conformations and bonding arrangements in the material.

Even though solid-state NMR can be used with PXRD to verify a proposed structure solid-state NMR can provide a lot of information that PXRD or XRD does not. Solid-state NMR is a non-destructive technique which does not require long range periodicity of materials. It can reliably locate light and heavy atoms. The following example from literature describes a use of solid-state NMR in terms of being used with PXRD but this by no means restricts solid-state NMR to this function.

Research conducted by Hughes et al in 2017 [66] aimed to showcase the advances in the PXRD and NMR approach for structure determination of powdered solids by solving the structure of a complex molecule which contained 90 atoms. The molecule under investigation dG(C₁₀) was studied in previous solid-state NMR studies [67, 68] and has many applications in the area of photoelectric devices. The structure is known to inter-convert between quartets and ribbons, therefore, it is important to understand the hydrogen bonding interactions that are present so that the preferred structural properties of dG(C₁₀) can be determined. It is a periodic solid and does not exhibit amorphism.

Solving the structure of dG(C₁₀) directly from PXRD proved very challenging notably, due to the presence of a very intense peak at $2\theta = 3.4^\circ$ the diffraction pattern representing more than 45% of the total diffraction intensity across the 2θ range which was recorded (see figure 3.1), as well as a very high background in this low-angle region due to x-ray scattering in air. Moreover, the large size and flexibility of dG(C₁₀) resulted in a large number of trial structures which gave similar fits to the data. In order to find the correct structure, it was necessary to obtain other information which could reduce the number of trial structures. Solid-state NMR studies of dG(C₁₀) provided this information, in particular the information on the strong intermolecular hydrogen bond of N-H...N between the atoms labelled N7 and N10 enabled the rejection of a lot of the trial structures suggested. Using the restraint information obtained from solid-state NMR thus enabled the correct solution of the structure to be found. The solid-state NMR parameters calculated from the final refined crystal structure were in good agreement with the experimentally obtained parameters, supporting this approach for accurate structure determination. Solid-state NMR calculated and experimental parameters, particularly isotropic chemical shifts, therefore can be used to verify that structures are correct. The

3.3. THE GAUGE INCLUDING PROJECTOR AUGMENTED WAVE METHOD (GIPAW)

structure solution of dG(C₁₀) shows that this method could be applied to molecules of even greater complexity in the future.

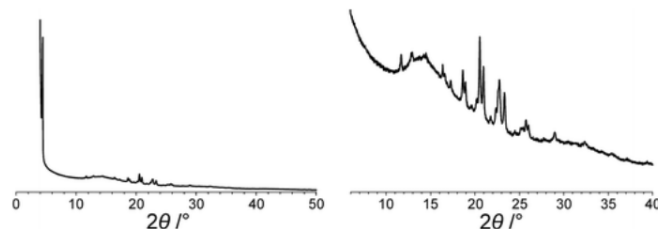


Figure 3.1: Experimental powder pattern for polymorph 1 of dG(C₁₀). The full powder XRD pattern is shown on the left; the expanded region from $2\theta = 6^\circ$ to 40° is shown on the right. Reproduction of figure 3 from [66]

3.3 The Gauge Including Projector Augmented Wave Method (GIPAW)

Combining experimental proton chemical shifts obtained using MAS and the quantum mechanical computations of proton shieldings can be used to determine the position of a proton atom in an intermolecular hydrogen bond [55]. This has been achieved using the GIPAW method implemented in CASTEP [69–72]. Crystallographic repetition was incorporated into quantum mechanical calculations which use DFT [71, 72] and the use of pseudopotentials.

Quantitative analysis of intermolecular interactions has been shown through the use of GIPAW using CASTEP when calculated chemical shift values from a full crystal have been compared to those from an isolated molecule [73]. Webber et al [74] combined 1D and 2D state of the art experimental solid-state NMR experiments combined with computed NMR parameters using the GIPAW method which is able to calculate chemical shift data for the full crystal structures and isolated molecules. $\Delta\delta_{cryst-mol}$ is calculated which provides valuable information on hydrogen bonding interactions and therefore packing arrangements in those structures. It was observed that there was a large $\Delta\delta_{cryst-mol}$ value of 5-6 ppm for the NH chemical shift related to the hydrogen bond of N-H...N, similar values for NH moieties $\Delta\delta_{cryst-mol}$ were observed in *L*-histidine ·HCl·H₂O [75] and uracil [76], which possess intermolecular N-H...O hydrogen bonds.

CHAPTER 3. NMR CRYSTALLOGRAPHY OF PHARMACEUTICAL SOLIDS

The potential of this technique has been recognised and utilised in this thesis to probe structures of pharmaceutical interest to gain an understanding of hydrogen bonding interactions present.

3.3.1 Isolated Molecule Calculations

In the field of NMR crystallography the method of isolated molecule calculations using DFT which employs the CASTEP code has been shown to aid structure determination, and identify interactions within the crystal structure of which hydrogen bonding is an example [53, 73, 76–84].

Isolated molecule calculations have been used in this thesis to provide insight into hydrogen bonding interactions in the crystal structure of pharmaceutical salts and cocrystals by comparing chemical shifts calculated for the full crystal structure and for an isolated molecule. This was first used to quantify weak hydrogen bonding interactions of CH...O in maltose [73] by Yates et al where the key finding was that directionality as well as a close H...O distance ($<2.7 \text{ \AA}$) is needed for a noticeable change in the ^1H chemical shift (upto 2 ppm) in C-H...O hydrogen bonding.

Until this technique was developed the evidence for C-H...O hydrogen bonds had been provided by diffraction techniques which showed the proximity of the CH hydrogen and the oxygen atoms (see reference [85] for an example in carbohydrates and reference [86] for an example on proteins). Yates et al wanted to distinguish if the close proximity which can be indicated by diffraction techniques was a bonding interaction or a result of close proximity due to packing arrangements determined by other interactions. NMR would be able to identify the presence of a hydrogen bond as NMR is sensitive to hydrogen atoms and thus hydrogen bonding. The approach of NMR crystallography which particularly focuses on using experiment and computation has been used previously to investigate the hydrogen bonds of N-H...O and O-H...O as well as π - π interactions on ^1H and ^{13}C solid-state NMR chemical shifts [55, 87–92]. The method involved determining the parameter $\Delta\delta_{\text{cryst-mol}}(^1\text{H})$ which is the difference between the ^1H isotropic chemical shift calculated for the full periodic crystal structure and that calculated for an isolated molecule. Using this parameter Yates et al were able to find a correlation between a large $\Delta\delta_{\text{cryst-mol}}(^1\text{H})$ and a short H...O distance and a CHO bond angle greater than 130° . Yates et al also point out that previous studies into classifying directionality in the C-H...O hydrogen bond using crystal structure data have failed to quantify the degree of bonding with the C-H...O proximity.

After the success of Yates et al [73] using isolated molecule calculations on the molecule of maltose it was subsequently applied to uracil where both the weak C-H...O and the more conventional N-H...O hydrogen bond were investigated [76]. The investigation found a difference of 2 ppm and 5 ppm respectively between the isolated molecule calculations of the ^1H chemical shift and the same calculation for the full crystal structure. Uldry et al [76] investigated not only intermolecular hydrogen bonding using computation and NMR but also intermolecular ring current effects. Molecules which contain hydrogen bond groups also commonly contain aromatic moieties, and intermolecular ring current effects were taken into account during the analysis of the ^1H chemical shift. This was not needed in the investigation by Yates et al [73] due to maltose having no aromatic moieties. The isolated molecule calculations were further used in research by Bradley et al in 2011 [83] in the study of the γ polymorph of indomethacin. Hydrogen bonding interactions were observed of the form O-H...O where a difference of 7 ppm was found between the isolated molecule and full crystal structure calculation.

All of the research undertaken above by the various research groups used the CASTEP code for the computation (for a brief non technical overview of CASTEP where key features are highlighted see reference [93]), however there are other codes available which can achieve similar results. Schmidt et al [75] have utilised the CPMD (Car-Parrinello Molecular Dynamics) code to analysis the bulk ^1H NMR chemical shifts for a series of biochemically relevant crystal structures using computation and NMR and have undertaken isolated molecule calculations. There are also other codes which can compute NMR parameters such as quantum espresso [94].

3.4 ^1H MAS NMR

Hydrogen atoms participating in a hydrogen bond result in high chemical shifts for their resonances [95]. High resolution spectra of ^1H can be obtained through techniques such as Combined Rotation And Multiple Pulse Spectroscopy (CRAMPS) [96, 97]. Technological advances have meant that MAS rates have been getting faster which has resulted in increases in resolution of the NMR spectra as resonances are narrowed. As the achievable MAS frequency has increased, 1D ^1H MAS NMR can be utilised for more compounds to identify hydrogen bond interactions, which are observed in the proton chemical shift generally above 10 ppm. Some studies [95, 98] have investigated hydrogen bonding interactions and have included correlations between proton chemical shifts and hydrogen bond length. These were obtained from materials which have known proton positions (or distances between relevant heavy atoms) from diffraction structures.

CHAPTER 3. NMR CRYSTALLOGRAPHY OF PHARMACEUTICAL SOLIDS

It is well known that strong dipolar couplings between protons cause broadening, in solid-state NMR spectra even when MAS is used. Even though ^1H - ^1H interactions cause this broadening the information that can be gained from ^1H - ^1H contacts is very valuable, when it is possible to access it. In fact ^1H - ^1H NMR constraints are being increasingly used for the characterisation of not only powders at natural isotropic abundance but also for isotropically enriched systems [99–102]. The usefulness of ^1H - ^1H interactions was shown by not only being useful for organic systems but also non-biological systems as was outlined by Geen et al (1994) [103] and by Brown et al (2001) [104]. The subsequent use of the CRAMPS experiment which produces direct high proton resolution in spectra [105, 106] has also aided structure determination and the assignment of resonances in the spectra. Furthermore, the use of the high resolution ^1H - ^1H DQ MAS experiment has also greatly aided the characterisation of molecules at natural abundance [97, 107].

3.4.1 ^1H Spin Diffusion NMR Experiments

For crystalline organic materials, ^1H spin diffusion NMR experiments [108–111] have shown to be a possible avenue to determine crystalline organic structures. ^1H is utilised which has a high natural abundance (99.99%) and as a result there are very strong dipolar couplings between ^1H - ^1H atoms. ^1H spin diffusion (exchange of magnetisation between ^1H - ^1H nuclear spins) in solids is facilitated by the dipolar coupling which is dependent on distance. Spin diffusion represents a potential way to determine the structure of a material (See the research by Elena et al [112] for more information on spin diffusion in organic solids and the theory behind it). The rate of spin diffusion however is not straightforward as it depends on other factors notably:

1. Orientation of internuclear vectors.
2. Chemical shift anisotropies of the coupled spins.
3. The coupled spin being coupled to other additional spins.
4. Rate of MAS [108].

Elena et al in 2006 noted that a large barrier to the progress in materials and molecular science was due to the inability of the scientific community to solve the crystal structure of powdered samples [112]. Elena et al suggested an approach that would allow the crystal structure of powdered samples (at natural abundance) to be solved. In particular this involved the combination of molecular modelling with experimental ^1H spin-diffusion data from high-resolution MAS NMR to solve the 3D structure of an organic molecule.

Isotropic labelling of a sample can help solve the crystal structure but where this is not possible, for example due to cost and time, structural studies of small organic molecules remains challenging. Using the approach detailed, the molecular packing of the small organic molecule, β -L-Aspartyl-L-alanine, under investigation was able to be determined to within a rmsd of 0.33 Å of the known coordinates.

Pickard et al in 2007 [113] further showed that using spin diffusion and DFT calculations could determine the packing of an organic molecule, β -L-Aspartyl-L-alanine. The root mean square of the atom to atom distances between the known structure and the results obtained from solid-state NMR differed by only 0.13 Å. This showed that the joint DFT and NMR method was a powerful approach to structure determination and had great potential in its application to determine other structures and further develop the methodology.

In fact in 2009 Salager et al [114] proved that ^1H spin diffusion could be used to determine the packing of a small organic drug molecule called thymol from 2D NMR experiments with calculated ^{13}C and ^1H NMR chemical shifts.

3.5 ^{13}C CPMAS NMR

The ^{13}C CP MAS experiment is another technique enabling crystal structures to be solved alongside the routine and commonly used methods of: vibrational spectroscopy, mid-infrared, Raman and XRD.

The ^{13}C CP MAS spectra can be used to identify the presence of a mixture of compounds by taking a “finger print” of that particular molecule [21, 115–117]. Identification for a mixture of compounds can be seen in the research conducted by Schmidt in 2005 [118] where the ^{13}C CP MAS spectrum was used to identify different polymorphic forms in a mixture. The stability of a polymorphic form can also be tested using variable temperature solid-state NMR: the resulting spectra can then be compared to see the point that one polymorphic form changes to another. Rubin-Preminger et al [119] investigated different polymorphic forms using variable temperature solid-state NMR, where it was shown that an increase in temperature led to greater amounts of particular polymorphic forms.

From 1995, the first steps beyond using solid-state NMR as a “fingerprint tool” occurred especially as high-field magnets were developed with the ability to spin at faster MAS rates. Solid-state NMR started to be used to investigate drug systems exhibiting, for example, polymorphism, hydration, solvation and to those exhibiting different salt form-

CHAPTER 3. NMR CRYSTALLOGRAPHY OF PHARMACEUTICAL SOLIDS

ation behaviours [29, 37, 120–126], thus being applicable to a wide variety of structures such as cocrystals, proteins, disordered solids, complex systems and phase mixtures.

An example from literature which has utilised the 1D ^{13}C CP MAS experiment and shows its benefit is a study by Reutzel-Edens et al [121]. ^{13}C CP MAS experiments were used to identify seven crystal forms of a pharmaceutical called olanzapine. Observation of the ^{13}C CP MAS spectra allowed the differentiation of the different compounds and all ^{13}C resonances were able to be assigned. The authors recognised that XRD could have been performed but noted that between two of the different forms the resulting diffraction patterns were difficult to differentiate, while the ^{13}C CP MAS NMR spectra highlighted significant differences.

In the pharmaceutical industry, it is important to identify the different amorphous forms present in a product to see their stability in respect to, for example, temperature, humidity as many are metastable, reverting into a more stable crystalline form. Amorphous forms can be identified in a ^{13}C CP MAS spectrum, as they usually form broad peaks in contrast to the narrow peaks formed by crystalline materials. The broad peaks arise due to the lack of long range periodic order which means that the nuclei experience a variety of different orientations resulting in the isotropic chemical shift values being distributed. The identification of an amorphous form was conducted by Apperley et al [127] on the pharmaceutical compound of indomethacin where a broad peak in the ^{13}C CP MAS spectrum was identified from the narrow peaks for the crystalline form.

MAS is able to average out most broadening effects which result from chemical shielding but not from dipolar coupling. MAS is therefore combined with decoupling pulse programs. In amorphous forms residual anisotropic interactions could be a cause of broadening and the amount of molecular motion. Broadening of amorphous forms arise due to a range of chemical environments present. Amorphous forms do not have long range periodic order in the crystal lattice but are instead described as disordered molecules. Due to the disorder there will be a large range of local chemical environments present. Solid-state NMR observes anisotropic interactions and results in the broadening of spectra in solid-state NMR. The broadening includes information on the chemistry, structure, and dynamics of the amorphous form (see section text2.2) Note that amorphous forms are not a focus of this thesis.

There is current interest in crystalline structures which exhibit more than one distinct molecule in the asymmetric unit, ($Z' > 1$) [128–130]. Crystals can possess more than one molecule of the same species in the asymmetric unit, which will be in different crystallographic sites, thus, having a different local chemical environment. The individual atoms which make up the asymmetric units will have different chemical shifts in the NMR

spectra although in some instances these differences can be very small and therefore not resolvable. Generally, in ^{13}C CP MAS NMR spectra, multiple resonances are observed when there is more than one molecule in the asymmetric unit cell. The number of resonances will indicate the number of molecules that are present. This information is extremely useful and can be used as a restraint in the attempt to solve crystal structures using PXRD. An example from literature which used the ^{13}C resonances to aid structure determination was presented by Balimann et al [131] in 1981, being one of the early instances where the NMR data was used in this way. Calcium acetate monohydrate showed four ^{13}C signals for the carboxyl carbons where, at the time of publication, XRD was not able to determine a structure for this molecule. In another example in 2002 by Schmidt et al [132], ^{13}C MAS NMR spectra showed that the polymorphic Form II of oxybuprocaine hydrochloride contained two molecules in the asymmetric unit, whereas Form I contained one molecule.

An application of MAS NMR to provide hydrogen bond information and therefore arrangements of structures can be shown from the early 1990s [133, 134]. The pharmaceutical compound of cortisone acetate (II) has three anhydrous forms and several solvates; ^{13}C CPMAS spectra was obtained for the different forms. The number of peaks in each of the different spectra were observed and it was identified that Form III had three molecules in the asymmetric unit cell, while all the others had one. While identification of the resonances was being conducted, it was also noted that there was a difference in chemical shift of the carbon atoms labelled as C5 and C22 in the structure. It was suggested that a cross over of the signals may be occurring and this could be facilitated by hydrogen bonding. Four of the seven forms investigated have a known crystal structure determined from XRD, therefore, the chemical shifts could be correlated with hydrogen bonding interactions. This data was then used to study the remaining 3 structures which did not have a known crystal structure and, by observing the differences and similarities in the chemical shift of the carbon atoms, it allowed conclusions about the hydrogen bonding interactions to be determined.

A more recent example from literature which uses ^{13}C resonances to aid structure determination by observing the number of distinct molecules in the asymmetric unit was published by Webber et al in 2010 [74]. The assignment of ^{13}C resonances for the six distinct molecules ($Z'=6$) was a challenge due to the small differences in chemical shift. However, Webber et al [74] presented the assignment of all 66 ^{13}C resonances in the six distinct molecules (11 resonances per distinct molecule) using ^1H - ^{13}C MAS-*J*-HMQC [135] 2D solid-state NMR experiments and GIPAW chemical shift calculations. High resolution in the ^1H dimension was required in order to assign the directly bonded CH, CH₂

CHAPTER 3. NMR CRYSTALLOGRAPHY OF PHARMACEUTICAL SOLIDS

or CH₃ groups and was achieved using ¹H homonuclear decoupling sequences [136], for example frequency-switched [137] and phase-modulated [138] Lee-Goldburg. Sakellariou et al [139] developed the DUMBO (Decoupling Under Mind Boggling Optimisation) set of homonuclear decoupling sequences which were utilised in the examples described below. In addition, coherence transfer between ¹³C and ¹H atoms through ¹J_{CH} couplings was also used. The assignments were possible due to the sensitivity of the proton chemical shift to intermolecular interactions such as hydrogen bonding [104, 140] and the use of the GIPAW calculation of NMR parameters. Webber et al therefore presented that quantitative insight can be gained into intermolecular interactions through the observation of NMR chemical shifts particularly when comparing calculations for the full crystal structure with those for isolated molecules. The results show that there were differences in the chemical environments for each of the independent molecules shown by the multiplicity of resonances, for example, the carbon atom labelled C5 in the material under investigation produced six distinct resonances at different chemical shifts.

Shifting the focus from the ¹³C spectra, a range of ¹H resonances of the protons attached to the aforementioned carbon atoms was observed. Even though the proton chemical shift range is smaller than that for carbon and the range of experimental ¹H resonances was small (up to 1 ppm for CH and CH₃ groups), the high resolution in the ¹H dimension allowed the resonances to be determined in the 2D experiment which are overlapped in a 1D ¹³C CPMAS spectrum. The GIPAW computed chemical shifts were in good agreement with the experimental ¹³C and ¹H chemical shifts. It was also noted that in the 2D ¹H-¹³C MAS-*J*-HMQC spectra recorded with ¹H FSLG (Frequency Switched Lee-Goldberg) decoupling, there was increased resolution than in the 2D experiment of ¹H DQ MAS highlighting the potential of the ¹H-¹³C MAS-*J*-HMQC in future use. Even though the ¹H DQ MAS experiment may have lower resolution, DQ peaks which involve NH protons are observed which allow intra and intermolecular proximities between the atoms due to hydrogen bonding interactions, to be determined.

Poppler et al [79] used SC XRD with solid-state NMR applied to a cocrystal of agro chemical relevance. Here, two dimensional ¹H-¹³C DQ MAS NMR was used to probe connectivity information within the molecules. ¹H NMR experimental chemical shifts were also compared to calculated values to gain insight on hydrogen bonding interactions and ring current effects, with the GIPAW calculations for the full crystal structure and also for isolated molecules also being carried out.

Harris et al [141] has presented research on the polymorph of oxybuprocaine hydrochloride. There are two molecules in the asymmetric unit cell resulting in splitting in the spectra. Here the range of NMR experiments used included a 2D ¹³C-¹³C IN-

ADEQUATE (Incredible Natural Abundance Double Quantum Transfer Experiment), ^1H - ^{13}C HETCOR and ^{13}C CP MAS. Particular focus was given to four ethyl groups which are attached to NH^+ nitrogens one resulting in an unusually low chemical shift in comparison to the three other groups. As can be seen later in this NH^+ is of particular importance in pharmaceutical compounds. Harris et al [141] acknowledge that measurement of dipolar couplings which give rise to structurally relevant information, usually involve isotropic labelling especially for compounds which are of pharmaceutical interest. Recent research in this area has investigated ^1H - ^1H dipolar couplings [104, 108, 142], but in the authors opinion the most reliable approach is that of using chemical shifts [55] which are additionally a source of deriving interatomic distance information [143]. Harris et al realise that crystal packing arrangements can result in molecular conformations that vary from those conformations with the lowest energy for an isolated molecule. Solid-state NMR chemical shifts provide data on molecular conformation as it is a sensitive probe of this. Harris et al use the solid-state NMR data to aid structure determination from the diffraction data. As NMR crystallography is able to determine the number of independent molecules inside the asymmetric unit cell by counting peaks in the resulting spectrum (i.e. for a crystal structure that has two molecules in the asymmetric unit one would expect to find a peak doublet in the ^{13}C or ^{15}N spectra). The magnitudes of the peaks however do not have to be the same and they can vary: dependent on the same factors which influence shielding. As a consequence the splittings which occur can also provide a means of finding out more about shielding. When there is more than two molecules inside the asymmetric unit it is difficult to identify the chemical shifts from experiment to the shielding information obtained from calculations in the 1D spectra as it is difficult to differentiate which resonances between to which independent molecule.

2D solid-state NMR spectra can help to resolve this issue and Harris et al have used the 2D INADEQUATE experiment to assign the peaks. Harris et al have acknowledged that a disadvantage of computation is that some researchers may not have access to the computing power needed to solve the full crystallographic structure as was the case with Harris et al. However the versatility of the CASTEP code allows the calculation of single molecules or parts of molecules thus significantly reducing the amount of computing time and power needed which is the approach which was taken by Harris et al and all of the computations they conducted were done so on a desktop PC.

3.6 ^{15}N in Solid-State NMR Experiments

Nitrogen is an important nucleus in pharmaceuticals products, thus nitrogen functional groups are of great interest in research due to their pharmacological properties [144]. Solid-state NMR is effective at identifying hydrogen bonds due to its sensitivity to the local atomic environment. The ^{15}N CP MAS solid-state NMR experiment, in particular, has the ability to identify hydrogen bonding interactions when the nitrogen atom is involved in the hydrogen bond: as a donor, acceptor and in protonation effects in salts and zwitterions [29, 121, 124, 126].

Below are some specific examples from the literature which use ^{15}N CP MAS experiments. The research by Smith et al [145] used PXRD with ^{13}C and ^{15}N NMR to find the structure of anhydrous theophylline. ^{15}N NMR provided data which was not obtainable from PXRD and thus identified two different structures: one structure had a hydrogen bond of the form $\text{N-H}\cdots\text{O}$ while the other structure contained a hydrogen bond of the form $\text{N-H}\cdots\text{N}$. Comparison between computed and experimental isotropic ^{15}N NMR chemical shift showed that the favoured structure was the one which contained the $\text{N-H}\cdots\text{N}$ hydrogen bond. MacLean et al [146] also demonstrated the benefit of using complementary techniques alongside ^{15}N solid-state NMR, notably PXRD.

Tatton et al [82] used a solid-state NMR method: $^1J_{15\text{N}-1\text{H}}$ spectral editing to characterise nitrogen functional groups in pharmaceutical compounds. One of the reasons the study of nitrogen functional groups is of interest is that protonation of an amine group by an acid can improve the dissolution of poorly soluble compounds. Protonation of a tertiary amine of a six-membered ring prevents nitrogen inversion and increases the rigidity of the ring [147]. This shows that whether nitrogen atoms are protonated is important in determining whether the compound is a salt or cocrystal. Tatton et al notes that a protonated amine can be determined by pK_a values when it is in solution using the general rule: the pK_a of the acid should be at least 2 pH units lower than the pK_a of the compound in its free base form [148]. This rule however is not 100% reliable as pK_a values can be difficult to determine and if protonation does occur in solution it does not mean that it will occur at the same nitrogen position when in a solid [149].

As a result, Tatton et al presented a ^{15}N spectral editing method which is based on one-bond ^{15}N - ^1H J -couplings which enables the differentiation between a different number of protons which are covalently bonded to a nitrogen atom. This provides the ability to differentiate whether ionization has occurred negating the need for the measurement of the pK_a value in solution. This experiment introduces an alternative method in being

3.6. ^{15}N IN SOLID-STATE NMR EXPERIMENTS

able to deduce whether protonation has occurred in a pharmaceutical compound, showing the potential application of the approach in the development of pharmaceutical products.

SCXRD and solid-state NMR are the techniques which are commonly used to determine the degree of proton transfer [150–152]. In particular, it is the ^{15}N solid-state NMR experiment which results in large changes in the isotropic chemical shift for aromatic systems [126, 153] but the chemical shift change that occurs for aliphatic nitrogens like tertiary amines is significantly reduced and difficulty may arise in seeing whether a shift has occurred [154]. The method of IR can also determine between a salt and cocrystal but is not consistent.

Stevens et al [155] has presented the method of X-ray photoelectron spectroscopy (XPS) [156] of being able to determine the degree of proton transfer [157, 158] due to the local chemical environment being altered at the protonation site in a salt. This was validated with ^{15}N solid-state NMR experiments and calculations. Determination of a salt or cocrystal by XPS was found due to a change in peak position in the XPS spectrum. ^{15}N solid-state NMR experiments have been used previously to identify and distinguish two-component molecular systems as hydrogen bonded or ionic [126, 153, 157–159]. Determining whether protonation has occurred in compounds especially where there are a lot of resonances using solid-state NMR can be found using a short-contact time [126] and dipolar dephasing experiments [160].

Stevens et al [155] carried out ^{15}N solid-state NMR experiments with calculations of NMR parameters and identified cocrystals due to the small magnitude of the shifts in the spectrum showing that proton transfer had not occurred [157, 158]. For salts, changes in shifts of 50-100 ppm are usual for protonation of aromatic, heterocyclic nitrogen [126, 153] and a salt was identified with a chemical shift change of at least 50 ppm to low frequencies for a C=N nitrogen signal (see figure 3.2), with DFT calculations aiding the investigation. Good agreement between calculation and experiment was achieved for chemical shifts (± 5 ppm) which allows comparison of calculated shifts for a salt and cocrystal. Stevens et al also found a correlation between the chemical shifts and hydrogen bond length, where shorter N-H lengths resulted in a more negative (lower frequency) chemical shift. Therefore, this approach was able to determine the degree of proton transfer in salts and cocrystals and also the position of protonation using XPS which was validated with ^{15}N solid-state NMR.

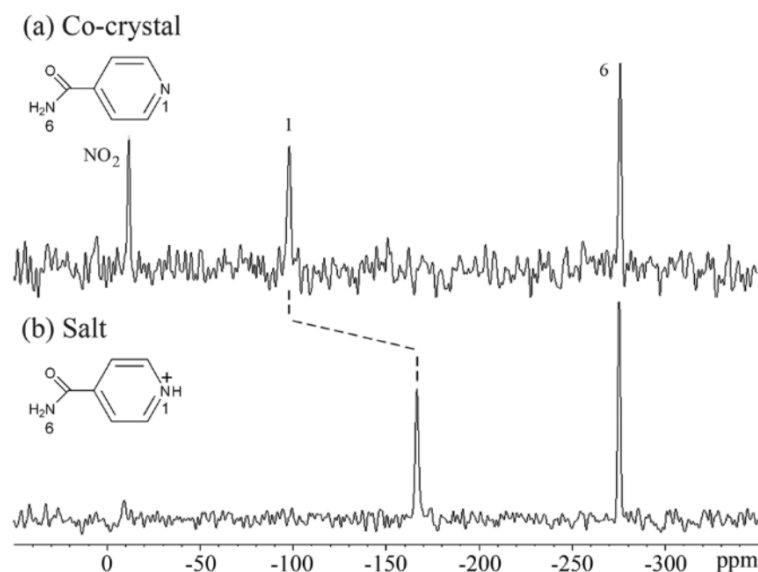


Figure 3.2: ^1H - ^{15}N CPMAS solid-state NMR spectra of (a) an isonicotinamide/4-hydroxy-3-nitrobenzoic acid cocrystal and (b) an isonicotinamide/2,4,6-trihydroxybenzoic acid salt, showing the change in ^{15}N chemical shift with proton transfer. Reproduced from [161].

3.7 Quadrupolar Nuclei

Quadrupolar nuclei were once thought to be inaccessible to solid-state NMR due to the large quadrupolar broadening observed in the resulting spectrum along with their low sensitivity. However, with the advancement in higher static magnetic fields, which reduce second-order quadrupolar broadening effects, improvements in hardware and new pulse sequences, quadrupolar nuclei are now accessible and able to provide valuable data.

The quadrupolar nuclei of ^{35}Cl has been utilised in solid-state NMR experiments on hydrochloride pharmaceutical salts [162]. ^{65}Cu solid-state NMR research has been conducted on a blue copper protein azurin to look into the electronic state of copper sites in proteins [163]. Another quadrupolar nucleus which is important in the pharmaceutical industry is that of ^{23}Na , and ^1H - ^{23}Na HETCOR (Heteronuclear Correlation) experiments are able to probe the local environment around the ^{23}Na nucleus to give hydrogen bonding information [23]. The quadrupolar interaction can also be sensitive to differences in the solid forms of the drug resulting in changes in the lineshape. This can be shown in the quadrupolar nucleus of ^{23}Na in research by Redman-Furey et al [164], Lester et al [165] and Vogt et al [23] where changes in the lineshape were identified for different

3.7. QUADRUPOLEAR NUCLEI

polymorphic forms and hydrates. The quadrupolar nuclei of ^2H , ^{17}O have also been used in research to look at mobility and structure of complex hydrate systems [23, 166]. The ^{14}N nucleus is now utilised in analysing pharmaceutical systems, and this section will provide an account of how the ^{14}N nucleus has probed pharmaceutical systems [167, 168]. The ^{14}N - ^1H HMQC experiment [167, 169, 170] has been shown to be able to probe hydrogen bonding interactions: in a guanosine derivative [68] and cimetidine (a pharmaceutical drug) [82] and has probed hydrogen bonding in cocrystals and amorphous dispersions [171].

The research by Tatton et al [171] in 2014 was one of the first times that the ^{14}N - ^1H HMQC experiment was used to investigate the hydrogen bonding interactions in a cocrystal as shown in figure 3.3.

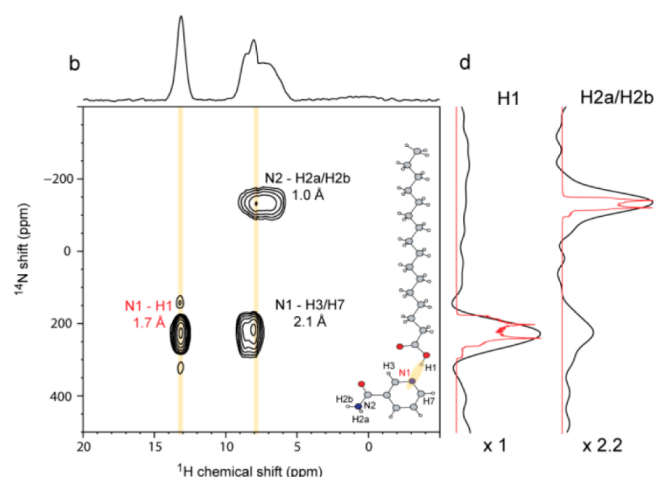


Figure 3.3: A ^{14}N - ^1H HMQC MAS NMR spectrum recorded for a nicotinamide palmitic acid cocrystal from [171].

Previous studies have researched cocrystals using solid-state NMR but using the nuclei of ^1H , ^{13}C and ^{15}N [160, 172, 173], but the ^{14}N - ^1H HMQC experiment has the advantage that it can directly probe hydrogen bonding interactions in a structure. Being able to investigate the nucleus of nitrogen is also important for the pharmaceutical industry as nitrogen is part of many pharmaceutical drug products and can directly participate in hydrogen bonds. As discussed in section 3.6, ^{15}N solid-state NMR experiments have been used to investigate pharmaceutical drug products [126, 145, 174], but experiments using this isotope of nitrogen is time intensive due to its low natural abundance. The advantage of using the quadrupolar ^{14}N nucleus is that more detailed structural information can be accessed through the EFG (Electric Field Gradient) parameter which is not possible

CHAPTER 3. NMR CRYSTALLOGRAPHY OF PHARMACEUTICAL SOLIDS

for non-quadrupolar nuclei like ^{15}N . It was observed that ^{14}N EFG parameters found by the ^{14}N nuclear quadrupole resonance [175, 176] and also by wide-line ^{14}N solid-state NMR [177] are sensitive to hydrogen bonds. It is not surprising that ^{14}N solid-state NMR is sensitive to hydrogen bonding interactions as it mirrors what is known about the ^{15}N nucleus being sensitive to hydrogen bonds. Furthermore using the ^{14}N - ^1H HMQC solid-state NMR, Tatton et al [171] concluded that this experiment has potential for the characterisation of cocrystals with hydrogen bonding interactions able to be identified. The hydrogen bond identified in that research was via an intermolecular NH cross peak. It was also found that the isotropic second-order quadrupolar shift was very sensitive to changes in the hydrogen bonding interaction. Tatton et al highlighted the potential of this technique when comparing a cocrystal with its constituent parts. The ^{14}N - ^1H HMQC solid-state NMR was also found to identify hydrogen bonding interactions in amorphous dispersions thus showing that the experiment can be used for crystalline solids and disordered solids. The technique used in this case would benefit from other complementary techniques such as PXRD or vibrational spectroscopy to gain a greater insight into the molecular interactions, as was the case with Poppler et al [79]. Tatton et al [82] also reported that correlations are observed between ^{14}N and ^1H through dipolar couplings, and therefore distance information can be determined through varying the dipolar recoupling time during the experiment. Longer range correlations (not directly protonated) will be able to be determined by using a longer decoupling time. In a recent example from the literature, Tatton et al in 2018 [78] used NMR crystallography to investigate the structure of a pharmaceutical, considering the technique of PXRD into the research methodology along with calculated and experimental ^{13}C , ^{15}N and ^1H solid-state NMR. Multi-dimensional NMR was also used and combined with the ^{14}N quadrupolar parameter again obtained from GIPAW calculation and experiment. This was supplemented by isolated molecule GIPAW calculations and led to the confirmation of the 3D packing arrangement of β -piroxicam thus showing that NMR crystallography is an effective tool to verify structures obtained from PXRD for increasingly complex cases.

NMR theory

An overview of solid-state NMR theory is presented here in relation to the research which was carried out in this thesis.¹

4.1 Spin Angular Momentum

Nuclei have three main intrinsic properties: mass, charge and spin. Nuclear isotopes are recognised by two important quantities: the spin quantum number, I , where

$$I = 0, \frac{1}{2}, 1, \frac{3}{2}, 2, \dots etc, \quad (4.1)$$

and the gyromagnetic ratio, γ .

Nuclei which have $I > 0$ possess a property known as spin angular momentum, S , whose magnitude is given by:

$$|S| = \hbar \sqrt{I(I+1)}. \quad (4.2)$$

When a magnetic field is applied to a system of nuclear spins, the degeneracy of the spin state (which is $(2I+1)$ fold degenerate) will be broken. This process is referred to as the Zeeman effect, where the splitting of the nuclear sub-levels occurs. NMR can thus

¹The ideas and equations which are presented therein are derived from the following references that can be referred to for a more detailed explanation [178–182].

CHAPTER 4. NMR THEORY

be described as the spectroscopy of the nuclear Zeeman sub-levels. For nuclear isotopes of $I = \frac{1}{2}$, the two-fold degenerate nuclear ground state splits into two sub-levels in the applied magnetic field. As discussed below, the size of the splitting is dependent on the nuclear isotope used, for example, the Zeeman splitting of a ^1H nucleus is approximately ten times larger than that for a ^{15}N nucleus.

For nuclei which have non-zero angular momentum, the z -component of I_z is quantised:

$$I_z = m\hbar, \quad (4.3)$$

where $m = I, I - 1, \dots, -I$. For nuclei which have $I = \frac{1}{2}$, including the isotopes of ^1H , ^{13}C and ^{15}N :

$$I_z = \frac{\pm\hbar}{2}. \quad (4.4)$$

Nuclei which have $I > 0$ are magnetic and have an intrinsic magnetic moment. This means they can be used in NMR experiments. Nuclei which have $I = 0$, which include the nuclear isotopes of ^{12}C , ^{16}O and ^{32}S , are magnetically inactive as they have no magnetic moment, and therefore cannot be used in NMR experiments.

The magnetic moment μ_z of nuclei with $I > 0$ is given by:

$$\mu_z = \gamma I_z, \quad (4.5)$$

where the magnetic moment is proportional to its angular momentum.

Nuclei with $I > \frac{1}{2}$ additionally possess an electric quadrupole moment which interacts with the EFG at the nucleus (see section 4.8.5 for more details). Roughly $\frac{2}{3}$ of all the nuclear isotopes are quadrupolar. The quadrupolar nucleus presented in this thesis is ^{14}N which has $I = 1$.

4.2 The NMR Experiment

4.2.1 The Vector Model

The vector model was introduced by Bloch and is a way to visualise what is happening to the nuclear spins in a sample when they are exposed to an external magnetic field during a NMR experiment. The Vector model mainly applies to uncoupled spins and therefore does have limitations. However, most of the language used in this thesis in respect to

NMR is derived from this method which is why it is introduced here and it explains the following concepts well.

4.2.2 Net Magnetisation and Thermal Equilibrium

When a nucleus, with $I > 0$, is placed in a magnetic field, there is an interaction between the nuclear magnetic moment and the applied field. For a nucleus with $I = \frac{1}{2}$, the energy of this interaction will depend on the angle between the magnetic moment and the applied field. For a nucleus with $I = \frac{1}{2}$, the lowest energy state is when the magnetic moment is aligned with the external magnetic field and the highest energy state is when the magnetic moment is aligned opposite to the external magnetic field. The energy of the whole system would be minimised if all of the spins were to align with the external field. However, due to the random thermal motion of molecules this does not occur and the thermal motion disrupts the alignment of the magnetic moments with the external field.

When the sample is not subject to an external magnetic field, the individual magnetic moments are randomly orientated so that, if summed over the entire sample, there will be no net magnetisation. When the sample is then put into the magnetic field, there is a preference for the magnetic moment to be aligned with the external field as this is the lower energy state of the system. However, it takes time for the magnetic moments to orientate into this preferred direction, so that when B_0 is first applied there is also no net magnetisation. It is only after a period of time (see below discussion of relaxation at the end of this section) that the magnetic moments will have aligned themselves so that there will be slightly more spins populated with B_0 (α) than against (β). This is known as the net magnetisation and the state of the system is said to be at thermal equilibrium or in a state of equilibrium magnetisation.

The net magnetisation or bulk magnetisation is controlled by the Boltzmann distribution. At thermal equilibrium, the Boltzmann distribution between the two states is given by:

$$\frac{p_\beta}{p_\alpha} = \exp\left(\frac{\Delta E}{k_B T}\right), \quad (4.6)$$

where p_β is the population state aligned with B_0 and p_α is the population state aligned anti-parallel with B_0 , k_B is the Boltzmann constant and T is the absolute temperature. Equation 4.6 states that there will be slightly more magnetic moments aligned with the applied field than against it, thus creating a net magnetisation which is aligned with the

applied field. This net magnetisation is represented by:

$$M_0 = \frac{\gamma^2 \hbar N B_0}{4k_B T}, \quad (4.7)$$

where N represents the number of spins.

The energy of a magnetic moment is independent of orientation in the x - y axis. This means there is no energetic preference of the magnetic moment in the transverse plane, and at equilibrium, x and y components of the individual magnetic moments will be random. Transverse components will cancel so there is no net magnetisation in the transverse plane at thermal equilibrium; M_0 is only aligned with B_0 .

Relaxation is the process whereby spins come into thermal equilibrium. T_1 relaxation describes the establishing or a return of the system to thermal equilibrium i.e. in the longitudinal z direction defined by the applied magnetic field, while T_2 is the transverse relaxation time and describes the de-phasing of the transverse magnetisation (see below).

4.2.3 Larmor Precession

At thermal equilibrium, once the net magnetisation vector is formed it is fixed in size and direction and does not vary over time. When M_0 is tipped away from the z -axis in an NMR experiment (see sub-section below on pulses), it will make an angle, β , with the z -axis. M_0 will rotate around the z -axis to create a cone shape with constant angle, β , see figure 4.1. This is called precession, where the precession frequency is the Larmor frequency.

Nuclei with $I > 0$, will precess around the B_0 magnetic field at the Larmor frequency, ω_0 , where:

$$|\omega_0| = |\gamma B_0|. \quad (4.8)$$

The Larmor frequency of the nuclear spins is very important in NMR as it is this quantity that is measured by the experiments. The Larmor frequency has a sign that is related to the sign of the γ (that can be positive or negative), but usually it is sufficient, as in this thesis, to only state the magnitude of Larmor frequency. The energy of the magnetic moment along B_0 is given by (and is displayed in figure 4.2):

$$E = -\mu_z B_0 = -m \hbar \gamma B_0, \quad (4.9)$$

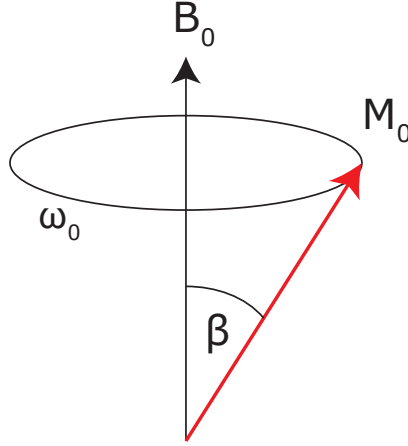


Figure 4.1: When the magnetisation vector, M_0 , is tilted away from the z -axis it rotates about the field direction, sweeping out a constant angle to z -axis, this is called precession and occurs at the Larmor frequency, ω_0 .

where for $I = \frac{1}{2}$ nuclei:

$$E(m = \pm \frac{1}{2}) = \frac{-\hbar\gamma B_0}{2}, \quad (4.10)$$

$$|\Delta E| = |\hbar\gamma B_0|, \quad (4.11)$$

or in units of Hz:

$$E = h\nu, \quad (4.12)$$

$$|\nu_0| = \left| \frac{\gamma B_0}{2\pi} \right|, \quad (4.13)$$

and rads^{-1}

$$E = \hbar\omega, \quad (4.14)$$

$$|\omega_0| = |\gamma B_0|. \quad (4.15)$$

4.2.4 Detection of the NMR Signal

The NMR signal reports on the Larmor frequency. If a coil aligned in the x - y plane surrounds the sample, the precessing magnetisation will induce a current in the coil

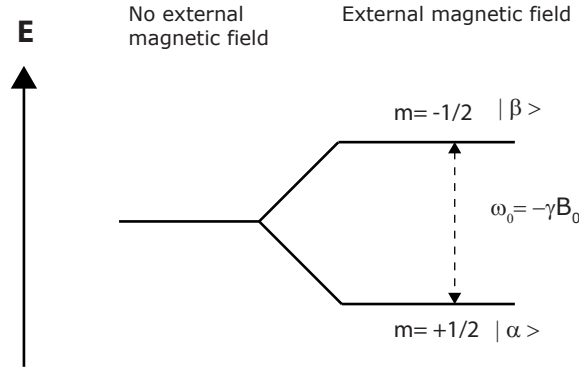


Figure 4.2: When an external magnetic field is applied to a spin system, the degeneracy is broken. This is known as the Zeeman effect, whereby splitting of the nuclear sub-levels occurs. For nuclei with $I = \frac{1}{2}$, as is shown in this example the nuclear ground state is two fold degenerate, splitting into two sub-levels in the applied magnetic field: represented by $m = -\frac{1}{2}$ ($|\beta\rangle$) and $m = \frac{1}{2}$ ($|\alpha\rangle$). The energy difference between the two levels corresponds to the Larmor frequency (ω_0).

which is amplified and recorded. The so-obtained NMR signal is known as the Free Induction Decay (FID). At time $t=0$ following a *rf* pulse (see below), the x -component of the M_0 vector which has been tilted through an angle, β , is $M_0 \sin \beta$, as shown in figure 4.3. As M_0 precesses at ω_0 around the z -axis, this initial x -component ($M_0 \sin \beta$) rotates at the same frequency in the x - y plane.

At time, t , the angle through which the vector has rotated is $\omega_0 t$, therefore:

$$M_x = M_0 \sin \beta \cos \omega_0 t \quad (4.16)$$

$$M_y = -M_0 \sin \beta \sin \omega_0 t. \quad (4.17)$$

Fourier transformation of the NMR signal due to M_x and M_y produces a single line at ω_0 , in the frequency-domain NMR spectrum.

Figure 4.4 displays how the signal shown in figure 4.3 evolves over time. For a negative Larmor frequency at time $t=0$ the magnetisation is first positioned along the x -axis. After a certain period of time (t) the magnetisation vector will rotate through an angle $\omega_0 t$. Figure 4.4 thus displays (using trigonometry) the x and y components of the magnetisation after a certain period of time.

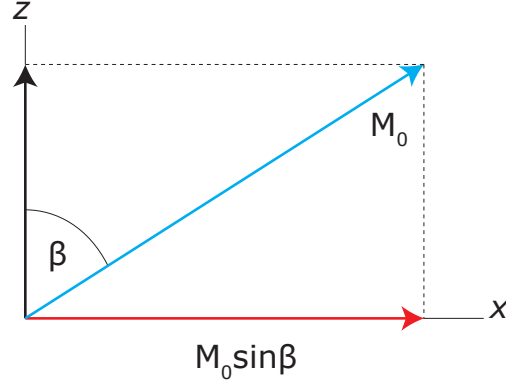


Figure 4.3: When the magnetisation vector, M_0 , is tilted by an angle, β , it results in the x -component of magnetisation being $M_0 \sin \beta$.

4.2.5 Pulses and the Rotating Frame of Reference

In NMR, there are two important magnetic fields to note: B_0 and B_1 .

B_0 : the strong, static, externally applied magnetic field in the z -direction.

B_1 : the weak oscillating (at ω_{rf}) radio frequency rf pulse which is perpendicular to B_0 .

It is B_1 which rotates the net-magnetisation from the equilibrium position aligned with B_0 and is given by:

$$B_1 = |B_1| \cos(\omega_{rf}t + \phi), \quad (4.18)$$

where ω_{rf} is the oscillation frequency of the rf pulse and ϕ represents the phase. The coil which is used to detect the precessing magnetisation is also used to generate B_1 .

To understand how the pulse can rotate the magnetisation into the x - y plane, the rotating reference frame needs to be introduced. This transformation into the rotating frame removes the time dependence of the B_1 field: in the rotating frame, B_1 will be viewed as a static field, thus allowing the motion of M_0 to be simply viewed as a rotation about the static field.

If the frequency of the rotating frame is ω_{rot} (this will be set equal to ω_{rf}) the apparent Larmor frequency in this frame will be, $\omega_0 - \omega_{rot}$. This difference in frequency is called the frequency offset, Ω :

$$\Omega = \omega_0 - \omega_{rot}. \quad (4.19)$$

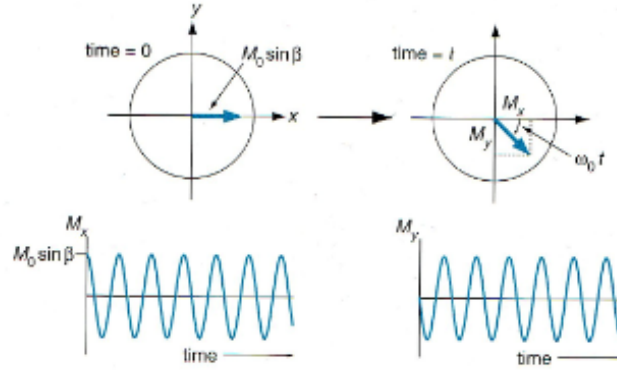


Figure 4.4: For a negative Larmor frequency, at time $t=0$ the magnetisation is positioned as $M_0 \sin \beta$ for the x -component and the y -component is zero. After time t , the angle through which the vector has rotated is $\omega_0 t$. Figure taken from [179].

In the rotating frame, if the frequency of precession is Ω , the resulting magnetic field ΔB is:

$$\Delta B = -\frac{\Omega}{\gamma}, \quad (4.20)$$

where ΔB is known as the residual field in the rotating frame. When ΔB becomes comparable with the B_1 field, the B_1 field then starts to influence the net magnetisation even though $B_1 \ll B_0$. In the rotating frame, ΔB (along x) and B_1 (along z) add to give an effective field, as shown in figure 4.5, and the magnetisation precesses around B_{eff} just as the magnetisation precesses around B_0 in the laboratory frame, therefore,

$$\omega_{eff} = |\gamma| B_{eff}. \quad (4.21)$$

If the offset is small, the effective field will lie close to the x -axis and net magnetisation will be rotated away from the z -axis. So although $B_0 \gg B_1$, the effect of B_0 is eliminated by setting the transmitter frequency (which produces the rf -field or pulse), ω_{rf} , close to the Larmor frequency, ω_0 , i.e. making the offset, Ω in equation 4.19, small.

The angle between ΔB and B_{eff} is the tilt angle, β , and using trigonometry in figure 4.5, β is given by:

$$\sin \beta = \frac{B_1}{B_{eff}}, \quad \cos \beta = \frac{\Delta B}{B_{eff}}, \quad \tan \beta = \frac{B_1}{\Delta B}. \quad (4.22)$$

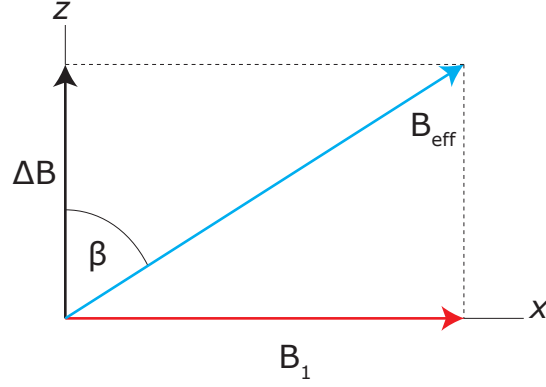


Figure 4.5: In the rotating frame, B_{eff} is the vector sum of the reduced field ΔB and the B_1 field. The tilt angle, β , is defined as the angle between B_{eff} and ΔB .

Therefore, when $\Omega = 0$ $\beta = \frac{\pi}{2}$, likewise if Ω is large $\beta \rightarrow 0$.

An on-resonance *rf*-pulse is when $\Omega = \omega_0 - \omega_{rf} = 0$. When an on-resonance *rf*-pulse is applied to the nuclear spins, the magnetisation which aligned with B_0 will nutate around the direction of the B_1 pulse, which is along the x -axis for $\phi = 0$. The nutation frequency of an *rf*-pulse is:

$$|\omega_1| = |\gamma B_1|. \quad (4.23)$$

For an on resonance pulse applied for a time t_p , the flip angle through which the magnetisation will rotate will be:

$$\Theta = \omega_1 t_p. \quad (4.24)$$

When an on resonance $\frac{\pi}{2}$ *rf*-pulse is applied, it creates transverse magnetisation, i.e. magnetisation in the x - y plane. Once the *rf*-pulse is turned off, the transverse magnetisation will precess around B_0 at the Larmor frequency. The NMR signal is generated in the coil, described previously. However, the NMR signal will decay due to the loss of transverse magnetisation specifically due to the transverse relaxation time, T_2 .

4.2.6 The Time and Frequency Domain Signals

The x and y components of magnetisation as detected in the rotating frame are described by starting from equations 4.16 and 4.17, as:

$$M_x = M_0 \sin \Theta \cos \Omega t, \quad (4.25)$$

$$M_y = -M_0 \sin \Theta \sin \Omega t. \quad (4.26)$$

For a $\Theta = \frac{\pi}{2}$ pulse, the x and y components of magnetisation become:

$$M_x = M_0 \cos \Omega t, \quad (4.27)$$

$$M_y = -M_0 \sin \Omega t. \quad (4.28)$$

The precession of the magnetisation induces a current in the coil surrounding the sample and the spectrometer is able to detect both M_x and M_y resulting in separate signals: S_x and S_y , which are digitalised and stored in the computer:

$$S_x = S_0 \cos \Omega t, \quad (4.29)$$

$$S_y = -S_0 \sin \Omega t. \quad (4.30)$$

Once the pulse is turned off, the magnetisation and thus the signal will decay over time due to relaxation processes. To take account of relaxation processes the signals presented in equations 4.29 and 4.30 become:

$$S_x = S_0 \cos \Omega t \exp\left(\frac{-t}{T_2}\right), \quad (4.31)$$

$$S_y = S_0 \sin \Omega t \exp\left(\frac{-t}{T_2}\right), \quad (4.32)$$

where T_2 the transverse relaxation time: the shorter the T_2 time, the quicker the loss of signal. The x and y components can be combined together into a single complex signal, $S(t)$, where S_x represents the real part of the signal and S_y the imaginary part:

$$S(t) = S_0 \exp(i\Omega t) \exp\left(\frac{-t}{T_2}\right). \quad (4.33)$$

Introducing $R = \frac{1}{T_2}$, leads to equation 4.33 being re-expressed as:

$$S(t) = S_0 \exp(i\Omega t) \exp(-Rt). \quad (4.34)$$

4.2.7 Absorption and Dispersive Lineshapes

Fourier Transformation (FT) of the time domain signal results in a frequency domain signal and thus a NMR spectrum:

$$S(t) \xrightarrow{\text{FT}} S(\omega) \quad (4.35)$$

$$S(t) = S_0 \exp(i\Omega t) \exp(-Rt) \xrightarrow{\text{FT}} \underbrace{\frac{S_0 R}{R^2 + (\omega - \Omega)^2}}_{\text{(REAL)}} + i \underbrace{\frac{-S_0(\omega - \Omega)}{R^2 + (\omega - \Omega)^2}}_{\text{(IMAGINARY)}}, \quad (4.36)$$

The real part of the spectrum is an absorption mode Lorentzian lineshape, whereas the imaginary part is a dispersion mode Lorentzian lineshape, as can be seen visually in figure 4.6. As can be seen from figure 4.6, the absorption lineshape is always positive, centred at $\Omega \text{ rads}^{-1}$ or $F_0 \text{ Hz}$ and symmetrical about Ω . The main features of the absorption and dispersive lineshapes can be viewed in Table 4.1.

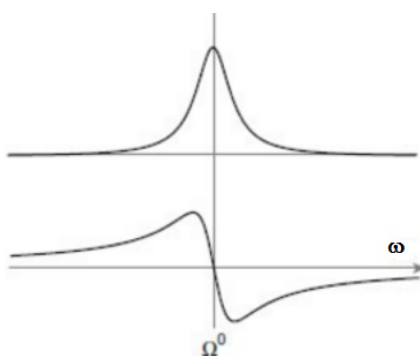


Figure 4.6: Fourier Transformation of an exponentially decaying time-domain signal, see equation 4.35, gives a complex frequency domain signal which has real and imaginary parts, see equation 4.36, represented by (top) absorption and (bottom) dispersion Lorentzian lineshapes, respectively. The absorption lineshape has only positive parts, in comparison the dispersion lineshape consists of both positive and negative parts and is broader. Figure reproduced from ref. [180].

In NMR, the dispersive lineshape is avoided as it is broader and half the height of the absorptive lineshape and it has both positive and negative parts unlike the absorptive lineshape which is all positive. In a crowded spectrum, this form of lineshape would make the spectrum difficult to interpret.

Table 4.1: Comparison of absorptive and dispersive lineshapes. [179]

	Absorption	Dispersion
lineshape (rad s ⁻¹)	$A(\omega) = \frac{R}{R^2 + (\omega - \Omega)^2}$	$D(\omega) = \frac{-(\omega - \Omega)}{R^2 + (\omega - \Omega)^2}$
lineshape (Hz)	$A(f) = \frac{R}{R^2 + 4\pi^2(f - F_0)^2}$	$D(f) = \frac{-2\pi(f - F_0)}{R^2 + 4\pi^2(f - F_0)^2}$
peak height	$\frac{1}{R}$	$\frac{1}{2R}$
width (rad s ⁻¹)	$2R$	$2(2 + \sqrt{3})R \approx 7.5R$
width (Hz)	$R/\pi \approx 0.32R$	$(2 + \sqrt{3})R/\pi \approx 1.2R$

where F_0 is the frequency at 0 i.e. equivalent to Ω_0 in the figure, where f is the frequency at a non-zero value.

4.3 Quantum Mechanical Description of NMR

The Hamiltonian \hat{H} determines the total energy (E) (the observable) of the spin system,

$$E = \langle \hat{H} \rangle = \langle \psi | \hat{H} | \psi \rangle, \quad (4.37)$$

where, specifically, E is the energy of a magnetic dipole in a magnetic field and ψ is the wavefunction that describes the spin system. Observables relating to the nuclear spin can be extracted using the spin-angular momentum operator \hat{I} , which can be expressed in terms of its x , y and z components of spin angular momentum.

$$\hat{I}^2 = \hat{I}_x^2 + \hat{I}_y^2 + \hat{I}_z^2, \quad (4.38)$$

which can be expressed, for $I = \frac{1}{2}$, in matrix form:

$$\hat{I}_x = \begin{pmatrix} 0 & \frac{1}{2} \\ \frac{1}{2} & 0 \end{pmatrix}, \quad \hat{I}_y = \begin{pmatrix} 0 & -\frac{1}{2}i \\ \frac{1}{2}i & 0 \end{pmatrix}, \quad \hat{I}_z = \begin{pmatrix} \frac{1}{2} & 0 \\ 0 & -\frac{1}{2} \end{pmatrix}. \quad (4.39)$$

These obey the following commutator relationships:

$$[\hat{I}, \hat{I}_z] = [\hat{I}\hat{I}_z - \hat{I}_z\hat{I}] = 0, \quad (4.40)$$

$$[\hat{I}_x, \hat{I}_y] = i\hat{I}_z. \quad (4.41)$$

Since one component of the spin angular momentum commutes with the total spin angular momentum, one component of the spin angular momentum is able to be specified at a given time. In NMR, by convention, this is \hat{I}_z . When the operators \hat{I}_z and \hat{I} act on

4.3. QUANTUM MECHANICAL DESCRIPTION OF NMR

$|\psi\rangle$:

$$\hat{I}^2 |\psi\rangle = \hbar(I+1) |\psi\rangle, \quad (4.42)$$

$$\hat{I}_z |\psi\rangle = \hbar m |\psi\rangle, \quad (4.43)$$

Remembering equation 4.8 for the Larmor frequency,

$$\hat{H} = -\gamma \hbar \hat{I}_z B_0 = \hbar \omega_0 \hat{I}_z. \quad (4.44)$$

For simplicity \hbar is omitted, giving (in units of rads^{-1}),

$$\hat{H} = \omega_0 \hat{I}_z. \quad (4.45)$$

The eigenstates of \hat{I}_z and thus of the Hamiltonian are $|\alpha\rangle$ (spin up) and $|\beta\rangle$ (spin down). The corresponding eigenvalues are:

$$\hat{I}_z |\alpha\rangle = +\frac{1}{2} |\alpha\rangle \quad \hat{I}_z |\beta\rangle = -\frac{1}{2} |\beta\rangle, \quad (4.46)$$

$$\hat{H}_Z |\alpha\rangle = +\frac{1}{2} \omega_0 |\alpha\rangle \quad \hat{H}_Z |\beta\rangle = -\frac{1}{2} \omega_0 |\beta\rangle. \quad (4.47)$$

As can be inferred from the above equations, $|\alpha\rangle$ and $|\beta\rangle$ are separated in energy by ω_0 (see figure 4.2). For nuclei which have $\gamma > 0$, ω_0 is negative, thus $|\alpha\rangle$ has a lower energy than $|\beta\rangle$.

In NMR, we want to know which eigenvalue will be found in a particular measurement. The average result of many measurements can be determined; this is called the expectation value, $\langle \hat{A} \rangle$ for an operator \hat{A} corresponding to the particular observable:

$$\langle \hat{A} \rangle = \langle \psi | \hat{A} | \psi \rangle. \quad (4.48)$$

A spin $\frac{1}{2}$ particle is not bound to the two eigenstates but may be in a state of superposition between the two:

$$|\psi\rangle = c_\alpha |\alpha\rangle + c_\beta |\beta\rangle, \quad (4.49)$$

whereby c_α and c_β are superposition coefficients which describe their contribution to each state. The only restriction on their values is that the state is normalised:

$$|c_\alpha|^2 + |c_\beta|^2 = 1. \quad (4.50)$$

CHAPTER 4. NMR THEORY

In vector form, equation 4.50 is represented as:

$$|\psi\rangle = \begin{pmatrix} c_\alpha \\ c_\beta \end{pmatrix}. \quad (4.51)$$

In the Dirac notation the bra vector, $\langle\psi|$, is the complex conjugate (represented by $^+$) of the ket vector, $|\psi\rangle$:

$$\langle\psi| = |\psi\rangle^+ = c_\alpha^* \langle\alpha| + c_\beta^* \langle\beta|. \quad (4.52)$$

In vector form, the expectation value is therefore represented by:

$$\langle\hat{A}\rangle = (c_\alpha^* c_\beta^*) \begin{pmatrix} A_{\alpha\alpha} & A_{\alpha\beta} \\ A_{\beta\alpha} & A_{\beta\beta} \end{pmatrix} \begin{pmatrix} c_\alpha \\ c_\beta \end{pmatrix}, \quad (4.53)$$

$$\langle\hat{A}\rangle = c_\alpha^* c_\alpha A_{\alpha\alpha} + c_\beta^* c_\beta A_{\beta\beta} + c_\alpha^* c_\beta A_{\alpha\beta} + c_\beta^* c_\alpha A_{\beta\alpha}. \quad (4.54)$$

The expectation value of the \hat{I}_z operator (see equation 4.39)is then given by:

$$\langle\hat{I}_z\rangle = \frac{1}{2}(c_\alpha c_\alpha^* - c_\beta c_\beta^*) = \frac{1}{2}|c_\alpha|^2 - \frac{1}{2}|c_\beta|^2. \quad (4.55)$$

This shows that the longitudinal component is related directly to finding the spin system in the α or β state.

$|\alpha\rangle$ and $|\beta\rangle$ are not eigenfunctions of \hat{I}_x or \hat{I}_y , but \hat{I}_x and \hat{I}_y act to convert between the two eigenstates:

$$\hat{I}_x |\alpha\rangle = \frac{1}{2} |\beta\rangle, \quad \hat{I}_x |\beta\rangle = \frac{1}{2} |\alpha\rangle, \quad (4.56)$$

$$\hat{I}_y |\alpha\rangle = \frac{1}{2} i |\beta\rangle, \quad \hat{I}_y |\beta\rangle = -\frac{1}{2} i |\alpha\rangle, \quad (4.57)$$

where the expectation values of \hat{I}_x and \hat{I}_y are:

$$\langle\hat{I}_x\rangle = \frac{1}{2} c_\alpha^* c_\beta + \frac{1}{2} c_\beta^* c_\alpha, \quad (4.58)$$

$$\langle\hat{I}_y\rangle = \frac{1}{2} i c_\beta^* c_\alpha - \frac{1}{2} i c_\alpha^* c_\beta. \quad (4.59)$$

4.4 The Density Operator

This section introduces the density operator, $\hat{\rho}$, and shows how it is well suited to linking to the expectation value of a NMR observable. The density operator is given by:

$$\hat{\rho} = \overline{|\psi\rangle\langle\psi|}, \quad (4.60)$$

where the over-bar indicates an ensemble average and, for simplicity, this notation will be assumed subsequently. The matrix representation of $\hat{\rho}$ is

$$\hat{\rho} = |\psi\rangle\langle\psi| = \begin{pmatrix} c_\alpha \\ c_\beta \end{pmatrix} (c_\alpha^* c_\beta^*) = \begin{pmatrix} c_\alpha c_\alpha^* & c_\alpha c_\beta^* \\ c_\beta c_\alpha^* & c_\beta c_\beta^* \end{pmatrix}. \quad (4.61)$$

Consider the product of $\hat{\rho}$ and \hat{A} in a matrix representation:

$$\begin{aligned} \hat{\rho}\hat{A} &= \begin{pmatrix} c_\alpha c_\alpha^* & c_\alpha c_\beta^* \\ c_\beta c_\alpha^* & c_\beta c_\beta^* \end{pmatrix} = \begin{pmatrix} A_{\alpha\alpha} & A_{\alpha\beta} \\ A_{\beta\alpha} & A_{\beta\beta} \end{pmatrix} \\ &= \begin{pmatrix} c_\alpha c_\alpha^* A_{\alpha\alpha} & c_\alpha c_\beta^* A_{\alpha\beta} \\ c_\beta c_\alpha^* A_{\beta\alpha} & c_\beta c_\beta^* A_{\beta\beta} \end{pmatrix}. \end{aligned} \quad (4.62)$$

comparing to equation 4.54 it is observed that, the expectation value is given by the trace of the product of $\hat{\rho}$ and \hat{A} :

$$\langle\hat{A}\rangle = \text{Tr}(\hat{\rho}\hat{A}). \quad (4.63)$$

Considering equations 4.45, 4.58 and 4.63, it is seen that $\langle\hat{I}_z\rangle$ is determined by $c_\alpha c_\alpha^*$ and $c_\beta c_\beta^*$ (on-diagonal terms), while $\langle\hat{I}_x\rangle$ and $\langle\hat{I}_y\rangle$ depend on $c_\alpha c_\beta^*$ and $c_\beta c_\alpha^*$ (off-diagonal terms). Thus, the on-diagonal terms correspond to population states, while the off-diagonal terms correspond to coherences.

Equation 4.63 is an important result, as the result of any macroscopic observation can be deduced from two spin operators, one representing the observable being measured and the other the state of the spin ensemble, therefore instead of specifying the microscopic states of all of the individual spins you can just specify the value of a single operator - the spin density operator.

As described in section 4.2, in NMR, spins act under *rf* pulses and periods of free-evolution is observed. This behaviour is described by the Time Dependent Schrödinger

Equation (TDSE):

$$\frac{d|\psi(t)\rangle}{dt} = -i\hat{H}|\psi(t)\rangle, \quad (4.64)$$

which leads to the following equation for the time dependence of density operator:

$$\frac{d\hat{\rho}(t)}{dt} = -i[\hat{H}, \hat{\rho}(t)] = -i\hat{H}\hat{\rho}(t) - \hat{\rho}(t)\hat{H}. \quad (4.65)$$

This is the Liouville-von Neumann equation of which the solution is:

$$\hat{\rho}(t) = \exp(-i\hat{H}t)\hat{\rho}(0)\exp(i\hat{H}t), \quad (4.66)$$

where $\hat{\rho}(t)$ is the density operator at time t and $\hat{\rho}(0)$ is the density operator at time 0. If we know the density operator at $t = 0$ and the Hamiltonians, we can also calculate it at $t = t$. If the Hamiltonian operator, \hat{H} , which describes the spin system between 0 and t , is constant over this time period, we can define a propagator, $\hat{U}(t)$:

$$\hat{U}(t) = \exp(-i\hat{H}t), \quad (4.67)$$

Equation 4.66 then becomes:

$$\hat{\rho}(t) = \hat{U}(t)\hat{\rho}(0)\hat{U}(t)^{-1}. \quad (4.68)$$

If \hat{H} is not constant, the propagator can be separated into a series of Hamiltonians (in chronological order) which act for a certain time period:

$$\hat{U}(t) = \exp(-i\hat{H}_n t_n) \dots \exp(-i\hat{H}_1 t_1). \quad (4.69)$$

NMR Hamiltonians are discussed in section 4.6.

4.5 Product Operators

Product operators are a quantum mechanical way to calculate the outcome of a multiple-pulse NMR experiment for spin $I = \frac{1}{2}$ nuclei by representing the state of the spin system using a combination of operators. The strength of this method is the ability to deal with coupled spin systems, while retaining the geometrical picture of the vector model.

4.5.1 Isolated Spin

For an isolated $I = \frac{1}{2}$ spin, there are four product operators which describe an NMR experiment:

$$\frac{1}{2}E \quad I_x \quad I_y \quad I_z \quad . \quad (4.70)$$

While $\frac{1}{2}E$ is the identity operator (included for formality), the I_x , I_y and I_z operators correspond to the x, y and z magnetisation of a single spin in the rotating frame, see figure 4.7.

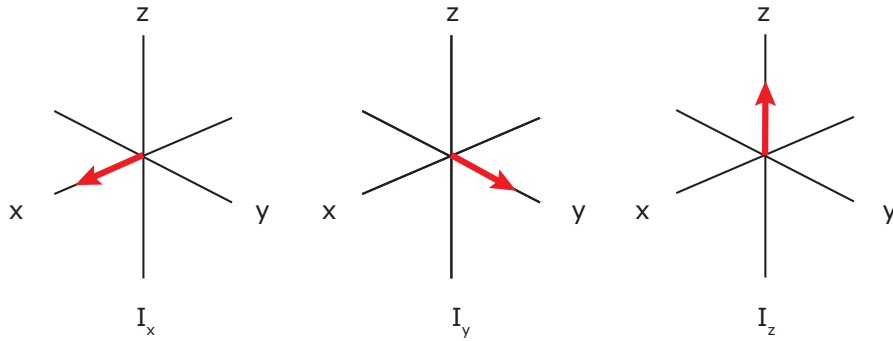


Figure 4.7: Vector model showing the product operators I_x , I_y and I_z for an isolated spin $\frac{1}{2}$ nucleus.

Remembering section 4.2.5, the effect of x and y pulses with a flip angle Θ on the x , y and z magnetisations of a single spin is shown in equation 4.71. Equation 4.71 shows two columns: corresponding to pulses with different phases, namely a x (left) and a y (right) pulse: (See figure 4.8 a and b, respectively)

$$\begin{array}{ll} I_x \xrightarrow{\theta_x} I_x & I_x \xrightarrow{\theta_y} I_x \cos \theta - I_z \sin \theta, \\ I_y \xrightarrow{\theta_x} I_y \cos \theta + I_z \sin \theta & I_y \xrightarrow{\theta_y} I_y, \\ I_z \xrightarrow{\theta_x} I_z \cos \theta - I_y \sin \theta & I_z \xrightarrow{\theta_y} I_z \cos \theta + I_x \sin \theta. \end{array} \quad (4.71)$$

In relation to the left-hand side equations: This means that for a flip angle of 90° with phase x applied to I_z (equilibrium magnetisation), the resulting magnetisation is aligned with the $-y$ axis. When the same pulse is applied to the I_y component this results in

the magnetisation being aligned along the z axis. The pulse has no effect upon the I_x component. For the right-hand side equations: This means that for a flip angle of 90° with phase y applied to I_z (equilibrium magnetisation), the resulting magnetisation is aligned with the x axis. When the same pulse is applied to the I_x component this, results in the magnetisation being aligned along the $-z$ axis. The pulse has no effect upon the I_y component.

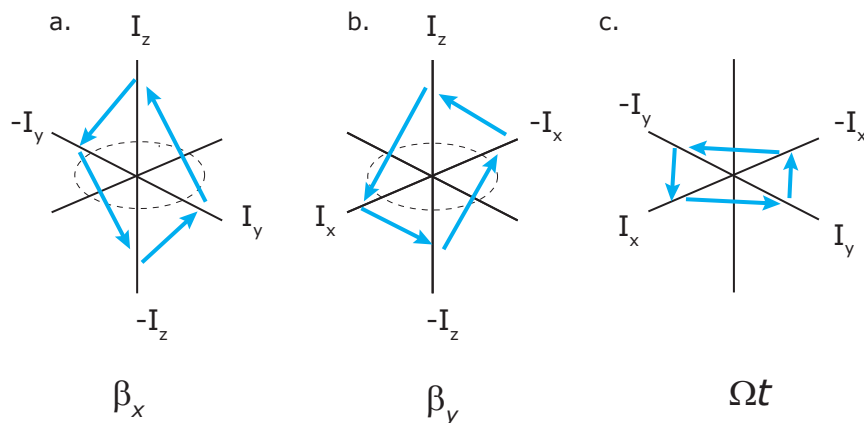


Figure 4.8: Representation of the transformation of the product operators of an isolated spin $\frac{1}{2}$ nucleus when x (a) or y (b) pulses with flip angle θ are applied, from equation 4.71. The effect of free precession for a time t at a resonance offset Ω from equation 4.72. Adapted from reference [182].

As shown in section 4.2.6, the vector model shows how the net magnetisation evolves under a resonance offset Ω for a time, t (see figure 4.8c):

$$\begin{aligned} I_x &\xrightarrow{\Omega t} I_x \cos \Omega t + I_y \sin \Omega t, \\ I_y &\xrightarrow{\Omega t} I_y \cos \Omega t - I_x \sin \Omega t, \\ I_z &\xrightarrow{\Omega t} I_z. \end{aligned} \tag{4.72}$$

Product operators can also be visualised via energy levels, as can be seen in figure 4.9 for a spin $I=\frac{1}{2}$ nucleus. The dotted lines show the 90° (see section 4.3) phase difference between I_x and I_y operators - this corresponds to the absorptive and dispersive lineshape in section 4.2.7. The I_z corresponds to a population state where the spin can be aligned with the external field (α) or against the external field (β) (see section 4.3). I_x and I_y are coherence states.

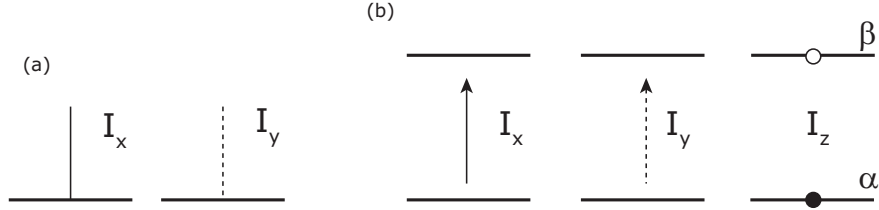


Figure 4.9: Product operators for a single spin $\frac{1}{2}$ nucleus: (a) schematic spectra, (b) energy level diagrams. The dashed line for I_y is to indicate the $\frac{\pi}{2}$ phase difference from I_x . The arrows show the transitions where there are associated product operators. The open circle shows a population deficit and the closed circle shows a population excess in the energy levels. Diagram adapted from [182].

The product operator method yields the same result as the vector model for an isolated spin; the usefulness of the product operator method is shown when coupled spins are used.

4.5.2 Coupled Spins

The product operators for a coupled spin system (I - S) are found by taking the products of the four operators introduced in equation 4.70.

		$\frac{1}{2}E$	S_x	S_y	S_z	
	$\frac{1}{2}E$	$\frac{1}{2}E$	S_x	S_y	S_z	
2 x	I_x	I_x	$2I_xS_x$	$2I_xS_y$	$2I_xS_z$	(4.73)
	I_y	I_y	$2I_yS_x$	$2I_yS_y$	$2I_yS_z$	
	I_z	I_z	$2I_zS_x$	$2I_zS_y$	$2I_zS_z$	

where the factor of 2 is for normalisation. The four product operators in the centre of the table are known as multiple-quantum coherences: $2I_xS_x$, $2I_xS_y$, $2I_yS_x$ and $2I_yS_y$. The other products operators can be related to the vector model where I_x , I_y , I_z , S_x , S_y and S_z are known as the in-phase operators, while $2I_xS_z$, $2I_yS_z$, $2I_zS_x$ and $2I_zS_y$ are anti-phase operators. The product operators of I_x , I_y , I_z and $2I_xS_z$, $2I_yS_z$ and $2I_zS_z$ are shown in the vector model representation in figure 4.10.

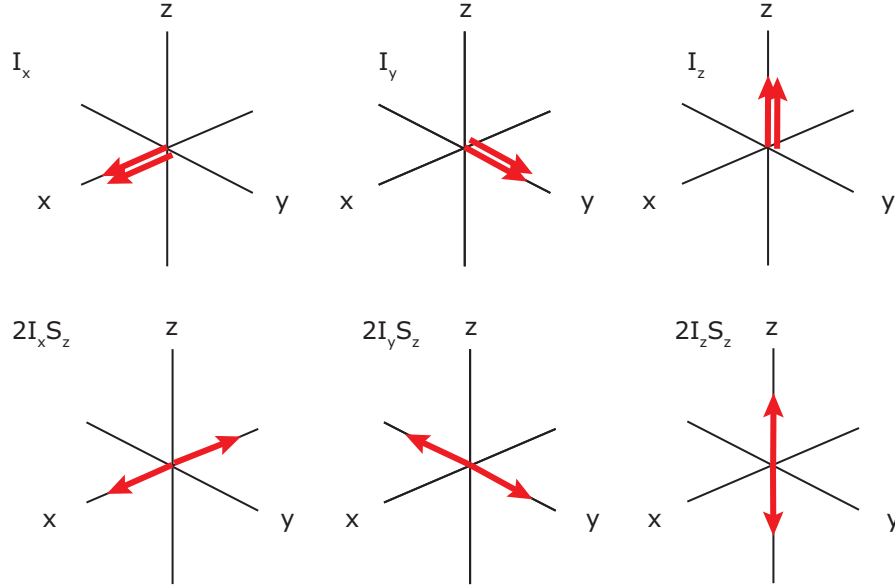


Figure 4.10: Representation of a selection of product operators from equation 4.73 for an I - S system, comprising the in-phase operators of I_x , I_y , I_z and the anti-phase operators of $2I_x S_z$, $2I_y S_z$ and $2I_z S_z$.

The evolution of I_x , I_y , I_z , $2I_x S_z$, $2I_y S_z$ and $2I_z S_z$ magnetisations under a J -coupling (J_{IS}) for a time period t is given by:

$$\begin{aligned}
 I_x &\xrightarrow{\pi J_{IS} t} I_x \cos \pi J_{IS} t + 2I_y S_z \sin \pi J_{IS} t, \\
 I_y &\xrightarrow{\pi J_{IS} t} I_y \cos \pi J_{IS} t - 2I_x S_z \sin \pi J_{IS} t, \\
 I_z &\xrightarrow{\pi J_{IS} t} I_z, \\
 2I_x S_z &\xrightarrow{\pi J_{IS} t} 2I_x S_z \cos \pi J_{IS} t + I_y \sin \pi J_{IS} t, \\
 2I_y S_z &\xrightarrow{\pi J_{IS} t} 2I_y S_z \cos \pi J_{IS} t - I_x \sin \pi J_{IS} t, \\
 2I_z S_z &\xrightarrow{\pi J_{IS} t} 2I_z S_z.
 \end{aligned} \tag{4.74}$$

Magnetisation in the first three cases in 4.74 resides upon the I spin, and is shown to evolve over time into a coupled state involving the I and S spin. This describes magnetisation transfer via J -coupling.

4.5.3 Multiple Quantum Coherences

If an isolated spin $\frac{1}{2}$ pair (I and S) is represented quantum mechanically there are four possible Zeeman transition states corresponding to whether a spin is aligned with the external field ($\alpha\alpha$) or against it ($\beta\beta$), as can be viewed in figure 4.11. Double quantum

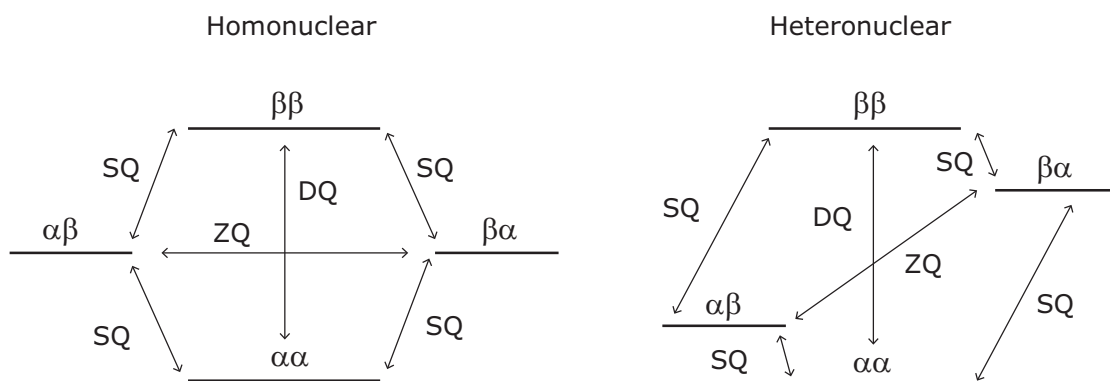


Figure 4.11: Energy level diagrams which represent the transitions which can take place between the different energy states: zero quantum (ZQ), single quantum (SQ) and double quantum (DQ), for a coupled spin pair in a homonuclear and heteronuclear coupling environment

coherences (DQ) are shown by transitions between the $\alpha\alpha$ and $\beta\beta$ energy levels, whilst zero quantum transitions result from transitions between the $\alpha\beta$ and $\beta\alpha$ energy levels. Single quantum transitions are shown by all other possible transitions. For homonuclear cases, the ZQ energy levels have essentially degenerate energy, while for heteronuclear cases the difference in energy between the levels can be 100s of MHz, therefore the dipole-dipole interaction (kHz range) is not enough to cause ZQ polarisation between the $\alpha\beta$ and $\beta\alpha$ states.

4.6 Hamiltonians and Interactions

A Hamiltonian operator can be used to describe all of the interactions in an NMR experiment:

$$\hat{H} = \hat{H}_z + \hat{H}_{rf} + \hat{H}_\sigma + \hat{H}_D + \hat{H}_Q + \hat{H}_J. \quad (4.75)$$

This Hamiltonian operator is for a non-metal, diamagnetic material; otherwise additional terms would need to be included.

CHAPTER 4. NMR THEORY

\hat{H}_z : Zeeman interaction Hamiltonian,

\hat{H}_{rf} : Hamiltonian associated with rf pulses,

\hat{H}_σ : Chemical shielding Hamiltonian,

\hat{H}_D : Dipolar coupling Hamiltonian,

\hat{H}_Q : Hamiltonian associated with quadrupolar coupling (for $I \geq 1$) and

\hat{H}_J : J coupling Hamiltonian.

\hat{H}_z and \hat{H}_{rf} are external interactions and the others are internal spin interactions. The spin interactions and their Hamiltonians can be represented by a Cartesian tensor:

$$\hat{H}_A = \hat{I} \cdot \tilde{A} \cdot \hat{S} = \begin{bmatrix} \hat{I}_x & \hat{I}_y & \hat{I}_z \end{bmatrix} \begin{bmatrix} A_{xx} & A_{xy} & A_{xz} \\ A_{yx} & A_{yy} & A_{yz} \\ A_{zx} & A_{zy} & A_{zz} \end{bmatrix} \begin{bmatrix} \hat{S}_x \\ \hat{S}_y \\ \hat{S}_z \end{bmatrix}, \quad (4.76)$$

where $A = \tilde{\sigma}, \tilde{D}, \tilde{J}, \tilde{Q}$ describes the interaction, \hat{I} is the spin operator and \hat{S} can be a further interacting spin operator or the external field.

4.6.1 The Radiofrequency Hamiltonian

As described in section 4.2 transverse magnetisation is needed to observe an NMR signal. This is a coherence state relating to the off-diagonal terms of the density matrix. Transverse magnetisation is achieved by manipulating the spins from their equilibrium position by applying a weak linearly oscillating magnetic field, in the x - y plane of the laboratory frame. The frequency of the oscillation ω_{rf} (the transmitter frequency of the B_1 magnetic field) must be comparable to the Larmor frequency or resonance frequency (ω_0) of the nuclear spins, such that $\omega_{rf} \approx \omega_0$. Since the rf field is time dependent, the energy is also time dependent:

$$E = -\mu \cdot B_1, \quad (4.77)$$

$$= -\gamma I \cdot B_1,$$

$$= -\gamma \begin{bmatrix} I_x & I_y & I_z \end{bmatrix} \begin{bmatrix} B_1 \cos(\omega_1 t) \\ B_1 \sin(\omega_1 t) \\ 0 \end{bmatrix}. \quad (4.78)$$

$$E = -\gamma B_1 [\cos(\omega_1 t) I_x + \sin(\omega_1 t) I_y]. \quad (4.79)$$

4.6. HAMILTONIANS AND INTERACTIONS

Replacing E , I_x and I_y with their equivalent operators generates the Hamiltonian:

$$\hat{H} = \omega_1[\hat{I}_x \cos(\omega_{rf}t + \phi) + \hat{I}_y \sin(\omega_{rf}t + \phi)], \quad (4.80)$$

where $\omega_1 = -\gamma_1 B_1$ is the nutation frequency (see section 4.2.5) and ϕ is the phase (i.e. for an x pulse) the linearly oscillating magnetic field is given by:

$$B_1(t) = 2B_1(\cos(\omega_{rf}t + \phi))i. \quad (4.81)$$

The effect of a pulse is to tilt the net magnetisation away from the z axis, where it precesses around the z axis (B_0) at the Larmor frequency. The B_1 field is made up of two angular frequencies rotating in opposite directions: $+\omega_{rf}$ and $-\omega_{rf}$. The latter $-\omega_{rf}$ term can be neglected as it is not in the same direction as the Larmor precession and is hundreds of MHz's off resonance, thus has little effect on the spins.

If viewed in a rotating frame (see section 4.2.5), which rotates about the z axis with angular frequency $+\omega_{rf}$, the rotating rf field will appear to be static. This allows a pulse to be viewed as a temporary application of a static magnetic field B_1 , orthogonal to B_0 . This has the effect of making the \hat{H}_{rf} Hamiltonian time independent:

$$\hat{H}_{rf}^{rot} = \omega_1[\hat{I}_x \cos(\phi) + \hat{I}_y \sin(\phi)]. \quad (4.82)$$

The solution to the Liouville-von Newman equation (4.66) describes the time dependence of the density operator under an rf pulse (with $\phi = 0$, i.e. an x pulse) as:

$$\hat{\rho}(t) = \exp(-i\omega_1 t \hat{I}_x) \hat{\rho}(0) \exp(i\omega_1 t \hat{I}_x). \quad (4.83)$$

At equilibrium, the spins are aligned with I_z (the constant of proportionality is set to one),

$$\hat{\rho}(0) = \hat{I}_z, \quad (4.84)$$

hence $\hat{\rho}(t)$ can be expressed in matrix form:

$$\hat{\rho}(t) = \frac{1}{2} \begin{bmatrix} \cos(\omega_1 t) & i \sin(\omega_1 t) \\ -i \sin(\omega_1 t) & \cos(\omega_1 t) \end{bmatrix}. \quad (4.85)$$

The rf pulse results in a population state shown by on-diagonal terms and coherence shown by off-diagonal terms. The expectation values of the \hat{I}_x , \hat{I}_y and \hat{I}_z operators can

be found using equation 4.63 giving:

$$\langle \hat{I}_x \rangle = T_r[\rho I_x] = 0, \quad (4.86)$$

$$\langle \hat{I}_y \rangle = T_r[\rho I_y] = \frac{1}{2} \sin(\omega_1 t), \quad (4.87)$$

$$\langle \hat{I}_z \rangle = T_r[\rho I_z] = \frac{1}{2} \cos(\omega_1 t). \quad (4.88)$$

The expectation values of \hat{I}_x , \hat{I}_y show that when an *rf* pulse is applied along the *x* axis, it oscillates at the nutation frequency and acts to rotate the net magnetisation about *x* by the angle, θ , known as the “flip angle” (see equation 4.24 in section 4.2.5 and figure 4.8 in section 4.5). t_p can be chosen to make β equal to $\frac{\pi}{2}$ if maximum excitation is needed (creating a coherence state) or π can be chosen to invert the equilibrium magnetisation known as population inversion.

4.6.2 Evolution Under an Offset

As described above in sections 4.2.6 and 4.5.1, a coherence state is created when an *rf* pulse is applied along the *x* axis with a phase angle of $\frac{\pi}{2}$. Once the pulse is turned off, the net magnetisation evolves in the transverse plane under a resonance offset (Ω). Thus, in the rotating frame the Zeeman Hamiltonian is expressed as:

$$\hat{H}_z^{rot} = (\omega_0 - \omega_{rf}) \hat{I}_z = \Omega \hat{I}_z. \quad (4.89)$$

The Liouville von-Neumann equation can be used to observe the state of transverse magnetisation under a resonance offset:

$$\hat{\rho}(t) = \exp(-i\Omega t \hat{I}_z) \hat{\rho}(0) \exp(i\Omega t \hat{I}_z), \quad (4.90)$$

where $\hat{\rho}(0) = \hat{I}_x$, hence

$$\hat{\rho}(t) = \begin{pmatrix} 0 & \frac{1}{2} \exp(-i\Omega t) \\ \frac{1}{2} \exp(i\Omega t) & 0 \end{pmatrix}. \quad (4.91)$$

The NMR signal is calculated by taking the trace of the product of $\hat{\rho}(t)$ and a raising operator,

$$\hat{I}_+ = \hat{I}_x + i\hat{I}_y = \begin{pmatrix} 0 & 1 \\ 0 & 0 \end{pmatrix}. \quad (4.92)$$

$$s(t) = Tr[\hat{\rho}\hat{I}_+] = Tr \begin{pmatrix} 0 & 0 \\ 0 & \frac{1}{2}exp(i\Omega_t) \end{pmatrix}, \quad (4.93)$$

$$= \frac{1}{2}exp(i\Omega_t) = \frac{1}{2}(cos(\Omega_t) + isin(\Omega_t)). \quad (4.94)$$

4.7 Frame Rotations and Tensors

For each interaction, a Principal Axes System (PAS) co-ordinate frame can be specified for which equation 4.76 can be simplified in order that only the diagonal terms of the interaction tensor \tilde{A} are present:

$$\hat{H}_A = \hat{I} \cdot \tilde{A} \cdot \hat{S} = \begin{bmatrix} \hat{I}_x \hat{I}_y \hat{I}_z \end{bmatrix} \begin{bmatrix} A_{xx} & 0 & 0 \\ 0 & A_{yy} & 0 \\ 0 & 0 & A_{zz} \end{bmatrix} \begin{bmatrix} \hat{S}_x \\ \hat{S}_y \\ \hat{S}_z \end{bmatrix}. \quad (4.95)$$

However using this co-ordinate system presents complications since the different internal interactions need to be described with respect to their own distinct reference frames. This means each interaction must be transformed from the PAS where only on-diagonal terms are considered (equation 4.95) into the laboratory reference frame. These transformations are best described in the spherical tensor notation, whereby, equation 4.95 is transformed into:

$$\hat{H} = \sum_{j=0}^2 \sum_{m=-j}^{+j} (-1)^m A_{jm} \hat{T}_{j-m}. \quad (4.96)$$

\hat{T}_{j-m} and \hat{A}_{jm} correspond to the spin and spatial components, respectively. The subscripts j and m refer to the rank of the tensor and the order of the tensor component, respectively, where m can take $2j + 1$ values ranging from $+j$ to $-j$. In the PAS, the Cartesian tensor is diagonal where A_{xx} , A_{yy} and A_{zz} are the only non zero terms, and equation 4.96 becomes:

$$\hat{H}_A^P = A_{00}^P \hat{T}_{00} + A_{20}^P \hat{T}_{20} + A_{22}^P \hat{T}_{2-2} + A_{2-2}^P \hat{T}_{22}. \quad (4.97)$$

A rotation between two frames (see figure 4.12), (X, Y, Z) and (x,y,z) can be described using Euler angles (labelled as α , β and γ). $\hat{R}(\alpha, \beta, \gamma)$ is the rotation operator which performs the rotation of an axis frame (x, y, z) by the Euler angles (α , β and γ). $\hat{R}(\alpha, \beta, \gamma)$

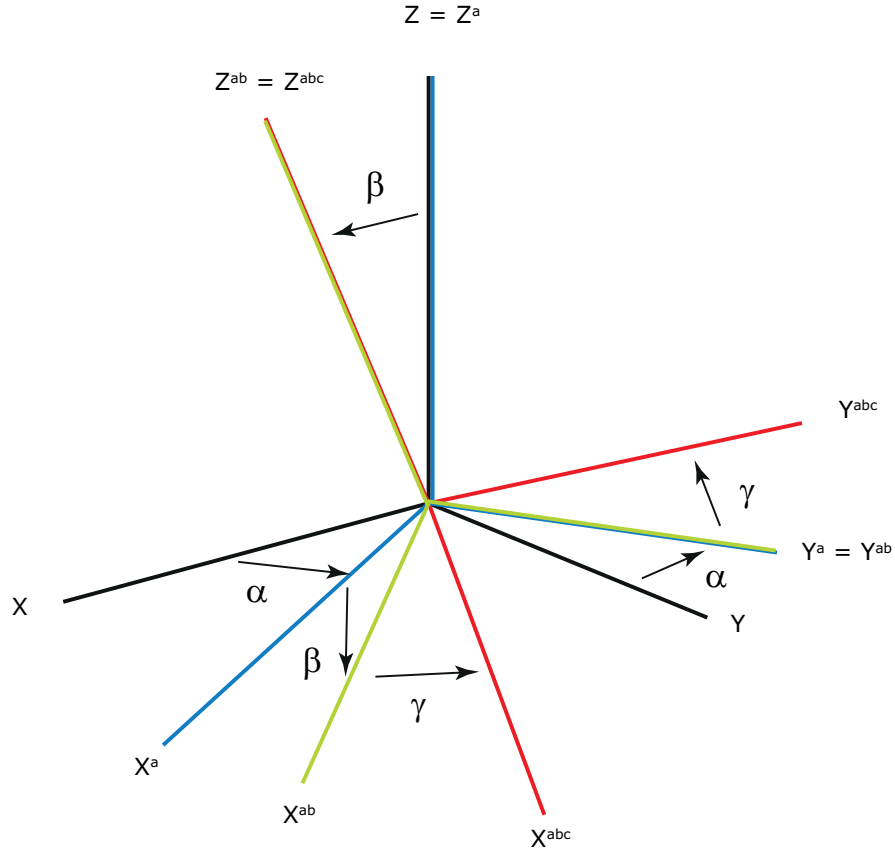


Figure 4.12: Euler angles defined in a Cartesian co-ordinate system

can be considered as a rotation by an angle γ about Z, then β about Y and α about Z, such that the complete rotation can be expressed as:

$$\hat{R}(\alpha, \beta, \gamma) = \hat{R}_Z(\alpha) \hat{R}_Y(\beta) \hat{R}_Z(\gamma), \quad (4.98)$$

where $\hat{R}_Z(\alpha)$ represents the rotation of of angle α about the Z axis.

A spherical tensor component A_{jm} is converted by a rotation into a sum of components with same rank but differing order:

$$R(A_{jm}^{start}) = \sum_{m=-j}^{m=+j} D_{mm}^j(\alpha_{PL}\beta_{PL}\gamma_{PL}) A_{jm}^{end}, \quad (4.99)$$

4.8. INTERNAL INTERACTIONS

where A_{jm}^{start} refers to the start frame and A_{jm}^{end} refers to the frame it is transformed to. The rotation matrix $D_{kl}^j(\alpha\beta\gamma)$ is given by:

$$D_{kl}^j(\alpha\beta\gamma) = \exp(-il\alpha)d_{kl}^j(\beta)\exp(-il\gamma), \quad (4.100)$$

where $d_{kl}^j(\beta)$ is a reduced Wigner rotation matrix and is a trigonometric function. Therefore, a rotation from the PAS to the lab frame (L) is given by:

$$A_{jm}^{L(end)} = \sum_m A_{jm}^{P(start)} D_{mm'}^j(\alpha_{PL}\beta_{PL}\gamma_{PL}). \quad (4.101)$$

The term secular refers to Hamiltonians describing nuclear spin interactions within a spin system which commutes with the Zeeman Hamiltonian. Except when large quadrupole interactions are present, components of the interaction Hamiltonian that do not commute with the Zeeman interaction can be ignored. When this occurs, second order terms need to be considered (see section 4.8.5 below). This is equivalent to considering the spin interaction Hamiltonians as first order perturbations of the dominant Zeeman interaction and considering only first order perturbation theory.

In the secular approximation, only spin terms \hat{T}_{jm} which commute with the Zeeman interaction \hat{I}_z are retained. The commutator is given by:

$$[\hat{I}_z, \hat{T}_{jm}] = m\hat{T}_{jm}, \quad (4.102)$$

where the commutator is 0 if $m = 0$. In the laboratory frame, the secular approximation means that only A_{j0}^L terms are retained.

$$\hat{H}^L = A_{00}^L \hat{T}_{00} + A_{20}^L \hat{T}_{20}, \quad (4.103)$$

where A_{00}^L represents the isotropic part of a given internal interaction and A_{20}^L is the anisotropic part.

4.8 Internal Interactions

4.8.1 Chemical Shielding

The shielding tensor σ links the magnetic field which results from the shielding of the nucleus by electrons, B_S , to the applied magnetic field B_0 .

$$B_S = -\sigma B_0. \quad (4.104)$$

CHAPTER 4. NMR THEORY

In the laboratory frame, tensors in Cartesian form are represented by a 3x3 matrix:

$$\begin{pmatrix} R_{xx} & R_{xy} & R_{xz} \\ R_{yx} & R_{yy} & R_{yz} \\ R_{zx} & R_{zy} & R_{zz} \end{pmatrix}. \quad (4.105)$$

If the applied field is along the z axis, the shielding field in each direction is:

$$B_{Sx} = -\sigma_{xz}B_0, \quad (4.106)$$

$$B_{Sy} = -\sigma_{yz}B_0, \quad (4.107)$$

$$B_{Sz} = -\sigma_{zz}B_0. \quad (4.108)$$

This shows that, for most anisotropic samples, the shielding field is not parallel to the applied field. Figure 4.13 distinguishes the case of an isotropic and anisotropic shielding.

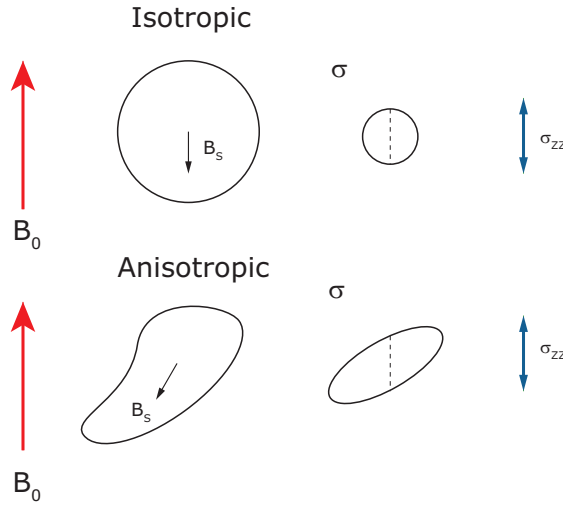


Figure 4.13: A representation of the shielding field (B_S) and the applied field (B_0) in an isotropic and anisotropic case. The shielding ellipsoids show the magnitude of the tensors in different orientations.

The principal components of the tensor in the PAS frame are shown here:

$$\begin{pmatrix} R_{xx} & 0 & 0 \\ 0 & R_{yy} & 0 \\ 0 & 0 & R_{zz} \end{pmatrix}. \quad (4.109)$$

4.8. INTERNAL INTERACTIONS

The isotropic average is given by:

$$R_{iso} = \frac{1}{3}(R_{XX} + R_{YY} + R_{ZZ}). \quad (4.110)$$

Considering shielding leads to chemical shift,

$$\delta = \frac{\omega_0 - \omega_0^{REF}}{\omega_0^{REF}} \times 10^6, \quad (4.111)$$

the chemical shift measures how much the electrons in surrounding bonds shield the nuclear spin. This is because the magnetic field B_0 induces an electronic current in the bonds surrounding the nucleus. The electrons which orbit the nucleus generate a magnetic field B_S which will add (deshields) or subtract (shields) from B_0 . The electrons are not spherically distributed around the nucleus so the field will be anisotropic, thus a tensor property. $-\sigma^{PAS} = \delta^{PAS}$, where δ measures de-shielding, such that the chemical shift tensor is given as:

$$\delta_{iso} = \frac{1}{3}(\delta_{XX} + \delta_{YY} + \delta_{ZZ}). \quad (4.112)$$

The asymmetry parameter is given by:

$$\eta_j = \frac{\delta_{YY} - \delta_{XX}}{\delta_{aniso}}, \quad (4.113)$$

and takes values from 0 to 1.

The frequency of precession of the nuclear spins is determined by the local field B_{loc} :

$$B_{loc} = B_0 + B_S. \quad (4.114)$$

The induced field, B_S , is typically $\sim 10^{-4}$ of B_0 , which is large enough to give measurable shifts in the precession frequency. The components of the induced field are given by (see equations 4.106, 4.107, 4.108):

$$\begin{pmatrix} B_{S,x} \\ B_{S,y} \\ B_{S,z} \end{pmatrix} = - \begin{pmatrix} \sigma_{xx} & \sigma_{xy} & \sigma_{xz} \\ \sigma_{yx} & \sigma_{yy} & \sigma_{yz} \\ \sigma_{zx} & \sigma_{zy} & \sigma_{zz} \end{pmatrix} \begin{pmatrix} 0 \\ 0 \\ B_0 \end{pmatrix}. \quad (4.115)$$

CHAPTER 4. NMR THEORY

The nuclear spin will interact with the induced magnetic field according to the Zeeman interaction giving the chemical shift Hamiltonian as:

$$\hat{H}_{cs} = \gamma\sigma_{xz}I_xB_0 + \gamma\sigma_{yz}I_yB_0 + \gamma\sigma_{zz}I_zB_0. \quad (4.116)$$

Using the secular approximation (see section 4.7) only the last term remains.

$$\hat{H}_{cs} = \gamma\sigma_{zz}I_zB_0. \quad (4.117)$$

The terms of the shielding tensor depend on the orientation of the molecule with respect to the external field.

$$\sigma_{zz} = \frac{1}{3} \left\{ \sum_{j=x,y,z} \sigma_j + \sum_{j=x,y,z} (3\cos^2\Theta_j - 1)\sigma_j \right\}, \quad (4.118)$$

where σ_j are the principal components of the shielding tensor, where each one is associated with the symmetry axis of the molecule (principal axes). The angles Θ_j represent the orientation of these axes with respect to B_0 for a particular molecule.

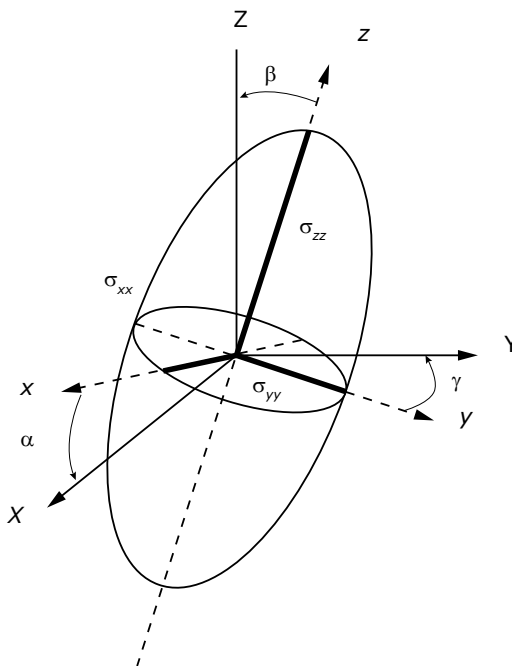


Figure 4.14: The shielding tensor, σ , represented by an ellipsoid (a second rank tensor) in the lab system (X, Y, Z) and PAS (x, y, z) where Euler angles α , β and γ define the orientation of the PAS relative to the lab frame.

The shielding tensor, σ , is thus represented by an ellipsoid which is a second rank tensor in the laboratory frame (X, Y, Z) and PAS (x, y, z) where Euler angles α , β and γ define the orientation of the PAS relative to the laboratory frame (see figure 4.14). For protons the shielding anisotropies are small (\sim upto 20 ppm) but they are upto \sim 200 ppm for ^{13}C and even larger for metallic nuclides.

4.8.2 Dipolar Coupling

Nuclear spins possess magnetic moments which can interact through space. This is called the dipolar coupling (see figure 4.15) in which its strength is dependent on the internuclear distance, r , and the orientation of the spins.

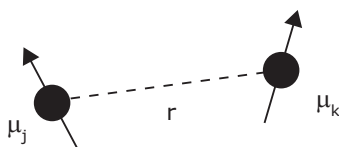


Figure 4.15: Representation of two magnetic dipoles which interact through space r .

There are two types of coupling: homonuclear and heteronuclear. Homonuclear refers to the coupling between like spins whereas heteronuclear refers to the coupling between unlike spins.

For two coupled spins I and S , the dipolar coupling Hamiltonian is given by:

$$\hat{H}_D = d \left(\hat{I} \cdot \hat{S} - \frac{3(\hat{I} \cdot \hat{r})(\hat{S} \cdot \hat{r})}{r^2} \right), \quad (4.119)$$

where \hat{r} and r are the unit vector and the magnitude of the vector between the two spins, respectively, and d is the magnitude of the through space interaction and is known as the dipolar coupling constant, given by:

$$d = -\frac{\mu_0}{4\pi} \frac{\gamma_I \gamma_S \hbar}{r^3}. \quad (4.120)$$

This is in units of rads^{-1} and, as a constant does not depend on orientation. The interaction can be seen to scale with the inverse cube of the internuclear distance, and scales linearly with the gyromagnetic ratio of each spin.

CHAPTER 4. NMR THEORY

In Cartesian tensor form, the dipolar Hamiltonian (angular frequency units), which is orientation dependent, can also be written as:

$$\hat{H}_D = 2\hat{I} \cdot \mathbf{D} \cdot \mathbf{S}. \quad (4.121)$$

\mathbf{S} represents the spin angular momentum and \mathbf{D} is the dipole coupling tensor which has principal values of $-\frac{d}{2}$, $-\frac{d}{2}$ and $+d$. \mathbf{D} describes how the magnetic field due to spin \mathbf{S} and felt at spin \mathbf{I} varies with the orientation of the \mathbf{I} - \mathbf{S} internuclear vector in the applied field. The dipole coupling tensor is traceless, $A_{xx} + A_{yy} + A_{zz} = 0$, and axially symmetric, $A_{xx} = A_{yy}$, resulting in no isotropic components. The Zeeman interaction is still the dominant interaction as the dipolar coupling strength for a ^1H - ^1H coupling is the order of 10's of kHz.

It is more useful to represent the dipolar Hamiltonian in spherical tensor form. As the dipolar interaction is traceless, only the A_{20}^P term remains, therefore, in its PAS, the Hamiltonian for the dipolar coupling of two nuclei is given by:

$$\hat{H}_D^P = A_{20}^P \hat{T}_{20}, \quad (4.122)$$

where the anisotropic term remains, with the spatial term given by:

$$A_{20}^P = \sqrt{6}d. \quad (4.123)$$

In order to rotate the spatial term in the PAS frame of the interaction to the laboratory frame where NMR measurements are taken, equation 4.101 is used to obtain:

$$A_{20}^L = A_{20}^P D_{00}^2, \quad (4.124)$$

$$A_{20}^L = \sqrt{6}d \exp(-i\alpha \cdot 0) d_{00}^2 \exp(-i\gamma \cdot 0), \quad (4.125)$$

$$A_{20}^L = \sqrt{6}d \frac{1}{2} (3\cos^2\beta - 1), \quad (4.126)$$

where the angle β is the angle between the internuclear vector and B_0 . The spin term corresponding to this is given by:

$$\hat{T}_{20} = \frac{1}{\sqrt{6}} (3\hat{I}_z \hat{S}_z - \hat{I} \cdot \hat{S}). \quad (4.127)$$

Combining equations 4.124 and 4.127, the dipolar Hamiltonian can be written in the laboratory frame as:

$$\hat{H}_D = d \frac{1}{2} (3\cos^2\beta - 1) (3\hat{I}_z \hat{S}_z - \hat{I} \cdot \hat{S}). \quad (4.128)$$

4.8. INTERNAL INTERACTIONS

As $\hat{I} \cdot \hat{S}$ can be written as $\hat{I}_x \hat{S}_x + \hat{I}_y \hat{S}_y + \hat{I}_z \hat{S}_z$, equation 4.128 can be written as:

$$\hat{H}_D = d \frac{1}{2} (3 \cos^2 \beta - 1) (2 \hat{I}_z \hat{S}_z - (\hat{I}_x \hat{S}_x + \hat{I}_y \hat{S}_y)). \quad (4.129)$$

For the homonuclear case, the matrix forms of the spin angular momentum operators are:

$$2 \hat{I}_z \hat{S}_z = \begin{pmatrix} \frac{1}{2} & 0 & 0 & 0 \\ 0 & -\frac{1}{2} & 0 & 0 \\ 0 & 0 & -\frac{1}{2} & 0 \\ 0 & 0 & 0 & \frac{1}{2} \end{pmatrix}, \quad \hat{I}_x \hat{S}_x + \hat{I}_y \hat{S}_y = \begin{pmatrix} 0 & 0 & 0 & 0 \\ 0 & 0 & \frac{1}{2} & 0 \\ 0 & \frac{1}{2} & 0 & 0 \\ 0 & 0 & 0 & 0 \end{pmatrix}. \quad (4.130)$$

However, for a static experiment for the heteronuclear case, the dipolar Hamiltonian is written as:

$$\hat{H}_{D,heter} = d \frac{1}{2} (3 \cos^2 \beta - 1) (2 \hat{I}_z \hat{S}_z), \quad (4.131)$$

here the off-diagonal terms in the corresponding matrix would be 0 as only the $2 \hat{I}_z \hat{S}_z$ term is considered. The on-diagonal elements are thus only considered, in other words the $\hat{I}_z \hat{S}_z$ term. Therefore, the spin eigenstates are the Zeeman interaction states: $\alpha\alpha$, $\alpha\beta$, $\beta\alpha$ and $\beta\beta$ shown in figure 4.11.

Under static conditions for an isolated pair of heteronuclear dipolar coupled nuclei in a powdered sample, the typical lineshape is described by the Pake Doublet shown in figure 4.16. The intensity of the signal at a given frequency depends on the probability of the angle. The angle of 90° is more common than 0° . (An analogy to the Earth can be used: there are more unique directions at the equator than there are unique directions at the poles.) The “horns” in the lineshape show when the sample is orientated perpendicular to B_0 , corresponding to the most probable situation. In spherical coordinates, there is a $\sin \theta$ weighting, thus the intensity is higher at $\theta = 90^\circ$. The “feet” of the lineshape correspond to when the principal axis of the coupling interaction is parallel to B_0 . The distance between the two horns is related to the dipolar coupling constant.

4.8.3 Magic Angle Spinning

Most of the interactions described have been anisotropic, whose strength is dependent on their orientation with respect to the external magnetic field. In solution, molecular tumbling occurs averaging the anisotropic interactions. In the solid state, this does not occur meaning anisotropic interactions remain and are observed. The orientation dependence of the anisotropic interactions are of the form $3 \cos^2 \theta - 1$, where θ is the

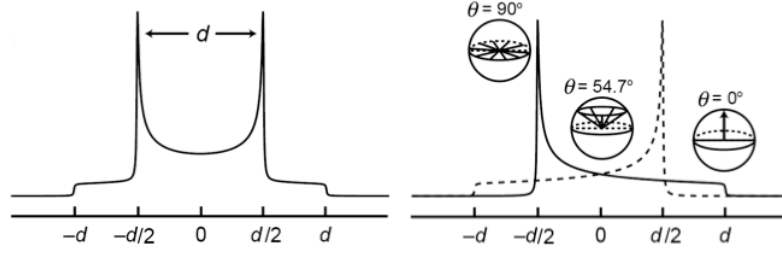


Figure 4.16: A typical Pake Doublet pattern for a pair of isolated heteronuclear nuclei in a powdered sample showing the distance, d , between “horns” [183].

angle describing the orientation of the spin interaction tensor with respect to the external field. θ takes all possible orientations in a powdered sample, as all possible orientations are sampled over the volume of the powder. Line broadening takes place as resonances from each of the possible orientations are summed (see figure 4.16).

A way to overcome this problem is to use Magic Angle Spinning (MAS) where samples are placed inside a rotor which is rotated about an axis at a specific orientation of $\Theta = 54.7^\circ$, the so-called “Magic Angle” to B_0 . This method effectively acts like the molecular tumbling in solution-state averaging the anisotropic interactions to 0.

To describe how MAS works, Euler angles (see section 4.12) are needed to describe rotations from the PAS to the laboratory frame. Two rotations are required: the first from the PAS to the rotor frame and the second from the rotor frame to the laboratory frame. The Euler angles associated with these rotations are given below:

Rotation from PAS to rotor frame : $\Omega_{PR} = (\alpha_{PL}, \beta_{PR}, \gamma_{PR})$

Rotation from rotor frame to laboratory frame : $\Omega_{RL} = (\alpha_{RL}, \beta_{RL}, \gamma_{RL})$,

where α_{RL} is the time-dependent angle through which the rotor rotates, β_{RL} is the angle of the rotor axis with respect to the external field and γ_{RL} defines the rotor phase. The spatial component of the anisotropic interaction tensor after the two rotations is given by:

$$A_{20}^L = A_{20}^{PAS} \sum_{m'=-2}^2 D_{0m'}^2(\alpha_{PL}, \beta_{PR}, \gamma_{PR}) d_{m'0}^2(\beta_{RL}) \exp(im' \omega_R t), \quad (4.132)$$

whereby, using the secular approximation, all other spatial terms are discarded except for the A_{20}^{PAS} term. For a complete revolution of the rotor over a time, τ_R , $2\pi/\omega_R$ terms with non-zero values of m' will average to 0,

$$\int_0^{\tau_R} \exp(im\omega_R t) dt = \begin{cases} \tau_R, m = 0 \\ 0, m \neq 0 \end{cases}. \quad (4.133)$$

Average Hamiltonian theory considers the Hamiltonian only at specific points in time, separated by the time interval, τ_R . In experiments, this can be achieved using rotor synchronisation where the signal is only detected at points separated by the rotor period. When the detection occurs over a rotor period and $m = 0$, equation 4.132 becomes:

$$\langle A_{20}^L \rangle = A_{20}^{PAS} \left[\frac{1}{4} (3 \cos^2 \beta_{PR} - 1)(3 \cos^2 \beta_{RL} - 1) \right]. \quad (4.134)$$

If β_{RL} is set to 54.7° , the magic angle, the anisotropy will reduce to 0 over a complete rotor period. However if rotor synchronisation is not achieved the interaction must be considered over all relevant spatial parts:

$$A_{20}^L = A_{20}^{PAS} \left(\frac{1}{2} \sin^2 \beta_{PR} \cos(2\gamma_{PR} + 2\omega_R t) - \sqrt{2} \sin 2\beta_{PR} \cos(\gamma_{PR} + \omega_R t) \right). \quad (4.135)$$

For MAS to produce a single line at isotropic chemical shift for a powder sample, the spinning rate must be fast in comparison to the anisotropy of the interaction being spun out. If the spinning occurs at a slower rate than the anisotropy as well as the isotropic chemical shift this produces spinning sidebands in the spectrum. Spinning sidebands are sharp lines radiating out from the line at the isotropic chemical shift and occur periodically at the spinning rate apart. There are ways to remove the spinning sidebands in a spectrum in order that the spectrum can more easily be interpreted. One way is to spin faster and therefore remove the anisotropies. Another way to ensure rotor synchronisation i.e. that a recorded FID is equal to the rotor period. The most used method however is to use a pulse sequence known as T_OTal Suppression of Spinning sidebands (TOSS)[184]. For the work that was conducted in this thesis the experiments used were rotor synchronised and for most of the experiments spinning occurred at rates of 60 kHz thus removing the anisotropies.

4.8.4 *J*-Coupling

The *J*-coupling interaction represents the indirect magnetic interactions of nuclear spins with each other, through the involvement of electrons. This is also known as scalar coupling. *J*-coupling occurs when the nuclear spin polarises an electron spin, the polarisation is then transferred to other bonded electrons which in turn polarise its nuclear spin.

Two spins have a measurable J -coupling only if they are linked together through a small number of chemical bonds, which include hydrogen bonds.

The J -coupling is not traceless, meaning it is not removed by molecular tumbling in solution-state NMR. The J -coupling has both isotropic and anisotropic components. The anisotropic part can usually be discarded due to its usually small magnitude as compared to the dipolar coupling. Overall, the size of the isotropic component is also relatively small compared to the other interactions, for example ~ 100 Hz for a one-bond CH coupling. The J -coupling Hamiltonian is given by:

$$\hat{H}_j = \sum_{i < j} \hat{I}_i \cdot \tilde{J} \cdot \hat{S}_j, \quad (4.136)$$

where \tilde{J} is the coupling tensor (Hz) as the interaction is independent of the external field, and \hat{I}_i and \hat{S}_j are the through bond coupled spins. The isotropic component is the scalar average of the interaction tensor:

$$J = \frac{1}{3}(J_{xx} + J_{yy} + J_{zz}). \quad (4.137)$$

The J -coupling results in the splitting of resonances in the NMR spectrum, with the distance between resonances separated by J , therefore the splitting does not change if the external field changes. J is rarely seen in solid-state NMR due to the strength of the other interactions namely the dipolar coupling broadening linewidths concealing the J -splitting.

4.8.5 Quadrupolar Coupling

The nuclear spin Hamiltonian contains terms describing the orientation dependence of the nuclear energy. Generally there are two terms: the electric and magnetic spin Hamiltonian. The electric spin Hamiltonian describes the way the nuclear electric energy changes, while the magnetic spin Hamiltonian describes the way the magnetic energy changes during rotation.

The electric charge of a nucleus can be broken down into multiple components:

E^0 : Electric charge +

E^1 : Electric dipole moment +

E^2 : Electric quadrupolar moment.

4.8. INTERNAL INTERACTIONS

If a nucleus is put into an electric potential field, $V(r)$, which is dependent on position it would acquire a stable position at the minimum of the electrical potential, but the electrical potential would still vary from side to side.

The electric field potential can be represented as a superposition of terms:

V^0 : Electric potential at the centre of the nucleus.

V^1 : Potential gradient at the centre of the nucleus (proportional to the difference in potential from one side of the nucleus to the other).

V^2 : Gradient of the gradient i.e. the gradient of the electric field (how much the slope of the potential changes from one side of the nucleus to the other).

Therefore the total contribution to the electric interaction is: $E_{lec} = E^{(0)} + E^{(1)} + E^{(2)} + \dots$ where each term comes from the interaction of a single multipole component of the charge distribution with a different aspect of the potential.

For spin $\frac{1}{2}$ nuclei, all electric multipoles vanish except the first term (spherical charge). This means that there are no electrical energy terms that depend on the orientation or internal structure of the nucleus. Therefore, it behaves as if it were a single point charge (for electric effects).

$$\hat{H}_J^{elec} = 0 \quad \text{for} \quad I = \frac{1}{2}, \quad (4.138)$$

and magnetically they behave like perfect frictionless gyroscopes.

Nuclei with $I > \frac{1}{2}$ are defined as quadrupolar nuclei, and the electrical charge distribution is not spherically symmetric and the situation is more complicated as there are now electric and magnetic effects to consider. The electric energy of the nucleus depends on its orientation with respect to the rest of the molecule. The most important term is the $E^{(2)}$ representing the interaction of the quadrupole charge distribution of the nucleus with the V^2 term.

The main orientation dependent electric term is the interaction of the electric quadrupole moment of the nucleus with the electric field gradient in the surrounding space. The quadrupole interaction depends on the nuclear quadrupole moment (property of nucleus) and the electric field gradient (property of environment - created by electrons at the nucleus). For quadrupolar nuclei, quadrupole coupling is of the order of MHz and for some nuclei 100's MHz. It can be an intra or inter-molecular interaction where the quadrupolar moment of the nucleus interacts strongly with the electric field gradients generated by the surrounding electron clouds.

Nuclear quadrupole moments for given nuclei do not accurately represent the typical magnitudes of the electric quadrupole interaction. For example, nuclei with large quadrupole moments may have small quadrupole couplings, if the nuclear environment is so symmetric that the local electric field gradients are small. The opposite however occurs for ^{14}N ($I = 1$) which has a relatively small electric quadrupole moment but is found in covalently bonded sites with large local field gradients. As a result the electric quadrupole coupling of ^{14}N is usually large, except in exceptional cases of high symmetry such as NH_4^+ sites and other quaternary ions. In the ^1H - ^{14}N HMQC experiment, detection is on the ^1H nucleus, the main advantages of this are:

1. From equation 4.5, it is shown that the nuclear magnetic moment is proportional to the gyromagnetic ratio, γ meaning that nuclei with higher γ values will have a larger macroscopic magnetic moment, therefore a stronger NMR signal.
2. From equations 4.9, 4.6, 4.7 and Figure 4.2, it is shown that the net (bulk) magnetisation and thus the resulting NMR signal is dependent on the Boltzmann distribution. The Boltzmann distribution is proportional to the Larmor frequency and therefore also proportional to γ this means that a larger Larmor frequency results in a larger Boltzmann distribution consequently resulting in a stronger NMR signal.
3. From equation 4.8, it is also shown that the Larmor frequency, ω_0 , is proportional to γ . An NMR signal is generated after the *rf* pulse is switched off and the transverse magnetisation precesses around the B_0 field at the Larmor frequency. The NMR signal is subsequently generated in a coil which surrounds the sample by electromagnetic induction (Faraday's Law). The induced current is thus dependent on the Larmor frequency meaning by having nuclei with larger γ values the NMR signal will be stronger.

Electric field gradient tensor

The electric field gradient (EFG) at a nuclear site is a tensor, and has principal values associated with three principal axes often close to the molecular symmetry axes. These values are V_{XX} , V_{YY} and V_{ZZ} that sum to zero.

$$\tilde{V} = \begin{pmatrix} V_{xx} & V_{xy} & V_{xz} \\ V_{yx} & V_{yy} & V_{yz} \\ V_{zx} & V_{zy} & V_{zz} \end{pmatrix}. \quad (4.139)$$

4.8. INTERNAL INTERACTIONS

The EFG at the site of a nucleus is usually specified using two parameters eq and η_Q , where eq is the largest principal value of the EFG tensor

$$eq = V_{ZZ}. \quad (4.140)$$

In the PAS, only the diagonal terms of equation 4.139 will be non-zero which leads to the asymmetry parameter η_Q (also referred to as the biaxiality of the EFG tensor):

$$\eta_Q = \frac{(V_{XX} - V_{YY})}{V_{ZZ}}, \quad (4.141)$$

where

$$V_{xx} \leq V_{yy} \leq V_{zz}. \quad (4.142)$$

η_Q gives the relative strength of the EFG in the three orthogonal directions and takes values from 0 - 1, where 0 denotes perfect spherical symmetry and 1 indicates high asymmetry.

An important term described by the PAS is the quadrupolar coupling constant C_Q (in Hz),

$$C_Q = \frac{eQV_{zz}}{h} = \frac{e^2qQ}{h}. \quad (4.143)$$

A low C_Q value means there is high symmetry, whereas larger C_Q values indicate that a large EFG traverses the nucleus. Typical values range from a few kHz to 100's MHz. This quantity is important for the research presented in this thesis.

Nuclear quadrupole Hamiltonian

If the electrical charge distribution around the nucleus is non-spherical, there is a further splitting of the Zeeman energy levels. The resulting Hamiltonian can be written as:

$$\hat{H}_Q = \frac{eQ}{2I(2I-1)} \hat{I} \cdot \tilde{V} \cdot \hat{I}, \quad (4.144)$$

where eQ is the nuclear quadrupole moment and \tilde{V} is a second rank tensor describing the electric field gradient (see equation 4.139). If the quadrupolar interaction \ll Zeeman interaction, the secular approximation is used and many of the terms are ignored (as was the case in chemical shift). Due to the large size of the quadrupolar interaction, it is

often necessary to include more than one term in the series.

$$\hat{H}_Q^{full} = \hat{H}_Q^1 + \hat{H}_Q^2 + \hat{H}_Q^3 + \dots \quad (4.145)$$

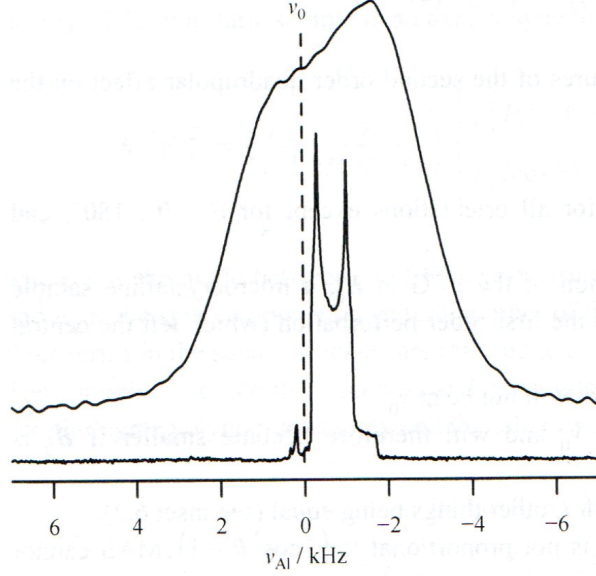


Figure 4.17: Spectra for a polycrystalline sample: top: static sample. Bottom: sample rotated at the magic angle. The isotropic chemical shift is indicated by ν_0 . There is a small peak at a slightly higher frequency than ν_0 which arises from the centerband of the inner satellite transition

Overview of the rotation of the Quadrupolar Hamiltonian from the PAS to the laboratory frame

Even though the quadrupolar interaction is large, it is the Zeeman interaction that still dominates. As a result, the Hamiltonian is rotated from the PAS to the laboratory frame. This is done using the spherical tensor form and applying the relevant rotation matrices. An overview of the relevant steps of how this is achieved is given below:

In the PAS, the quadrupolar Hamiltonian is given by:

$$\hat{H}_Q^P = \frac{2\pi}{2I(2I-1)} \left(A_{20}^P \hat{T}_{20} - A_{22}^P \hat{T}_{2-2} - A_{2-2}^P \hat{T}_{22} \right), \quad (4.146)$$

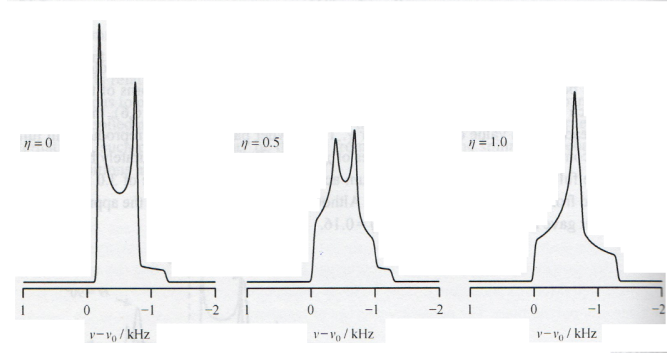


Figure 4.18: Simulated second order MAS quadrupolar powder patterns for a spin 3/2 nuclei

where the spatial terms are:

$$A_{20}^P = \sqrt{\frac{3}{2}} C_Q, \quad (4.147)$$

and

$$A_{2-2}^P = A_{2-2}^P = \frac{1}{2} \eta_Q C_Q. \quad (4.148)$$

In the laboratory frame, the full Hamiltonian in spherical tensor form is:

$$\hat{H}_Q^L = \frac{2\pi}{2I(2I-1)} \left(A_{20}^L \hat{T}_{20} - A_{21}^L \hat{T}_{2-1} - A_{2-1}^L \hat{T}_{21} + A_{22}^L \hat{T}_{2-2} + A_{2-2}^L \hat{T}_{22} \right). \quad (4.149)$$

When only the first order perturbation is considered, the secular approximation can be used, meaning all terms except the A_{20}^L spatial term can be ignored:

$$A_{20}^L = A_{20}^P D_{00}^2 + A_{22}^P D_{20}^2 + A_{2-2}^P D_{-20}^2. \quad (4.150)$$

The spatial component of the Hamiltonian in the laboratory frame using first order perturbation is:

$$A_{20}^L = \sqrt{\frac{3}{2}} \frac{C_Q}{2I(2I-1)} \frac{1}{2} [(3 \cos^2 \beta_{PL} - 1) + \eta_Q \sin^2 \beta_{PL} \cos^2 \alpha_{PL}]. \quad (4.151)$$

Therefore, the first-order quadrupolar Hamiltonian is:

$$\hat{H}_Q^L = \sqrt{\frac{3}{2}} \frac{C_Q}{2I(2I-1)} \frac{1}{2} [(3 \cos^2 \beta_{PL} - 1) + \eta_Q \sin^2 \beta_{PL} \cos^2 \alpha_{PL}] \hat{T}_{20}. \quad (4.152)$$

CHAPTER 4. NMR THEORY

The first-order perturbation to the Zeeman energy levels is expressed as:

$$E_m^{(1)} = \langle m | \hat{H}^1 | m \rangle. \quad (4.153)$$

When the quadroupolar Hamiltonian is substituted into this equation, it results in a first-order perturbation of the Zeeman transition energy, m ,:

$$E_m^{(1)} = \sqrt{\frac{3}{2}} \frac{C_Q}{2I(2I-1)} \frac{1}{2} (3m^2 - I(I+1)) [(3 \cos^2 \beta_{PL} - 1) + \eta_Q \sin^2 \beta_{PL} \cos^2 \alpha_{PL}]. \quad (4.154)$$

Equation 4.154 is about the first-order quadroupolar interaction that is removed by MAS when averaged over one rotor period.

For spin $I=1$ nuclei, such as ^{14}N , there are three possible energy levels ($m = -1, 0, 1$), thus two possible energy transitions. When looking at a first-order perturbation to the Zeeman interaction, transitions between $m = +1$ and $m = -1$ remain unchanged, but for transitions which occur between $m=0$ and $m=+1$, and $m=0$ and $m=-1$ the transition energy differs to the total Zeeman splitting.

As the quadroupolar coupling is large in most cases, the second-order perturbation of the quadroupolar Hamiltonian must be considered. This is given by

$$E_m^{(2)} = \sum_{m \neq n} \frac{\langle n | \hat{H}^1 | m \rangle \langle m | \hat{H}^1 | n \rangle}{E_n^{(0)} - E_m^{(0)}}. \quad (4.155)$$

The secular approximation is only valid for first-order perturbations, consequently all $A_{(2-m, \dots, m)}^L$ terms must be used. Calculation is achieved using the same method as was done for the A_{20}^L term in the first-order perturbation. This is achieved by multiplying A_{2m}^2 spatial terms. The multiplication of $A_{2m}^2 \cdot A_{2m}^2$ yields zeroth, second and fourth rank Wigner rotation matrices. These have important influences of MAS quadroupolar lineshapes. The second order perturbation is given by:

$$E_m^{(2)} = - \left(\frac{C_Q}{4I(2I-1)^2} \right) \frac{2}{\omega_0} m \left[[I(I+1) - 3m^2] D_{00}^{0(Q)} + [8I(I+1) - 12m^2 - 3] D_{20}^{2(Q)} + [18I(I+1) - 34m^2 - 5] D_{40}^{4(Q)} \right], \quad (4.156)$$

where

$$D_{00}^{0(Q)} = -\frac{1}{5}(3 + \eta_Q^2) \quad (4.157)$$

$$D_{20}^{2(Q)} = \left[(\eta_Q^2 - 3)(3 \cos^2 \beta_{PL} - 1) + 6\eta_Q \sin^2 \beta_{PL} \cos^2 \alpha_{PL} \right] \quad (4.158)$$

$$D_{40}^{4(Q)} = \frac{1}{8} \left[\frac{1}{140}(18 + \eta_Q^2)(35 \cos^4 \beta_{PL} - 30 \cos^2 \beta_{PL} + 3) + \frac{3}{7}\eta_Q^2 \sin^2 \beta_{PL}(7 \cos^2 \beta_{PL} - 1) \cos 2\alpha_{RL} + \frac{1}{4}\eta_Q^2 \sin^4 \beta_{PL} \cos 4\alpha_{RL} \right]. \quad (4.159)$$

A second order perturbation perturbs the energy levels further than in the first order case. As mentioned previously, the second order perturbation is inversely proportional to ω_0 , and the consequences experimentally are that the effects of the interaction are reduced if the external magnetic field is increased.

The zeroth-rank term (which is isotropic) adds a second isotropic shift to that of chemical shift to the spectra of quadrupolar nuclei. The isotropic second-order quadrupolar shift, δ_{QIS} is defined in the ppm scale for a (m to $m-1$) transition as:

$$\delta_{QIS} = -\frac{3}{40} \frac{P_Q^2}{v_0} \frac{[I(I+1) - 9m(m-1) - 3]}{[I^2(2I-1)^2]} \times 10^6. \quad (4.160)$$

When $I=1$ and $m = 0, 1$, the expression becomes:

$$\delta_{QIS} = -\frac{3}{40} \frac{P_Q^2}{v_0} \times 10^6, \quad (4.161)$$

where the quadrupolar product, P_Q , is defined as:

$$P_Q = C_Q \sqrt{1 + \frac{\eta_Q^2}{3}}. \quad (4.162)$$

Below outlines the effect that the magnetic field strength has on equation 4.160. The following examples use data taken from table 7.6. For ^{14}N Larmor frequencies of 21.7 MHz, 28.9 MHz, 36.1 MHz and 43.3 MHz δ_{QIS} equals 350 ppm, 263 ppm, 210 ppm and 175 ppm, respectively. The examples show that as the magnetic field strength increases the effect on δ_{QIS} is that it decreases in a non-linear fashion. Equations 4.160 and 4.161 show that the magnitude of the the nitrogen atom labelled 1 in $\text{NH}^+:\text{COO}^-$ is inversely

proportional to the Larmor frequency. As an example, consider $C_Q = -1.4$ MHz and $\eta=0.3$ corresponding to $\text{NH}^+:\text{COO}^-$ (see table 7.6).

4.9 Summary

This theory chapter has introduced the key concepts and language that will be needed to understand the results presented subsequently. The next chapter builds upon this by introducing the different NMR experiments used in my research.

Experimental Techniques

5.1 Introduction

Technological advancements in achieving faster MAS rates [185–189] accompanied with the development of improved ^1H homonuclear decoupling sequences has meant that solid-state NMR has extended its application to a greater number of systems and to those with greater complexity [66, 78] due to the high-resolution ^1H spectrum which results. The application of solid-state NMR has thus been applied to pharmaceuticals (the main focus of this thesis) [190], supramolecular chemistry and polymers [191], inorganic materials and paramagnetic compounds [192], and proteins [53]. This chapter aims to introduce how the various NMR experiments used throughout this investigation are applied and the underlying concepts which are utilised. This chapter begins by detailing how a 2D solid-state NMR experiment is produced and how this differs from a 1D experiment, along with how the lineshapes seen in the spectra are formed. Section 5.5 provides a description of further underlying concepts, notably phase-cycling is introduced detailing how the excitation of coherences is achieved and how this leads to observable coherence. Sections 5.3, 5.7 and 5.8 describe the different NMR experiments which were used in thesis namely: ^1H fast MAS one pulse, ^1H - ^{13}C cross polarisation CPMAS with ^1H decoupling (both homo- and heteronuclear), ^1H double-quantum (DQ) and ^{14}N - ^1H HMQC, specifically recoupling techniques alongside the description of the complementary techniques of the calculation of NMR parameters and PXRD.

5.2 ^1H Decoupling

MAS (see chapter 4 section 4.8.3) acts to achieve high resolution in the spectrum for ^1H and heteronuclei, such as ^{13}C , by removing line broadening due to anisotropic interactions. As a result of the removal of line broadening, structural and dynamic information is lost. By using recoupling methods specifically BABA and POST-C7 [193] to reintroduce the ^1H - ^1H dipolar coupling to create DQ coherences in DQ MAS experiments and heteronuclear ^{14}N - ^1H dipolar couplings in the ^{14}N - ^1H HMQC experiment, this key information can be reclaimed.

Heteronuclear dipolar-decoupling is concerned with experiments that observe the species with the lower natural abundance (dilute nucleus). In the experiments used in this thesis this concerns the nuclei of: ^{13}C , and the dipolar couplings of ^{13}C - ^1H (i.e. X-H) respectively. MAS is not enough to completely resolve peaks but couplings can be removed if during acquisition the protons are irradiated with a broadband decoupling sequence.

Effective decoupling of heteronuclear spin interactions is important in ^{13}C and ^{15}N NMR of organic solids, whereby decoupling schemes can efficiently reduce the ^{13}C linewidth to $\sim 1\%$ of its non-decoupled value. Heteronuclear decoupling consists of continuously irradiating the nucleus ^1H (or the abundant spin) at a frequency at or very close to resonance. This excites transitions between the α and β states in the ^1H spins. The rate of these transitions is controlled by the amplitude of the *rf*-pulses. If the applied frequency to the ^1H spins is high enough, the transitions will be fast in comparison to the size of the heteronuclear dipolar coupling, which is averaged by the transitions. For a coupling to be reduced to a very small size, it requires that the nutation frequency is at least three times higher than the size of the largest X-H coupling. However, the nutation frequency is generally set to 100 kHz, thus meeting this requirement.

Heteronuclear decoupling was first used in solution-state NMR using simple single frequency, continuous wave (CW), irradiation to decouple interactions [194]. CW achieves decoupling by the application of a continuous wave decoupling pulse that lasts for the duration of the acquisition. CW can still be used but it has become ineffective as static magnetic fields and spinning frequencies have increased.

Two Pulse Phase Modulation (TPPM) was introduced by Bennett et al [195], and consists of a repeating unit of two pulses with the same nominal nutation angle, τ_p , and phase difference $\Delta\phi$. Optimal values are in the region of; $\tau_p \simeq 170^\circ$ and $\Delta\phi \simeq 15^\circ$ but the phase difference between the two pulses can be in the range of 10 - 50° [194].

Following on from the success of TPPM, the SPINAL (Small Phase Incremental Alteration Sequences) sequences, notably SPINAL-64, was introduced which combines the TPPM scheme with a phase super-cycle. They were originally developed for decoupling in liquid crystal ^{13}C NMR. The basic element of the sequences is as follows;

$$Q = P(10^\circ)\overline{P(10^\circ)}P(15^\circ)\overline{P(15^\circ)}P(20^\circ)\overline{P(20^\circ)}P(15^\circ)\overline{P(15^\circ)}, \quad (5.1)$$

where $P(m)$ denotes a pulse with nutation angle of $\sim 165^\circ$ and of phase m , the bar indicates that the output phases are all negated, e.g. $\overline{P(10^\circ)}$ corresponds to an output phase of -10° [196]. This element is 'super-cycled' to generate a family of sequences, e.g. SPINAL-64,

$$SPINAL - 64 = Q\overline{Q}\overline{Q}\overline{Q}\overline{Q}\overline{Q}\overline{Q}\overline{Q}. \quad (5.2)$$

5.3 ^1H - ^{13}C CPMAS

The CP experiment was first developed by Hartman and Hahn [197] whereby coupling transfer of magnetisation from the abundant nucleus (^1H) to the dilute nucleus (^{13}C) takes place via heteronuclear dipolar coupling. This enhances the signal of the dilute nucleus due to an increase in its net magnetisation. As a result of this process, a CP experiment can overcome two problems in working with dilute nuclei:

1. their low sensitivity, due to a low γ ,
2. the long T_1 relaxation times (typically tens of seconds in ^{13}C) which increases experimental times for one-pulse ^{13}C NMR. (Please note that ^1H T_1 relaxation times in a crystalline API can also be very long.)

In a CP experiment (see Figure 5.1), experimental times are shortened as it is the ^1H relaxation time which determines the return of the nuclear spins to equilibrium and ^1H T_1 relaxation times are usually shorter due to the strong homonuclear dipolar couplings which exist.

A $\frac{\pi}{2}$ pulse is applied along the x -axis of spin I rotating the bulk magnetisation onto the $-y$ -axis. This is followed by the contact time in which a second 90° phase shifted ^1H pulse spin locks the magnetisation, while simultaneously a pulse is applied at the frequency of the S spin. The time these pulses are applied for is called the contact time,

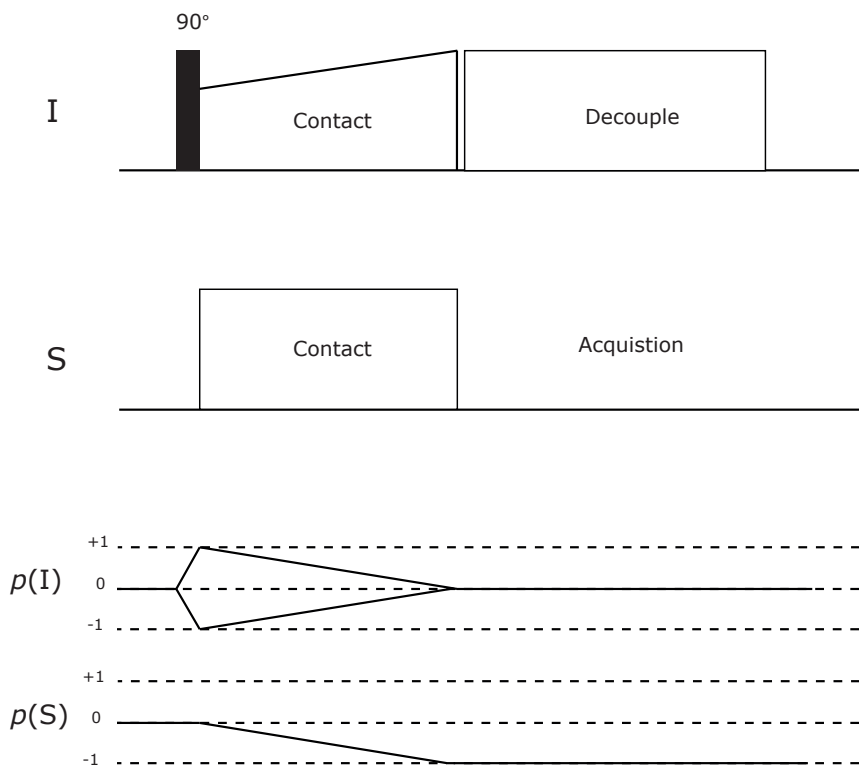


Figure 5.1: A pulse sequence showing a Cross Polarisation experiment between the abundant spin I and the dilute spin S . A 90° rf pulse is applied to the I nucleus along the x axis to rotate the bulk magnetisation into the transverse plane. During the contact time, rf irradiation is applied to both I and S which transfers the magnetisation from the more abundant I nuclei to the less abundant S nuclei, if the Hartman-Hahn (see equations 5.3 and 5.4) condition is satisfied. The diagram shows a ramped rf pulse (i.e. with changing nutation frequency, ν_1) on ^1H . During the acquisition time, decoupling is applied to the I nuclei, so that I - S interactions are removed. A coherence transfer pathway diagram is as shown where it can be seen that single quantum coherence (observable state) is on the S nucleus during acquisition.

where the magnetisation transfers from the I to the S spin allowing magnetisation to build up on the S spin during this period. The contact time can be varied as different chemical environments determine how fast the transfer occurs. Typically the contact time is longer for non-proton bonded nuclei as the magnetisation takes longer to reach these sites. The signal is then acquired while heteronuclear decoupling is applied to the I spin.

The optimum conditions for magnetisation transfer during the contact time occur when the I and S rf fields meet the Hartman-Hahn match condition, i.e. cross polarisation occurs when the I and S nutation frequencies are equal, between the dipolar coupled spins whereby (for a static experiment):

$$\gamma_I B_1(I) = \gamma_S B_1(S). \quad (5.3)$$

The experiment was originally developed for static samples however this matching condition works for $^1\text{H}/^{13}\text{C}$ CP with MAS. This means that spinning at lower MAS rates has little effect on the strong hononuclear interactions. Under MAS the match condition is modified when faster MAS is used, for example, when the ^1H spectrum breaks into sidebands, the MAS condition must be included in the matching condition:

$$\gamma_I B_1(I) = \gamma_S B_1(S) \pm n\omega_r \quad n = 1, 2, 3, \dots, \quad (5.4)$$

however cross polarisation is less efficient at faster MAS and the match condition is very difficult but this can be solved by using ramped cross polarisation on the I spin as shown in Figure 5.1. Here the rf is “swept” [198] through the matching condition, meaning the matching conditions for different parts of the sample will be met at some point during the ramp.

Figure 5.2 shows the effect of varying the contact time in a ^1H - ^{13}C CP MAS experiment on L -alanine conducted at a ^1H Larmor frequency 500 MHz and a MAS frequency of 10 kHz. The contact time was varied from 500 μs to 5000 μs in increments of 500 μs . In L -alanine there are three different carbon environments. The three carbon environments consist of a methyl group, a carbonxylate group and a CH group; as the CH dipolar coupling for the groups are all different (noting also rotation of the methyl protons around the C-C axis), the rate of magnetisation transfer from the protons to the carbons will also vary. There was not a single time that gave the best signal to noise ratio for each of the three peaks, therefore a compromise of 1 ms was used as it gave the best sensitivity overall. The resulting three peaks in the spectrum of L -alanine: COO^- , CH and CH_3 presented in Figure 5.3 correspond to three vital setup parameters.

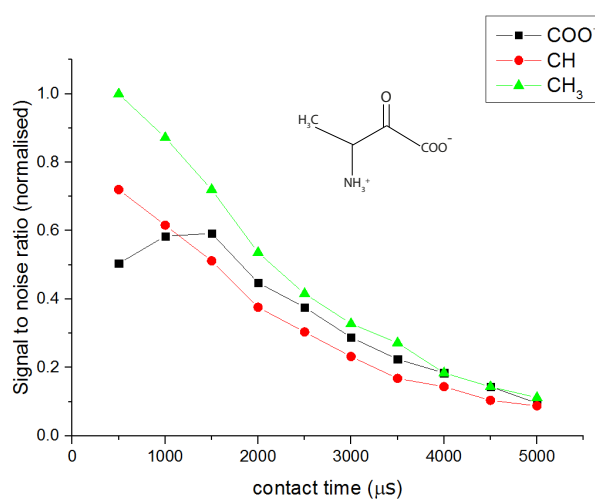


Figure 5.2: Graph showing how the signal to noise ratio (normalised) for the CH₃ peak (green), CH peak (red) and the COO⁻ peak (black) in *L*-alanine varies as a function of contact time (μs) in a ^1H - ^{13}C CP MAS (10 kHz) experiment at a ^1H Larmor frequency of 500 MHz. The optimum contact time used in subsequent CP experiments was 1 ms as this provided the best overall signal to noise ratio for all 3 peaks.

The carboxylate COO^- resonance is sensitive to the magic angle negating the need for an alternative method which uses KBr. Thus the packing of KBr (Potassium Bromide) into a rotor, conducting a ^{79}Br NMR experiment, analysing the spectrum, and ejecting the sample, is not required [199]. The linewidth of the carboxylate COO^- peak is as sensitive as the KBr method in ensuring that the magic angle is accurately set.

The linewidth of the CH resonance is sensitive to how well the ^1H decoupling is optimised with larger linewidths indicating the decoupling sequence needs optimisation and a narrow linewidth indicating the decoupling sequence is set up well. The heteronuclear decoupling sequences that have been used in this research is TPPM [195] and SPINAL-64 [196] (see section 5.2).

The linewidth of the methyl, CH_3 resonance provides an indication of how well the magnet is shimmed. Furthermore, the ^1H - ^{13}C CPMAS experiment is conducted on the setup sample of *L*-alanine to optimise the 90° pulse length (and thus the ^1H nutation frequency) and also reference the ^{13}C isotropic chemical shift: where the methyl resonance is set to 20.5 ppm, the CH resonance to 51.1 ppm and the COO^- resonance is set to 177.8 ppm, and using these is equivalent to using the reference compound of adamantane at a resonance of 38.5 ppm or 29.5 ppm, corresponding to TMS at 0 ppm [200].

Also note that ^1H referencing is also able to be conducted on *L*-alanine when a fast ^1H MAS NMR spectrum is recorded. The three ^1H resonances of CH_3 , CH and COO^- are equal to 1.3, 3.5 and 8.8 ppm respectively and this is equivalent to using adamantane at 1.85 ppm corresponding to TMS at 0 ppm [201].

Figure 5.3 shows a ^{13}C CP MAS spectrum of *L*-alanine at 500 MHz. It emphasises the importance of calibrating the pulse length in proton decoupling sequences as shown by the difference in the intensities of the resulting signals. It shows the effect of changing the TPPM proton decoupling pulse length. The blue spectrum indicates a pulse length of 4 μs , and the red spectrum shows a pulse length of 5 μs , in both cases for a ^1H nutation frequency of 100 kHz. An overlay of the two spectra is displayed, with zoomed in regions of the carbonyl, CH and methyl peaks respectively. The greatest signal to noise ratio obtained was for a pulse length of 5 μs (red). The better performance of 5 μs corresponds to a π pulse, where best TPPM performance occurs as noted in [194]. Factors which affect ^1H decoupling sequences have been explored in the recent paper by Frantsuzov et al [202] where flip angle and phase of pulses is also explored in terms of the effect on the TPPM sequence. The effect on a spectrum of having the pulse length at 4 μs and 5 μs is shown in figure 5.3. The carbonyl peak does not show much difference between line widths and signal to noise ratio, but there is a visible difference in sensitivity on the

CH and CH₃ peaks. The best ¹H decoupling performance is obtained for a pulse length corresponding to a flip angle of 180° [5 μs at ν₁(¹H) = 100 kHz].

For organic molecules at natural isotropic abundance, there is an important difference between ¹³C and ¹H MAS NMR; this difference is the linewidth in the resulting spectra. For the nuclei of ¹³C, the linewidth can be regarded as independent of the MAS frequency, whereas for the nuclei of ¹H, the linewidth is not independent of the MAS frequency and narrows when MAS frequency increases. The reason for the difference between ¹³C and ¹H nuclei for the dependence on the MAS frequency arises from the different dominant anisotropic interactions. For ¹³C, the dominant interaction is the CSA (as ¹³C-¹H dipolar couplings are in essence removed by ¹H decoupling) and for ¹H the dominant interaction is the ¹H-¹H homonuclear dipolar couplings. The CSA is an inhomogeneous interaction where the broadening is refocused over a rotor period. Homonuclear dipolar coupling, however, is known as a homogeneous interaction so that for coupled nuclei (>3) the broadening is not refocused over a rotor period due to the Hamiltonians not commuting (see section 4.8.2).

5.4 2D NMR

In general, all 2D experiments consist of four sections, represented visually in figure 5.4 [182], and described below:

- 1. Preparation period** The preparation period creates transverse magnetization. This can be achieved, for example, with a 90° pulse or alternatively a CP experiment can generate transverse magnetization. (More information on coherences and CP experiments can be found in chapter 4 and section 5.3).
- 2. Evolution period** The evolution period which has a duration of t_1 is not fixed. The coherence evolves under the influence of chemical shifts and spin-spin couplings (or the quadrupolar interaction for $I \geq 1$). The coherences evolved during t_1 need not be directly observable, for example, it could be multiple quantum coherences which could be evolving.
- 3. Mixing period** The mixing period is where the coherence that is present at the end of the evolution period is converted into an observable signal (single quantum coherence). Here the coupling of nuclei, for example, can also be seen.
- 4. Detection** The observable signal is detected in the last part of the experiment, t_2 .

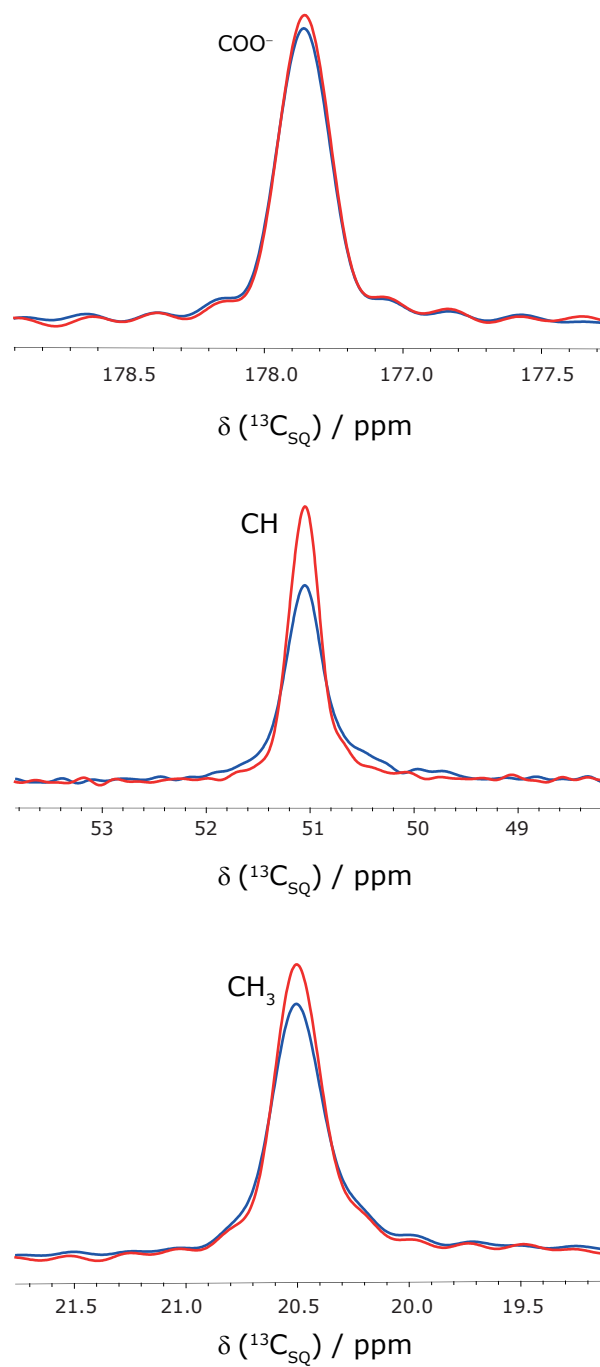


Figure 5.3: ^{13}C CP MAS spectra of *L*-alanine showing the effect of changing the TPPM proton decoupling pulse length. The blue spectrum indicates a pulse length of $4\ \mu\text{s}$, and the red spectrum shows a pulse length of $5\ \mu\text{s}$, in both cases for a ^1H nutation frequency of 100 kHz. An overlay of the two spectra is displayed, with zoomed in regions of the carbonyl, CH and methyl peaks respectively. The greatest signal to noise ratio obtained was for a pulse length of $5\ \mu\text{s}$ (red).

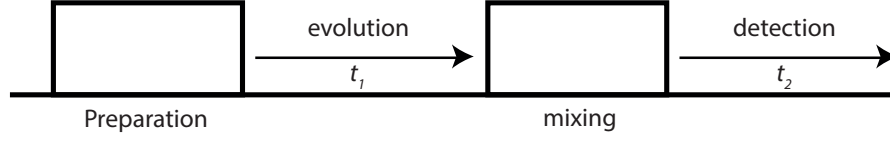


Figure 5.4: The general sequence for a 2D NMR experiment showing the four main stages: Preparation, Evolution, Mixing and Detection. The preparation and mixing periods consist of a single pulse or can be a series of pulses and delays. The coherence generated in the preparation period evolves for a time t_1 ; during the mixing period, the coherence that is present at the end of the t_1 evolution period is converted into an observable signal, which is detected during the acquisition time t_2 .

A series of FIDs are recorded, as a function of t_1 and this results in a 2D dataset. The time-domain signal resulting from one implementation (amplitude-modulated in t_1) of a 2D experiment shown in figure 5.4 is represented by:

$$s(t_1, t_2) = \cos \Omega t_1 \exp(-t_1/T_2) \exp(-t_2/T_2), \quad (5.5)$$

where T_2 is the spin-spin relaxation time. For simplicity, the abbreviations A_k^\pm and D_k^\pm are used for absorptive and dispersive lineshapes centred at frequency $\pm\Omega$ in the F_k dimension. Complex Fourier transformation of $\exp(\pm\Omega t_k) \exp(-t_k/T_2)$ gives $A_k^\pm + D_k^\pm$ (Fourier transformation of NMR lineshapes was first visited in section 4.2.4). Fourier transform of $s(t_1, t_2)$ first, with respect to t_2 and, then, t_1 will give a mixture of 2D absorption and dispersion lineshapes. Phase twist lineshapes are undesirable due to broad “wings” in the spectrum and negative regions (refer to chapter 4, where figure 4.6 shows that dispersion lines are broader). To obtain a 2D absorption lineshape, it is necessary to record and separately store two, 2D time-domain signals, one with cosine modulation and the other with sine modulation with respect to t_1 , an example of a popular method which does this is by States, Haberkorn and Ruben in 1982 [203]. This is achieved by repeating the experiment with different pulse phases. The final Fourier Transformation is shown below (see relevant literature [179] for a full description):

$$S(F_1, F_2) = [A_1^+ - iD_1^+][A_2^+] = A_1^+ A_2^+ - iD_1^+ A_2^+ \quad (5.6)$$

The real part represents a two-dimensional absorption lineshape at frequency $(F_1, F_2) = (+\Omega, +\Omega)$ [203].

5.5 Phase Cycling

Phase cycling suppresses unwanted coherences. The selection of a specific coherence order involves manipulating different coherence states using *rf* pulses and repeating experiments using the same pulse sequence. When experiments are repeated, the phases of the pulses and the receiver are changed so that over a whole cycle the signals arising from unwanted coherences destructively interfere, leaving signals from the desired coherences. The resulting FIDs are then added together.

The $p = 0$ coherence order represents the population state and zero-quantum operators (i.e. the thermal equilibrium state), and $p \pm 1$, $p \pm 2$, $p \pm 3$...etc represents single, double and triple quantum coherence orders, however only the $p = -1$ coherence state is directly observable. During an NMR experiment, different coherence orders are selected to allow different interactions to be observed, for example, double quantum coherence can be selected to probe the dipolar interaction between two spin $\frac{1}{2}$ nuclei. It is possible to control and manipulate the coherence orders (e.g. in free precession intervals) and for each experiment a coherence transfer pathway diagram can be drawn to indicate the wanted coherence orders (coherence transfer pathway diagrams are presented below for the ^1H - ^{13}C CPMAS, ^1H DQ MAS, and ^{14}N - ^1H HMQC experiments).

Phase cycles are constructed using two golden rules [179]:

Rule 1 If the phase of a pulse (or group of pulses) is shifted by $\Delta\phi$, then a coherence undergoing a change in coherence order Δp experiences a phase shift $-\Delta\phi$. Δp as detected by the receiver.

Rule 2 If a phase cycle uses steps of $\frac{360^\circ}{N}$ then, along with the desired pathway, all pathways corresponding to $\Delta p \pm nN$ where $n = 1, 2, 3...$ will also be selected. Other pathways are suppressed.

The coherence order remains constant during periods of free evolution such as t_1 and t_2 (see above discussion of figure 5.4). The importance of phase cycling can be seen from the experiments presented in this chapter, see Figures 5.1, 5.6 and 5.7. Note that all NMR experiments start at thermal equilibrium thus the coherence order is always $p = 0$ at the beginning of the experiment. As will be seen, all NMR experiments start at thermal equilibrium thus the coherence order is always $p = 0$ at the beginning of the experiment (see figure 5.6).

5.6 Recoupling

The pulse sequence: $90^\circ - \tau - 90^\circ$ was first used in solution-state NMR to excite multiple quantum coherences. The pulse sequence was used with MAS where the excitation and reconversion time is half a rotor period ($\frac{\tau_R}{2}$) [204]. For the solid-state NMR experiments used in this thesis the BABA recoupling method was employed, [205] [206] which uses two $90^\circ - \tau - 90^\circ$ pulse segments which have a time period of half a rotor period. The phases in the adjoining pulse segments are shifted by 90° : $90_x^\circ - \tau - 90_x^\circ$ and $90_y^\circ - \tau - 90_y^\circ$. The name BABA originates from the pulse segments being applied BACK-to-BACK. The phase shift counteracts the effect of the physical rotation due to MAS, hence recoupling the dipolar interaction. Recoupling sequences can be classified as amplitude or phase modulated. The ^1H DQ MAS experiment which implements the BABA recoupling technique requires that the t_1 increment is set equal to one rotor period (More information on the ^1H DQ MAS experiment can be found in section 5.7). In amplitude-modulated sequences if the t_1 increment is not set equal to one rotor period it results in a pattern of symmetric spinning sidebands, the origin of which is discussed in Friedrich et al [207]. In phase-modulated sequences the spinning sideband pattern is asymmetric where the intensity is concentrated in a single sideband. The maximum intensity is shifted by a multiple of the spinning frequency away from the DQ frequency. In reality this shift is not important as long as correct referencing is carried out.

Rotary resonance recoupling achieves recoupling by using a continuous wave *rf*-field ω_1 that matches twice the MAS frequency ω_r ; this is referred to as the $n = 2$ rotary resonance condition where:

$$n = \frac{\omega_1}{\omega_r}. \quad (5.7)$$

At $n = 2$, rotary resonance re-introduces the heteronuclear dipolar coupling under MAS but not the homonuclear interaction.

5.7 ^1H DQ MAS

The 2D solid-state ^1H DQ MAS NMR experiment is a powerful probe of ^1H - ^1H proximities due to DQ coherences which are created when there is a significant dipolar coupling between ^1H nuclei, indicating that there is a close proximity between those atoms. The close proximity due to the dipolar coupling is $\propto \frac{1}{r^3}$, where r is the internuclear distance (see equation 4.120 and Figure 4.15). The ^1H DQ MAS pulse sequence used in this thesis employs one rotor period of BABA recoupling [205, 206] (refer to section 5.6) for

5.8. HETERONUCLEAR MULTIPLE QUANTUM COHERENCE SPECTROSCOPY

the excitation and reconversion of DQ coherence, and ensures that the t_1 increment is rotor synchronised.

Figure 5.5 is an example of a ^1H DQ MAS spectrum of *L*-alanine recorded at 500 MHz at a spinning frequency of 30 kHz using one rotor period of BABA recoupling (see pulse sequence and coherence transfer pathway diagram in figure 5.6). The positions of peaks are indicated and labelled. The DQ frequency corresponding to a double-quantum coherence is the sum of the two single-quantum frequencies. DQ coherences can exist between like protons, for example $\text{CH}_3 - \text{CH}_3$, where a single peak in the notation (ν_1, ν_2) is observed at $(2\nu_A, \nu_A)$, and lie on the $F_1 = 2F_2$ diagonal line. DQ coherences between unlike spins can be observed by appearance of two peaks at $(\nu_A + \nu_B, \nu_A)$ and $(\nu_A + \nu_B, \nu_B)$, also referred to as cross peaks, one each side of the diagonal line. ν_1 denotes the centre of the peak for the F_1 dimension and ν_2 for the F_2 dimension.

For an isolated spin pair, the efficiency of DQ coherence excitation and reconversion is proportional to the dipolar coupling constant squared, see equation 4.120, (valid to a first approximation). The peaks give an indication of ^1H - ^1H proximities as dipole-dipole coupling is dependent on internuclear distance, and relative DQ peak intensity is therefore, again to a first approximation, proportional to $\frac{1}{r^6}$. By looking at the relative intensities of peaks in the ^1H DQ MAS spectrum in Figure 5.5 insight into the dipolar interactions between the three different proton environments (NH_3 , CH and CH_3) in *L*-alanine and hence proton-proton proximities can be gained [208]: From Figure 5.5, the auto peak of CH_3 is the most intense, this is followed by the auto peak of NH_3 , and the weakest peak is the CH-CH auto peak which corresponds to only a longer intermolecular proximity. The other three peaks show interactions between different hydrogen atoms in *L*-alanine and it is observed that there is an interaction between CH- CH_3 , NH_3 - CH_3 and NH_3 -CH.

5.8 Heteronuclear Multiple Quantum Coherence Spectroscopy

Nitrogen environments are of great importance in pharmaceutical solids, therefore it is necessary to be able to observe nitrogen in solid-state NMR experiments. Nitrogen has two nuclear isotopes: ^{14}N and ^{15}N . Until recently, experiments involving ^{15}N were predominately used due to its higher gyromagnetic ratio and spin $\frac{1}{2}$ property. However, developments with pulse sequences allow the use of the spin $I = 1$, ^{14}N quadrupolar nuclear isotope to probe pharmaceutical solids via solid-state NMR.

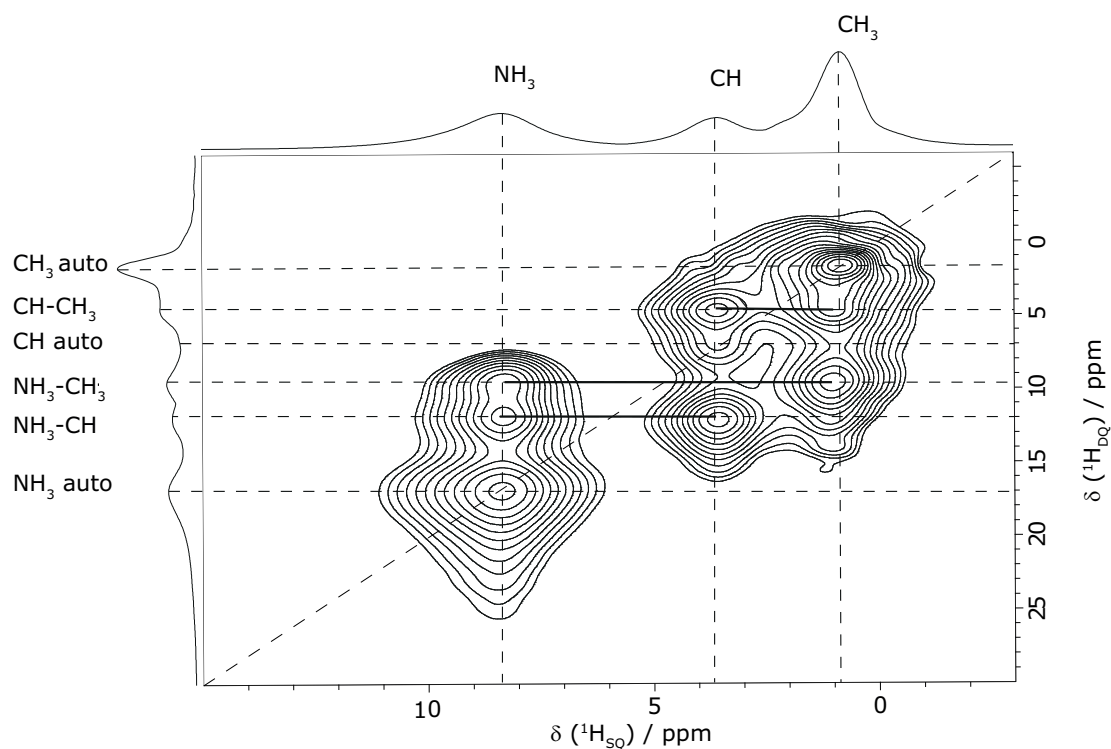


Figure 5.5: A ^1H - ^1H DQ-SQ spectrum with skyline projections of *L*-alanine, recorded at 500 MHz and 30 kHz MAS using one rotor period of BABA recoupling. A 2.5 mm HXY probe was used in double resonance mode. 32 transients were co-added for each of 128 t_1 FIDs, with a recycle relay of 3 s, corresponding to a total experimental time of 3.5 hours, and the ^1H 90° pulse length was 4 μs . The base contour level is set at 5% of the maximum peak height.

5.8. HETERONUCLEAR MULTIPLE QUANTUM COHERENCE SPECTROSCOPY

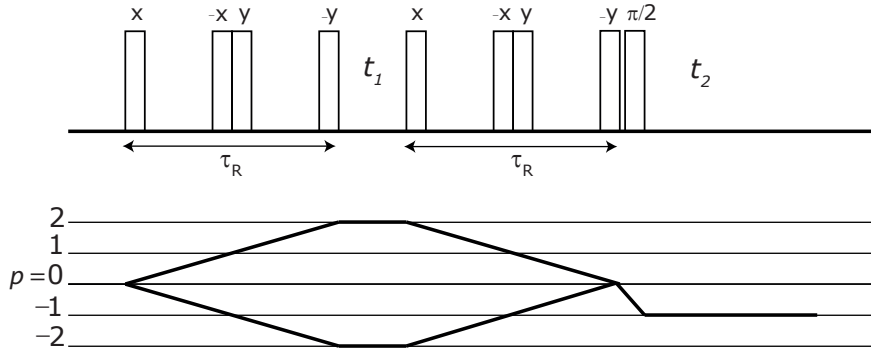


Figure 5.6: A ^1H DQ MAS experiment using a BABA pulse sequence, shown alongside its coherence transfer pathway. The experiment starts at thermal equilibrium where the coherence order (p) is 0. During the preparation period, double quantum coherence is excited, indicated by $p = \pm 2$. The double quantum coherence evolves for time t_1 and is then reconverted back into a population state (corresponding to $p = 0$). A 90° pulse converts the population state into single quantum coherence which is observable.

In the HMQC experiment, direct detection occurs on the nucleus with the higher gyromagnetic ratio i.e. the ^1H nucleus, and this has the advantage of enhancing the sensitivity of the experiment rather than directly detecting on the nucleus with the lower gyromagnetic ratio. In fact the ratio of the hydrogen to nitrogen 14 gyromagnetic ratio is approximately 14 times greater. Heteronuclear Multiple Quantum Coherence Spectroscopy or HMQC was first used in liquids in 1979 and subsequently the experiment has been adapted for use with solids using MAS. In this thesis, this experiment is used for the indirect detection of ^{14}N lineshapes through direct proton acquisition.

Figure 5.7 shows the pulse sequence and the coherence transfer pathway for a ^{14}N - ^1H HMQC experiment. The HMQC experiment can be described using product operators (product operators were first introduced in section 4.5). The following description of the experiment is shown for J coupling but the same approach can be employed to evolution under ^1H - ^{14}N dipolar couplings. Here, the I spin represents ^1H nuclei and the S spin represents the ^{14}N nuclei. This discussion is based on that presented in reference [179]: The first 90° pulse on I creates $-\hat{I}_y$ magnetisation which evolves during period a (the different experimental periods are depicted in figure 5.7) under J coupling to give:

$$-\cos(\pi J_{IS}\tau)\hat{I}_y + -\sin(\pi J_{IS}\tau)2\hat{I}_x\hat{S}_z. \quad (5.8)$$

The evolution of the I spin resonance offset is ignored due to the spin echo over period f, i.e. the spin echo is created by the 180° pulse on ^1H placed in the centre of t_1 and runs

CHAPTER 5. EXPERIMENTAL TECHNIQUES

from the first pulse to the start of the acquisition period. This results in the resonance offset (Ω) being refocused over this period (f). The first 90° pulse applied to S has no effect on the first term shown in equation 5.8, but the second term is changed into a multiple quantum coherence giving:

$$-\sin(\pi J_{IS}\tau)2\hat{I}_x\hat{S}_y. \quad (5.9)$$

Subsequently, the first term in equation 5.8 is neglected as it is removed by phase cycling. The multiple quantum term is not affected by the evolution of the coupling between the I and S spins therefore, only the evolution under the S spin resonance offset needs to be considered which affects the S spin operator \hat{S}_y :

$$-\sin(\pi J_{IS}\tau)2\hat{I}_x\hat{S}_y \xrightarrow{\Omega_s t_1 \hat{S}_z} -\cos(\Omega_s t_1)\sin(\pi J_{IS}\tau)2\hat{I}_x\hat{S}_y + \sin(\Omega_s t_1)\sin(\pi J_{IS}\tau)2\hat{I}_x\hat{S}_x. \quad (5.10)$$

A 90° pulse is then applied to S (shown by period d in figure 5.7). This pulse is about the x -axis therefore it will have no effect on the term $2\hat{I}_x\hat{S}_x$ shown in equation 5.10, but does rotate $-2\hat{I}_x\hat{S}_y$ into $-2\hat{I}_x\hat{S}_z$ which is anti-phase magnetisation on the I spin. Therefore, the observable term at the start of period e is:

$$-\cos(\Omega_s t_1)\sin(\pi J_{IS}\tau)2\hat{I}_x\hat{S}_z. \quad (5.11)$$

There is then evolution under the J coupling during period e, whereby anti-phase magnetisation is converted into in-phase magnetisation:

$$-\cos(\Omega_s t_1)\sin(\pi J_{IS}\tau)2\hat{I}_x\hat{S}_z \xrightarrow{2\pi J_{IS}\tau} \cos(\pi J_{IS}\tau)\cos(\Omega_s t_1)\sin(\pi J_{IS}\tau)2\hat{I}_x\hat{S}_z - \sin(\pi J_{IS}\tau)\cos(\Omega_s t_1)\sin(\pi J_{IS}\tau)\hat{I}_y. \quad (5.12)$$

Broadband decoupling of the S spin during acquisition means only the in-phase term is observable, therefore the only observable term is:

$$-[\sin(\pi J_{IS}\tau)]^2 \cos(\Omega_s t_1)\hat{I}_y. \quad (5.13)$$

The intensity of the peaks depends on the delay τ where the optimum value is $\frac{1}{(2J_{IS})}$ as this makes $\sin(\pi J_{IS}\tau) = 1$.

Without recoupling, the HMQC experiment relies on J -coupling and residual second-order quadrupolar dipolar coupling remaining under MAS for coherence transfer (coherence transfer is shown in figure 5.7). In the ^{14}N - ^1H HMQC pulse sequence used in this thesis [167], ^{14}N - ^1H heteronuclear dipolar couplings are recoupled using the rotary

5.8. HETERONUCLEAR MULTIPLE QUANTUM COHERENCE SPECTROSCOPY

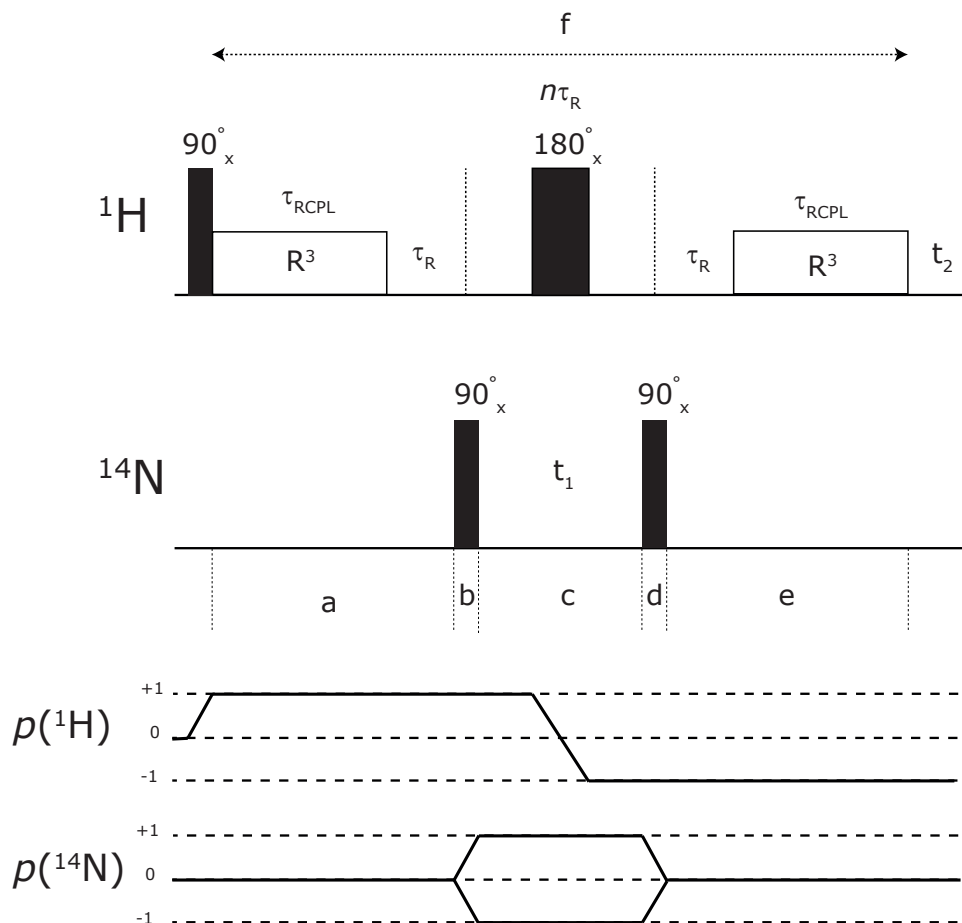


Figure 5.7: Pulse sequence and coherence transfer pathway for a ^{14}N - ^1H HMQC experiment. Note in this work, rotary resonance recoupling (R^3) is employed at $\nu_1 = 2\nu_{\text{R}}$. Equilibrium magnetisation is first excited on the ^1H spin and becomes anti-phase during τ_{RCPL} . The anti-phase magnetisation is then transformed into multiple quantum coherence by the first 90° pulse on the ^{14}N spin. After a period of evolution, t_1 , the coherence is transformed back into anti-phase magnetisation on the ^1H spin by the second 90° pulse on the ^{14}N spin. The anti-phase magnetisation then evolves back into in-phase ^1H magnetisation that is then observed in t_2 .

resonance recoupling R^3 (refer to section 5.7) sequence so as to counteract the effect of averaging by MAS of the ^{14}N - ^1H heteronuclear dipolar couplings to zero and to generate ^{14}N - ^1H heteronuclear MQ coherences. The experiment also relies on the rotor-synchronised evolution time, t_1 , at the magic angle to average the large ^{14}N first order quadrupolar interaction. A key attraction is the ability to vary the number of rotor periods for which a recoupling pulse is applied, thus allowing correlation peaks between directly bonded NH, NH_2 or NH_3 groups, or longer range proximities to be observed.

In this thesis, referencing of the ^{14}N chemical shift is relative to neat CH_3NO_2 using the ^{14}N resonance of NH_4Cl (a powdered solid) at -341.2 ppm as an external reference (see table 2 in [201]). In order to convert from the chemical shift scale commonly used in protein NMR, it is necessary to add 379.5 ppm to the values obtained from the IUPAC reference (see appendix 1 of [209]), of liquid ammonia at -50°C [210].

5.9 NMR Crystallography combining ^1H MAS NMR Techniques, GIPAW Calculation of NMR Parameters and Complementary Experimental Methods

For known crystal structures (usually found by XRD), solid-state NMR can be used with the calculation of NMR parameters to aid analysis. The NMR parameters which are of most interest are those of chemical shielding and EFG tensors, with the EFG tensors providing the quadrupolar parameters for a spin ≥ 1 , for example ^{14}N . NMR crystallography is the term used to describe this combination of experimental and calculation, supported by a Collaborative Computational Project for NMR Crystallography (CCP-NC) for which a common file (.magres) has been developed for calculated NMR, where a web-based viewing portal: MagresView has been used in this thesis to view, interpret and analyse the calculated data [211]. In the research conducted in this thesis the most vital complementary technique is PXRD, where phase purity of the sample is tested, before solid-state NMR experiments are carried out. From previous studies which have utilised NMR crystallography where the calculation of the NMR parameters of the isotropic chemical shift of ^{13}C and ^1H when compared to their experimental value they have been shown to be in good agreement with each other within typically 1% of the chemical shift range for diamagnetic samples which is equal to ± 0.2 ppm for ^1H and ± 2.0 ppm for ^{13}C [80]. The calculation of NMR parameters can also be utilised for isolated molecule calculations in order to compare the results obtained for the full crystal struc-

ture. A comparison ($\Delta\delta_{C-M}$) provides information on intermolecular interactions such as hydrogen bonding shown in the literature [83].

An overview of the foundations of the theory primarily Density Functional Theory (DFT) and Hartree-Fock Theory (HF) will be discussed. The exchange-correlation is introduced along with descriptions of the basis set and the use of pseudopotentials. The physical and computational approximations used in calculations are also presented and the importance of the GIPAW method in able to generate the NMR parameters. The section will end with an outlook on where computational approaches can go in terms of NMR. Charpentier 2011 [212] provides a detailed review of the PAW/GIPAW approach for quantum mechanical calculations and their application to the study of solids.

This section is based upon information contained in the following review articles on first principles calculations: Pickard et al, 2012 [80] and, Ashbrook and McKay, 2016 [81].

Ab initio or first principles calculations of NMR parameters have become an important tool for characterisation of molecules. Currently XRD is the most commonly used tool for characterisation of materials. This method works best for materials which have long range periodic order and for when a single crystal is available. It is able to accurately locate the position of heavy atoms, however, proton positions are less reliable. ^1H solid-state NMR is very sensitive to the local environment around the proton and thus provides accurate information on spatial proximities and chemical connectivity. As a result these two methods are being regularly used together, as the one provides what the other is lacking. The addition of calculated NMR parameters enables the prediction of isotropic chemical shifts thus enabling the verification of structures determined by diffraction. The calculation of parameters also allows greater insight into hydrogen bonding interactions when the results are used with visualisation softwares, for example, MagresView and Mercury.

In high resolution solid-state NMR spectra may still have overlapping spectral lineshapes which make it difficult to assign spectra to specific chemical sites in the molecule. This is where the use of ab initio calculations of NMR parameters first appeared. In 2001, the GIPAW (Gauge Including Projector Augmented Wave) approach was introduced [71]. This enabled the calculation of magnetic shielding based on: DFT, a plane-wave basis set, pseudopotentials and PAW [213]. This method used the periodicity of the solid, i.e. the unit cell, to provide accurate calculations for all atoms, simultaneously saving time and cost. The GIPAW method was especially significant in NMR as it allowed the accurate calculation of solid-state NMR tensors.

Approximating the Schrödinger Equation

The foundations on which the calculations are built are the approaches of DFT and Hartree-Fock (HF). The purpose of the calculations is to approximate the Time Independent Schrödinger Equation (TISE) to obtain the total energy from which the NMR parameters can be calculated.

Firstly, the Born-Oppenheimer approximation is used which assumes that the motion of the nuclei and the electrons can be separated (This means that the wavefunction of a molecule can be broken into its electronic and nuclear components). This is because nuclei are around three orders of magnitude heavier than electrons which means they are much slower than electrons. Electrons, on the other hand, adjust instantaneously to nuclear positions. When electron motion is calculated, the nuclear co-ordinates can be treated as parameters. The nuclear mass is set to infinity and the kinetic energy term of the nuclei in the Schrödinger equation is ignored.

The HF method is then employed which approximates the wave function and the energy of a quantum-many body system in a stationary state. It assumes that the N-body wave function can be approximated by a Slater determinant (as electrons are fermions). Using the variational method, N -coupled equations for N spin orbitals can be derived. The solution of the equations gives the HF wavefunction and the energy of the system. It is from the energy that the NMR parameters can be determined. This approach uses first order perturbation theory. The self-interaction terms in the Schrödinger equation: the Coulomb and exchange interactions cancel. However, many correlations which are especially important in solid-state NMR are absent.

DFT is introduced to overcome the many-body wavefunction problem. The Hohenberg-Kohn theorem can be used in which the ground state density completely defines the physical system, i.e. the density is a simple function in 3-D space.

Using DFT, the electronic energy is given by:

$$E_0[\rho(r)] = E_{Ne}[\rho(r)] + T_S[\rho(r)] + J[\rho(r)] + E_{XC}[\rho(r)], \quad (5.14)$$

where: E_0 is the electronic energy ground state, E_{Ne} is the nucleus-electron interaction energy, T_S is the kinetic energy of non-interacting electrons and J is the classical Coulomb interaction between electrons [81]. The E_{XC} exchange-correlation interaction between electrons is not exactly known. This has resulted in the development of exchange-correlation functionals in which the user can apply the exchange-correlation functional which best fits their needs. The exchange-correlation functional that was used in this

research was of the generalised gradient approximation (GGA) type, where the gradient of the electron density is included. The GGA functional used in this thesis was that of Perdew, Burke and Ernzerhof (PBE) [214] (see later).

As most solids have long range periodic order Bloch's theorem can be used:

$$V(r + L) = V(r), \quad (5.15)$$

where $V(r)$ is the potential at r and $V(r + L)$ is the potential at r displaced by lattice vector L . This reduces the system to a single unit cell. As the electron density ρ is periodic, the magnitude of the wavefunction Φ_r is periodic. But the wavefunction is only quasi-periodic:

$$\Phi_k(r) = e^{ik \cdot r} u_k(r), \quad (5.16)$$

where $e^{ik \cdot r}$ is an arbitrary phase factor and $u_k(r)$ is a periodic function.

Basis Set

Most solid-state DFT codes represent the wavefunction by a plane-wave basis set. A basis set is a set of functions combined linearly to create molecular orbitals. The orbitals are mathematical functions which describe the wave nature of electrons in atoms. The wavefunctions of the system are represented as vectors. Operators are represented as matrices (rank two tensors) in a finite basis. The plane-wave basis set has a finite number of plane-wave functions.

A large calculation could use 10^5 plane-waves to represent wavefunctions. To truncate the basis set, the sum is limited to a set of reciprocal lattice vectors, G contained within a sphere where the radius of this sphere is defined as the cutoff energy, E_{cut} :

$$\frac{1}{2}|k + G| \leq E_{cut}. \quad (5.17)$$

The cutoff energy is found by increasing E_{cut} until convergence of the calculation has been reached. The presented calculations in this thesis used a cutoff energy of 800 eV.

Pseudopotentials

The basis set is used with a pseudopotential (effective core potential) to replace the effects of the core electrons. The electrons in a molecule are either described as core or

CHAPTER 5. EXPERIMENTAL TECHNIQUES

valence electrons. The pseudopotential is used so that the plane waves only describe the valence electrons. Therefore two approximations are used:

- 1. The frozen core approximation.** Core electrons are concentrated very close to the atomic nuclei. This would result in large wavefunctions and density gradients near nuclei which are not easily described by a plane wave basis set unless high cut-off energies and small wavelengths are used. The Schrödinger equation therefore contains a modified effective potential term in place of the Coulomb potential term for the core electrons. It acts in a way that only the chemically active valence electrons are considered while the core electrons are "frozen". They are grouped together with the nuclei as rigid non-polarisable ion cores, these electrons are effectively removed in the calculation.
- 2. Smooth effective potential** The oscillations of the valence wavefunctions close to the nucleus do not directly contribute to bonding. As a result, the Coulomb potential and the interaction between the core and valence electrons is replaced by a smooth effective potential. This acts in a defined region around the nucleus.

These approximations are the pseudopotentials and are used when dealing outside of the core region. The pseudopotentials used require that pseudo and all electron valence eigenstates have the same energies and amplitude outside a sphere of cutoff radius r_c . For NMR however, electronic structure close to the nucleus is needed but this can be recovered. The PAW transformation enabled this and was refined by the development of the GIPAW method. This is based on DFT, plane-wave basis set, pseudopotentials and PAW allowing NMR parameters to be calculated with an all electron accuracy. The periodic boundary conditions allow a solid-state calculation to be performed by enabling the accurate calculation of NMR tensors in solids, thus results can be applied to structural and also chemical purposes. If the cut-off radius of the pseudopotential is large it is referred to as soft. This means that it will converge (see section that follows for more information on convergence) more rapidly, but the drawback is that it is not as transferable.

Overview of GIPAW Method

How a calculation is performed

To perform a calculation requires an initial starting point for the crystal structure of the material, which gives the unit cell parameters and the positions of the atoms within the unit cell. In my research this was obtained using XRD. Most small molecule crystal

structures obtained using XRD are deposited in the Cambridge Structural Database (CCDC) which can be obtained freely in the form of a .cif file. The .cif files allow the molecule to be viewed in the relevant software, for example, the viewing software used in this research was that of Diamond, Mercury and Jmol. From the software the positions of all the atoms and the unit cell parameters can be extracted.

The minimisation of the ground state provides forces on all of the atoms and the stress on the unit cell. If the forces are "large", this shows that the atom positions need to be optimised and that a geometry optimisation calculation needs to be performed. This allows the positions of the atoms (and, if desired, the unit cell parameters to vary, although unit cell parameters are generally accurately determined by XRD) to vary in order to minimise the force (stress) on the system. Typically, the geometry optimisation calculations that were performed in this work were carried out until the energy, forces and displacements on the atoms were around 0.000001 eV, 0.1 eV⁻¹ and 0.001 eV⁻¹.

Once a satisfactory geometry optimisation calculation has been performed, a GIPAW calculation is performed which will output the NMR tensors. In the CASTEP code this calculation is referred to as MAGRES. From experience it is the geometry optimisation calculation of the crystal structure which takes the most time with some of my systems taking days to complete (dependent on the size of the system). The MAGRES task, however, is completed in a relatively short time period.

Accuracy

The calculations require the user to select an exchange-correlation functional, an important physical approximation. If the correct functional is chosen, the closer the solution to the Schrödinger equation and subsequently the more accurate the NMR parameters will be. For NMR calculations, the exchange-correlation functional used has employed the GGA functional by Perdew, Burke and Ernzerhof. This has been found to agree well with experiment with discrepancies on the order to 2% of the chemical shift range.

In order to ensure the reliability of a calculation, convergence has to have occurred. Two important parameters are the plane-wave cut-off energy and spacing between k-points. k-points are used to take averages of the properties over the electron brillouin zone. It is important also to state that while NMR experiments (in this thesis) were conducted at room temperature, typically 21°C, calculations are performed at 0 K i.e. static configuration of atoms (from diffraction). It has been shown that the possible difference for temperature effects could be 0.5 ppm in ¹H chemical shifts [84]. The ¹H chemical shift is known to decrease with an increase in temperature. Notably, the unit cell

CHAPTER 5. EXPERIMENTAL TECHNIQUES

is sensitive to temperature providing one explanation for the chemical shift dependence on temperature.

Outlook

There are constant improvements in experimental techniques, for example, in NMR: higher field strengths and faster MAS rates. Computationally, there are also constant improvements in: efficiency and accuracy of the calculations. However, it has been realised that a method used on its own does not provide the best results. Making use of other complementary techniques produces the best results and this has led to NMR crystallography where a combination of techniques is used together. In this work, NMR, XRD and computation have all been applied together, without this approach the results would not have been possible.

Experimental Techniques and Computational Details

6.1 Introduction

This chapter presents the experimental and computational details for the experiments and calculations performed for the results presented in this thesis: for chapter 7 which presents results on the nicotinamide system: the salt and cocrystal system of Isonicotinamide/4-hydroxy-3-nitrobenzoic acid and Isonicotinamide/2,4,6-trihydroxybenzoate, chapter 8 which presents results on the bipyridine system: the salt and cocrystal system of 4,4'-Bipyridine/5-Sulfosalicylic salt (4BPY/sulfo) and 4,4'-Bipyridine/Phthalic Co-crystal (4BPY/phthalic), chapter 9 which presents results on citric acid, its cocrystals and a citrate salt of sildenafil.

6.2 Experimental Details

6.2.1 Sample Preparation

Isonicotinamide/4-hydroxy-3-nitrobenzoic acid and Isonicotinamide/2,4,6-trihydroxybenzoate [161] and 4,4'-Bipyridine/5-Sulfosalicylic salt (4BPY/sulfo) and 4,4'-Bipyridine/Phthalic Co-crystal (4BPY/phthalic) [215] were provided by J.S. Stevens (University of Manchester). Citric Acid and sildenafil citrate was obtained from Sigma Alrich and were used without further preparation. Caffeine citric acid was made by Dr. Manishkumar R. Shimpi, Luleå University of Technology.

6.2.2 Solid-State NMR Experiments

Experiments were performed using a Bruker Avance II+ spectrometer operating at a Larmor frequency of 600 MHz ($B_0 = 14.1$ T), a Bruker Avance III spectrometer operating at a ^1H Larmor frequency of 500 MHz ($B_0 = 11.7$ T) and a Bruker Avance III HD spectrometer operating at a Larmor frequency of 700 MHz ($B_0 = 16.4$ T). All experiments were performed at room temperature. The ^1H 90° pulse duration was $2.5\ \mu\text{s}$. A recycle delay of 60 s was used for all samples, except for citric acid monohydrate where 90 s was used. Recycle delays were calibrated for each sample to see which delay time gave the greatest signal intensity.

Unless otherwise stated, a 1.3 mm HXY probe was used in double resonance mode at a MAS frequency of 60 kHz. In all two-dimensional experiments, the States-TPPI (Two Pulse Phase Increment) method was used to achieve sign discrimination in F_1 and the t_1 increment was set equal to one rotor period.

^1H chemical shifts were referenced with respect to *L*-alanine (1.3 ppm for the CH_3 ^1H resonance) corresponding to TMS at 0 ppm. ^{14}N shifts were referenced relative to solid ammonium chloride (NH_4Cl) at -341.2 ppm, but a secondary reference was used, namely the dipeptide β -AspAla ($\text{C}_7\text{H}_{12}\text{N}_2\text{O}_5$), where the NH_3 peak is centred at -284 ppm at 14.1 Tesla [216]. To convert to the chemical shift scale frequently used in protein ^{15}N NMR, where the alternative IUPAC (The International Union of Pure and Applied Chemistry) reference (see Appendix 1 of Ref. [217]) is liquid ammonia at 50°C , it is necessary to add 379.5 ppm to the given values [210].

^1H - ^1H DQ/SQ MAS Experiments

A ^1H - ^1H double-quantum (DQ)/ single-quantum (SQ) magic angle spinning (MAS) experiment employed the BAcK-to-BAcK (BABA) [205, 218] scheme to recouple the homonuclear ^1H - ^1H dipolar interaction for a duration of one rotor period. A nested 16 step phase cycle was used to select $\Delta p = \pm 2$ on the DQ excitation pulses (4 steps) and $\Delta p = -1$ on the z -filter 90° pulse.

^{14}N - ^1H - HMQC experiments

Rotary resonance recoupling (R^3) with an $n = 2$ resonance condition using an x , $-x$ phase inversion of individual block lengths of one rotor period (i.e. of duration $16.7\ \mu\text{s}$) was employed. The ^{14}N pulse length used in experiments was of duration $11\ \mu\text{s}$. The ^{14}N pulse duration was determined by optimising the signal. The value of the pulse chosen depends on the size of the quadrupolar coupling constant [82]. A four step nested phase

cycle was used to select changes in coherence order $\Delta p = \pm 1$ (on the first ^1H pulse, 2 steps) and $\Delta p = \pm 1$ (on the final ^{14}N pulse, 2 steps).

6.3 PXRD

In this thesis PXRD was carried out on samples to test the phase purity before solid-state NMR experiments are carried out. The predicted PXRD pattern is generated from, for example, a .cif file which has been deposited in the CSD (Cambridge Structure Database) and with the use of a software program such as Mercury a predicted diffraction pattern is able to be created. This predicted diffraction pattern can then be compared to the experimental diffraction pattern. When analysing the two diffraction patterns it is important to ensure there are no intensity peaks in the experimental pattern at a 2θ angle for which there is not a peak in the predicted pattern. However, the absence of an experimental intensity peak at a predicted angle (2θ) can arise due to crystalline preferred orientation effects.

6.3.1 PXRD of citric acid monohydrate

PXRD was carried out on the sample of citric acid to see whether that the crystal structure deposited in the CSD matched the physical sample. The CSD contains numerous crystal structures under “citric acid” so first calculations had to be performed to see which of these deposited crystal structures was a match for the citric acid sample. Investigations into the anhydrous citric acid and citric acid monohydrate structures were conducted and calculations were performed on the structures under the refcodes found in the CSD: CITARC ([219]), CITARC10 ([220]), CITARC11 ([221]), CITARC01 ([222]), CITARC02 ([223]) and CITARC12 ([223]) in order to determine the best match.

The diffraction patterns shown in figure 6.1 were obtained using the crystal structure information from the refcodes of: CITARC for anhydrous citric acid (shown by the red diffraction pattern), and CITARC11 for citric acid monohydrate (shown by the blue diffraction pattern). The two diffraction patterns from CITARC11 and CITARC were then combined with the experimental citric acid sample that was obtained from Sigma Aldrich (shown by the black diffraction pattern). As a result, the experimentally investigated sample is shown to correspond to citric acid monohydrate: the black peaks for the experimental diffraction pattern in figure 6.1 coincide with the peaks from the CITARC11 CSD structure (citric acid monohydrate).

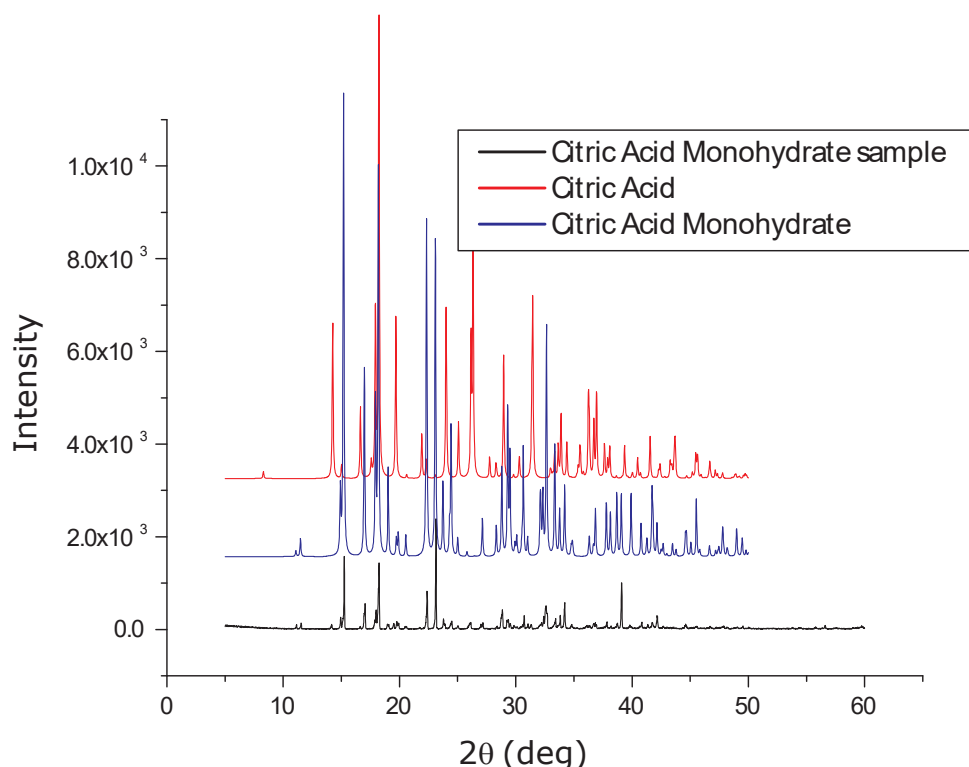


Figure 6.1: Experimental PXRD data of the sample of citric acid monohydrate (black diffraction pattern, bottom) compared with predicted PXRD data for the CSD structures of anhydrous citric acid (red diffraction pattern, top) and citric acid monohydrate (blue diffraction pattern, middle).

6.3.2 PXRD for Isonicotinamide Salt and Cocrystal

PXRD was conducted on the samples to ensure the sample matched the crystal structure that was in the CSD and that the sample had remained stable during transportation. Figure 6.2 shows a PXRD pattern of isonicotinamide/ 2,4,6- trihydroxybenzoate salt ($1\text{-NH}^+ : 2\text{-COO}^-$) where the black diffraction pattern represents the experimental data of the salt and the red diffraction pattern represents the PXRD pattern obtained from the cif file which was provided by Stevens et al [161]. Figure 6.3 displays the PXRD pattern of isonicotinamide/4-hydroxy-3-nitrobenzoic acid co-crystal ($1\text{-N}:3\text{-COOH}$) where the black diffraction pattern represents the experimental data of the salt whereas the red diffraction pattern represents the PXRD pattern obtained from the cif file contained in the CSD under reference RINHUT [161].

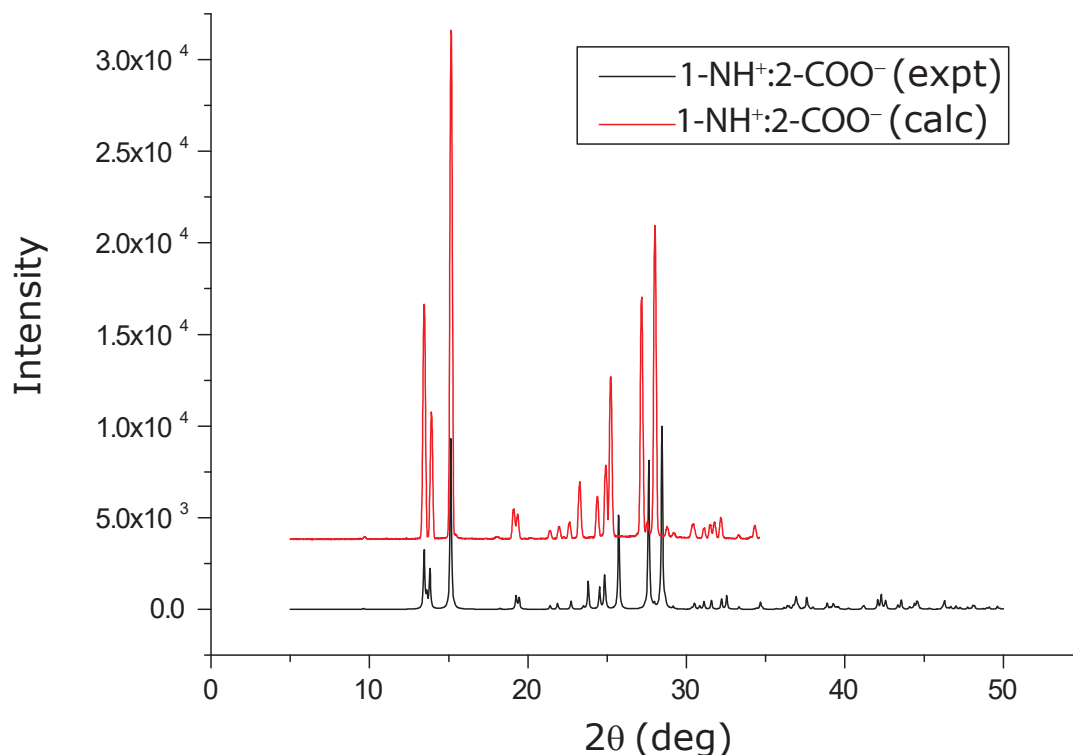


Figure 6.2: Experimental PXRD pattern of an isonicotinamide/4-hydroxy-3-nitrobenzoic acid co-crystal (1-N:3-COOH) where the black line represents the experimental data of the salt whereas the red line represents the PXRD pattern obtained from the cif file contained in the CSD, RINHUT, under reference [161].

Note that the powder patterns between experiment and calculation match well. The criteria used to assess the comparison of the patterns was that peaks are allowed to be seen in experiment and not the calculated, however not the other way around. The 2θ values depend on the unit cell parameters. Diffraction patterns from deposited structures in the CSD will have differed from the presented experimental diffraction patterns in this thesis where all were recorded at ambient room temperature. The unit cell is dependent on temperature therefore where there is a temperature difference between the experimental pattern, and the calculated pattern a deviation between peaks will therefore be present especially at higher angles. In this respect, note that the structures in reference [161] were determined at a temperature of 100 K. Preferred orientation effects are present notably in figure 6.3.

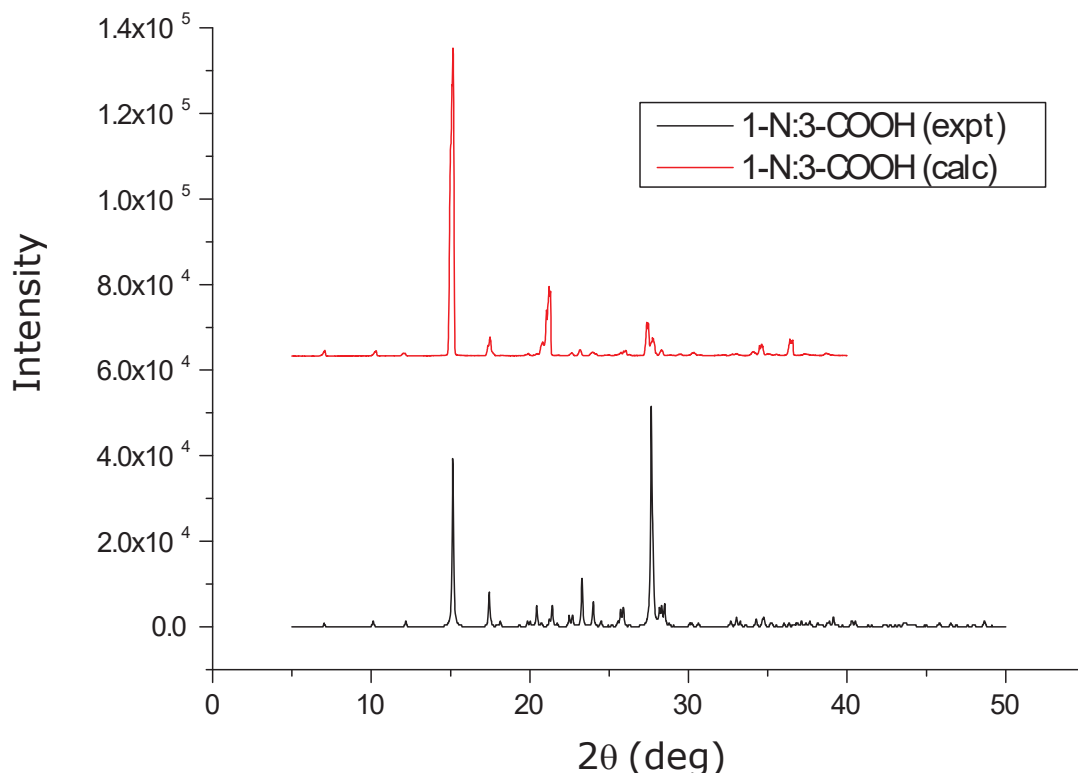


Figure 6.3: Experimental PXRD pattern of an isonicotinamide/4-hydroxy-3-nitrobenzoic acid co-crystal (1-N:3-COOH) where the black line represents the experimental data of the salt, whereas the red line represents the PXRD pattern obtained from the cif file contained in the CSD under reference [161].

6.4 Computational Details

First principles calculations were performed using the CASTEP code, academic release version 8.0, which uses the GIPAW method [71, 72]. All calculations used a PBE (Perdew-Burke-Ernzerhof (functional)) exchange-correlation functional. Geometry optimisation calculations were performed using the crystal structures determined from diffraction, references for these compounds can be found in table 6.1 along with the number of atoms in the full crystallographic unit cell, Z , Z' , and, for the geometry optimisation and NMR calculations, the cut-off energy and the k -point spacing. The calculations were performed with the unit cell parameters fixed (using cell parameters from diffraction data) but all molecular species inside the cell were allowed to vary (the positions of all atoms were relaxed). Energies, forces and displacements were converged to better than

6.4. COMPUTATIONAL DETAILS

0.000001 eV, 0.1 eV \AA^{-1} and 0.001 \AA , respectively. Distances and angles stated in this thesis are for geometry optimised structures.

Table 6.1: Computational details of the results which are presented in this thesis showing: refcodes (from CSD) with paper reference, number of atoms in the full crystallographic unit cell, Z, Z' and k-point spacing $\times 2\pi \text{ \AA}^{-1}$.

Molecule	CIF REFCODE from CCDC	Atoms in full crystallographic unit cell	Z	Z'	k-point spacing $\times 2\pi \text{ \AA}^{-1}$
1-NH ⁺ :2-COO ⁻	BIZTOV01 [161]	132	4	1	0.05
1-N:3-COOH	RINHUT [161]	264	8	1	0.05
4-NH ⁺ :5-COO ⁻	DUBFEN [215]	160	4	1	0.05
4-N:6-COOH	SUXVOW [224]	228	4	0.5	0.05
Citric Acid	CITRAC11 [221]	84	4	1	0.1
Theophylline Citric Acid Monohydrate	KIGKAN [225]	180	4	1	0.1
Caffeine Citric Acid	KIGKER [225]	90	2	1	0.1
Betaine Citric Acid	XOBHIF [226]	160	2	1	0.1
Paracetamol Citric Acid	AMUBAM [227]	512	8	1	0.05
Nicotinamide Citric Acid	CUYXUQ [228]	102	2	1	0.1
Nitrofurantoin Citric Acid	LEWTAK [229]	176	4	1	0.1
Piracetam Citric Acid	RUCFAX [230]	656	4	1	0.1
Sildenafil Citrate Monohydrate	QEGTUT [231]	696	8	1	0.05

Isolated molecule calculations were performed by extracting a single molecule from the geometry optimised crystal structure. The molecule was then used to create a periodically repeating unit cell containing this molecule with enlarged unit cell dimensions of: isonicotinamide ($18 \times 18 \times 13 \text{ \AA}$), 4-hydroxy-3-nitrobenzoic acid ($10 \times 20 \times 23 \text{ \AA}$), 2,4,6-trihydroxybenzoate ($18 \times 18 \times 13 \text{ \AA}$), 4,4'-bipyridine ($16 \times 19 \times 17 \text{ \AA}$), phthalic acid ($19 \times 13 \times 18 \text{ \AA}$), sulfosalicylic salt ($16 \times 19 \times 17 \text{ \AA}$) and citric acid monohydrate ($12 \times 15 \times 21 \text{ \AA}$). The use of this value ensures that the periodically repeating unit cells are far enough apart from each other to ensure intermolecular interactions do not take place - effectively removing intermolecular interactions. The numbers used were chosen based on unit cell parameters obtained from PXRD data and increased by at least 5 \AA until intermolecular interactions were not observed. The NMR shieldings are then calculated without any further geometry optimization. For isolated molecule calculations, in the CASTEP input file a line was added to indicate when the molecule had a charge [79].

Scheme to determine $\Delta\delta_{\text{cryst-mol}}$

Below is the method that was used to determine $\Delta\delta_{\text{cryst-mol}}$ noting that isolated molecule refers to the NMR parameters being calculated for an individual molecule as extracted from the geometry optimised full crystal structure and then contained within a large unit cell, effectively removing intermolecular interactions (see above section for specific details on how this is achieved):

1. Determine full crystal $\delta_{\text{ISO}}^{\text{calc}}$ ($\delta_{\text{ISO}}^{\text{calc}} = \sigma_{\text{ref}} - \sigma_{\text{iso}}$)
2. Determine isolated $\delta_{\text{ISO}}^{\text{calc}}$ ($\delta_{\text{ISO}}^{\text{calc}} = \sigma_{\text{ref}} - \sigma_{\text{iso}}$)
3. Determine $\Delta\delta_{\text{cryst-mol}}$ ($\Delta\delta_{\text{cryst-mol}} = \delta_{\text{ISO}}^{\text{calc}} - \sigma_{\text{iso}}$)

In order to compare isotropic chemical shifts measured experimentally with the values extracted from the NMR shielding calculations, a conversion is needed: $\delta_{\text{iso}} = \sigma_{\text{ref}} - \sigma_{\text{iso}}$, where σ_{iso} is the absolute chemical shielding value generated from the CASTEP calculations. In this thesis, the reference shielding was calculated from experimental isotropic chemical shifts and calculated shieldings (see table 6.2) and figure 6.4. It is noted that it is common practice to calculate a specific reference shielding for each system (see, e.g., Supplementary Table 8 of Ref [232]), though average values over a range of compounds are also available [233].

This gave a σ_{ref} value of 170.1 for ^{13}C and 30.1 for ^1H for citric acid monohydrate.

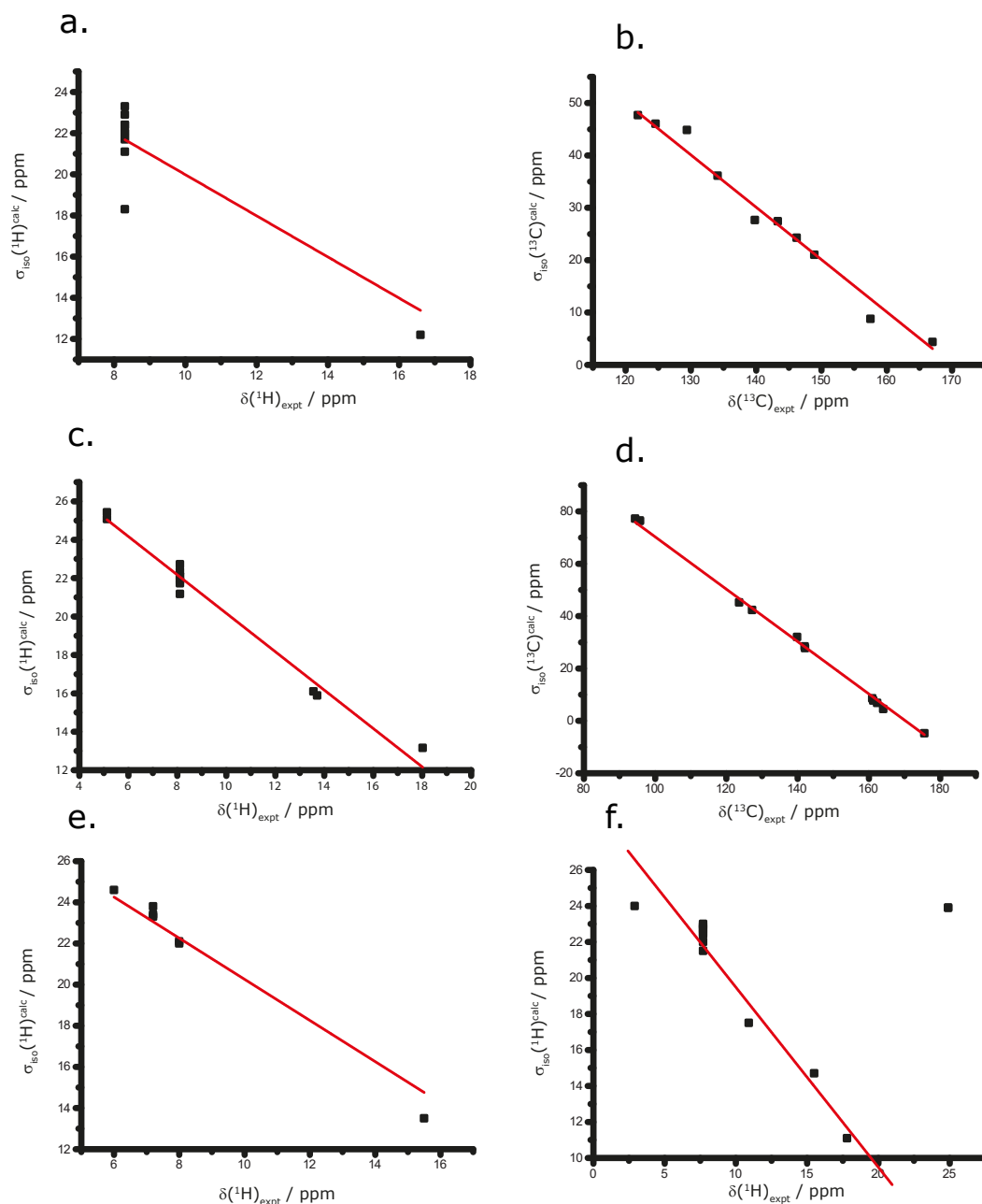


Figure 6.4: In order to compare isotropic chemical shifts measured experimentally with the values extracted from the NMR shielding calculations, a conversion is needed: $\delta_{iso} = \sigma_{ref} - \sigma_{iso}$, where σ_{iso} is the absolute chemical shielding value generated from the CASTEP calculations. The reference shielding was calculated from experimental isotropic chemical shifts and calculated shieldings. Data is presented for a. 1-NH⁺:2-COO⁻, b. 1-NH⁺:2-COO⁻, c. 1-N:3-COOH, d. 1-N:3-COOH, e. 4-N:6-COOH and f. 4-NH⁺:5-SO₃⁻

Table 6.2: Reference shielding as calculated from experimental isotropic chemical shifts and calculated shieldings

Chemical	^1H ref value/ppm	^{13}C ref value/ppm
1-NH ⁺ :2-COO ⁻	30.2	170.3
1-N:3-COOH	30.0	170.1
4-N:6-COOH	30.3	
4-NH ⁺ :5-SO ₃ ⁻	30.4	

CHAPTER 6. EXPERIMENTAL TECHNIQUES AND COMPUTATIONAL DETAILS

Determining Protonation in Pharmaceutical Compounds using NMR Crystallography: An Isonicotinamide Salt and Co-crystal

7.1 Introduction

This and the following chapter compare a salt and a co-crystal. The salt consists of two molecules which are ionised, while the co-crystal consists of two neutral molecules.

Research presented here and in the subsequent chapter has studied the nitrogen site in two separate salt/cocrystal systems using NMR crystallography to identify when protonation has occurred (when a proton has transferred from the acid to base, i.e. co-crystal to salt form). 1D one-pulse ^1H MAS NMR and ^1H - ^1H DQ MAS NMR solid-state NMR experiments are used alongside 2D ^{14}N - ^1H HMQC experiments to probe protonation. The ^{14}N shift in the 2D ^{14}N - ^1H HMQC experiment is shown to change significantly upon protonation of the nitrogen site, where changes in shift with magnitude of hundreds of ppm are observed. Further evidence of protonation is provided by the variation of the recoupling time in 2D ^{14}N - ^1H HMQC experiments to probe ^{14}N - ^1H proximities.

The experimental data complements data obtained from GIPAW calculations of NMR chemical shielding and quadrupolar interactions which show that the combined experimental and calculation approach is viable in determining the presence of a salt or co-crystal form. In addition, the trend in P_Q values of the chosen nitrogen site becoming higher upon protonation is observed and noted, providing avenue for further study. Single

CHAPTER 7. PROTONATION IN PHARMACEUTICAL COMPOUNDS: ISONICOTINAMIDE SALT AND CO-CRYSTAL

crystal to full molecule calculations are also performed and give detailed information on bonding structures and hydrogen bond strength within the molecules. This insight complements that from ^1H chemical shifts which are known to be sensitive to hydrogen bonding [54, 75, 79, 98, 234]

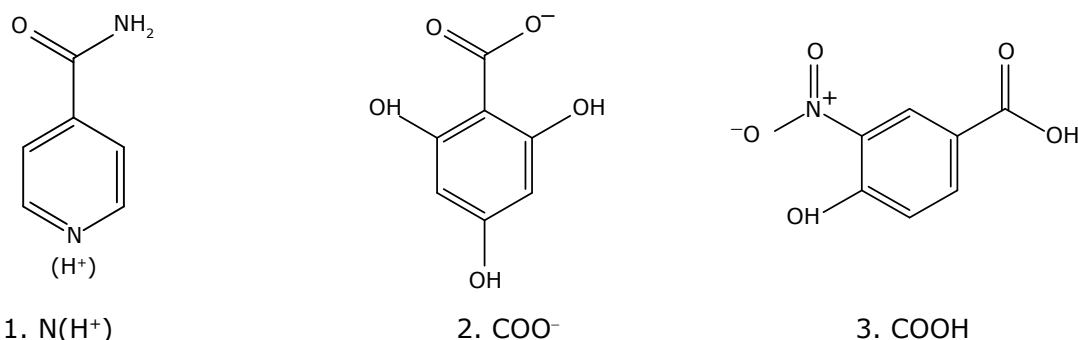


Figure 7.1: Molecular structures for isonicotinamide/ 2,4,6- trihydroxybenzoate salt (1-NH⁺:2-COO⁻) and isonicotinamide/4-hydroxy-3-nitrobenzoic acid co-crystal (1-N:3-COOH).

The individual components of the salt and co-crystal systems considered in this chapter are shown in Figure 7.1. Specifically, an isonicotinamide/ 2,4,6- trihydroxybenzoate salt (1-NH⁺:2-COO⁻) and an isonicotinamide/4-hydroxy-3-nitrobenzoic acid co-crystal (1-N:3-COOH) whereby ^{15}N CP MAS NMR spectra have been presented previously [215]. Here the isonicotinamide is present in both cases while the acid molecule changes: 1-N:3-COOH (co-crystal) contains a neutral pyridine N group, while this group is protonated in 1-NH⁺:2-COO⁻ (salt). Crystal structures of 1-N:3-COOH and 1-NH⁺:2-COO⁻ (CSD refcodes RINHUT and BIZTOV01, respectively) were determined in reference [161], where ^{15}N CP MAS spectra are also presented. Both cases have $Z' = 1$, where Z' refers to the number of molecules in the crystallographic asymmetric unit.

7.2 One-dimensional ^1H MAS NMR Spectra

One-pulse ^1H MAS NMR spectra of 1-NH⁺:2-COO⁻ and 1-N:3-COOH are presented in figure 7.3a and 7.3b, respectively. Together with the experimental spectra (black lines), figure 7.3 also presents stick spectra that represent ^1H chemical shifts calculated by the GIPAW method. Specifically, red bars correspond to calculations for the full crystal structure, while green and blue bars show ^1H chemical shifts calculated for isolated isonicotinamide and the acid molecules, as extracted from the crystal structures. Table

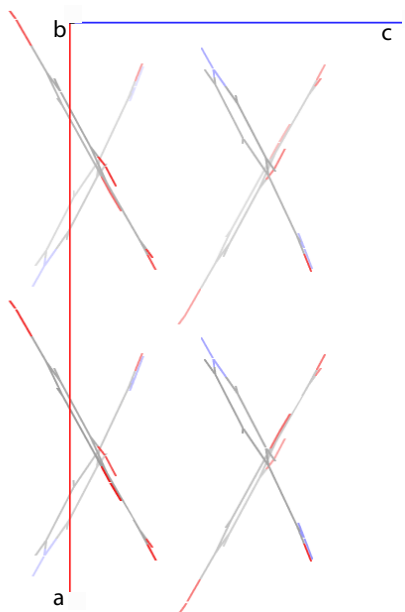


Figure 7.2: Crystal packing of the Isonicotinamide/ 2,4,6- trihydroxybenzoate salt ($1\text{-NH}^+:2\text{-COO}^-$) (CSD code BIZOV01).

7.1 compares the experimental ^1H chemical shifts to those calculated by the GIPAW method; the difference, $\Delta\delta_{C-M}$, corresponds to the change in the calculated chemical shift from the isolated molecule to the full crystal structure, i.e., that shown by the change in the position of the green/blue bars to the red bars in figure 7.3.

The $\Delta\delta_{C-M}$ values for the OH groups of the acids which concern the hydrogen atoms of H41 and H45 in $1\text{-NH}^+:2\text{-COO}^-$ and H5 in 1-N:3-COOH are of interest. Experimental and calculated spectra show higher ^1H chemical shifts (see table 7.1) for the hydrogen atoms involved in these OH groups indicating that strong hydrogen bonds are present (see table 7.2). However, the $\Delta\delta_{C-M}$ values are negative (between -1.5 and -2.9 ppm) because the OH protons all form intramolecular OH...O hydrogen-bonds with the significant $\Delta\delta_{C-M}$ values due to ring currents (see figure 7.4 for a representation of these OH...O hydrogen bonds in $1\text{-NH}^+:2\text{-COO}^-$). The hydrogen atom of H33 in $1\text{-NH}^+:2\text{-COO}^-$ has a $\Delta\delta_{C-M}$ change of 4.9 ppm. It is involved in the hydrogen bond of O13-H33...O1, where $d(\text{H}\dots\text{Y})$ is 1.74 Å, $d(\text{X}\dots\text{Y})$ is 2.72 Å and $\angle\text{XHY}$ is 170.3°. The NH_2 group in $1\text{-NH}^+:2\text{-COO}^-$ also exhibits significant $\Delta\delta_{C-M}$ values. Here, the hydrogen atoms of H21 and H25 make N5-H21...O21 and N5-H25...O17 hydrogen bonds, respectively. The $\Delta\delta_{C-M}$ value for the hydrogen atom of H21 is 4.3 ppm, with a $d(\text{H}\dots\text{Y})$ of 1.96 Å, $d(\text{X}\dots\text{Y})$ of

CHAPTER 7. PROTONATION IN PHARMACEUTICAL COMPOUNDS: ISONICOTINAMIDE SALT AND CO-CRYSTAL

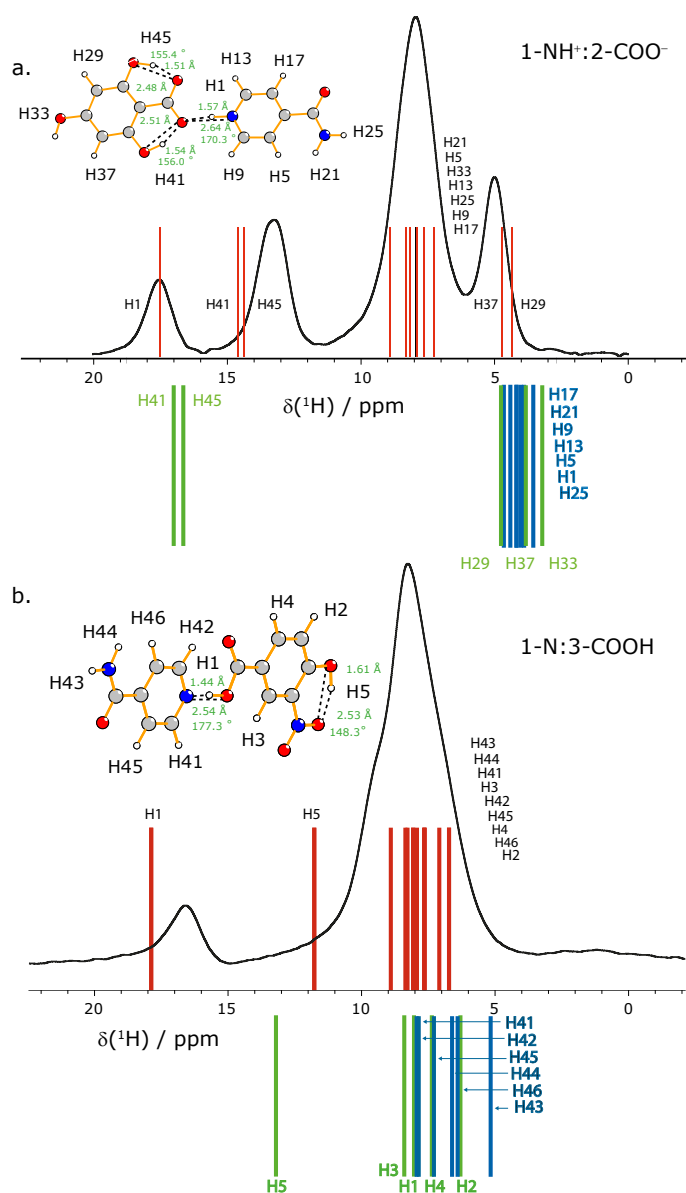


Figure 7.3: ^1H (600 MHz) one-pulse MAS NMR spectra of (a) 1-NH⁺:2-COO⁻ and (b) 1-N:3-COOH recorded at a MAS frequency of (a) 60 kHz and (b) 55 kHz. The experimental spectra (black lines) are compared to stick representations of calculated (GIPAW) ^1H chemical shifts for the full crystal structure (red) and isolated isonicotinamide (blue) and carboxylate salt or carboxylic acid molecules (green). 256 transients were co-added in both cases. Nitrogen, oxygen, carbon and hydrogen atoms are represented by the colours blue, red, grey and white, respectively. Figure 7.2b includes some weak signals at around 0-4 ppm which is due to an impurity. Nitrogen, oxygen, carbon and hydrogen atoms are represented by the colours blue, red, grey and white, respectively.

7.2. ONE-DIMENSIONAL ^1H MAS NMR SPECTRA

Table 7.1: Experimental and GIPAW calculated ^1H chemical shifts (in ppm) for 1-NH $^+$:2-COO $^-$ and 1-N:3-COOH

Atom label	$\delta_{iso}(\text{expt})$	Calculated †		
		$\delta_{iso}(\text{cryst})^a$	$\delta_{iso}(\text{molc})^a$	$\Delta\delta_{C-M}$
1-NH $^+$:2-COO $^-$				
H1	17.6	16.8	4.0	12.8
H5	8.0	8.3	4.1	4.1
H9	8.0	7.6	4.3	3.4
H13	8.0	7.9	4.3	3.6
H17	8.0	7.3	4.7	2.5
H21	8.0	8.8	4.5	4.3
H25	8.0	7.9	3.7	4.2
H29	5.0	4.6	4.7	-0.2
H33	8.0	8.1	3.2	4.9
H37	5.0	4.9	3.8	1.1
H41	13.3	14.1	17.0	-2.9
H45	13.3	13.9	16.7	-2.8
1-N:3-COOH				
H1	16.6	17.8	8.0	9.8
H2	8.3	6.7	6.3	0.5
H3	8.3	8.0	8.4	-0.4
H4	8.3	7.6	7.3	0.3
H5	8.3	11.7	13.2	-1.5
H41	8.3	8.2	7.9	0.3
H42	8.3	7.9	7.8	0.1
H43	8.3	8.9	5.1	3.8
H44	8.3	8.3	6.6	1.8
H45	8.3	7.0	7.3	-0.2
H46	8.3	7.6	6.4	1.2

† Calculated using $\delta = \sigma_{ref} - \sigma_{calc}$, where $\sigma_{ref} = 30.0$ ppm.

CHAPTER 7. PROTONATION IN PHARMACEUTICAL COMPOUNDS: ISONICOTINAMIDE SALT AND CO-CRYSTAL

Table 7.2: Hydrogen-bond distances and geometry for cases where $\Delta\delta_{C-M}$ has magnitude greater than 2 ppm for 1-NH⁺:2-COO⁻ and 1-N:3-COOH.

H Atom	Hydrogen bond	$d(H...Y)$ / Å	$d(X...Y)$ / Å	$\angle XHY$ / °	δ_{iso}^{calc} / ppm (<i>fullcrystal</i>)	$\Delta\delta_{C-M}$ /ppm
1-NH ⁺ :2-COO ⁻						
1	N1-H1...O5	1.57	2.64	170.1	16.8	12.8
5	C5-H5...O21	2.10	3.14	159.3	8.3	4.2
9	C9-H9...O13	2.38	3.43	146.6	7.6	3.3
13	C13-H13...O9	2.37	3.50	138.7	7.9	3.6
17	C21-H17...O9	2.52	3.20	116.2	7.3	2.5
21	N5-H21...O21	1.96	2.98	173.8	8.8	4.3
25	N5-H25...O17	1.96	2.90	151.0	7.9	4.2
33	O13-H33...O1	1.74	2.72	170.3	8.1	4.9
41	O21-H41...O5	1.51	2.48	149.4	14.1	-2.9
45	O9-H45...O17	1.54	2.51	156.0	13.9	-2.8
1-N:3-COOH						
1	O1-H1...N9	1.44	2.54	177.3	17.8	9.8
43	N10-H43...O41	1.84	2.87	174.7	8.9	3.8

2.98 Å and $\angle XHY$ of 173.8°. The $\Delta\delta_{C-M}$ for the hydrogen atom of H25 is 4.2 ppm, with a $d(H...Y)$ of 1.96 Å, $d(X...Y)$ of 2.90 Å and $\angle HXY$ of 151.0°. This chemical shift difference is similar to that for N-H...O hydrogen bonds considered in reference [76].

The NH₂ group in 1-N:3-COOH has a $\Delta\delta_{C-M}$ of 3.8 ppm for the N10-H43...O41 hydrogen bond with a $d(H...Y)$ of 1.84 Å, $d(X...Y)$ of 2.87 Å and $\angle XHY$ of 174.7°.

Table 7.2 lists the occurrence of four so-called C-H...O weak hydrogen bonds for the salt [76, 92], see also figure 7.5. This involves the hydrogen atoms of H5, H9, H13 and H17 with a $\Delta\delta_{C-M}$ value of 4.2, 3.3, 3.6 and 2.5 ppm, respectively. This is to be compared to values of 2.0 and 2.2 ppm for CH protons involved in CH...O weak hydrogen bonding in 4-cyano-4'-ethynylbiphenyl [76]. By comparison, for the co-crystal, no such significant $\Delta\delta_{C-M}$ ppm values are seen for the potential CH hydrogen bond donors.

7.3 ¹H-¹H DQ MAS NMR Spectra

Figure 7.6 presents ¹H-¹H DQ MAS NMR spectra of 1-NH⁺:2-COO⁻ (figure 7.6 a) and 1-N:3-COOH (figure 7.6 b). For specific resolved DQ peaks, close ¹H-¹H proximities are stated in figure 7.6, while all ¹H-¹H proximities < 3.5 Å are shown in table 7.3 & 7.4.

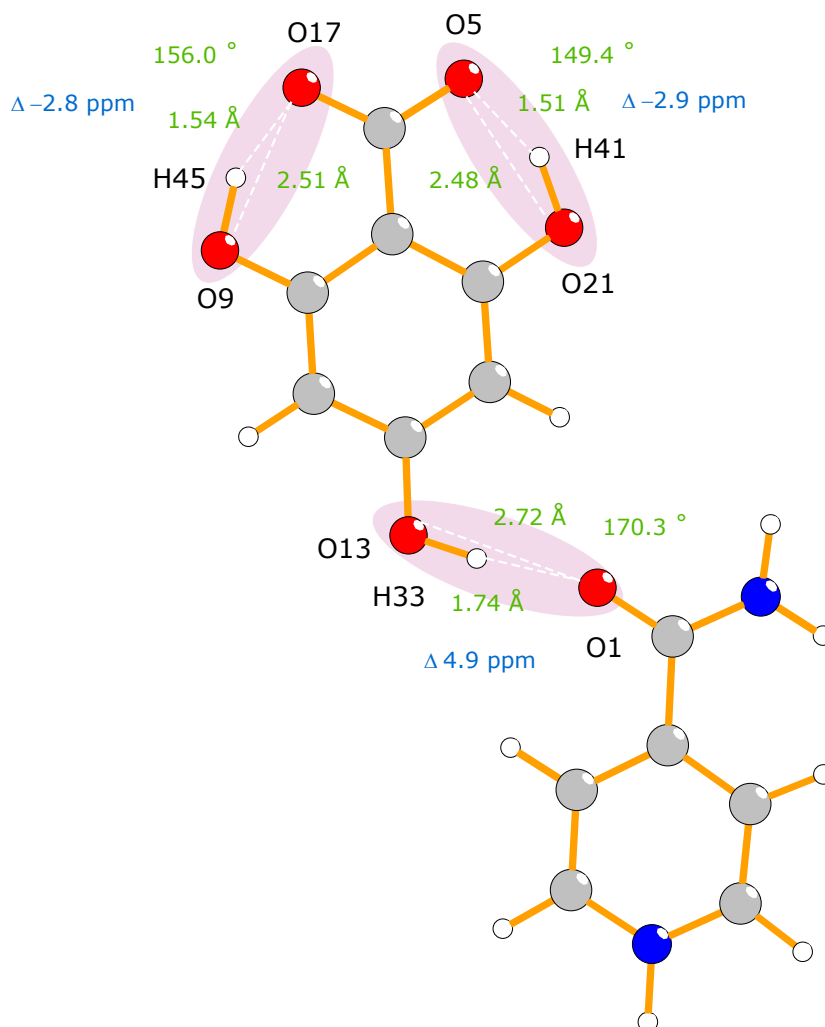


Figure 7.4: O-H...O hydrogen bonds in 1-NH⁺:2-COO⁻ which have a $\Delta\delta_{C-M}$ of magnitude greater than 2 ppm. $d(\text{H}\dots\text{Y})$, $d(\text{X}\dots\text{Y})$, $\angle\text{XHY}$ and $\Delta\delta_{C-M}$ calculated values are displayed for each hydrogen bond which can also be viewed in Table 7.2. Nitrogen, oxygen, carbon and hydrogen atoms are represented by the colours blue, red, grey and white, respectively.

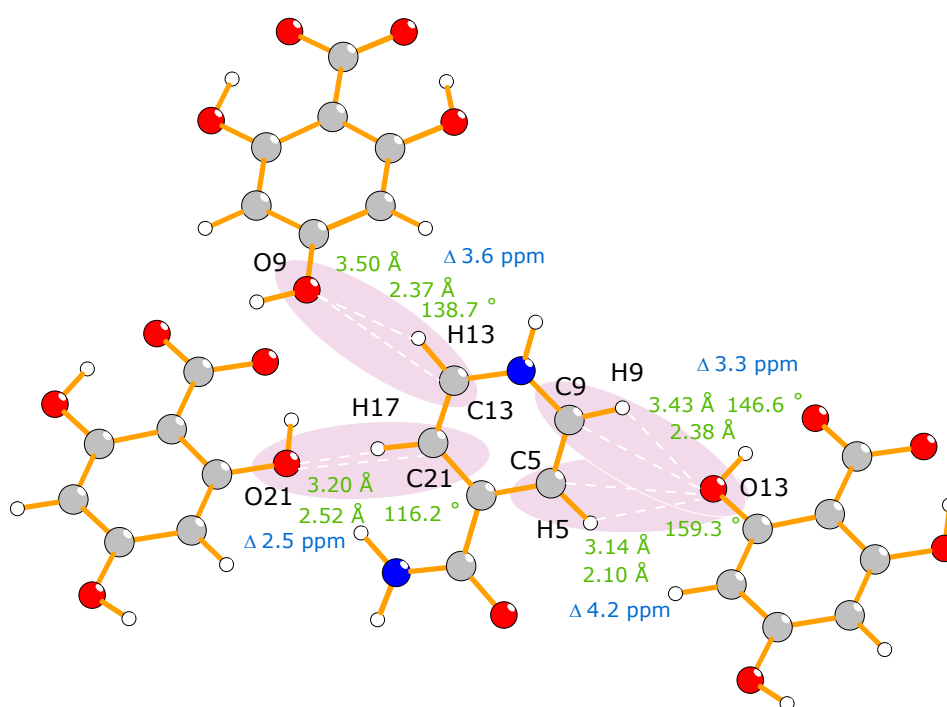


Figure 7.5: C-H...O hydrogen bonds in 1-NH⁺:2-COO⁻ which have a $\Delta\delta_{\text{C-M}}$ of greater than 2 ppm. $d(\text{H}\cdots\text{Y})$, $d(\text{X}\cdots\text{Y})$, $\angle\text{XHY}$ and $\Delta\delta_{\text{C-M}}$ calculated values are displayed for each hydrogen bond which can also be viewed in table 7.2. Nitrogen, oxygen, carbon and hydrogen atoms are represented by the colours blue, red, grey and white, respectively.

7.3. ^1H - ^1H DQ MAS NMR SPECTRA

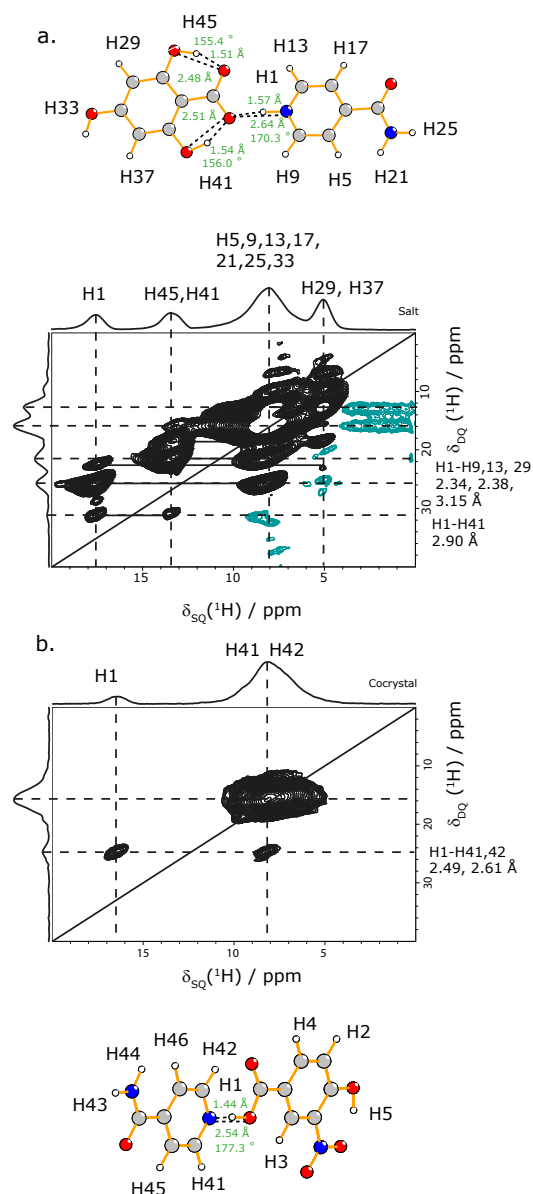


Figure 7.6: ^1H - ^1H DQ-SQ MAS NMR spectra with skyline projections of (a) 1-NH $^+$:2-COO $^-$ and (b) 1-N:3-COOH, recorded using 1 rotor period of BABA recoupling at a MAS frequency of (a) 60 and (b) 55 kHz. 16 transients were co-added for each of the 70 t_1 FIDs, corresponding to a total experiment time of 20 h. The base contour level is (a) 4% and (b) 9% of the maximum peak height. Nitrogen, oxygen, carbon and hydrogen atoms are represented by the colours blue, red, grey and white, respectively.

CHAPTER 7. PROTONATION IN PHARMACEUTICAL COMPOUNDS: ISONICOTINAMIDE SALT AND CO-CRYSTAL

The observation of a DQ MAS correlation is indicative of a ^1H - ^1H proximity under 3.5 to 4 Å as has been identified in the following references [53, 235] (see section text5.7 for more details).

The ^1H - ^1H DQ MAS NMR experiment allows ^1H - ^1H resonances to be probed upto 3.5 to 4 Å to be probed [53, 235]. The value of 3.5 Å was chosen as the cut-off in this thesis to indicate closer ^1H - ^1H proximities.

Figure 7.6a shows a ^1H - ^1H DQ MAS NMR spectra of 1-NH⁺:2-COO⁻ with skyline projections of 1-NH⁺:2-COO⁻ using 1 rotor period of BABA recoupling at a MAS frequency of 60 kHz. Figure 7.6b shows a ^1H - ^1H DQ MAS NMR spectra of 1-N:3-COOH with skyline projections of 1-N:3-COOH using 1 rotor period of BABA recoupling at a MAS frequency of 55 kHz.

As is obvious upon viewing figures 7.6a and 7.6b figure 7.6a is more "crowded" than in figure 7.6b. The "crowding" is due to the spectrum displaying more ^1H - ^1H proximities under 3.5 Å. The important proximities of both 1-NH⁺:2-COO⁻ and 1-N:3-COOH are shown to the right hand side of figure 7.6, next to the intensities in the spectra.

As the ^1H - ^1H DQ MAS NMR experiment involves the ^1H atom the ability to identify ^1H atoms involved in hydrogen bonds is possible as in the ^1H one pulse MAS NMR experiment discussed previously. Therefore, the H1 atom (the atom involved in the hydrogen bond in both the salt and cocrystal) the atom with the highest chemical shift is highlighted in figures 7.6a and 7.6b. This experiment is therefore able to show hydrogen atoms participating in hydrogen bonds (with chemical shifts generally above 10 ppm) and is also able to indicate other interactions (in this case ^1H - ^1H interactions) taking place in the local chemical environment of that hydrogen atom.

Figure 7.6a shows that H1 interacts with H9, H13, H29 and H41 (see figure 7.6a for the positions of H9, H13, H29 and H41 in 1-NH⁺:2-COO⁻) these interactions are shown by the peak intensities in the spectrum. The use of GIPAW calculations with the ^1H - ^1H DQ MAS NMR experiment is also able to provide distance information between the H1 atom and H9, H13, H29 and H41 with distances of 2.34, 2.38, 3.15 and 2.90 Å, respectively.

In figure 7.6b the spectrum is less crowded with less ^1H - ^1H proximities under 3.5 Å observed for 1-N:3-COOH. Here the H1 atom involved in the strong hydrogen bond of interest is also interacting with H41 and H42 with GIAPW indicating that these proximities are 2.49 and 2.61 Å.

The local chemical environment affects the chemical shift value of, for example, H1. Therefore, the DQ MAS experiment shows that besides the hydrogen bond interaction there are other interactions which contribute towards the chemical shift value of the atoms.

The subsequent tables show the power of using experiment (DQ MAS) and GIPAW data together as proximities between all hydrogen atoms in the samples are able to be provided. This can allow a pharmaceutical company/developer to gain an excellent structural picture of the chemical environments in those samples. This can then be used for example in studying atoms of interest, finding patterns in data and developing new drug products. Not only can the GIPAW data provide distance information but it also indicates whether the proximity is between an intra or intermolecular hydrogen atom. The distance information for 1-NH⁺:2-COO⁻ is shown in table 7.3 and distance information for 1-N:3-COOH is shown in table 7.3. As can be seen by the crowding of the spectra of figure 7.6a there are a lot more entries in table 7.3 than in table 7.3 due to the presence of more interactions than in figure 7.6b.

7.4 ^{14}N - ^1H HMQC MAS NMR spectra

Figure 7.7 presents 2D ^{14}N - ^1H HMQC spectra of (a) 1-NH⁺:2-COO⁻ and (b,c) 1-N:3-COOH for a τ_{RCPL} duration of (a) 160 μs (b) 133 μs and (c) 600 μs . For a short τ_{RCPL} duration, as in (a) and (b), usually only one-bond NH correlations are observed. For a τ_{RCPL} duration of 600 μs , one-bond and longer-range NH correlations are observed [68, 216].

Recoupling times were chosen to probe short range and long range correlations. All recoupling times are synchronised with the MAS frequency. As the recoupling times are rotor synchronised only specific values can be chosen. For probing long range correlations the chosen value was 600 μs as this value was deemed large enough to show the long range correlation in the samples chosen although other longer recoupling times could also have been used. In reference [236] for the samples of nicotinamide and nicotinamide palmitic acid cocrystal, spectra are shown for the recoupling time of 666.7 μs . Additionally, for the sample PVP-acetaminophen recoupling times of 533.3 μs , 400 μs and 666.7 μs , where the longer time reveals, like here, longer range (typically up to 2.5 Å) N...H proximities as well as one bond N-H connectivities.) The short recoupling times were chosen as at longer recoupling times other interactions would appear in the spectrum making the results less clear. Other recoupling times around the values chosen could also have been used.

Consider figure 7.7a corresponding to 1-NH⁺:2-COO⁻ with a short recoupling duration of 160 μs , where a strong correlation between the pyridine nitrogen atom (N1) and the directly bonded hydrogen atom (H1) can be observed with an intense peak at $\delta(^1\text{H}) = 17.6$ ppm and $\delta(^{14}\text{N}) = -94$ ppm. The distance N1-H1 is 1.08 Å. All ^{14}N - ^1H distances

CHAPTER 7. PROTONATION IN PHARMACEUTICAL COMPOUNDS: ISONICOTINAMIDE SALT AND CO-CRYSTAL

Table 7.3: ^1H - ^1H distances^a ($\angle 3.5 \text{ \AA}$) and SQ and DQ ^1H chemical shifts for the geometry-optimised (CASTEP) crystal structure of $1\text{-NH}^+;2\text{-COO}^-$.[†]

^1H Atom	$\delta_{SQ}(^1\text{H})$ / ppm	^1H Atom	Distance / \AA	$\delta_{DQ}(^1\text{H})$ / ppm
H1	17.6	H9	2.35	25.6
		H13	2.38	25.6
		<i>H41</i>	<i>2.90</i>	<i>30.9</i>
		<i>H29</i>	<i>3.15</i>	<i>22.6</i>
		<i>H33</i>	<i>3.41</i>	<i>22.6</i>
		<i>H37</i>	<i>3.43</i>	<i>22.6</i>
H5	8.0	H21	1.93	16.0
		<i>H41</i>	<i>2.45</i>	<i>21.3</i>
		H9	2.46	16.0
		<i>H45</i>	<i>3.02</i>	<i>21.3</i>
H9	8.0	<i>H29</i>	<i>2.31</i>	<i>13.0</i>
		H1	2.35	25.6
		H5	2.46	16.0
		<i>H33</i>	<i>3.20</i>	<i>13.0</i>
		<i>H29</i>	<i>3.36</i>	<i>13.0</i>
		H13	2.38	25.6
H13	8.0	H17	2.50	16.0
		<i>H45</i>	<i>2.66</i>	<i>21.3</i>
		<i>H25</i>	<i>2.83</i>	<i>16.0</i>
		<i>H21</i>	<i>2.93</i>	<i>16.0</i>
		<i>H25</i>	<i>3.36</i>	<i>16.0</i>
		<i>H37</i>	<i>3.46</i>	<i>13.0</i>
		H17	2.50	16.0
		<i>H33</i>	<i>2.65</i>	<i>13.0</i>
H17	8.0	<i>H29</i>	<i>2.97</i>	<i>13.0</i>
		<i>H45</i>	<i>3.26</i>	<i>21.3</i>
		<i>H37</i>	<i>3.47</i>	<i>13.0</i>
		H25	1.73	16.0
		H5	1.93	16.0
H21	8.0	<i>H41</i>	<i>2.65</i>	<i>21.3</i>
		<i>H37</i>	<i>2.92</i>	<i>13.0</i>
		<i>H13</i>	<i>2.93</i>	<i>16.0</i>
		H21	1.73	16.0
		<i>H45</i>	<i>2.39</i>	<i>21.3</i>
H25	8.0	<i>H13</i>	<i>2.83</i>	<i>16.0</i>
		<i>H37</i>	<i>3.29</i>	<i>13.0</i>
		<i>H13</i>	<i>3.36</i>	<i>16.0</i>
		<i>H37</i>	<i>3.45</i>	<i>13.0</i>

[†]Intermolecular distances are shown in italics.

7.4. ^{14}N - ^1H HMQC MAS NMR SPECTRA

Table 7.3: Continuation of table 7.3.

^1H Atom	$\delta_{SQ}(^1\text{H})$ / ppm	^1H Atom	Distance / Å	$\delta_{DQ}(^1\text{H})$ / ppm
H29	5.0	<i>H9</i>	<i>2.31</i>	<i>13.0</i>
		<i>H41</i>	<i>2.94</i>	<i>18.3</i>
		<i>H17</i>	<i>2.97</i>	<i>13.0</i>
		<i>H1</i>	<i>3.15</i>	<i>22.6</i>
		<i>H9</i>	<i>3.36</i>	<i>13.0</i>
H33	8.0	<i>H37</i>	<i>2.27</i>	<i>13.0</i>
		<i>H17</i>	<i>2.65</i>	<i>16.0</i>
		<i>H9</i>	<i>3.20</i>	<i>16.0</i>
		<i>H41</i>	<i>3.33</i>	<i>21.3</i>
		<i>H1</i>	<i>3.41</i>	<i>25.6</i>
H37	5.0	<i>H33</i>	<i>2.27</i>	<i>10.0</i>
		<i>H21</i>	<i>2.92</i>	<i>13.0</i>
		<i>H25</i>	<i>3.29</i>	<i>13.0</i>
		<i>H1</i>	<i>3.43</i>	<i>22.6</i>
		<i>H25</i>	<i>3.45</i>	<i>13.0</i>
		<i>H13</i>	<i>3.46</i>	<i>13.0</i>
		<i>H45</i>	<i>3.47</i>	<i>18.3</i>
		<i>H17</i>	<i>3.47</i>	<i>13.0</i>
		<i>H5</i>	<i>2.45</i>	<i>21.3</i>
H41	13.3	<i>H21</i>	<i>2.65</i>	<i>21.3</i>
		<i>H1</i>	<i>2.90</i>	<i>30.9</i>
		<i>H29</i>	<i>2.94</i>	<i>18.3</i>
		<i>H33</i>	<i>3.33</i>	<i>18.3</i>
		<i>H25</i>	<i>2.39</i>	<i>21.3</i>
H45	13.3	<i>H13</i>	<i>2.66</i>	<i>21.3</i>
		<i>H5</i>	<i>3.02</i>	<i>21.3</i>
		<i>H17</i>	<i>3.26</i>	<i>21.3</i>
		<i>H37</i>	<i>3.47</i>	<i>18.3</i>

CHAPTER 7. PROTONATION IN PHARMACEUTICAL COMPOUNDS: ISONICOTINAMIDE SALT AND CO-CRYSTAL

Table 7.4: ^1H - ^1H distances ($< 3.5 \text{ \AA}$) and SQ and DQ ^1H chemical shifts for the geometry-optimised (CASTEP) crystal structure of 1-N:3-COOH.[†]

^1H Atom	$\delta_{SQ}(^1\text{H}) / \text{ppm}$	^1H Atom	Distance / \AA	$\delta_{DQ}(^1\text{H}) / \text{ppm}$
H1	15.6	<i>H42</i>	<i>2.49</i>	<i>23.5</i>
		<i>H41</i>	<i>2.61</i>	<i>23.8</i>
		<i>H3</i>	<i>3.19</i>	<i>23.6</i>
		H3	3.45	23.6
H2	11.7	H4	2.45	19.3
H3	8.0	<i>H1</i>	<i>3.19</i>	<i>23.6</i>
		H1	3.45	23.6
H4	7.6	H2	2.45	19.3
H41	8.2	H45	2.53	15.2
		<i>H1</i>	<i>2.61</i>	<i>23.8</i>
H42	7.9	<i>H1</i>	<i>2.49</i>	<i>23.5</i>
		H46	2.51	15.5
		<i>H44</i>	<i>3.48</i>	<i>16.2</i>
H43	8.9	H44	1.77	17.6
H44	8.3	H43	1.77	17.6
		H46	2.01	15.9
		<i>H42</i>	<i>3.48</i>	<i>16.2</i>
H45	7.0	H41	2.53	15.2
H46	7.6	H44	2.01	15.9
		H42	2.51	15.5

[†]Intermolecular distances are shown in italics.

7.4. ^{14}N - ^1H HMQC MAS NMR SPECTRA

under 2.5 \AA are listed in table 7.5. A less intense peak is also observed for the NH_2 (N5) nitrogen atom to the directly bonded hydrogen atoms of H21 and H25 with distances of 1.02 \AA in both cases. These are all directly bonded and note the absence of longer range correlations between nitrogen atoms and hydrogen atoms due to the short τ_{RCPL} duration of $160 \mu\text{s}$ used in the experiment.

Consider figure 7.7b that shows a spectrum of 1-N:3-COOH in which a short τ_{RCPL} duration of $133 \mu\text{s}$ was used. A correlation can be observed for the NH_2 (N10) nitrogen and the directly bonded protons (H43 and H44). The one-bond distances to H43 and H44 from N10 are 1.03 and 1.02 \AA , respectively (see table 7.5). Once more note the absence of other longer range correlations in figure 7.7b.

Consider figure 7.7c that presents a ^{14}N - ^1H spectrum for 1-N:3-COOH for a τ_{RCPL} duration of $600 \mu\text{s}$. A correlation can be observed as in figure 7.7b for the NH_2 (N10) nitrogen and the directly bonded protons (H43 and H44), but additionally a correlation is observed between pyridine (N9) and the carboxylic acid hydrogen in 4-hydroxy-3-nitrobenzoic acid (H1). This is an intermolecular hydrogen bond ($\text{O1-H1}\dots\text{N9}$) where the N9-H1 distance is 1.44 \AA .

Table 7.5: N-H distances upto (2.5 \AA) and ^{14}N and ^1H NMR shifts for 1-NH $^+$:2-COO $^-$ and 1-N:3-COOH. ^a

^{14}N Atom	$\delta(^{14}\text{N})_{\text{calc}}^b$	$\delta(^{14}\text{N})_{\text{expt}}$	^1H Atom	$\delta(^1\text{H})_{\text{expt}}$	$\delta(^1\text{H})_{\text{calc}}$	^1H - ^{14}N Distance / \AA
N1 (NH $^+$)	-93.0	-90	H1	17.6	16.8	1.1
			H13	8.0	7.9	2.1
			H9	8.0	7.6	2.1
N5 (NH $_2$)	47.5	35	H25	8.0	7.9	1.0
			H21	8.0	8.8	1.0
N1 (NO $_2$)	37.6	-30	H5	8.3	11.7	2.3
N9 (N...H)	445.2	435	H1	16.6	17.8	1.4
			H42	8.3	7.9	2.1
			H41	8.3	8.2	2.1
N10 (NH $_2$)	-6	-12	H44	8.3	8.3	1.0
			H43	8.3	8.9	1.0

^a δ_{iso} is calculated using equation $\delta(^{15}\text{N})_{\text{expt}} + \delta_{\text{ISO}}^Q(^{14}\text{N})_{\text{calc}}$ for a (^{14}N) of 43.3 MHz

Figure 7.7 shows that the ^{14}N - ^1H HMQC experiment allows the proximity of a directly bonded proton to a nitrogen environment to be observed, thus indicating whether the

CHAPTER 7. PROTONATION IN PHARMACEUTICAL COMPOUNDS: ISONICOTINAMIDE SALT AND CO-CRYSTAL

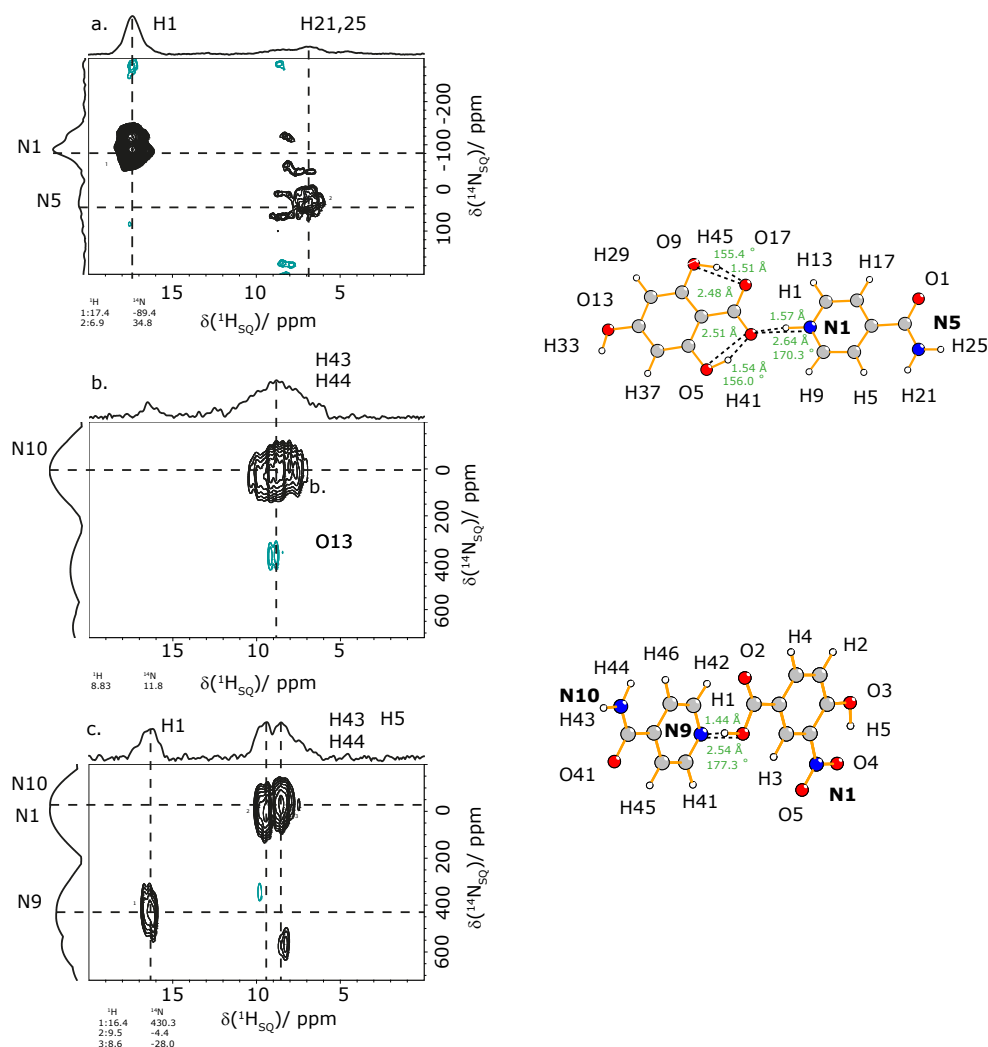


Figure 7.7: ^{14}N - ^1H (600 MHz) - HMQC MAS (60 kHz) spectra recorded using $n = 2$ rotary resonance recoupling for (a) 1-NH $^+$:2-COO $^-$ and (b, c) 1-N:3-COOH for a τ_{RCPL} duration of (a) 160 μs , (b) 133 μs and (c) 600 μs . 36 (a) and 16 (b,c) transients were coadded for each of 74 (a) and 80 (b,c) t_1 FIDs, corresponding to a total experimental time of 26 h (a), 22 h (b) and 18 h (c). The base contour level is at 14 % (a), 51% (b) and 53% (c) of the maximum peak height. Nitrogen, oxygen, carbon and hydrogen atoms are represented by the colours blue, red, grey and white, respectively.

sample is a salt or co-crystal. There is a subtle change from a salt to co-crystal as indicated by the N-H distances in table 7.5 with the directly bonded NH^+ having a distance of 1.43 Å in the salt compared to the N of 1.53 Å in the co-crystal. The difference between the two is that the geometry surrounding the nitrogen site becomes more symmetric in the salt form. Figure 7.7a is for 1- NH^+ :2- COO^- , which contains a hydrogen atom directly bonded to a nitrogen atom. When a similar recoupling time is used to probe one-bond proximities between the same nitrogen environment (N...H) in 1-N:3-COOH, where the nitrogen atom of interest in pyridine (N9) is not directly bonded to a hydrogen atom, a peak is not visible (figure 7.7b). Only when a recoupling time which probes longer range correlations is used (here 600 μs) does the N9 proximity to the carboxylic acid hydrogen H1 become visible in figure 7.7c (N9-H1). The low intensity at $\delta(^{14}\text{N}) \sim 550$ ppm and $\delta(^1\text{H}) \sim 9$ ppm is a small artefact peak.

Of particular interest is the large difference in $\delta(^{14}\text{N})$ shifts between the co-crystal and the salt upon protonation of the nitrogen atom, $\delta(^{14}\text{N}_{\text{calc}})$, see table 7.5. The $\delta(^{14}\text{N}_{\text{calc}})$ shift changes by 530.3 ppm upon protonation from 445.2 (co-crystal) to -93.0 (salt) ppm. This is a more noticeable change than was presented in figure 7 of reference [161] where the co-crystal to salt chemical shift changed by -68.8 ppm upon protonation using ^{15}N CP MAS data. Therefore, the ^{14}N shift is a very clear indicator of protonation of a nitrogen site, noting that reference [171] also shows such changes in the compounds of nicotinamide and nicotinamide palmitic acid co-crystal.

Table 7.6 presents calculated quadrupolar parameters as well as experimental ^{14}N shifts for both the salt and co-crystal. It is evident that the protonation of the nitrogen site causes the P_Q value changes from -3.7 MHz in the co-crystal to -1.3 MHz in the salt. This is due to the site becoming more symmetric in the salt form when directly bonded to the extra hydrogen atom and the P_Q value alters as a result. This leads to the noticeable change in the $\delta(^{14}\text{N})_{\text{calc}}$ shift discussed above, with the P_Q value also clearly indicating whether protonation has occurred.

Table 7.6: A comparison of experimental and GIPAW calculated ^{15}N isotropic chemical shifts and ^{14}N quadrupolar parameters and shifts for 1- $\text{NH}^+:\text{COO}^-$ and 1-N:3-COOH.

Material	N Atom	Chemistry	$\delta_{iso}(^{15}\text{N})_{calc}$	$\delta_{iso}(^{15}\text{N})_{expt}^*$	η_Q^\dagger	C_Q /MHz	P_Q^\ddagger /MHz	δ_{ISO}^Q ** /ppm (<i>calc</i>)	$\delta(^{14}\text{N})_{calc}$ / ppm ††	$\delta(^{14}\text{N})_{expt}$ / ppm
$\text{NH}^+:\text{COO}^-$	1	NH^+	-167.3	-166.0	0.3	-1.4	-1.4	73.0	-93.0	-90
$\text{NH}^+:\text{COO}^-$	5	NH_2	-266.0	-275.0	0.3	-2.9	-3.0	322.5	47.5	35
N:COOH	1	NO_2	-18.4	-11.6	0.5	-1.1	-1.1	49.2	37.6	-12
N:COOH	9	N...H	-99.0	-97.9	0.3	-3.9	-4.0	543.0	445.2	435
N:COOH	10	NH_2	-264.9	-275.7	0.4	-2.6	-2.6	269.7	-6.0	-30

* Experimental data obtained from reference [161]

† see equation 4.141 in chapter 4

‡ see equation 4.162 in chapter 4

** see equation 4.112 in chapter 4

$^{\dagger\dagger} \delta(^{14}\text{N})_{calc} = \delta(^{15}\text{N})_{expt}^a + \delta_{ISO}^Q(^{14}\text{N})_{calc}$

7.5 Conclusion

Figure 7.3 with its corresponding table (table 7.1) highlights some of the main findings of the research conducted in this chapter. Both figures 7.3a (1-NH⁺:COO⁻) and 7.3b (1-N:3-COOH) show experimental chemical shifts alongside corresponding GIPAW calculated chemical shifts. The use of the calculated shifts allows the assignment, for example, of any unresolved peaks in the spectrum. This can be seen in figure 7.3a, for example, where there is an intense unresolved peak at around 6-10 ppm. This intense peak represents a number of different chemical environments which experiment alone cannot determine. However, with the aid of calculated chemical shifts the local chemical environments "hidden" in experiment are able to be revealed.

A key area of the research conducted focused on identifying and probing hydrogen bonds. The ¹H chemical shift is a sensitive probe of hydrogen bonding interactions with protons involved in hydrogen bonds typically having a chemical shift greater than 10 ppm. Generally, the "stronger" the hydrogen bond the greater the chemical shift. This enables the identification of the "strongest" hydrogen bonds in a compound. In figure 7.3a the proton with the highest chemical shift was identified as being the hydrogen atom with the H1 label, which from the accompanying molecular representation shows that H1 is indeed participating in a hydrogen bond and that it is the focus of the research i.e. identifying proton transfer.

So-called "isolated molecule" calculations (which effectively removes all intermolecular interactions) were utilised in the research. Figures 7.3a and 7.3b show visually the benefits of using such calculations in NMR crystallography (isolated structures identified by the green and blue stick representations). For example, figure 7.3a is able to clearly identify that the hydrogen atoms of H41 and H45 participate in intramolecular interactions. Table 7.1 then presents the calculated difference between the so-called isolated molecule calculations and the full crystal structure, showing the change in chemical shift which results from a lattice structure. The greatest change between so-called isolated molecule calculations and the full crystal structure ($\Delta\delta_{C-M}$) is for the H1 atom with a change of 12.8 ppm.

Figure 7.3b, for the compound of 1-N:3-COOH, identified the largest $\Delta\delta_{C-M}$ also as being for the H1 atom which a change of 9.8 ppm. At this stage of the investigation it is clear that it is the H1 atom which is the area of interest for the identification of a salt or a cocrystal with it participating in the "strongest" hydrogen bonding interaction in the two compounds (verified experimentally and by calculation) and having the greatest $\Delta\delta_{C-M}$.

CHAPTER 7. PROTONATION IN PHARMACEUTICAL COMPOUNDS: ISONICOTINAMIDE SALT AND CO-CRYSTAL

Using calculations with experiments allows specific hydrogen bonding parameters to be identified notably $d(\text{H}\dots\text{Y})$, $d(\text{X}\dots\text{Y})$, $\angle\text{XHY}$ (see table 7.2). This allows so-called "weak" hydrogen bonds, of the form $\text{C-H}\dots\text{O}$, to be identified, as shown in figure 7.5. Previous studies which have investigated $\text{C-H}\dots\text{O}$ bonds identified the $\Delta\delta_{\text{C-M}}$ being in the range of 2.0 to 2.2 ppm. However, the research presented here identified values greater than 2.2 ppm with values of 4.2, 3.3, 3.6 and 2.5 being found for $1\text{-NH}^+:\text{COO}^-$. There were no such hydrogen bonds found in 1-N:3-COOH .

Figure 7.7 with accompanying table 7.5 shows that a salt $1\text{-NH}^+:\text{COO}^-$ is able to be identified from a cocrystal 1-N:3-COOH . Using a ^{14}N - ^1H (600 MHz) - HMQC MAS experiment which takes advantage of the sensitivity of the hydrogen atom and the quadrupolar nature of the ^{14}N nuclear isotope. A hydrogen atom involved in protonation where the ^{14}N and the ^1H are ionically bound will have a shorter distance between them than a hydrogen atom involved in a cocrystal where the ^{14}N and the ^1H are non-ionically bound. The interactions involving H1 in the salt and cocrystal are (able to be represented in figure 7.7 due to GIPAW calculations) shown by $\text{N-H}\dots\text{O}$ and $\text{O-H}\dots\text{N}$ hydrogen bonds respectively. The N-H distance in $1\text{-NH}^+:\text{COO}^-$ was shown to be 1.08 Å whereas the $\text{H}\dots\text{N}$ distance in 1-N:3-COOH was shown to be 1.44 Å. It is this difference in distance that is able to be differentiated by the ^{14}N - ^1H (600 MHz) - HMQC MAS experiment and determine the salt from the cocrystal.

There were two main findings of the ^{14}N - ^1H (600 MHz) - HMQC MAS experiment: the significant change in the experimental ^{14}N shift upon protonation and the ability of the experiment to identify directly bound ^{14}N - ^1H interactions in comparison to ^{14}N - ^1H interactions at a much greater distance.

Firstly, the ^{14}N - ^1H (600 MHz) - HMQC MAS experiment is able to select recoupling times which enable only very close interactions (i.e. those directly bonded) to be measured. This was shown in figure 7.7b with 1-N:3-COOH where a short recoupling time of 133 μs was used to identify only directly bound N-H distances. Note that longer range interactions, involving N9 are absent from the spectrum. Figure 7.7c then uses a larger recoupling time which enables short and long range ^{14}N - ^1H interactions to be identified. The short-range interactions involving N10 and the longer range interactions involving N9 are present in the spectrum. The fact that figure 7.7b shows that the $\text{H1}\dots\text{N9}$ interaction is not directly bound indicates that the sample was a cocrystal. As figure 7.7a showed that the N1-H1 interaction was a directly bound one, this shows that the sample was a salt.

Secondly, the $\delta(^{14}\text{N}_{\text{calc}})$ shift changes by 580.2 ppm upon protonation from 445.2 (cocrystal) to -93.0 (salt) ppm. Where the experimental shift was found to change by 525

7.5. CONCLUSION

ppm. This is a more noticeable change than was presented in figure 7 of reference [161] where the co-crystal to salt chemical shift changed by -68.8 ppm upon protonation using ^{15}N CP MAS data. Therefore, the ^{14}N shift is a very clear indicator of protonation of a nitrogen site.

**CHAPTER 7. PROTONATION IN PHARMACEUTICAL
COMPOUNDS: ISONICOTINAMIDE SALT AND CO-CRYSTAL**

Determining Protonation in Pharmaceutical Compounds using NMR Crystallography: A Bipyridine Salt and Co-crystal

8.1 Introduction

This chapter considers 4,4'-bipyridine-5-sulfosalicylic acid ($4\text{-NH}^+ : 5\text{-SO}_3^-$) and 4,4'-bipyridine/phthalic acid ($4\text{-N} : 6\text{-COOH}$). Here the 4,4'-bipyridine molecule is present in both cases while the acid molecule changes: $4\text{-N} : 6\text{-COOH}$ (co-crystal) contains a neutral pyridine N group, while the nitrogen is protonated in $4\text{-NH}^+ : 5\text{-SO}_3^-$ (salt) see figure 8.1. As for the isonicotinamide systems in the previous chapter, both cases have $Z' = 1$. The crystal structures of $4\text{-NH}^+ : 5\text{-SO}_3^-$ and $4\text{-N} : 6\text{-COOH}$ were obtained from the CSD: refcodes DUBFEN [215] and SUXVOW [224], respectively.

Experimental results (1D ^1H one-pulse MAS NMR, ^1H - ^1H DQ MAS NMR and 2D ^{14}N - ^1H HMQC) are shown alongside NMR parameters calculated using the GIPAW method as implemented in the CASTEP software [69–71].

8.2 One-dimensional ^1H MAS NMR Spectra

One pulse ^1H MAS NMR spectra of $4\text{-NH}^+ : 5\text{-COO}^-$ and $4\text{-N} : 6\text{-COOH}$ are presented in figure 8.3a and figure 8.3b. As mentioned previously hydrogen atoms which have a chemical shift greater than ~ 10 ppm are involved in hydrogen bonding interactions

CHAPTER 8. PROTONATION IN PHARMACEUTICAL COMPOUNDS: BIPYRIDINE SALT AND CO-CRYSTAL

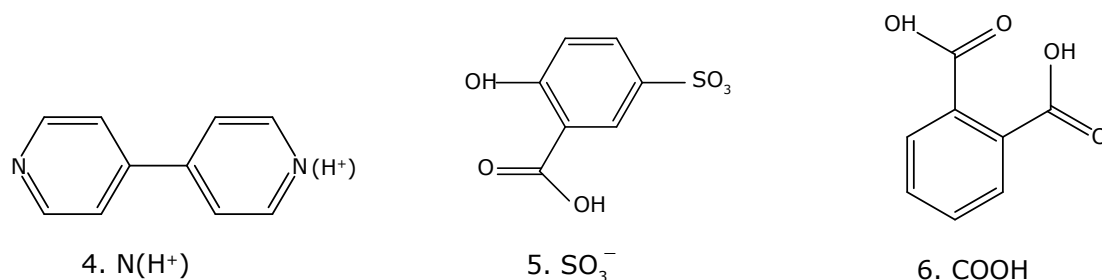


Figure 8.1: Molecular structures for 4,4'-bipyridine5-sulfosalicylic acid (4-NH⁺:5-SO₃⁻) and 4,4'-bipyridine/phthalic acid (4-N:6-COOH).

where higher chemical shifts result from a stronger hydrogen bond. Figure 8.3a shows that the hydrogen atoms H4 (carboxylic acid), H23 (NH) and H5 have a high chemical shift, thus indicating that these atoms will be part of a hydrogen bond, with H4 having the strongest interaction due to its higher chemical shift. Note that in figure 8.3 there is a peak at 3 ppm that is due to an impurity.

The bipyridine systems that are considered in this chapter are different from the isonicotinamide systems presented in the previous chapter in respect to the molecular symmetry that is exhibited. Figure 8.4 indicates the symmetry that is present in 4-N:6-COOH, whereby both constituent molecules contain mirror-plane symmetry. This is also observed in figure 8.3b where it can be seen that there are two hydrogen atom labels for each calculated line for the full crystal molecule since the chemical shift values for these atoms are identical. 4-NH⁺:5-COO⁻, however, does not contain this degree of symmetry as phthalic acid is replaced with 4,4'-bipyridine5-sulfosalicylic acid and one of the pyridine nitrogen atoms in 4,4'-bipyridine molecule becomes protonated thus removing the symmetry. Of particular interest in the bipyridine system is how the protonated and un-protonated pyridine nitrogen atoms in 4-NH⁺:5-COO⁻ interact with the hydrogen atoms around them.

Consider first the H4 carboxylic acid hydrogen atom of 4-NH⁺:5-COO⁻, as this has the highest chemical shift, thus indicating that this forms the strongest hydrogen bond with a pyridine nitrogen atom O4-H4...N1. Table 8.1 shows that this corresponds to a $d(\text{H}\dots\text{Y})$ of 1.43 Å, $d(\text{X}\dots\text{Y})$ of 2.53 Å and $\angle \text{XHY}$ of 170.5°. The experimental chemical shift is 17.8 ppm, while the calculated value is 18.9 ppm. In 4-N:6-COOH, a similar hydrogen bond forms between a hydrogen atom from the carboxylic group of the acid and the nitrogen atom of the pyridine molecule, of the form O9/O10-H17/H18...N1. Table 8.1 presents the hydrogen bond values for H17/H18 with a $d(\text{H}\dots\text{Y})$ of 1.53 Å, $d(\text{X}\dots\text{Y})$ of

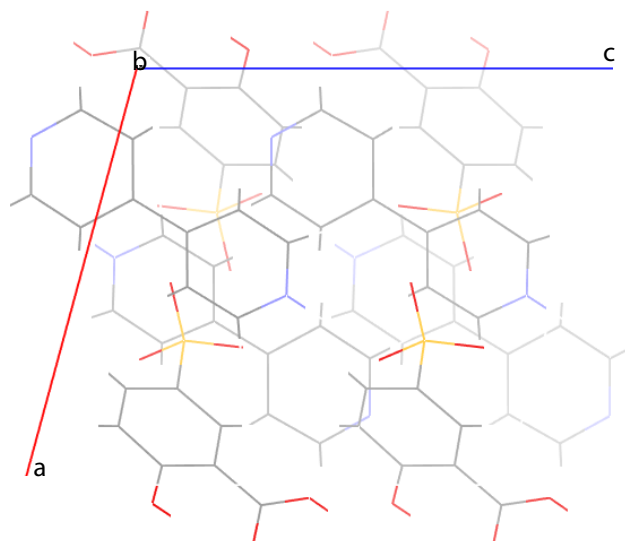


Figure 8.2: Molecular packing for the CSD (DUBFEN) structure of 4,4-bipyridine5-sulfosalicylic acid ($4\text{-NH}^+ : 5\text{-SO}_3^-$).

2.59 Å and $\angle \text{XHY}$ of 174.0. As figure 8.3b shows, the experimental chemical shift is at 15.5 ppm with a calculated value of 16.5 ppm. This indicates that the H17/H18 hydrogen atom in 4-N:6-COOH has a chemical shift value that is slightly less than that of the H4 hydrogen atom in $4\text{-NH}^+ : 5\text{-COO}^-$, this is consistent with the $d(\text{H}\dots\text{Y})$ distance being 0.10 Å shorter in $4\text{-NH}^+ : 5\text{-COO}^-$ as compared to in 4-N:6-COOH , although the bond angle is 170.5 ° compared to 174.0 ° in 4-N:6-COOH .

Figure 8.3a shows that the H23 hydrogen atom has the second strongest hydrogen bond interaction with an experimental chemical shift of 15.5 ppm and a calculated value of 15.3 ppm, roughly 2.5 ppm less than that of the H4 hydrogen atom. The difference between these hydrogen bonds is that H4 forms a $\text{O-H}\dots\text{N}$ hydrogen bond with the un-protonated pyridine nitrogen atom of 4,4'-bipyridine, while H23 forms a $\text{N-H}\dots\text{O}$ hydrogen bond $\text{N2-H23}\dots\text{O5}$, where O5 oxygen atom is directly bonded to the Sulphur atom. Table 8.1 shows that both $d(\text{H}\dots\text{Y})$ and $d(\text{X}\dots\text{Y})$ are longer for the latter $\text{N2-H23}\dots\text{O5}$ hydrogen bond.

Figure 8.3 additionally highlights a difference between the $4\text{-NH}^+ : 5\text{-COO}^-$ and 4-N:6-COOH molecules in regard to hydrogen atoms involved in $\text{CH}\dots\text{O}$ weak hydrogen bonding. In figure 8.3b which displays a ^1H spectrum of 4-N:6-COOH , all isolated and full crystal structure calculated values occur above 5 ppm, whereas figure 8.3a shows that, in

CHAPTER 8. PROTONATION IN PHARMACEUTICAL COMPOUNDS: BIPYRIDINE SALT AND CO-CRYSTAL

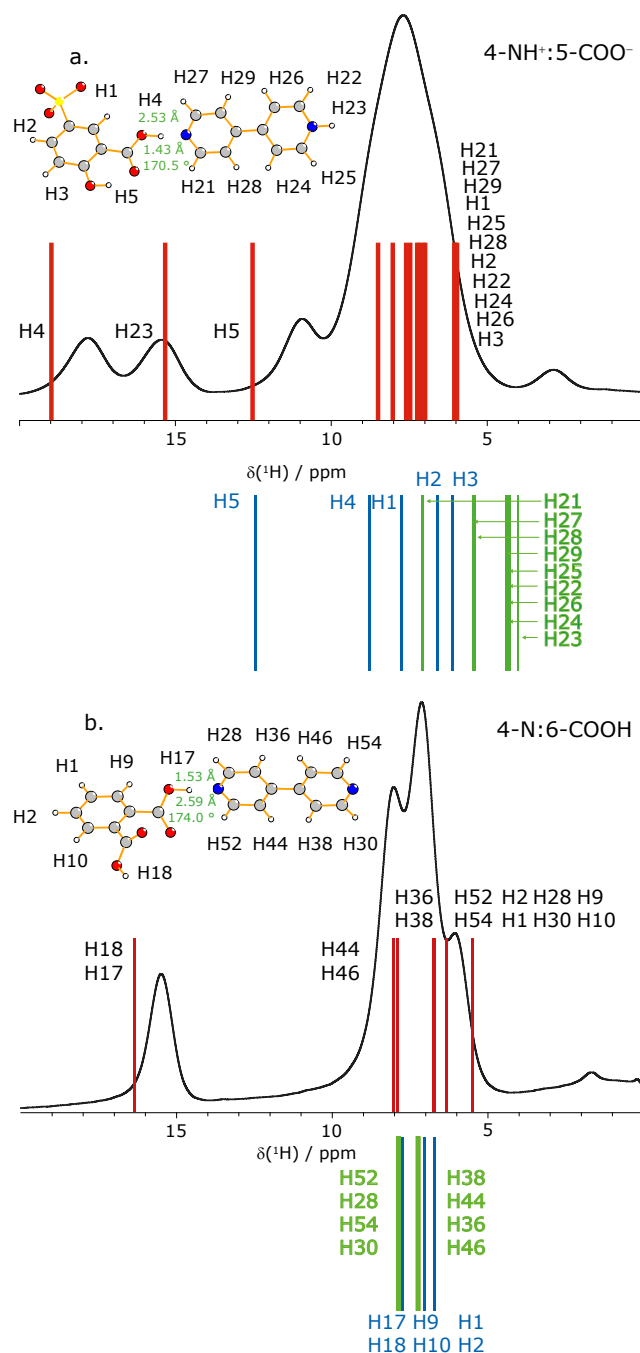


Figure 8.3: ^1H (600 MHz) one-pulse MAS NMR spectra of (a) 4-NH⁺:5-COO⁻ and (b) 4-N:6-COOH. The experimental spectra (black lines) are compared to stick representations of calculated (GIPAW) ^1H chemical shifts for the full crystal structure (red) and isolated acid (blue) and 4,4'-bipyridine molecules (green). 256 transients were co-added in both cases. Sulfur, nitrogen, oxygen, carbon and hydrogen atoms are represented by the colours yellow, blue, red, grey and white, respectively.

8.3. ^1H - ^1H DQ MAS NMR SPECTRA

the salt, the majority of the hydrogen atoms in the 4,4'-bipyridine molecule in the isolated molecule are below 5 ppm, as can be seen in table 8.2. However, while in the co-crystal, the hydrogen atoms in the 4,4'-bipyridine molecule change by roughly 1 ppm (table 8.2), in the salt the change is more significant especially involving the hydrogen atoms of H22, H25 and H29, for which weak hydrogen bonding interactions are highlighted in figure 8.5. The chemical shift value of each of these atoms changes by greater than 2 ppm for $\Delta\delta_{C-M}$ (see table 8.3), that indicates that intermolecular interactions are taking place. The interactions that are occurring are C-H...O hydrogen bonding interactions taking place with oxygen atoms of the 4,4-bipyridine5-sulfosalicylic acid molecule. The largest change occurs for the hydrogen atom of H25 where the change is 2.8 ppm resulting from a $d(\text{H}\dots\text{Y})$ value of 2.18 Å, a $d(\text{X}\dots\text{Y})$ value of 3.21 Å and a $\angle\text{XHY}$ value of 157.7°.

Table 8.1: Hydrogen-bond distances and geometry for cases where $\Delta\delta_{C-M}$ has magnitude greater than 2 ppm for 4-NH⁺:5-COO⁻ and 4-N:6-COOH.

H Atom	Hydrogen bond	$d(\text{H}\dots\text{Y})$ / Å	$d(\text{X}\dots\text{Y})$ / Å	$\angle\text{XHY}$ /°	δ_{iso}^{calc} /ppm (full crystal)	$\Delta\delta_{C-M}$ /ppm
4-NH ⁺ :5-COO ⁻						
4	O4-H4...N1	1.43	2.53	170.5	18.9	10.2
22	C34-H22...O3	2.31	3.13	130.5	7.0	2.6
23	N2-H23...O5	1.56	2.64	178.0	15.3	11.2
25	C33-H25...O2	2.18	3.21	157.7	7.3	2.8
29	C36-H29...O1	2.40	3.46	165.2	7.6	2.2
4-N:6-COOH						
17	O9-H17...N1	1.53	2.59	174.0	16.5	8.9
18	O9-H17...N1	1.53	2.59	174.0	16.5	8.9

8.3 ^1H - ^1H DQ MAS NMR Spectra

Figure 8.6 presents ^1H - ^1H DQ-SQ MAS 2D NMR spectra of (a) 4-NH⁺:5-COO⁻ and (b) 4-N:6-COOH together with views of the asymmetric unit cell showing intermolecular hydrogen bonding interactions for the carboxylic acid OH. Cross peaks correspond to H-H proximities closer than 3.5 Å (see tables 8.3 and 8.4). In figure 8.6a for 4-NH⁺:5-COO⁻, cross peaks due to a proximity between H4 and H23 and hydrogen atoms in the aromatic region are observed. As stated in figure 8.6b, the closest aromatic proton to the COOH (H17/H18) is H54 at a distance of 2.62 Å in 4-N:6-COOH. In addition, a H4-H5

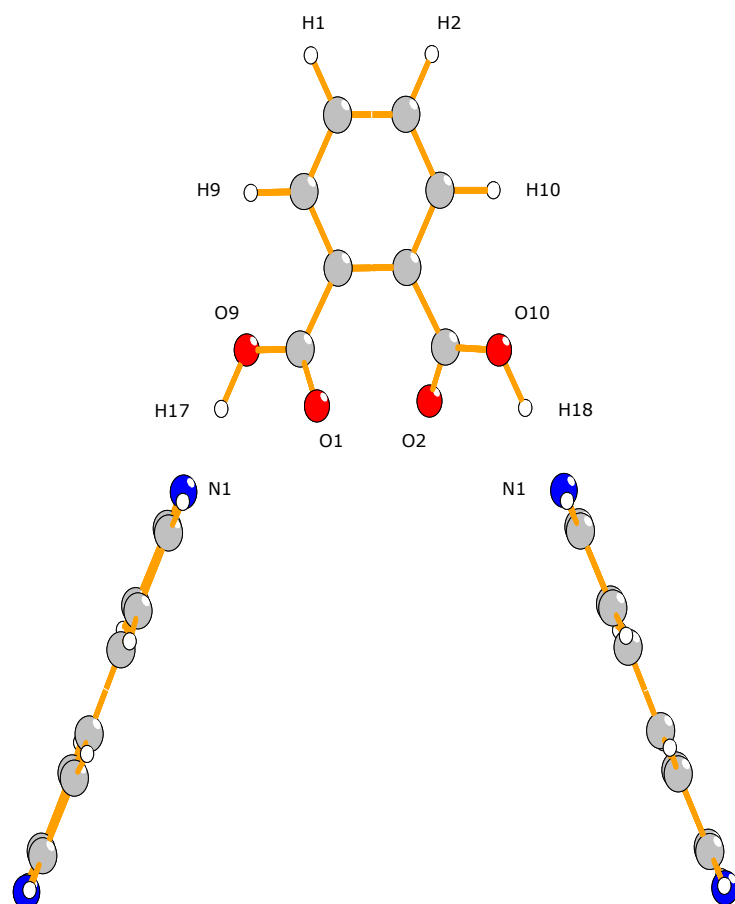


Figure 8.4: A representation of the crystal structure of 4-N:6-COOH showing the mirror symmetry of the phthalic acid and bipyridine molecules, whereby the symmetric H17 and H18 carboxylic acid hydrogen atoms of phthalic acid form hydrogen bonds with the pyridine nitrogen atom in the 4,4'-bipyridine molecule. Sulfur, nitrogen, oxygen, carbon and hydrogen atoms are represented by the colours yellow, blue, red, grey and white, respectively.

8.3. ^1H - ^1H DQ MAS NMR SPECTRA

Table 8.2: Experimental and GIPAW calculated ^1H chemical shifts (in ppm) for 4-NH⁺:5-COO⁻ and 4-N:6-COOH.[†]

Atom label	$\delta_{iso}(\text{expt})$	Calculated		
		$\delta_{iso}(\text{cryst})$	$\delta_{iso}(\text{molc})$	$\Delta\delta_{C-M}$
4-NH ⁺ :5-COO ⁻				
H1	7.7	7.5	7.8	-0.3
H2	7.7	7.1	6.6	0.5
H3	2.9	6.0	6.1	-0.1
H4	17.8	18.9	8.8	10.1
H5	10.9	12.5	12.4	0.1
H21	7.7	8.5	7.1	1.4
H22	7.7	7.0	4.4	2.6
H23	15.5	15.3	4.1	11.3
H24	24.9	6.1	4.3	1.7
H25	7.7	7.3	4.5	2.8
H26	24.9	6.1	4.3	1.7
H27	7.7	8.0	7.1	0.9
H28	7.7	7.2	5.5	1.7
H29	7.7	7.6	5.4	2.2
4-N:6-COOH				
H1	7.2	6.6	6.6	0.0
H2	7.2	6.6	6.6	0.0
H9	6.0	5.4	6.9	-1.5
H10	6.0	5.4	6.9	-1.5
H17	15.5	16.5	7.6	8.9
H18	15.5	16.5	7.6	8.9
H28	7.2	6.2	7.8	-1.6
H30	7.2	6.2	7.8	-1.6
H36	8.0	7.9	7.2	0.7
H38	8.0	7.9	7.2	0.7
H44	8.0	8.0	7.2	0.8
H46	8.0	8.0	7.2	0.8
H52	7.2	6.7	7.8	-1.1
H54	7.2	6.7	7.8	-1.1

[†]Calculated using $\delta = \sigma_{ref} - \sigma_{calc}$, where $\sigma_{ref} = 30.0$ ppm.

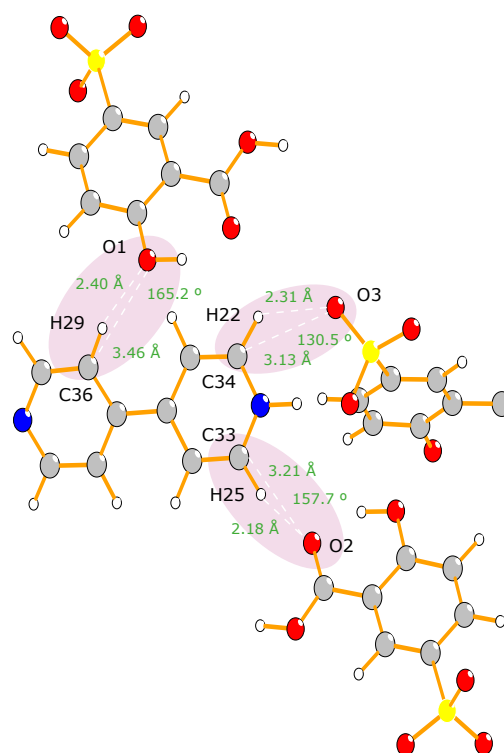


Figure 8.5: C-H...O bonds for 4-NH⁺:5-COO⁻ which have a $\Delta\delta_{C-M}$ of > 2 ppm (see table 8.1). Sulfur, nitrogen, oxygen, carbon and hydrogen atoms are represented by the colours yellow, blue, red, grey and white, respectively.

8.3. ^1H - ^1H DQ MAS NMR SPECTRA

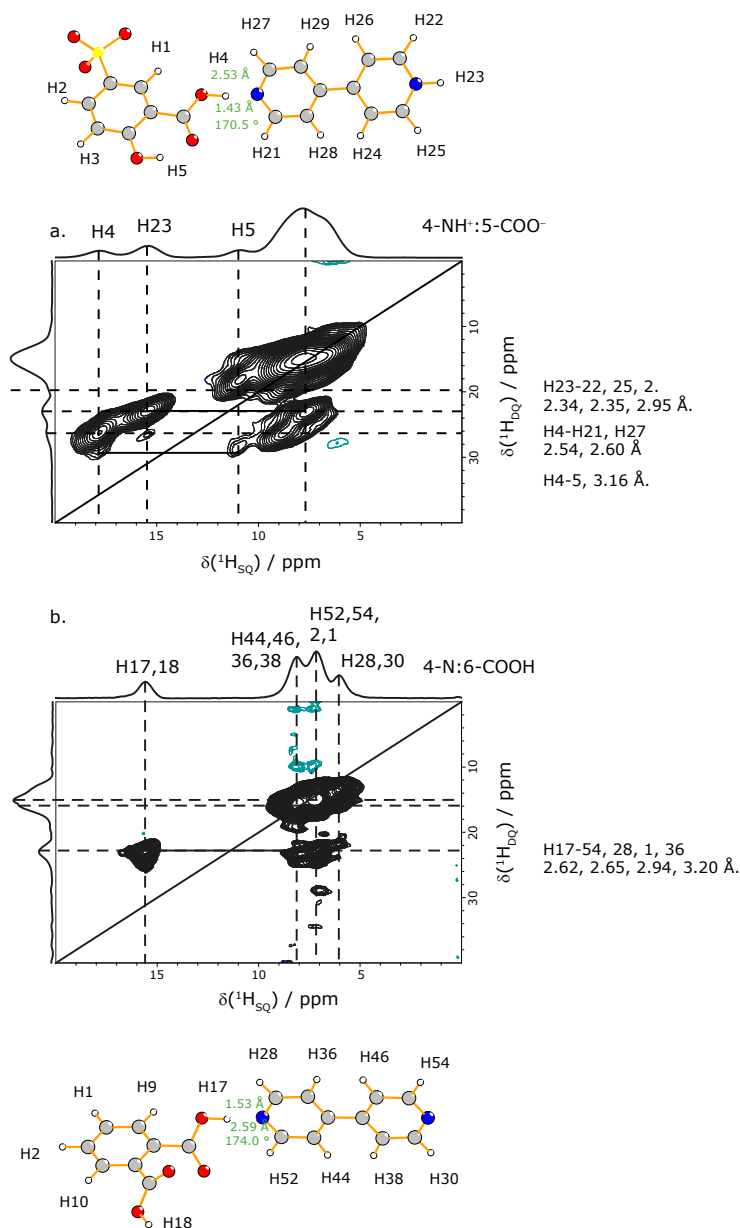


Figure 8.6: ^1H - ^1H (600 MHz) DQ-SQ MAS spectra with skyline projections of (a) 4-NH⁺:5-COO⁻ and (b) 4-N:6-COOH, recorded using 1 period of BABA recoupling at a MAS frequency of 60 kHz. 16 transients were co-added for each of the 70 t_1 FIDs, corresponding to a total experiment time of 20 h. The base contour level is (a) 2% and (b) 5% of the maximum peak height. Sulfur, nitrogen, oxygen, carbon and hydrogen atoms are represented by the colours yellow, blue, red, grey and white, respectively.

CHAPTER 8. PROTONATION IN PHARMACEUTICAL COMPOUNDS: BIPYRIDINE SALT AND CO-CRYSTAL

cross peak is observed due to an intermolecular proximity with ^1H - ^1H distances shown to the right of the observed cross peak in figure 8.6.

The observation of a DQ MAS correlation is indicative of a ^1H - ^1H proximity under 3.5 to 4 Å as been identified in the following references [53, 235].

The ^1H - ^1H DQ MAS NMR experiment allows ^1H - ^1H resonances to be probed upto 3.5 to 4 Å to be probed [53, 235]. The value of 3.5 Å was chosen as the cut-off in this thesis to indicate closer ^1H - ^1H proximities.

Figure 8.6a (re-phased) shows a ^1H - ^1H DQ MAS NMR spectra of 4-NH⁺:5-COO⁻ with skyline projections of 4-NH⁺:5-COO⁻ using 1 rotor period of BABA recoupling at a MAS frequency of 60 kHz. Figure 7.6b (re-phased) shows a ^1H - ^1H DQ MAS NMR spectra of 4-N:6-COOH with skyline projections of 4-N:6-COOH using 1 rotor period of BABA recoupling at a MAS frequency of 60 kHz.

As the ^1H - ^1H DQ MAS NMR experiment involves the ^1H atom the ability to identify ^1H atoms involved in hydrogen bonds is possible as in the ^1H one pulse MAS NMR experiment discussed previously. The important proximities (in respect to the focus of this thesis) of both 4-NH⁺:5-COO⁻ and 4-N:6-COOH are shown to the right hand side of figure 8.6, next to the intensities in the spectra. This experiment is therefore able to show hydrogen atoms participating in hydrogen bonds (with chemical shifts generally above 10 ppm) and is also able to indicate other interactions (in this case ^1H - ^1H interactions) taking place in the local chemical environment of that hydrogen atom.

The H4 atom in 4-NH⁺:5-COO⁻ is the atom involved in the hydrogen bond of interest (i.e. protonation). The H4 atom participating in the hydrogen bond is represented by the molecules above the spectrum in figure 8.6a where the key hydrogen bond parameters are presented. The spectrum of figure 8.6a shows that the H4 atom is indeed involved in a hydrogen bond by having a high chemical shift value above 10 ppm. The spectrum of figure 8.6a also shows that H4 is in close proximity to other hydrogen atoms. The use of GIPAW calculations with the ^1H - ^1H DQ MAS NMR experiment is also able to provide distance information. The hydrogen atoms in close proximity to H4 are shown by the peak intensities in the spectrum with distance information provided to the right hand side of the spectrum. It can therefore be deduced that H4 is in close proximity to H23-22, H25, H2, H21, H27 and H5 with corresponding distances of 2.34, 2.35, 2.95, 2.54, 2.60 and 3.16 Å. It can also be seen upon viewing the representation of 4-NH⁺:5-COO⁻ above figure 8.6a that the interactions involving H4 comprise of both intra and intermolecular interactions. For example, the H4-H21 interaction is an intermolecular interaction as the H21 atom is situated on a different molecule to H4. Whereas the H4-H5 interaction is an intramolecular interaction as the H5 atom is situated on the same molecule.

In figure 8.6b the H17/H18 atom involved in the strong hydrogen bond of interest is also interacting with H54, H28, H1 and H36 with GIPAW indicating that these proximities are 2.62, 2.65, 2.94 and 3.20 Å respectively. The DQ MAS experiment, therefore, is able to show that besides the hydrogen bond interaction there are other interactions which contribute towards the chemical shift value.

The subsequent tables show the power of using experiment (DQ MAS) and GIPAW data together as proximities between all hydrogen atoms in the samples are able to be provided. This can allow a pharmaceutical company/developer to gain an excellent structural picture of the chemical environments in those samples. This can then be used for example in studying atoms of interest, finding patterns in data and developing new drug products. Not only can the GIPAW data provide distance information but it also indicates whether the proximities is between an intra or intermolecular hydrogen atom. The distance information for 4-NH⁺:5-COO⁻ is shown in table 8.3 and distance information for 4-N:6-COOH is shown in table 8.3.

8.4 ^{14}N - ^1H HMQC MAS NMR Spectra

Figure 8.7a presents a 2D ^{14}N - ^1H HMQC spectrum of 4-NH⁺:5-COO⁻ recorded with a τ_{RCPL} duration of 133 μs . For such a short duration, the strongest cross peak is due to a one-bond correlation specifically between the nitrogen atom N2 and H23, i.e. a cross peak at a shift of -115 ppm in the $^{14}\text{N}_{\text{SQ}}$ dimension and 15.3 ppm (calc) (15.5 ppm (expt)) in the $^1\text{H}_{\text{SQ}}$ dimension, for a bond length of 1.08 Å (see table 8.5).

Figure 8.7b presents a ^{14}N - ^1H spectrum obtained for 4-NH⁺:5-COO⁻ with a τ_{RCPL} duration of 600 μs which allows cross peaks due to longer range ^{14}N - ^1H proximities to be observed. The N2-H23 correlation can be seen as in figure 8.7a along with the longer range correlation of N2-H22 and N2-H25 which has a distance of 2.06 Å and 2.08 Å (table 8.5) and a shift of -115 ppm in the $^{14}\text{N}_{\text{SQ}}$ dimension and 7.0 ppm and 7.3 ppm in the $^1\text{H}_{\text{SQ}}$ dimension, respectively. Additionally, interactions involving the un-protonated nitrogen atom (N1) can be seen: N1-H4 which has a distance of 1.43 Å and N1-H27 and N1-H21 with a distance of 2.07 and 2.08 Å with a shift of 366 ($\delta(^{14}\text{N})_{\text{expt}}$) ppm in the $^{14}\text{N}_{\text{SQ}}$ dimension and 8.0 and 8.5 ppm in the $^1\text{H}_{\text{SQ}}$ dimension, respectively.

As 4-N:6-COOH does not contain any directly bonded hydrogen atoms to the nitrogen site, a longer recoupling time is used to observe the N1-H17/18 interaction which is part of the hydrogen bond O9-H17...N1 noted in figure 8.7. At short recoupling times comparable to that in figure 8.7a, this interaction would not be observable as the N1-H17/18 is 1.53

CHAPTER 8. PROTONATION IN PHARMACEUTICAL COMPOUNDS: BIPYRIDINE SALT AND CO-CRYSTAL

Table 8.3: ^1H - ^1H distances^a ($< 3.5 \text{ \AA}$) and SQ and DQ ^1H chemical shifts for the geometry-optimised crystal structure of $4\text{-NH}^+ : 5\text{-COO}^-$.[†]

^1H Atom	$\delta_{\text{SQ}}(^1\text{H}) / \text{ppm}$	^1H Atom	Distance / \AA	$\delta_{\text{DQ}}(^1\text{H}) / \text{ppm}$
<i>H1</i>	<i>7.7</i>	<i>H2</i>	<i>2.28</i>	<i>15.4</i>
		<i>H3</i>	<i>2.58</i>	<i>10.6</i>
		<i>H27</i>	<i>2.62</i>	<i>15.4</i>
		<i>H29</i>	<i>3.41</i>	<i>15.4</i>
		H4	3.45	25.5
<i>H2</i>	<i>7.7</i>	<i>H1</i>	<i>2.28</i>	<i>15.4</i>
		<i>H28</i>	<i>2.33</i>	<i>15.4</i>
		H3	2.45	10.6
		<i>H23</i>	<i>2.95</i>	<i>23.2</i>
		<i>H24</i>	<i>3.19</i>	<i>32.6</i>
H3	2.9	H2	2.45	10.6
		<i>H29</i>	<i>2.53</i>	<i>10.6</i>
		<i>H1</i>	<i>2.58</i>	<i>10.6</i>
		<i>H27</i>	<i>2.93</i>	<i>10.6</i>
		<i>H27</i>	<i>3.14</i>	<i>10.6</i>
		<i>H29</i>	<i>3.26</i>	<i>10.6</i>
		<i>H24</i>	<i>3.32</i>	<i>27.8</i>
H4	17.8	H21	2.54	25.5
		<i>H27</i>	<i>2.60</i>	<i>25.5</i>
		<i>H26</i>	<i>3.06</i>	<i>42.7</i>
		<i>H5</i>	<i>3.16</i>	<i>28.7</i>
		H1	3.45	25.5
		<i>H25</i>	<i>3.48</i>	<i>25.5</i>
<i>H5</i>	<i>10.9</i>	<i>H26</i>	<i>2.80</i>	<i>35.8</i>
		<i>H25</i>	<i>3.08</i>	<i>18.6</i>
		<i>H29</i>	<i>3.12</i>	<i>18.6</i>
		<i>H4</i>	<i>3.16</i>	<i>28.7</i>
		<i>H27</i>	<i>3.26</i>	<i>18.6</i>
		<i>H23</i>	<i>3.33</i>	<i>26.4</i>
		<i>H22</i>	<i>3.39</i>	<i>18.6</i>
H21	7.7	H28	2.46	15.4
		<i>H4</i>	<i>2.54</i>	<i>25.5</i>
		<i>H24</i>	<i>2.78</i>	<i>32.6</i>
		<i>H26</i>	<i>2.87</i>	<i>32.6</i>
		<i>H25</i>	<i>3.06</i>	<i>15.4</i>
		<i>H22</i>	<i>3.28</i>	<i>15.4</i>
H22	7.7	H23	2.34	23.2
		H26	2.53	32.6
		<i>H25</i>	<i>3.21</i>	<i>15.4</i>
		<i>H28</i>	<i>3.23</i>	<i>15.4</i>
		<i>H21</i>	<i>3.28</i>	<i>15.4</i>
		<i>H5</i>	<i>3.39</i>	<i>18.6</i>

[†]Intermolecular distances are shown in italics.

8.4. ^{14}N - ^1H HMQC MAS NMR SPECTRA

Table 8.3: Continuation of table 8.3.[†]

^1H Atom	$\delta_{SQ}(^1\text{H})$ / ppm	^1H Atom	Distance Å	$\delta_{DQ}(^1\text{H})$ / ppm
H23	15.5	H22	2.34	23.2
		H25	2.35	23.2
		<i>H2</i>	<i>2.95</i>	<i>23.2</i>
		<i>H5</i>	<i>3.33</i>	<i>26.4</i>
		<i>H23</i>	<i>3.35</i>	<i>31.0</i>
H24	24.9	H28	2.30	32.6
		H25	2.52	32.6
		<i>H21</i>	<i>2.78</i>	<i>32.6</i>
		<i>H28</i>	<i>2.88</i>	<i>32.6</i>
		<i>H2</i>	<i>3.19</i>	<i>32.6</i>
H25	7.7	<i>H3</i>	<i>3.32</i>	<i>27.8</i>
		H23	2.35	23.2
		H24	2.52	32.6
		<i>H21</i>	<i>3.06</i>	<i>15.4</i>
		<i>H5</i>	<i>3.08</i>	<i>18.6</i>
H26	24.9	<i>H22</i>	<i>3.21</i>	<i>15.4</i>
		<i>H4</i>	<i>3.48</i>	<i>25.5</i>
		H29	2.31	32.6
		H22	2.53	32.6
		<i>H5</i>	<i>2.80</i>	<i>35.8</i>
H27	7.7	<i>H21</i>	<i>2.87</i>	<i>32.6</i>
		<i>H4</i>	<i>3.06</i>	<i>42.7</i>
		H29	2.51	15.4
		<i>H4</i>	<i>2.60</i>	<i>25.5</i>
		<i>H1</i>	<i>2.62</i>	<i>15.4</i>
H28	7.7	<i>H3</i>	<i>2.93</i>	<i>10.6</i>
		<i>H29</i>	<i>3.02</i>	<i>15.4</i>
		<i>H3</i>	<i>2.93</i>	<i>10.6</i>
		<i>H5</i>	<i>3.26</i>	<i>18.6</i>
		H24	2.30	32.6
H29	7.7	<i>H2</i>	<i>2.33</i>	<i>15.4</i>
		<i>H21</i>	<i>2.46</i>	<i>15.4</i>
		<i>H24</i>	<i>2.88</i>	<i>32.6</i>
		<i>H22</i>	<i>3.23</i>	<i>15.4</i>
		H26	2.31	32.6
		H27	2.51	15.4
		<i>H3</i>	<i>2.53</i>	<i>10.6</i>
		<i>H27</i>	<i>3.02</i>	<i>15.4</i>
		<i>H5</i>	<i>3.12</i>	<i>18.6</i>
		<i>H3</i>	<i>3.26</i>	<i>10.6</i>
		<i>H1</i>	<i>3.41</i>	<i>15.4</i>

[†]Intermolecular distances are shown in italics.

CHAPTER 8. PROTONATION IN PHARMACEUTICAL COMPOUNDS: BIPYRIDINE SALT AND CO-CRYSTAL

Table 8.4: ^1H - ^1H distances^a (< 3.5 Å) and SQ and DQ ^1H chemical shifts for the geometry-optimised (GIPAW) crystal structure of 4-N:6-COOH.[†]

^1H Atom	$\delta_{SQ}(^1\text{H})$ / ppm	^1H Atom	Distance / Å	$\delta_{DQ}(^1\text{H})$ / ppm
H1	7.2	H1	2.47	14.4
		H9	2.50	13.2
		<i>H46</i>	<i>2.90</i>	<i>15.2</i>
		<i>H17</i>	<i>2.94</i>	<i>22.7</i>
		<i>H54</i>	<i>3.03</i>	<i>14.4</i>
		<i>H46</i>	<i>3.09</i>	<i>15.2</i>
		<i>H54</i>	<i>3.19</i>	<i>14.4</i>
H9	6.0	H1	2.50	13.2
		<i>H28</i>	<i>3.00</i>	<i>12.2</i>
		<i>H54</i>	<i>3.01</i>	<i>13.2</i>
		<i>H46</i>	<i>3.09</i>	<i>14.0</i>
H17	15.5	H54	2.62	22.7
		<i>H28</i>	<i>2.65</i>	<i>21.7</i>
		<i>H1</i>	<i>2.94</i>	<i>22.7</i>
		<i>H36</i>	<i>3.20</i>	<i>23.5</i>
H28	6.2	H36	2.46	14.2
		<i>H17</i>	<i>2.65</i>	<i>21.7</i>
		<i>H9</i>	<i>3.00</i>	<i>12.2</i>
H36	8.0	H46	1.99	16.0
		H28	2.46	14.2
		<i>H17</i>	<i>3.20</i>	<i>23.5</i>
H46	8.0	H36	1.99	16.0
		H54	2.46	15.2
		<i>H1</i>	<i>2.90</i>	<i>15.2</i>
		<i>H9</i>	<i>3.09</i>	<i>14.0</i>
		<i>H1</i>	<i>3.09</i>	<i>15.2</i>
H54	7.2	H46	2.46	15.2
		<i>H17</i>	<i>2.62</i>	<i>22.7</i>
		<i>H9</i>	<i>3.01</i>	<i>7.2</i>
		<i>H1</i>	<i>3.03</i>	<i>14.4</i>
		<i>H1</i>	<i>3.19</i>	<i>14.4</i>

[†]Intermolecular distances are shown in italics.

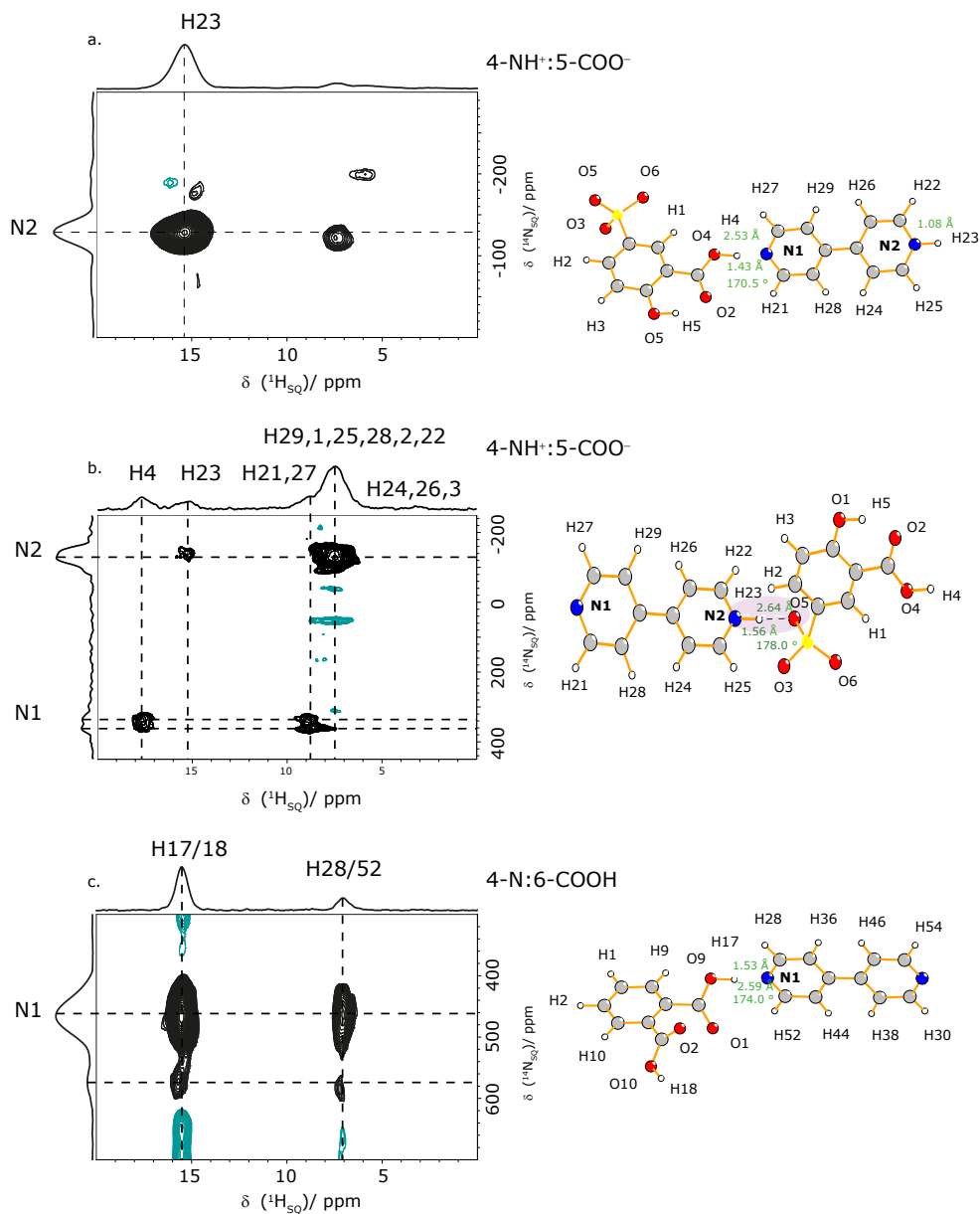


Figure 8.7: ^{14}N - ^1H (600 MHz) - HMQC MAS (60 kHz) NMR spectra recorded using $n = 2$ rotary resonance recoupling for (a,b) 4-NH $^+$:5-COO $^-$ and (c) 4-N:6-COOH for a τ_{RCPL} duration of (a) 133 μs , (b) 600 μs and (c) 400 μs . 16 (a,b,c) transients were coadded for each of the 70 (a,c) and 90 (b) t_1 FIDs, corresponding to a total experiment time of 12 h (a,c) and 24 h (b). The base contour level is 2% (a), 4% (b) and 17% (c) of the maximum peak height. Sulfur, nitrogen, oxygen, carbon and hydrogen atoms are represented by the colours yellow, blue, red, grey and white, respectively.

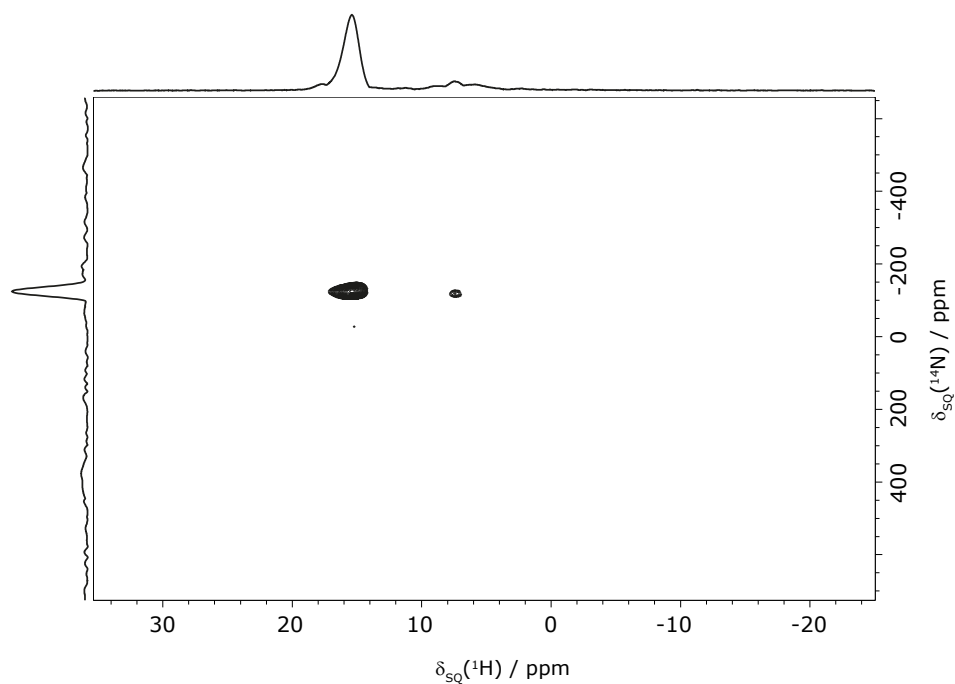


Figure 8.8: ^{14}N - ^1H (600 MHz) - HMQC MAS (60 kHz) spectra recorded using $n = 2$ rotary resonance recoupling for $4\text{-NH}^+;5\text{-COO}^-$ for a τ_{RCPL} duration of $133 \mu\text{s}$. 16 transients were coadded for each of the 70 t_1 FIDs, corresponding to a total experiment time of 12 h . The base contour level is 2% of the maximum peak height.

8.4. ^{14}N - ^1H HMQC MAS NMR SPECTRA

Table 8.5: N-H distances upto (2.5 Å) and experimental and GIPAW calculated ^{14}N and ^1H NMR shifts (in ppm) for 4-NH⁺:5-COO⁻ and 4-N:6-COOH.

^{14}N Atom	$\delta(^{14}\text{N})_{\text{calc}}^\dagger$	$\delta(^{14}\text{N})_{\text{expt}}$	^1H Atom	$\delta(^1\text{H})_{\text{expt}}$	$\delta(^1\text{H})_{\text{calc}}$	^1H - ^{14}N distance / Å
4-NH ⁺ :5-COO ⁻						
N1 (NH ⁺)	408.4	366	H4	17.8	18.9	1.43
			H27	7.7	8.0	2.07
			H21	7.7	8.5	2.08
N2 (NH)	-107.8	-123	H23	15.5	15.3	1.08
			H22	7.7	7.0	2.06
			H25	7.7	7.3	2.08
4-N:6-COOH						
N1 (N)	491.1	465	H17	15.5	16.5	1.53
			H52	7.2	6.7	2.07
			H28	7.2	6.2	2.08

[†]Calculated using $\delta(^{15}\text{N})_{\text{expt}} + \delta_{\text{ISO}}^Q(^{14}\text{N})_{\text{calc}}$ for a ω_0 (^{14}N) of 43.3 MHz.

Å. Additionally, N1-H28 and N1-H52 cross peaks due to the intramolecular proximities are observed in figure 8.7c.

Figure 8.7c and tables 8.5 and 8.6 show that the 4-N:6-COOH ^{14}N shift is 464 ppm experimentally with the calculated value (achieved using a calculated value of the ^{15}N chemical shift) being 434 ppm, while the 4-NH⁺:5-COO⁻ $\delta^{14}\text{N}$ shift is -130 ppm experimentally with the calculated value being -115 ppm. The difference between the ^{14}N chemical shift from the 4-N:6-COOH to 4-NH⁺:5-COO⁻ is 593 ppm experimentally and 548 ppm calculated. When compared with 1-NH⁺:2-COO⁻ and 1-N:3-COOH described in the previous chapter, this again shows a big difference in the ^{14}N shift upon protonation of the nitrogen site. No peaks to N1 are seen in the short recoupling time spectrum, as is evident from figure 8.8 where the full ^{14}N spectral range is shown.

Table 8.6 shows that the P_Q value (MHz) changes from -3.6 MHz in the 4-N:6-COOH to -1.2 MHz in the 4-NH⁺:5-COO⁻. These values are comparable to the P_Q values of 1-NH⁺:2-COO⁻ and 1-N:3-COOH in the previous chapter, where the P_Q values changed from -3.7 MHz in 1-N:3-COOH to -1.3 MHz in 1-NH⁺:2-COO⁻. This is again due to the site becoming more symmetric. The values may be similar as both systems involved a pyridine nitrogen atom.

Table 8.6: A comparison of experimental and GIPAW calculated ^{15}N isotropic chemical shifts and ^{14}N shifts for 4-NH $^+$:5-COO $^-$ and 4-N:6-COOH.

Material	N Atom	Chemistry	$\delta_{iso}(^{15}\text{N})_{calc}$	η_Q^\dagger	C_Q /MHz	P_Q^\ddagger /MHz	δ_{ISO}^Q ** /ppm (<i>calc</i>)	$\delta(^{14}\text{N})_{calc}$ / ppm ††	$\delta(^{14}\text{N})_{expt}$ / ppm
4-NH $^+$:5-COO $^-$	1	NH $^+$	-105.1	0.3	-3.5	-3.4	513.5	408.4	366
4-NH $^+$:5-COO $^-$	2	NH	-172.9	0.6	-1.2	-1.2	65.1	-107.8	-123
4-N:6-COOH	4	NH $^+$	-92.6	0.3	-3.8	-3.6	583.7	491.1	465
4-N:6-COOH	6	NH $^+$	-92.6	0.3	-3.8	-3.6	583.7	491.1	465

† see equation 4.141 in chapter 4

‡ see equation 4.162 in chapter 4

**see equation 4.112 in chapter 4

$^{\dagger\dagger}\delta(^{14}\text{N})_{calc} = \delta(^{15}\text{N})_{expt}^a + \delta_{ISO}^Q(^{14}\text{N})_{calc}$

8.5 Conclusion

The main findings of the techniques used in this thesis were first described in the conclusion section of chapter 7 whereby the main benefits of using so-called isolated molecule GIPAW chemical shift calculations and the 2D ^{14}N - ^1H HMQC experiment were explained. The investigation in this chapter extends the range of investigated compounds: $4\text{-NH}^+;5\text{-COO}^-$ and $4\text{-N};6\text{-COOH}$.

Of particular interest with the compounds studied in this chapter was the symmetrical nature of the cocrystal ($4\text{-N};6\text{-COOH}$). The mirror symmetry of the phthalic acid and bipyridene molecules where the symmetric H17 and H18 carboxylic acid hydrogen atoms of phthalic acid form hydrogen bonds with the pyridine nitrogen atom in the 4,4'-bipyridine molecule can be seen in figure 8.4. The symmetry of the molecule can also be identified in figure 8.3b whereby the calculated (GIPAW) spectrum (red lines) represent two chemical shift values where the chemical shift value of one atom is exactly the same as that of its mirror form. For example, H17 and H18: the carboxylic acid hydrogen atoms of phthalic acid are mirror copies of each other and have exactly the same chemical shift value. Having the same chemical shift value means that both H17 and H18 experience exactly the same local chemical environment.

Figure 8.3 with accompanying table 8.2 identifies the hydrogen atoms of interest in the salt ($4\text{-NH}^+;5\text{-COO}^-$) and cocrystal ($4\text{-N};6\text{-COOH}$), H4 and H17/H18 respectively. These represent the hydrogen atoms which have the greatest experimental and calculated chemical shifts: 17.8 ppm and 18.9 ppm respectively for $4\text{-NH}^+;5\text{-COO}^-$ and 15.5 ppm and 16.5 ppm respectively for $4\text{-N};6\text{-COOH}$.

The isolated molecule calculations additionally indicated that there was an intramolecular hydrogen bond in $4\text{-NH}^+;5\text{-COO}^-$ involving H5. The chemical shift of all other atoms in $4\text{-NH}^+;5\text{-COO}^-$ was found to move to a higher value in the full crystal structure. The $\Delta\delta_{C-M}$ for H4 in $4\text{-NH}^+;5\text{-COO}^-$ was found to be 10.2 ppm and 8.9 ppm for $4\text{-N};6\text{-COOH}$. As in chapter 7, there were also some "weak" hydrogen bonds identified of the form: C-H...O, as shown in table 8.1. These also had a relatively high $\Delta\delta_{C-M}$ as compared to previous studies with values of 2.6 ppm (C34-H22...O3), 2.8 ppm (C33-H25...O2) and 2.2 ppm (C36-H29...O1). Again, no "weak" hydrogen bonds were found in the cocrystal.

The ^1H - ^1H DQ MAS NMR experiment was important as it allowed close proximities between ^1H - ^1H atoms (<3.5 Å) to be identified. Table 8.3, for example, is able to identify 6 hydrogen atoms that are in close proximity to H4. The closest intramolecular interaction was found to be to H21 with a distance of 2.54 ppm whereas the closest

CHAPTER 8. PROTONATION IN PHARMACEUTICAL COMPOUNDS: BIPYRIDINE SALT AND CO-CRYSTAL

intermolecular interaction was with H27 with a distance of 2.60 ppm. GIPAW data therefore provides distances between ^1H - ^1H interactions and identifies whether it is an intramolecular or intermolecular interaction. This provides a wealth of information which enables a crystallographic profile to be built up of the compounds under investigation. The ^{14}N - ^1H (600 MHz) - HMQC MAS experiment shown in figure 8.7 and 8.8 with accompanying table 8.5 show that the $4\text{-NH}^+;5\text{-COO}^-$ salt can be distinguished from $4\text{-N};6\text{-COOH}$ cocrystal. Figures 8.7a and 8.7b, with 8.8 showing a zoomed out view of 8.7b, represent $4\text{-NH}^+;5\text{-COO}^-$ whereas figure 8.7c corresponds to $4\text{-N};6\text{-COOH}$. Figure 8.7a (also shown in figure 8.8) was taken using a short recoupling time and shows only directly bonded interactions: those of N2-H23 which has a distance of 1.08 Å. Figure 8.7b shows a spectrum where a longer recoupling time was used. Both short (N2-H23) and long range interactions can be seen. However, only by using a long recoupling time can the O-H...N interaction in the cocrystal can be identified, whereby the H...N distance is 1.53 Å. A cocrystal will have a greater distance between the nitrogen atom of interest and the hydrogen atom of interest than in a salt where the hydrogen and nitrogen atom form an ionic bond. Using hydrogen bonding parameters a cocrystal will have: $d(\text{X...Y}) = d(^1\text{H...}^{14}\text{N})$; and a salt will have: $d(\text{H...Y}) = (^1\text{H...}^{14}\text{N})$ thus allowing differentiation in an ^{14}N - ^1H HMQC MAS experiment by varying the recoupling times. As in chapter 7 the difference between the ^{14}N chemical shift from the cocrystal to the salt is significant: the change in the ^{14}N chemical shift from $4\text{-N};6\text{-COOH}$ to $4\text{-NH}^+;5\text{-COO}^-$ was found to be 593 ppm experimentally and 548 ppm calculated.

Citric acid, co-crystals and a citrate salt

9.1 Introduction

This chapter presents research on co-crystals and a salt where citric acid is present in all samples investigated. Research was conducted into the effect citric acid had on the various APIs in terms of hydrogen bonding inside the co-crystal. The research involved XRD, calculation of NMR parameters and solid-state NMR experiments. Specifically, this research has explored via the use of experiment and calculation (using the GIPAW method) the effect citric acid has on various APIs and what differences are found in the hydrogen bonding interactions in the cocrystals. The research has mainly been calculation based due to the difficulty in acquiring citric acid cocrystals which have a known crystal structure and are stable. Solely having a known crystal structure is necessary to perform calculations. Citric acid has 3 carboxylic acid groups and an OH, see figure 9.1. There are a total of 8 hydrogen atoms which have been numbered from 1-8: H1-H4 are the hydrogen atoms in a CH environment, H6 is the hydrogen atom involved in an alcohol group and the hydrogen atoms H5, H7 and H8 are the hydrogen atoms in the carboxylic acid functional groups.

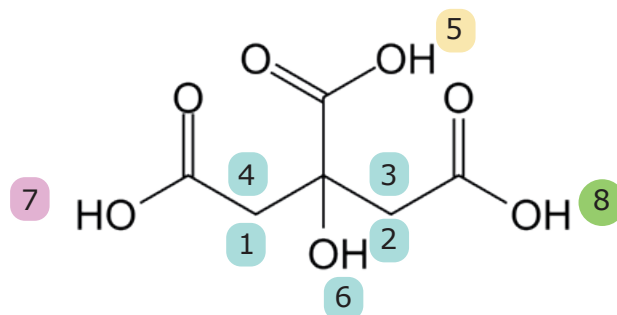


Figure 9.1: The chemical structure of citric acid, CSD refcode CITRAC11, with the numbering of the eight hydrogen atoms.

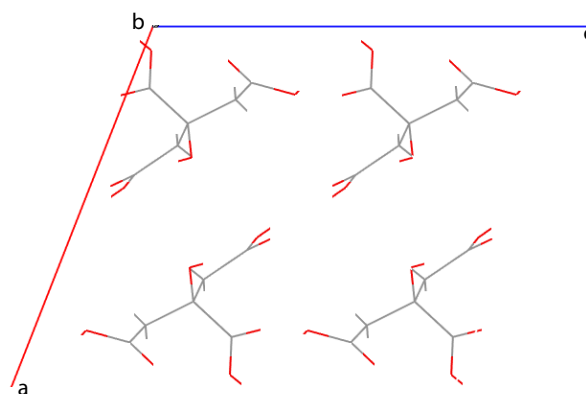


Figure 9.2: Packing of Citric acid with the unit cell shown.

9.2 Solid-State NMR of Citric Acid

9.2.1 Experimental and GIPAW Calculated ^1H Chemical Shifts

A ^1H one-pulse MAS NMR spectrum of citric acid is shown in figure 9.3, with the observed ^1H chemical shifts listed in table 9.1. Note that a ^1H MAS spectrum of citric acid has previously been presented by Miah et al [237].

The $\delta(^1\text{H})_{\text{expt}}$ and $\delta(^1\text{H})_{\text{calc}}$ values for H5, H7 and H8 in citric acid show high values indicating a hydrogen bond has been formed. This is emphasised further when a calculation is performed with an isolated molecule of citric acid (where no intermolecular interactions can occur).

9.2. SOLID-STATE NMR OF CITRIC ACID

Table 9.1: Experimental and GIPAW calculated (full crystal and isolated molecule) ^1H chemical shifts (in ppm) for citric acid.[†]

	$\delta(^1\text{H})_{\text{expt}}$	$\delta(^1\text{H})_{\text{calc}}^{\dagger}$ (crystal)	$\delta(^1\text{H})_{\text{calc}}$ (molecule)	$\Delta\delta_{C-M}$
H1	1.3	1.7	1.9	-0.2
H2	1.3	1.8	1.9	-0.1
H3	3.2	2.6	2.1	0.5
H4	3.2	2.5	2.2	0.3
H5	11.1	13.1	6.2	6.9
H6	5.1	4.5	2.5	2.0
H7	14.4	16.1	7.1	9.0
H8	10.3	12.3	6.5	5.8

[†] $\delta_{\text{ISO}} = -[\sigma_{\text{ISO}} - \sigma_{\text{ref}}]$ where σ_{ref} is 30 ppm.

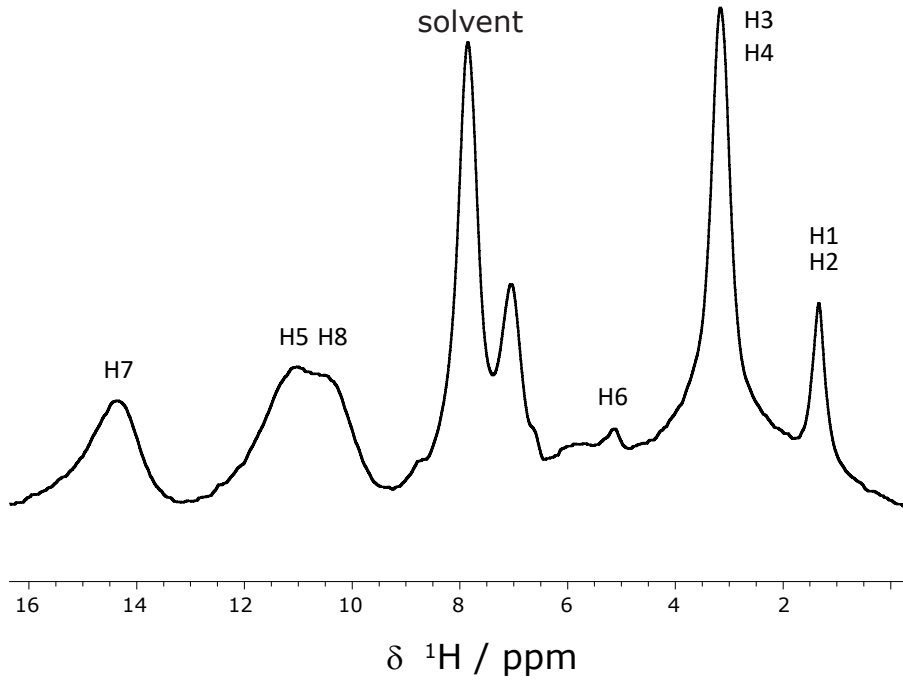


Figure 9.3: A one-Pulse ^1H (500 MHz) MAS (30 kHz) spectrum of Citric Acid - see assignment in table 9.1.

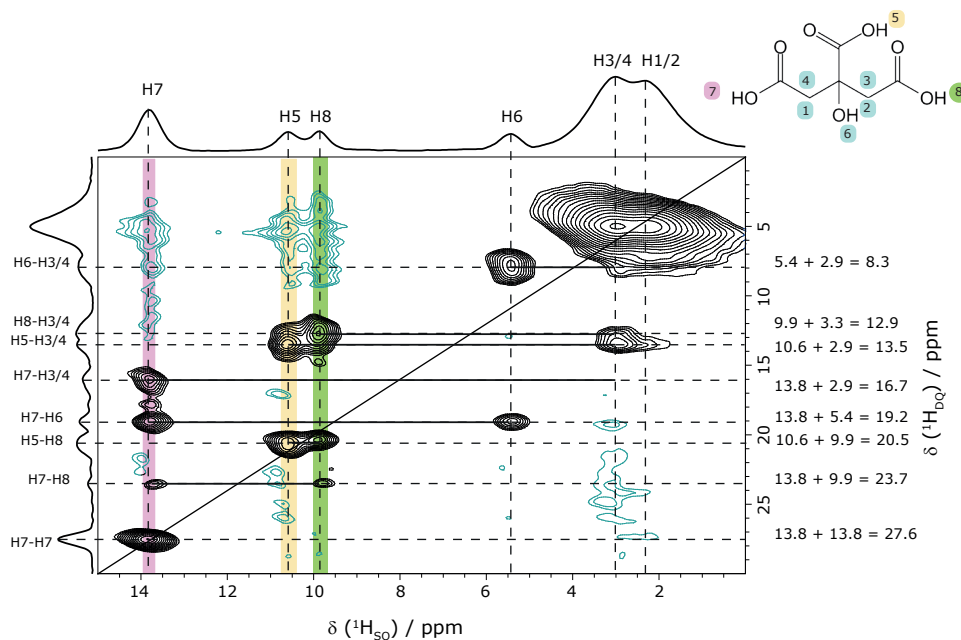
9.2.2 ^1H - ^1H DQ-SQ NMR


Figure 9.4: A ^1H - ^1H DQ-SQ MAS NMR spectrum with skyline projections of citric acid, recorded at 600 MHz and 60 kHz MAS using one rotor period of BABA recoupling.

A ^1H - ^1H DQ-SQ MAS, spectrum of citric acid is shown in figure 9.4. The ^1H - ^1H distances corresponding to the observed cross peaks for the carboxylic acid protons are shown in table 9.2. Table 9.2 shows that the closest H-H interaction is between the atoms of H7-H7 with a distance of 2.25 Å, followed by H7-H6 with 2.69 Å, H5-H5 with 3.11 Å, H8-H6 with 3.26 Å and H7-H8 with 3.40 Å. Note that the solvent present in figure 9.3 is not present in figure 9.4 as these experiments were completed using different sized rotors.

 9.2.3 ^{13}C CPMAS NMR

Figure 9.5 shows an experimental ^{13}C CP MAS spectrum of citric acid with table 9.3 showing experimental and calculated ^{13}C isotropic chemical shift values: $\delta(^{13}\text{C})_{\text{expt}}$, $\delta(^{13}\text{C})_{\text{calc}}$ and $\delta(^{13}\text{C})_{\text{calc}} / \text{ppm}$ (isolated molecule). The comparison of the (^{13}C and ^1H) chemical shifts indicates how sensitive the ^1H chemical shift is to hydrogen bond interactions as the ^{13}C chemical shift does not change significantly upon changing from an isolated molecule to the full crystal structure when considering that the ^{13}C chemical

9.2. SOLID-STATE NMR OF CITRIC ACID

Table 9.2: H-H distances in citric acid ($< 4 \text{ \AA}$) corresponding to ^1H - ^1H DQ peaks in Figure 9.4.

^1H - ^1H DQ peaks (COOH)	Distances (\AA)
H7-H7	2.25
H7-H6	2.69
H5-H5	3.11
H8-H6	3.26
H7-H8	3.40

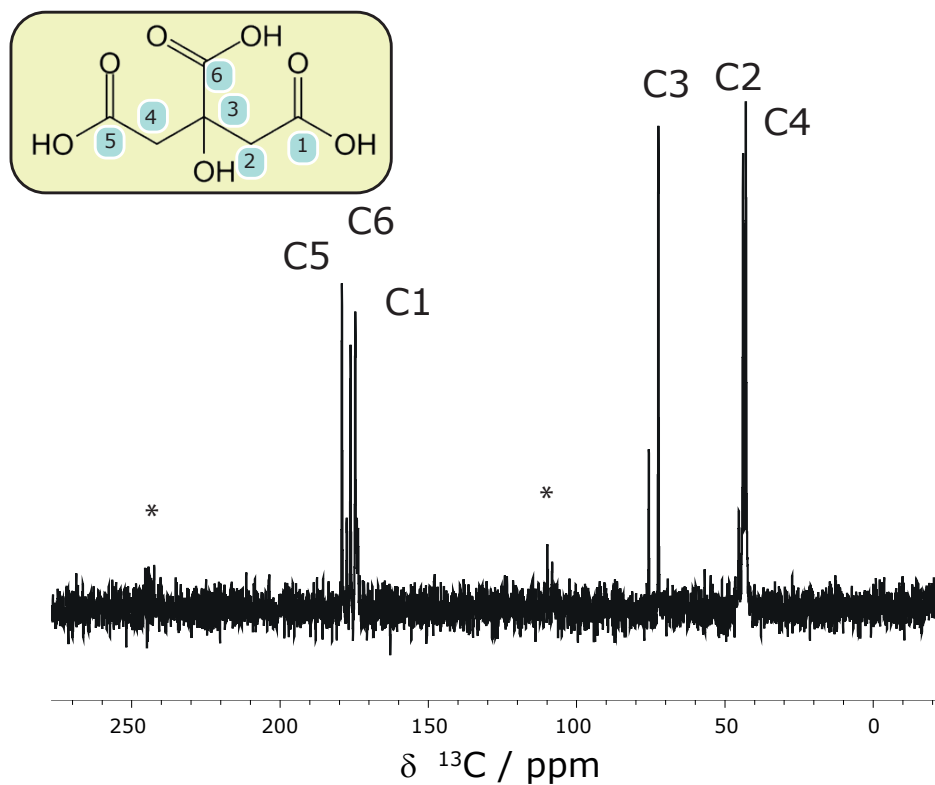


Figure 9.5: A ^1H (500 MHz) - ^{13}C CPMAS (12.5 kHz) NMR spectrum of citric acid showing the six carbon sites. * indicates spinning sidebands.

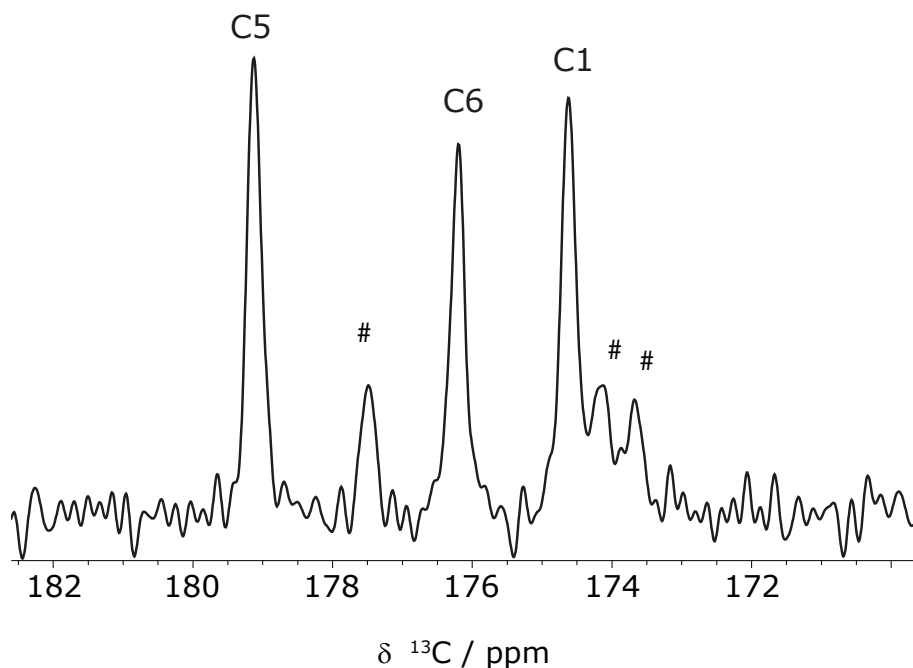


Figure 9.6: A ^1H (500 MHz) - ^{13}C CPMAS (12.5 kHz) NMR spectrum of citric acid showing a zoomed in region of the spectrum.

Table 9.3: Experimental and calculated (full crystal and isolated molecule) ^{13}C chemical shifts (in ppm) for citric acid.*

Carbon site	$\delta(^{13}\text{C})_{\text{expt}}$	$\delta(^{13}\text{C})_{\text{calc}}$ full crystal	$\delta(^{13}\text{C})_{\text{calc}}$ (isolated molecule)	$\Delta\delta_{C-M}$
C1	179.2	176.9	174.7	2.2
C2	44.0	40.5	41.8	-1.3
C3	72.0	72.6	76.5	-3.9
C4	43.0	38.6	39.4	-0.9
C5	174.6	181.5	178.0	3.6
C6	176.2	179.0	178.6	0.3

*With a reference shielding of 170.2 for ^{13}C .

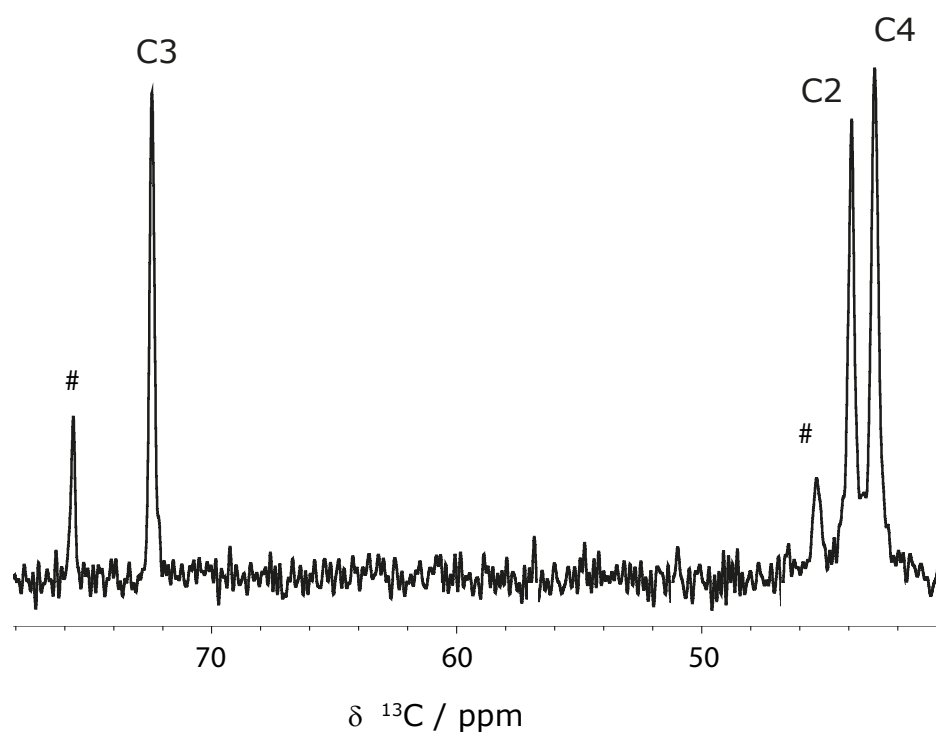


Figure 9.7: A ^1H (500 MHz) - ^{13}C CPMAS (12.5 kHz) NMR spectrum of citric acid showing a zoomed in region of the spectrum.

shift range is ~ 200 ppm (as compared to ~ 20 ppm for ^1H). Figure 9.5 shows the six carbon sites labelled from 1 to 6, other peaks are present and these are due to impurities. The impurities indicated by # in figures 9.6 and 9.7 maybe the result of the sample containing a mixture of two citric acid solid state forms.

9.3 NMR Crystallography of Citric Acid and Citric Acid Cocrystals

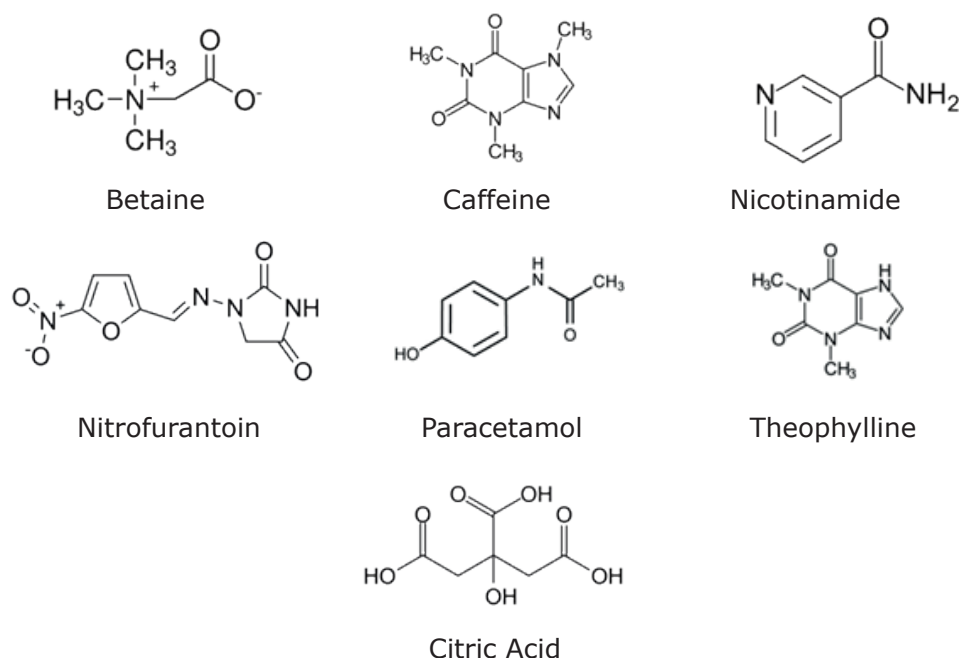


Figure 9.8: The structures of betaine, caffeine, nicotinamide, nitrofurantoin, paracetamol and theophylline which form cocrystals with citric acid.

Table 9.4 presents absolute calculated shieldings, σ_{XX} , σ_{YY} , σ_{ZZ} , σ_{ISO} and $\delta_{ISO} = -[\sigma_{ISO} - \sigma_{ref}]$ for all of the hydrogen atoms within citric acid and the corresponding hydrogens when the citric acid is in a cocrystal form with betaine, caffeine, nicotinamide, nitrofurantoin, paracetamol and theophylline (see table 6.1 for CIF refcodes from the CCDC and key calculation information). The structures of these molecules is presented in figure 9.8.

9.3. NMR CRYSTALLOGRAPHY OF CITRIC ACID AND CITRIC ACID COCRYSTALS

Table 9.4: Calculated shieldings, σ_{XX} , σ_{YY} , σ_{ZZ} , σ_{ISO} and $\delta_{ISO} = -[\sigma_{ISO} - \sigma_{ref}]$ for all of the hydrogen atoms within citric acid and the comparative hydrogens when the citric acid is in a cocrystal form with betaine, caffeine, nicotinamide, nitrofurantoin, paracetamol and theophylline.[†]

Structure	H atom (labelling, as in Fig.9.1)	σ_{XX}	σ_{YY}	σ_{ZZ}	σ_{ISO} calc (absolute)	$\delta_{ISO} =$ $-[\sigma_{ISO} - \sigma_{ref}]$
Citric Acid CITRC11	1	26.25	27.70	31.08	28.34	1.66
	2	25.08	27.16	32.49	28.24	1.76
	3	24.51	26.01	31.59	27.37	2.63
	4	23.03	26.35	33.36	27.55	2.45
	5	6.91	11.94	31.84	16.89	13.11
	6	17.12	20.75	38.67	25.52	4.48
	7	2.43	5.85	33.41	13.90	16.10
	8	9.14	11.26	32.63	17.67	12.33
Betaine co-crystal XOBHIF	Equivalent hydrogen atom in citric acid					
8	1	24.64	25.811	33.09	27.84	2.16
6	2	24.94	25.53	32.37	27.61	2.39
5	3	24.87	26.65	32.62	28.02	1.96
7	4	25.04	26.41	31.09	27.51	2.49
2	5	4.43	8.25	34.79	15.82	14.18
4	6	14.84	21.86	39.90	25.34	4.66
1	7	5.79	8.10	34.12	15.99	14.01
3	8	4.92	5.39	34.47	14.93	15.07
Caffeine co-crystal KIGKER						
8	1	23.38	26.01	32.32	27.24	2.76
5	2	24.69	26.58	31.06	27.44	2.56
6	3	30.45	27.98	22.94	27.12	2.88
7	4	22.48	26.20	32.75	27.14	2.86
4	5	7.19	9.78	34.44	17.14	12.86
1	6	17.04	22.39	38.68	26.04	3.96
3	7	11.73	15.55	33.29	20.19	9.81
2	8	5.53	6.81	33.99	15.44	14.56

[†] σ_{ref} was 30.9 ppm.

CHAPTER 9. CITRIC ACID, CO-CRYSTALS AND A CITRATE SALT

Table 9.4: Continuation of table 9.4

Structure (CIF Refcode)	H atom	σ_{XX}	σ_{YY}	σ_{ZZ}	σ_{ISO} calc (absolute)	$\delta_{ISO} =$ $-\left[\sigma_{ISO} - \sigma_{ref}\right]$
Nicotinamide co-crystal CUYXUQ						
26	1	24.83	25.16	30.49	26.83	3.17
27	2	25.24	25.92	31.17	27.44	2.56
28	3	31.77	29.74	26.23	29.25	0.75
25	4	24.05	26.12	31.90	27.36	2.64
31	5	-0.16	3.43	33.80	12.36	17.64
32	6	17.94	23.73	39.70	27.12	2.88
29	7	1.62	5.63	31.58	12.94	17.06
30	8	4.74	8.48	33.27	15.50	14.50
Nitrofurantoin co-crystal LEWTAK						
25	1	31.50	28.81	22.18	27.50	2.50
28	2	24.74	26.68	34.84	28.75	1.25
27	3	25.22	28.14	32.80	28.72	1.28
26	4	24.11	26.70	33.18	28.00	2.00
30	5	10.66	13.04	35.04	19.64	10.36
32	6	16.35	19.09	40.66	25.66	4.64
29	7	8.89	11.35	32.80	17.68	12.32
31	8	7.06	12.49	33.01	17.52	12.48
Paracetamol co-crystal AMUBAM						
4	1	30.91	27.88	24.13	27.64	2.36
1	2	25.52	27.58	30.91	28.00	2.00
2	3	24.51	27.24	33.22	28.32	1.68
3	4	22.50	24.72	32.74	26.65	3.35
6	5	8.24	8.51	37.01	17.92	12.08
5	6	13.28	16.16	40.27	23.24	6.76
8	7	8.47	9.44	32.32	16.74	13.26
7	8	7.05	7.42	32.15	15.54	14.46
Theophylline co-crystal KIGKAN						
38	1	32.38	28.45	24.17	28.33	1.67
39	2	25.52	26.17	31.08	27.59	2.41
40	3	24.93	25.18	34.59	28.23	1.77
37	4	23.72	24.68	31.86	26.75	3.25
35	5	5.87	6.50	36.39	16.25	13.75
36	6	13.40	18.07	37.91	23.13	6.87
33	7	3.92	4.82	36.37	15.03	14.97
34	8	9.58	15.14	33.86	19.53	10.47

9.3. NMR CRYSTALLOGRAPHY OF CITRIC ACID AND CITRIC ACID COCRYSTALS

The importance of geometry optimisation calculations before NMR parameters are extracted can be shown by comparing the values obtained in table 9.5 which shows the difference between $\delta(^1\text{H})_{calc}$ and $\delta(^1\text{H})_{no\text{geo}opt}$ for the hydrogen sites of the cocrystals of caffeine-citric acid, theophylline citric acid and betaine citric acid, when geometry optimisation calculations are or are not performed. It is shown that all values of $\delta(^1\text{H})_{no\text{geo}opt}$ are lower than $\delta(^1\text{H})_{calc}$, and are not meaningful compared to experiment.

Table 9.5: Calculated (GIPAW) ^1H isotropic chemical shift with and without geometry optimisation and $\Delta\delta(^1\text{H})_{\text{calc}} - \delta(^1\text{H})_{\text{nogeoopt}}$ for the theophylline citric acid, piracetam-citric acid and betaine citric acid cocrystals.

Hydrogen Atom	Betaine			Theophylline			Caffeine		
	$\delta(^1H)_{\text{calc}}$ / ppm	$\delta(^1H)_{\text{nogeoopt}}$	$\delta(^1H)_{\text{calc}} -$ $\delta(^1H)_{\text{nogeoopt}}$ / ppm	$\delta(^1H)_{\text{calc}}$ / ppm	$\delta(^1H)_{\text{nogeoopt}}$	$\delta(^1H)_{\text{calc}} -$ $\delta(^1H)_{\text{nogeoopt}}$ / ppm	$\delta(^1H)_{\text{calc}}$ / ppm	$\delta(^1H)_{\text{nogeoopt}}$	$\delta(^1H)_{\text{calc}} -$ $\delta(^1H)_{\text{nogeoopt}}$ / ppm
H1	2.16	-0.75	2.91	1.67	-1.44	3.11	2.76	0.32	2.44
H2	2.39	-1.64	4.03	2.41	-0.78	3.19	2.56	0.44	2.12
H3	1.96	-1.63	3.59	1.77	-1.3	3.07	2.88	0.28	2.6
H4	2.49	-1.52	4.01	3.25	-0.21	3.46	2.86	0.76	2.1
H5	14.18	8.96	5.22	13.75	5.78	7.97	12.86	5.99	6.87
H6	4.66	-7.78	12.44	6.87	-1.44	8.31	3.96	-1.61	5.57
H7	14.01	7.63	6.38	14.97	6.46	8.51	9.81	6.99	2.82
H8	15.07	14.4	0.67	10.47	4.02	6.45	14.56	0.32	14.24

9.3. NMR CRYSTALLOGRAPHY OF CITRIC ACID AND CITRIC ACID COCRYSTALS

Overall from table 9.4, the $\delta(^1\text{H})$ value of the hydrogen atoms H1-H8 in each of the different cocrystals follow a similar pattern: 1-3 ppm for CH_2 groups, 4-6 ppm for alcohol groups, and values of over 12 ppm for the carboxylic acid groups. Hydrogens which are predominately involved in hydrogen bonding; the carboxylic acid groups (H5, H7, H8) all have a high ppm and this is true for each of the calculations that have been performed. However, even though there are these similarities between the cocrystals there are also significant differences in the actual ppm values, one example is that of H5 in the Nicotinamide citric acid cocrystal which has the highest isotropic ^1H chemical shift of 17.6 ppm (see figure 9.9) compared to the hydrogen atom in the same position in the Nitrofurantoin citric acid cocrystal: 10.4 ppm for H5, a difference between them of 7.3 ppm. The following discussion will look into possible reasons for differences like this and highlights other interesting aspects found from the calculated data.

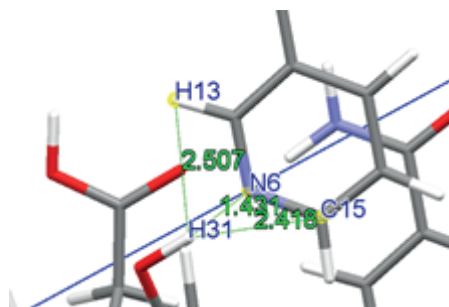


Figure 9.9: The hydrogen bond between H31 (H5 with citric acid labelling) and the N6 of the nicotinamide aromatic ring.

The alcohol group of the citric acid part of the cocrystal involves the hydrogen atom of H6 (see Figure 9.1). Table 9.4 shows, for the citric acid molecule, when it is not part of a cocrystal, that the $\delta_{iso}(\text{calc}) (^1\text{H})$ of H6 is 4.5 ppm. The highest and lowest values obtained for $\delta_{iso} (^1\text{H})$ of H6 in the cocrystals is 6.9 ppm for theophylline citric acid and 2.9 ppm for Nicotinamide citric acid, a difference of 4.0 ppm. This corresponds to closer $d(\text{X}\dots\text{Y})$ and $d(\text{H}\dots\text{X})$ in the former case. In the Nicotinamide citric acid cocrystal, H6 has a close intermolecular $\text{OH}\dots\text{O}$ hydrogen bonding interaction with an oxygen atom ($d(\text{X}\dots\text{Y})$: 3.0 Å, $d(\text{H}\dots\text{X})$: 2.3 Å and $\angle\text{HXY}$ 145.8°). In the theophylline citric acid cocrystal, H6 has a close intermolecular interaction with an oxygen atom also ($d(\text{X}\dots\text{Y})$: 2.8 Å, $d(\text{H}\dots\text{X})$: 2.0 Å and $\angle\text{HXY}$ 141.0°). For this example of the nicotinamide citric acid cocrystal and the theophylline citric acid cocrystal, the difference in the $\delta_{iso} (^1\text{H})$ of H6 is 4 ppm.

There are three carboxylic acid groups in citric acid. In all of the cocrystals investigated, the hydrogen atoms in citric acid have a chemical shift higher than 9.5 ppm. Table 9.6 shows the hydrogen bond parameters of the hydrogen atoms (H5, H7 and H8) of the carboxylic acid groups of the cocrystals of citric acid as well as for citric acid above.

The highest δ_{iso} (^1H) of 17.6 ppm value obtained from all of the calculations performed was for the carboxylic hydrogen atom labelled H31 (H5 with citric acid labelling) which formed a hydrogen bond with N6 of the nicotinamide aromatic ring (see figure 9.9). The $d(\text{H}\dots\text{X})$ and $d(\text{H}\dots\text{Y})$ of this $\text{OH}\dots\text{N}$ hydrogen bond are 1.47 and 2.54 Å and are the shortest in table 9.6.

Low δ_{iso} (^1H) values obtained were for the H5 atom of the nitrofurantoin citric acid cocrystal and the H8 of the theophylline citric acid cocrystal with a δ_{iso} of 10.4 and 10.5 ppm, respectively, where the close interaction is intermolecularly with an oxygen atom with $d(\text{X}\dots\text{Y})$ of 2.62 and 2.70 Å, respectively.

From the calculated results, figure 9.10 shows the correlation between isotropic ^1H chemical shift (δ_{ISO}) and $d(\text{X}\dots\text{Y})$ Å, along with the structures of the cocrystals of citric acid. Figure 9.10, shows that as the value of (δ_{ISO}) (^1H) decreases, the value of $d(\text{X}\dots\text{Y})$ Å increases. The lowest δ_{iso} (^1H) of 9.8 ppm is for H7 in the theophylline citric acid cocrystal.

As a general rule, it can be seen that the greater the chemical shift the stronger the hydrogen bond. Further shown in figure 9.11 are the interesting hydrogen bonding interactions of H5, H7 and H8 in the nicotinamide citric acid cocrystal. Here the $d(\text{X}\dots\text{Y})$ and $\angle \text{HXY}$ are all similar, but there is a markedly lower (δ_{iso}) (^1H) of 14.5 ppm for H8 in a $\text{OH}\dots\text{O}$ hydrogen bond as compared to H5 and H7 in the $\text{OH}\dots\text{N}$ hydrogen bond.

9.4 Caffeine-Citric Acid Cocrystal

In this section the Caffeine citric acid cocrystal is presented with PXRD patterns, experimental solid-state NMR and extraction of NMR parameters from calculated data.

A sample of the caffeine citric acid cocrystal was obtained which allowed verification of the calculated NMR parameters when solid-state NMR experiments were conducted. The first step was to check that the physical sample which was made matched the crystal structure which was deposited in the CSD and that the sample had remained stable during transportation.

Figure 9.12 shows the diffraction pattern for the structure deposited in the CSD (see table 6.1 for paper reference and refcode) and with the physical sample. In the PXRD pattern the caffeine citric acid cocrystal is shown where the black line represents the

9.4. CAFFEINE-CITRIC ACID COCRYSTAL

Table 9.6: Hydrogen bond parameters after geometry optimisation, with $\angle \text{HXY} \geq 125^\circ$, of the hydrogen atoms (H5, H7 and H8) of the carboxylic acid groups on its own and in co-crystals.

Hydrogen Atom	Hydrogen Atom as in citric acid	Hydrogen Bond (H...X)	$d(\text{H}\dots\text{X})$ / Å	$d(\text{X}\dots\text{Y})$ / Å	$\angle \text{HXY}$ / °	$\delta(^1\text{H})_{iso}$ calc/ppm
Citric Acid						
H5		H5-O2	1.61	2.62	173.4	13.11
H7		H7-O5	1.51	2.55	176.1	16.10
H8		H8-O3	1.65	2.59	154.6	12.33
Betaine						
H2	H5	H5-O15	1.56	2.57	168.2	14.18
H1	H7	H7-O15	1.57	2.58	171.2	14.01
H3	H8	H8-O1	1.55	2.57	174.4	15.07
Caffeine						
H4	H5	H5-O16	1.60	2.58	161.9	12.86
H3	H7	H7-O5	1.76	2.75	169.1	9.81
H2	H8	H8-N3	1.61	2.65	176.8	14.56
Nicotinamide						
H31	H5	H5-N6	1.43	2.54	171.4	17.64
H29	H7	H7-N2	1.51	2.58	169.8	17.06
H30	H8	H8-O3	1.52	2.56	170.0	14.50
Nitrofurantoin						
H30	H5	H5-O21	1.62	2.62	168.2	10.36
H29	H7	H7-O25	1.63	2.63	169.7	12.32
H31	H8	H8-O2	1.70	2.63	151.7	12.48
H31	H8	H8-N3	2.55	3.29	129.6	12.48
H31	H8	H8-N1	2.97	3.91	156.4	12.48
Theophylline						
H35	H5	H5-O37	1.60	2.62	179.0	13.75
H33	H7	H7-O37	1.54	2.57	175.0	14.97
H34	H8	H8-O1	1.72	2.70	162.8	10.47

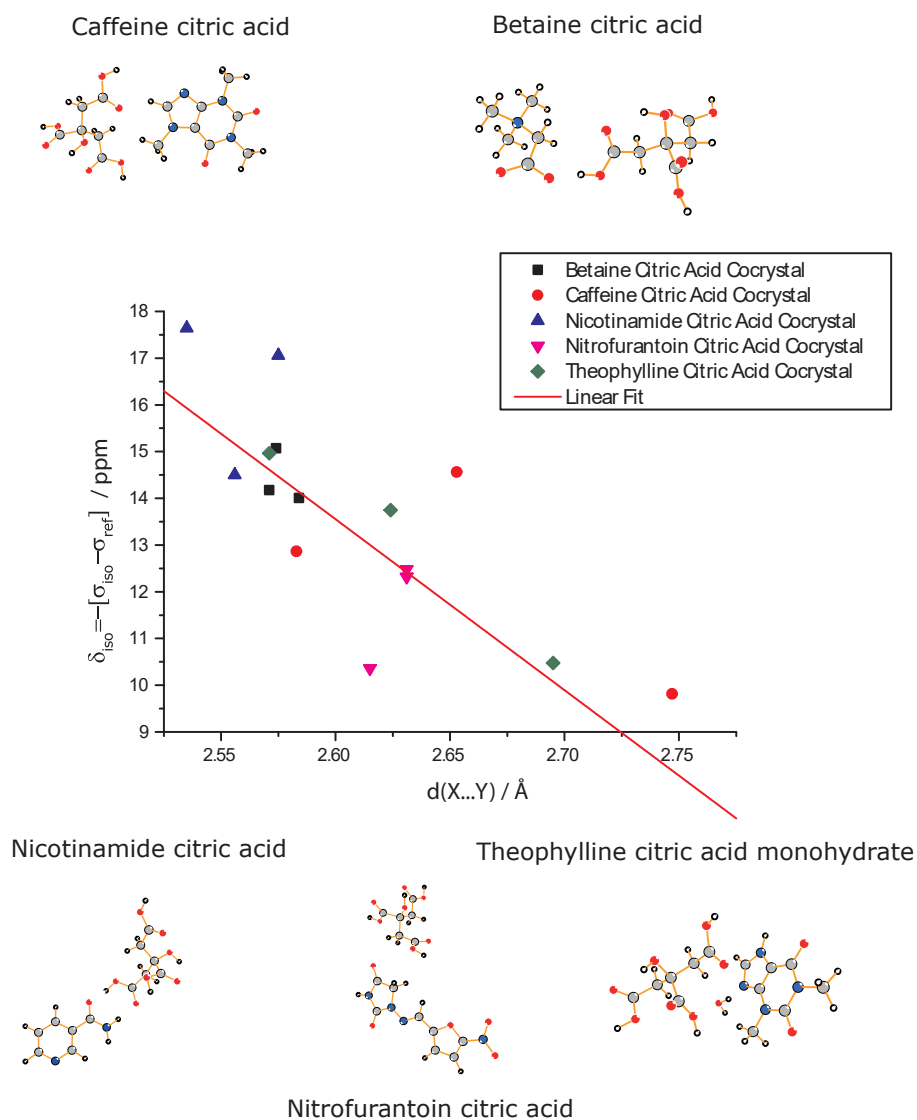


Figure 9.10: The trend between calculated isotropic ^1H chemical shift (δ_{ISO}) and $d(\text{X}\dots\text{Y})$ for carboxylic acid protons in citric acid co-crystals. Sulfur, nitrogen, oxygen, carbon and hydrogen atoms are represented by the colours yellow, blue, red, grey and white, respectively.

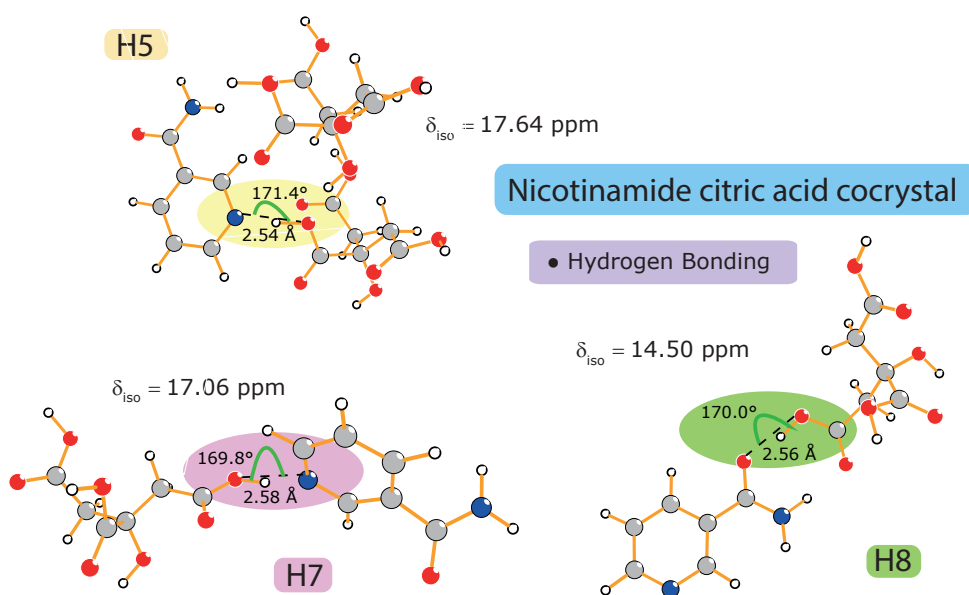


Figure 9.11: The hydrogen bonding interactions of the carboxylic acid groups in the cocrystal of nicotinamide citric acid. Sulfur, nitrogen, oxygen, carbon and hydrogen atoms are represented by the colours yellow, blue, red, grey and white, respectively.

experimental PXRD and the red line represents the PXRD pattern obtained from the cif file. Additional lines in the experimental PXRD pattern correspond to solid-state forms of the individual components of the cocrystal.

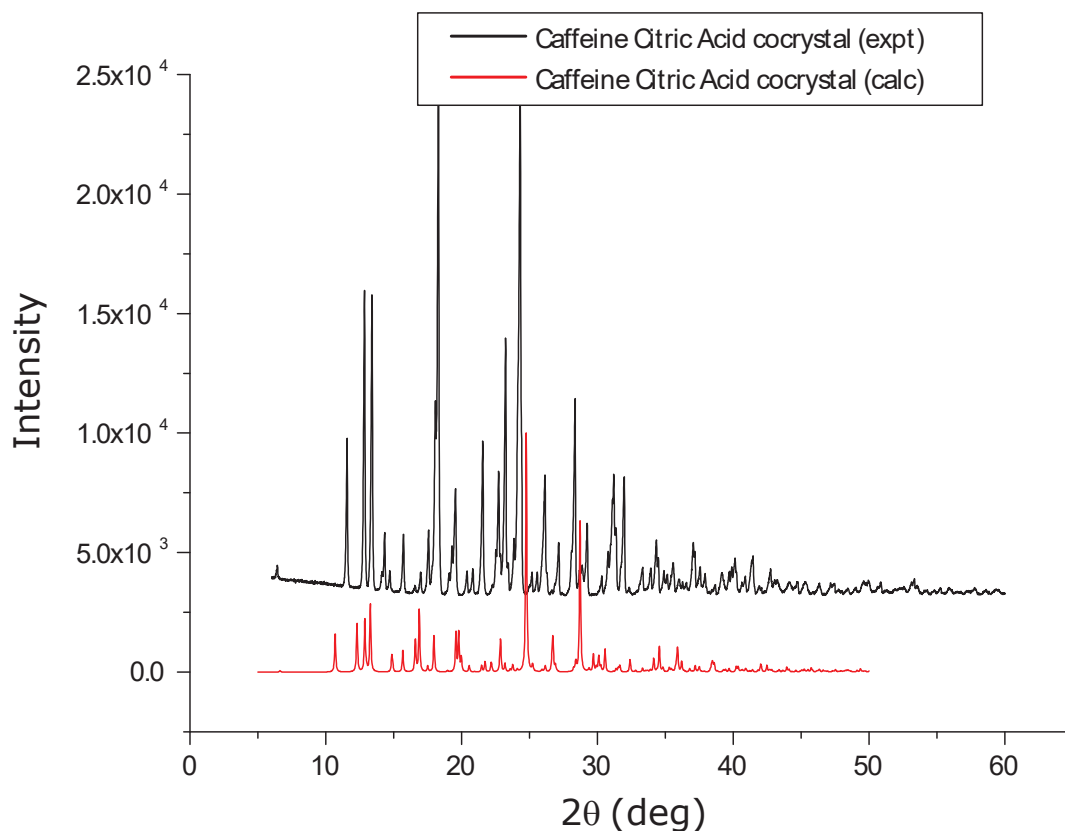


Figure 9.12: PXRD of Caffeine citric acid cocrystal where the black line represents the experimental PXRD and the red line represents the PXRD pattern obtained from the cif file (See table 6.1 for paper reference and refcode) .

Figure 9.14a shows a ^1H MAS NMR spectrum of the caffeine citric acid cocrystal with the calculated ^1H (δ_{ISO}) values shown alongside the experimental spectrum. Figure 9.14 shows that the experimental and calculated results are in good agreement. The experiment was conducted on a spectrometer which operates at a Larmor frequency of 700 MHz in order to resolve the ^1H (δ_{ISO}) values of the hydrogen atoms in the Caffeine citric acid cocrystal. As can be seen from the experimental data there are two broad peaks one of which is at a higher chemical shift in the region which indicate there are hydrogen bonding interactions. This higher peak must be due to the hydrogen atoms

of H5, H7 and H8 as it is these which according to calculation are taking part in the strongest hydrogen bonds in this instance.

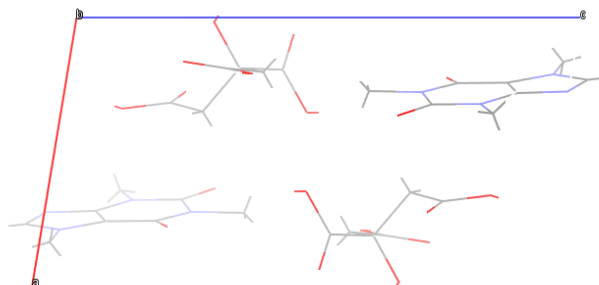


Figure 9.13: Molecular structure for the caffeine citric acid cocrystal

Figure 9.14b shows a ^{13}C CPMAS NMR spectrum of caffeine citric acid cocrystal alongside the calculated ^{13}C isotropic value and as can be seen they are in good agreement with each other.

9.5 Sildenafil Citrate

The protonation of systems which contain nitrogen sites in pharmaceutical compounds has been observed and discussed in chapters 7 and 8 using, in particular, the experimental results of 1D one-pulse ^1H MAS NMR, ^1H - ^1H DQ MAS NMR and 2D ^{14}N - ^1H HMQC experiments alongside alongside NMR parameters calculated using the GIPAW method as implemented in the CASTEP software [69–72].

The ^{14}N shift in the 2D ^{14}N - ^1H HMQC experiment was shown to change significantly upon protonation of the nitrogen site, and changes in shift with magnitude of hundreds of ppm were observed. Further evidence of protonation was provided by the variation of the recoupling time in 2D ^{14}N - ^1H HMQC experiments to probe ^{14}N - ^1H proximities.

An observation from the results of chapters 7 and 8 was that when the nitrogen site was protonated the P_Q value (MHz) changed, for example, in the nicotinamide system the P_Q value (MHz) changed from -3.7 (cocrystal) to -1.3 (salt). This was because the site became more symmetric in the salt form when directly bonded to the extra hydrogen atom and thus the P_Q value alters. In addition to the noticeable change in the $\delta(^{14}\text{N})_{\text{calc}}$ shift upon protonation, chapters 7 and 8 highlighted the possibility of also incorporating P_Q values to determine protonation in organic compounds.

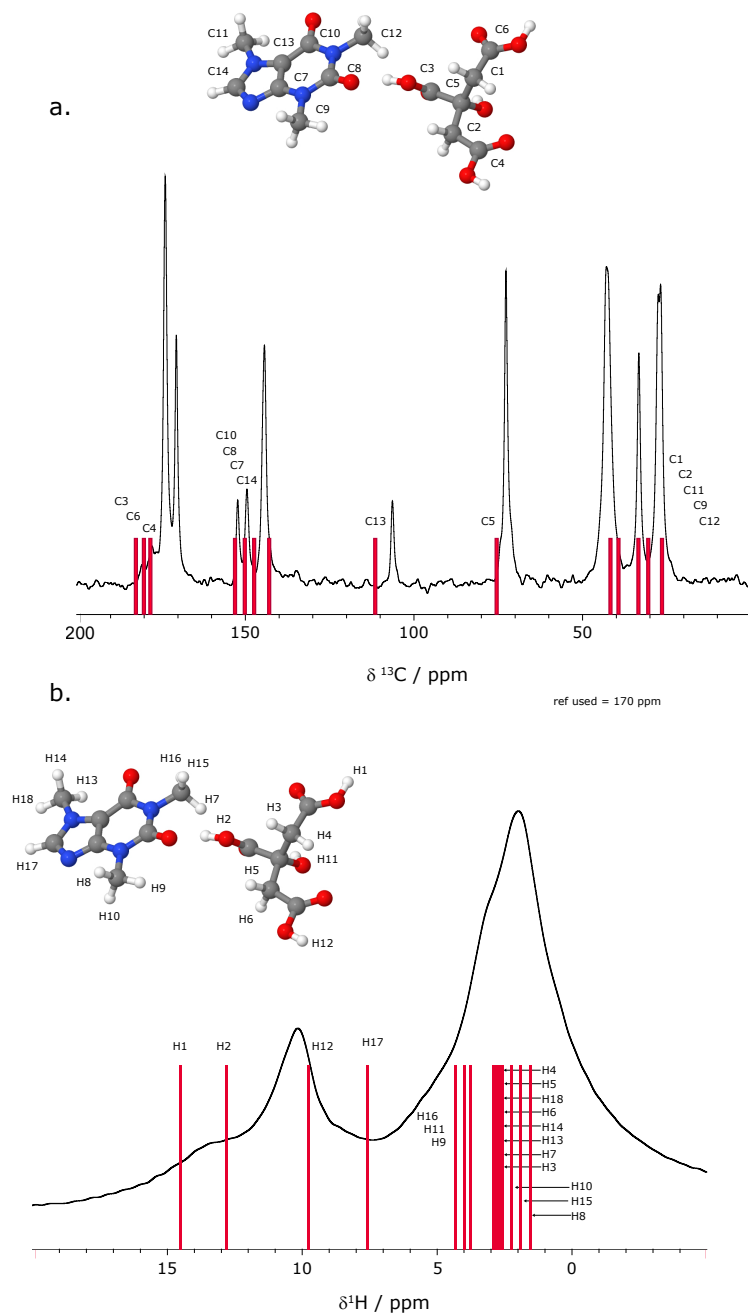


Figure 9.14: Spectra of (a) A ^1H one-pulse MAS NMR spectrum of a caffeine citric acid cocrystal and (b) a ^{13}C CPMAS NMR spectrum of a caffeine citric acid cocrystal. Stick spectra correspond to GIPAW calculated chemical shifts. Sulfur, nitrogen, oxygen, carbon and hydrogen atoms are represented by the colours yellow, blue, red, grey and white, respectively.

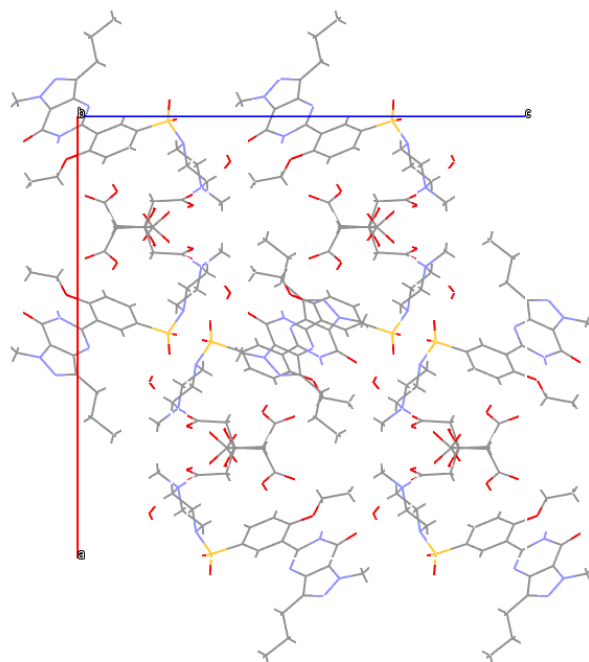


Figure 9.15: Packing of Sildenafil Citrate Monohydrate with the unit cell axes shown.

This section considers sildenafil citrate monohydrate, noting a recent diffraction study by Sawatdee et al [238] (see figure ??) and a recent NMR crystallography study by Abraham et al [239].

A one-pulse spectrum of ^1H MAS NMR sildenafil citrate monohydrate, as shown in figure 9.17, is presented in figure 9.16 alongside corresponding calculated ^1H NMR values obtained using the GIPAW method as implemented in the CASTEP software.

Figure 9.16 clearly shows two hydrogen atoms which have a high chemical shift (thus participating in a strong hydrogen bond). The two highest ^1H chemical shifts are calculated as being at 13.2 and 18.2 ppm, respectively. These hydrogen atoms represent two COOH groups in the citrate anion, which exhibit OH...N and OH...O intermolecular hydrogen bonding to a ring nitrogen and a citrate carboxylate oxygen, respectively, with hydrogen bonding parameters of $d(\text{H}\dots\text{N}) = 1.76 \text{ \AA}$, $d(\text{O}\dots\text{N}) = 2.70 \text{ \AA}$ and $\angle \text{OHN} = 162^\circ$ and $d(\text{H}\dots\text{O}) = 1.40 \text{ \AA}$, $d(\text{O}\dots\text{O}) = 2.46 \text{ \AA}$ and 168° , respectively. Figure 9.16 additionally shows further hydrogen bonds participating in hydrogen bonding interactions, as shown by the red lines around 10 ppm. Furthermore, there is a large unresolved peak occupying 0-5 ppm of the spectrum and this represents the majority of the hydrogen atoms in the structure which are not part of a hydrogen bond interaction.

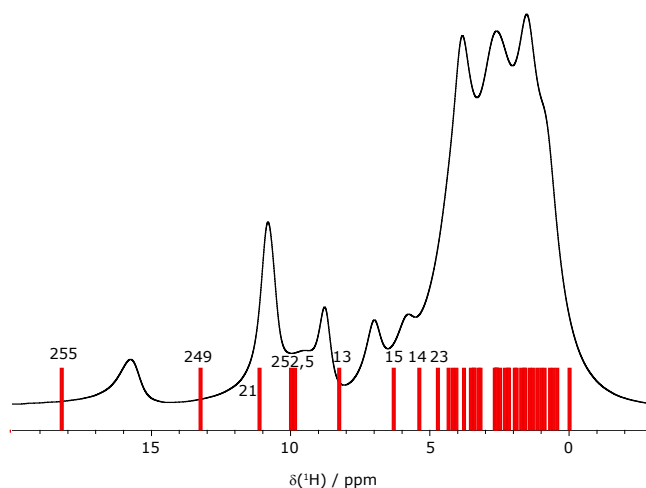


Figure 9.16: A ^1H (600 MHz) one-pulse MAS NMR spectrum of sildenafil citrate monohydrate recorded at a MAS frequency of 60 kHz. The experimental spectrum (black line) is compared to a stick representation of calculated (GIPAW) ^1H chemical shifts for the full crystal structure (red).

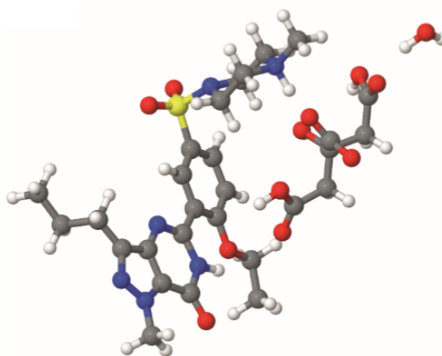


Figure 9.17: An image of sildenafil citrate monohydrate obtained using GIPAW and viewed via MagresView. Sulfur, nitrogen, oxygen, carbon and hydrogen atoms are represented by the colours yellow, blue, red, grey and white, respectively.

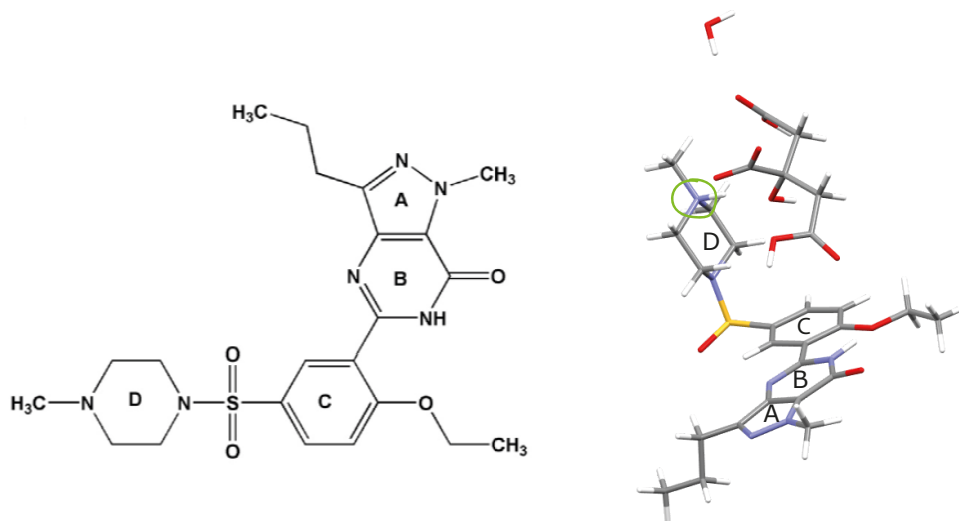


Figure 9.18: Sildenafil citrate monohydrate wherein the nitrogen area of interest is circled and ring structures have been numbered for reference. Sulfur, nitrogen, oxygen, carbon and hydrogen atoms are represented by the colours yellow, blue, red, grey and white, respectively.

A ^1H - ^1H DQ-SQ MAS spectrum was recorded of sildenafil citrate monohydrate, as shown in figure 9.20 and this provided detail about the close interactions between hydrogen atoms. The results showed the presence of a few close hydrogen interactions, focusing on the hydrogen atom involved in the strong hydrogen bond at around 15 ppm this was shown to have a close interaction to a hydrogen atom at around 9.5 ppm. Viewing the calculated results using software such as Diamond allows the identification of the specific hydrogen atoms involved and pinpoints them on the structure of the compound.

The ^{14}N - ^1H HMQC MAS spectrum, shown in Figure 9.21, for a short recoupling time indicates that there is one close N-H interaction in sildenafil citrate monohydrate and this N-H interaction relates to the hydrogen atom with the ppm value of around 15 ppm. The results that would be expected from a ^{14}N - ^1H HMQC MAS spectrum would be for a short recoupling (as used in Figure 9.21 of 133 μs) there would be no resonance in this area but as the recoupling time was increased in value to a recoupling time of 600 μs a resonance would be expected to appear. The presence of the resonance at the longer recoupling time would be indication that this method is able to identify a pharmaceutical salt from a cocrystal for nitrogen sites similar to that found in sildenafil citrate monohydrate as well as for nitrogen sites demonstrated in chapters 7 and 8.

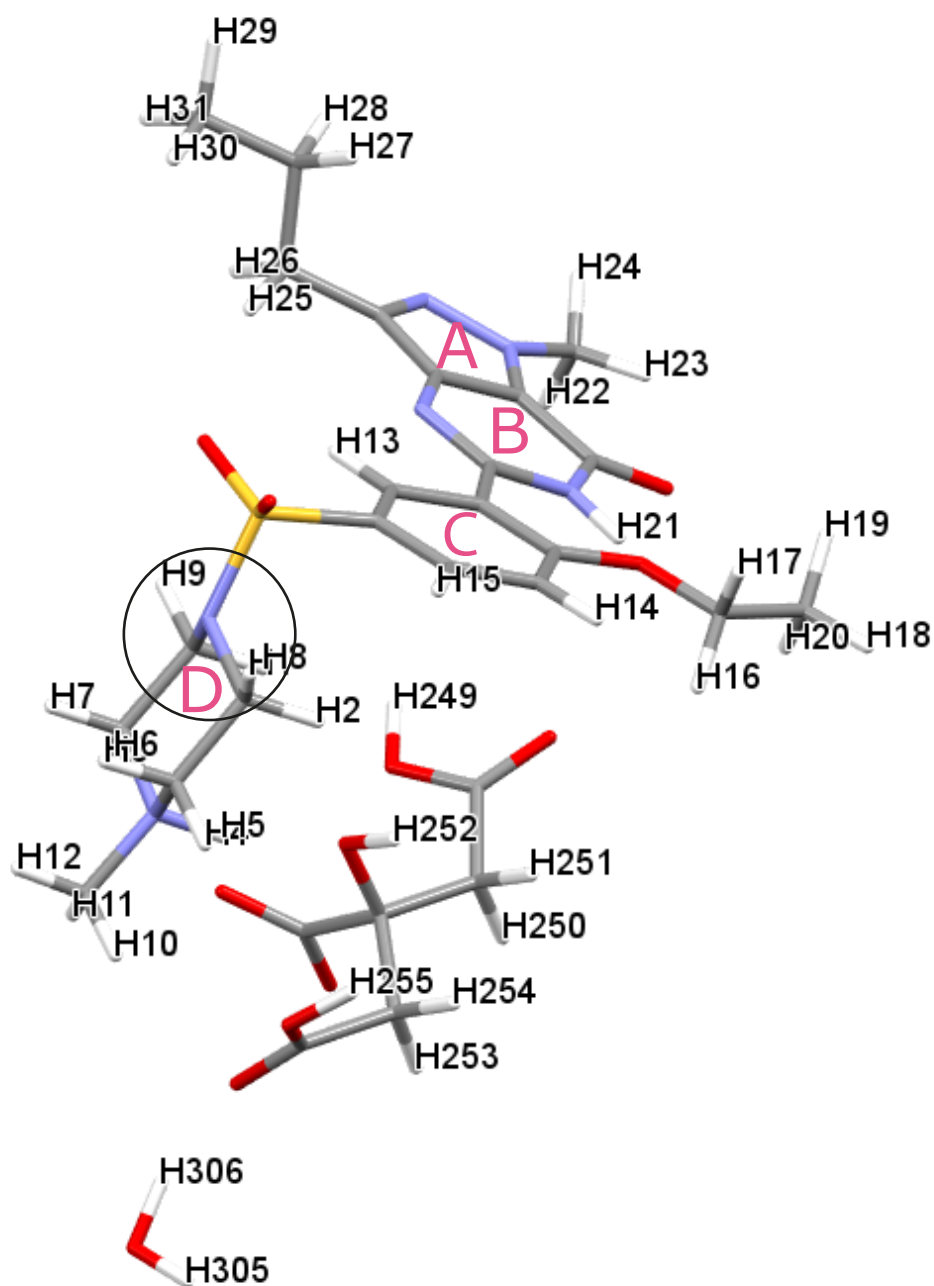


Figure 9.19: Sildenafil citrate monohydrate with hydrogen atom labels and the nitrogen area of interest highlighted. Sulfur, nitrogen, oxygen, carbon and hydrogen atoms are represented by the colours yellow, blue, red, grey and white, respectively.

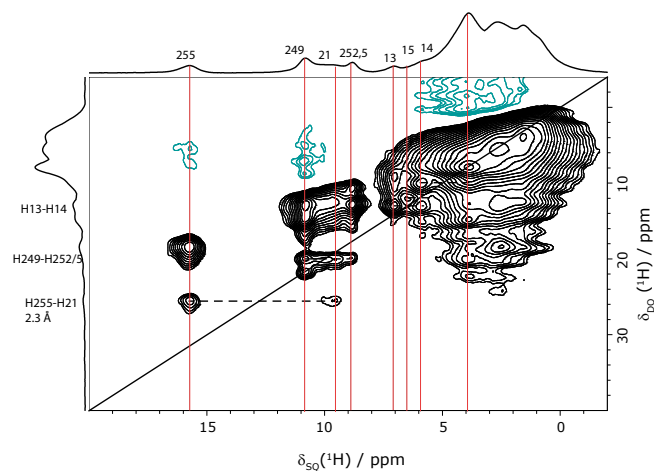


Figure 9.20: ^1H - ^1H (600 MHz) DQ-SQ MAS NMR spectrum with skyline projections of sildenafil citrate monohydrate using 1 rotor period of BABA recoupling at a MAS frequency of 60 kHz. 16 transients were co-added for each of the 64 t_1 FIDs, corresponding to a total experiment time of 10 h.

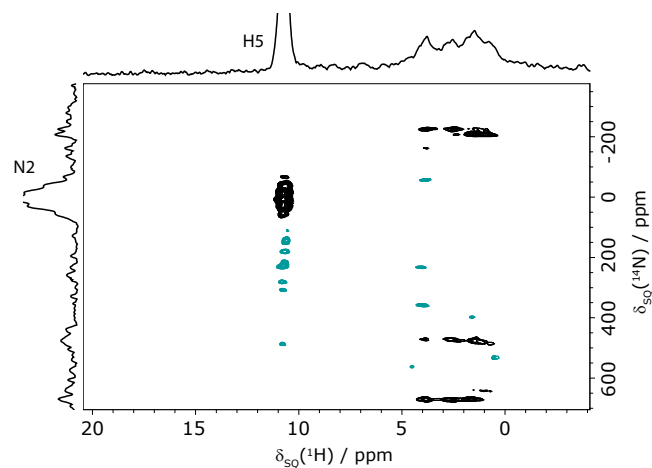


Figure 9.21: A ^{14}N - ^1H (600 MHz)- HMQC MAS (60 kHz) NMR spectrum recorded using $n=2$ rotary resonance recoupling for sildenafil citrate monohydrate for a τ_{RCPL} duration of $133 \mu\text{s}$. 16 transients were co-added for 80 t_1 FIDs, corresponding to a total experiment time of 18 h.

CHAPTER 9. CITRIC ACID, CO-CRYSTALS AND A CITRATE SALT

Table 9.7: GIPAW calculated ^{15}N isotropic chemical shifts and ^{14}N shifts for sildenafil citrate monohydrate

N Atom	$\delta_{iso}(^{15}\text{N})_{calc}$	η_Q^\dagger	C_Q /MHz	P_Q^\ddagger /MHz	δ_{ISO}^{Q**} /ppm (<i>calc</i>)	$\delta(^{14}\text{N})_{calc}$ / ppm ††
1	−76.4	0.20	−5.2	−5.2	1077.4	1001.0
2	−153.9	0.16	−1.5	−1.5	94.4	−59.5
3	−131.9	0.55	−2.3	−2.4	231.4	99.5
4	−204.7	0.12	−3.9	−3.9	616.5	411.8
5	−264.6	0.55	−3.5	−3.6	529.7	265.1
6	−342.3	0.88	−3.9	−4.4	783.6	441.3

† see equation 4.141 in chapter 4

‡ see equation 4.162 in chapter 4

** see equation 4.112 in chapter 4

$^{\dagger\dagger}\delta(^{14}\text{N})_{calc} = \delta(^{15}\text{N})_{calc}^a + \delta_{ISO}^{Q}(^{14}\text{N})_{calc}$

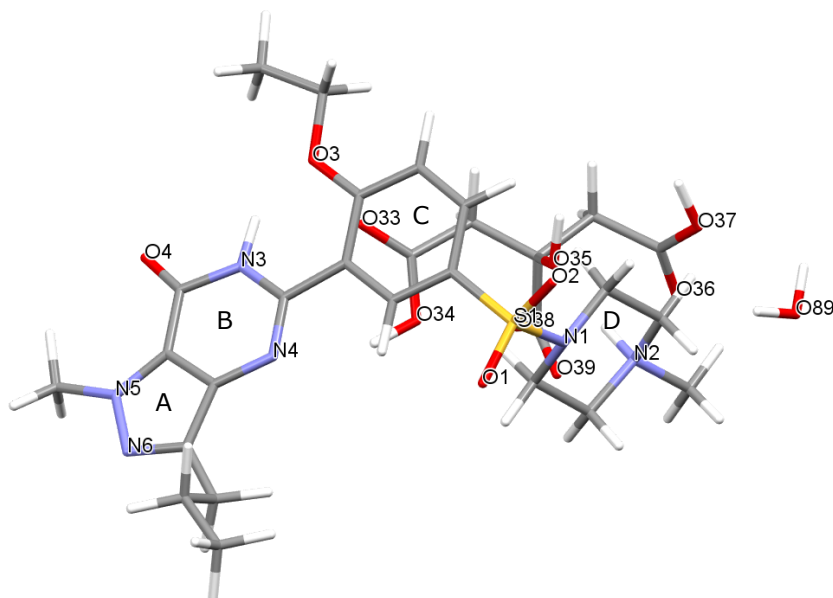


Figure 9.22: Sildenafil Citrate Monohydrate: highlighting the nitrogen atoms contained in table 9.7. Sulfur, nitrogen, oxygen, carbon and hydrogen atoms are represented by the colours yellow, blue, red, grey and white, respectively.

In the GIPAW calculation the two highest ^1H chemical shifts are for two COOH groups in the citrate anion - note that as compared to the structure in figure 9.18, there is a carboxylate citrate group and one of the nitrogens in the saturated 6-membered ring (in ring D in figure 9.18) is protonated, as shown in figure 9.17. The NH groups in the sildenafil molecule have calculated ^1H chemical shift of 11.1 (ring B in figure 9.18) and 9.8 (ring D in figure 9.18) ppm.

Figure 9.21 displays a ^{14}N - ^1H spectrum conducted at $133\ \mu\text{s}$, thus observing short range couplings i.e. ^{14}N - ^1H interactions which are directly bonded. This NH interaction is due to a NH group in a ring structure. The NH group in ring B in figure 9.18 exhibits intramolecular NH...O hydrogen bonding with $d(\text{H}\dots\text{O}) = 1.82\ \text{\AA}$, $d(\text{N}\dots\text{O}) = 2.62\ \text{\AA}$ and $\angle \text{NHO} = 131^\circ$, while the other NH group has an NH...O intermolecular hydrogen bond with the citrate alcohol oxygen with $d(\text{H}\dots\text{O}) = 1.74\ \text{\AA}$, $d(\text{N}\dots\text{O}) = 2.76\ \text{\AA}$ and $\angle \text{NHO} = 161^\circ$. The GIPAW calculated ^1H chemical shifts are 11.1 and 9.8 ppm, with calculated ^{14}N quadrupolar parameters of $C_Q = 2.3\ \text{MHz}$, $\eta = 0.55$, and $C_Q = 1.5\ \text{MHz}$, $\eta = 0.16$, and a calculated ^{14}N chemical shift difference of 126 ppm. The calculated ^{14}N chemical shift difference of 126 ppm almost exactly counteracts the difference in the calculated isotropic quadrupolar second-order shift, thus explaining why only one intense cross peak is seen in the ^{14}N - ^1H spectrum in figure 9.21. Note that the calculated C_Q of the other nitrogen in ring D has magnitude 5.2 MHz, showing the marked reduction on protonation associated with a more symmetric environment.

The N2 atom in 9.18 is the area of interest. An initial comparison of data can be taken regarding the experimental data of sildenafil citrate monohydrate and the calculated data of sildenafil citrate monohydrate. The calculated data can be found in table 9.7 and the experimental quadrupolar data can be viewed in figure 9.21. The experimental peak in figure 9.21 is shown to occur at 10.8 ppm and 7.6 ppm for the ^1H and ^{14}N atom, respectively. The corresponding data from the GIPAW calculations are $-0.1\ \text{ppm}$ and $-59.5\ \text{ppm}$ for the ^1H and ^{14}N atom, respectively. The difference between the calculated and experimental data for the ^{14}N atom is $-51.9\ \text{ppm}$. This misalignment of the calculated and experimental data equates to roughly 5.7 % of the ^{14}N spectrum, whose range is from 0 to 900 ppm. Considering, the calculations are taken at 0 K and the experimental data was taken at ambient room temperature the initial results are promising. A possible continuation of the investigation would be to conduct variable temperature experiments and cool the sample. Cooling the sample would theoretically provide a greater match between the calculated and experimental results as the difference in temperatures of the two methods would be closer.

9.6 Outlook

Looking into the future obtaining a larger sample size of calculated data would be welcome to give more confidence to the findings - for this to be the case more structures which have citric acid as a coformer would need to be deposited in the CSD and where the number of atoms in the unit cell is of a manageable number in order for calculations to be completed on those crystal structures. In addition it would also be advantageous to have experimental data for all of the calculated structures to verify the calculated data. This is more difficult to achieve due to the difficulty in making stable cocrystals that would remain stable long enough for PXRD experiments and a number of solid-state NMR experiments to be completed over a period of time. The investigation could be further extended to look into different coformer molecules which have a particular functional group of interest for the pharmaceutical industry, for example in the thesis chapter 7 the functional group of NH^+ was of interest in the API. At the moment multi-functional excipients are of interest to the pharmaceutical industry as the cost of developing and producing pharmaceutical products increases a multi-functional excipient would save money and reduce regularity issues while also providing benefits to drug products. Understanding the bonding interactions in these new multi-functional excipients would therefore benefit the industry as the knowledge could then be used to design these excipients.

9.7 Conclusion

Table 9.1 shows the experimental and GIPAW calculated (full crystal and isolated molecule) ^1H chemical shifts (in ppm) for citric acid. Table 9.3 shows the experimental and GIPAW calculated (full crystal and isolated molecule) ^{13}C chemical shifts (in ppm) for citric acid. If the two tables are compared it is possible to see that $\Delta\delta_{C-M}$ is generally greater for ^1H atoms than ^{13}C especially when involved in a hydrogen bonding interaction. The greatest $\Delta\delta_{C-M}$ value for a hydrogen atom of citric acid was 9.0 ppm (H7) whereas the greatest $\Delta\delta_{C-M}$ value for a ^{13}C atom of citric acid was 3.6 ppm (C5). These values represent 45 % and 1.8 % of the ^1H and ^{13}C spectrum, respectively. This proves the sensitivity of the hydrogen atom to hydrogen bonding interactions.

Table 9.5 shows the importance of NMR crystallography which uses geometry optimisation calculations and not relying on values obtained from diffraction alone. The greatest chemical shift difference between a calculation which uses geometry optimisation and one

which solely relies on diffraction values was found to be 14.24 ppm for the H8 atom in the citric acid-caffeine cocrystal. This accounts for 71% of the ^1H chemical shift range. Figure 9.10 which uses information from table 9.6 was able to show the trend between calculated isotropic ^1H chemical shift and $d(\text{X}\dots\text{Y})$ for carboxylic acid protons in citric acid co-crystals. The general trend showed that the greater the chemical shift the stronger the hydrogen bond.

The initial results obtained from sildenafil citrate seem to indicate that the results obtained in chapters 7 and 8 will be able to be repeated. This is a positive step forward in the research as sildenafil citrate represents a different nitrogen environment than is found in isonicotinamide/ 2,4,6- trihydroxybenzoate salt ($1\text{-NH}^+ : 2\text{-COO}^-$) and isonicotinamide/4-hydroxy-3-nitrobenzoic acid co-crystal ($1\text{-N} : 3\text{-COOH}$) (see figure 7.1 for chemical structures) and 4,4-bipyridine 5-sulfosalicylic acid ($4\text{-NH}^+ : 5\text{-SO}_3^-$) and 4,4'-bipyridine/phthalic acid ($4\text{-N} : 6\text{-COOH}$) (see figure 8.1 for chemical structures). Figure 9.16 highlights the hydrogen atoms with chemical shifts above 10 ppm and thus those which are most likely to participate in a hydrogen bond. Figure 9.21 is able to identify the ionic bond involving the N2 nitrogen atom which a ^1H chemical shift of 10.8 ppm and a ^{14}N chemical shift of 7.6 ppm.

CHAPTER 9. CITRIC ACID, CO-CRYSTALS AND A CITRATE SALT

Trends in Experimental & Calculated NMR Parameters for Hydrogen Bonds

10.1 Overview

Tables 10.1 and 10.2 consider examples of hydrogen bonding interactions from literature and this thesis for which a DFT geometry optimisation of the crystal structure was performed, followed by the calculation of NMR parameters by the GIPAW method. Specifically, ^1H chemical shifts and ^{14}N quadrupolar parameters are considered in Table 10.1 and 10.2, respectively.

Table 10.1: GIPAW calculated and experimental ^1H chemical shifts for nitrogen-containing hydrogen bonds.

Compound	Hydrogen Bond Type	δ_{calc}/ppm full crystal	$\Delta\delta_{CM}/\text{ppm}$	expt ^1H ppm	X...Y	H...Y	$\angle\text{XHY}^\circ$	Reference
G OH2'A	O-H...O	3.6	7.5		2.65	1.74	173.5	[63]
G OH'5 A	O-H...O	3.8	6.2		2.70	1.72	168.0	[63]
G OH'5 B	O-H...O	3.8	6.8		2.65	1.65	173.5	[63]
G OH'3 A	O-H...O	4.1	5.5		2.82	1.83	173.7	[63]
G OH'3 B	O-H...O	4.1	7.8		2.64	1.65	164.3	[63]
dG(C3) ₂	N-H...N	5.8	5.3		2.87	1.81	178.7	[63]
γ -Indomethacin	O-H...O	7.0	7.2	12.7	2.65	1.64	173.1	[83]
4-NH ⁺ :5-SO ₃ ⁻	C-H...O	7.0	2.6	7.7	3.13	2.31	130.5	
4-NH ⁺ :5-SO ₃ ⁻	C-H...O	7.3	2.8	7.7	3.21	2.18	157.7	
1-NH ⁺ :2-COO ⁻	C-H...O	7.6	3.3	8.0	3.34	2.38	146.6	
1-NH ⁺ :2-COO ⁻	N-H...O	7.9	4.2	8.0	2.90	1.96	151.0	
4-NH ⁺ :5-SO ₃ ⁻	C-H...O	7.9	2.2	7.7	3.46	2.40	165.2	
dG(C3) ₂	N-H...N	8.1	6.4		2.93	1.87	177.7	[63]
1-NH ⁺ :2-COO ⁻	O-H...O	8.1	4.9	5.0	2.72	1.74	170.3	
1-NH ⁺ :2-COO ⁻	N-H...O	8.8	4.3	8.0	2.98	1.96	173.8	
Uracil	N-H...O	11.2	5.4	10.8	2.83	1.79	172.1	[76]
Uracil	N-H...O	11.7	5.1	11.2	2.84	1.80	174.8	[76]
G (H1) A	N-H...N	12.1	5.1	12.1	2.85	1.79	178.6	[63]
G(H1) B	N-H...N	13.0	5.9	13.1	2.79	1.72	179.6	[63]
Gace H1 B	O-H...N	13.0	6.4		2.68	1.68	170.2	[63]
NAPRO-A Naproxen	O-H...O	13.6	7.0	11.5	2.67	1.79	174.3	[240]
4-NH ⁺ :5-SO ₃ ⁻	N-H...O	15.3	11.2	15.5	2.64	1.56	178.0	
1-NH ⁺ :2-COO ⁻	N-H...O	16.8	12.8	17.6	2.64	1.57	170.1	
1-N:3-COOH	O-H...N	17.8	9.8	15.6	2.54	1.44	177.3	
4-NH ⁺ :5-SO ₃ ⁻	O-H...N	18.9	10.5	17.8	2.53	1.43	170.5	

Remembering the discussion in section 2.3, hydrogen bonding interactions of interest in pharmaceutical compounds which have been studied in this thesis are those of:

- N-H...N
- N-H...O
- O-H...O
- O-H...N
- C-H...O

10.2 ^1H Chemical Shifts

10.2.1 Hydrogen Bonds and $\Delta\delta_{C-M}$ From Literature

All of the compounds listed in table 10.1 have had isolated molecule calculations performed on them therefore the parameter $\Delta\delta_{C-M}$ was able to be extracted. The $\Delta\delta_{C-M}$ value is useful as it shows whether the atoms are taking part in intermolecular interactions. The larger the $\Delta\delta_{C-M}$ value the greater the change in the local chemical environment surrounding that particular atom when the isolated molecule is compared to the full crystal structure. The change in $\Delta\delta_{C-M}$ can be due to atoms participating in hydrogen bond interactions, ring current effects, π - π interactions or Van der Waals. As can be seen from the compounds extracted from literature & this thesis (see Table 10.1) there is a change in all of the atoms between isolated molecule and full crystal structure. The smallest $\Delta\delta_{C-M}$ value from the literature was for the crystal structure of Uracil from [76] with a $\Delta\delta_{C-M}$ of 5.1 and 5.4 ppm were determined for two distinct N-H...O hydrogen bonds (note that the $d(\text{X...Y})$, $d(\text{H...Y})$ and the XHY angle are 2.84 Å, 1.80 Å and 174.8°, and 2.83 Å, 1.79 Å and 172.1°), where the ^1H experimental NMR chemical shift was determined as 11.2 and 10.8 ppm.

The values for the hydrogen bonds of uracil [76] can be compared to a higher value of $\Delta\delta_{C-M}$ of 7.2 ppm from the literature for carboxylic acid groups in γ -indomethacin which exhibits an O-H...O hydrogen bond with an experimental ^1H NMR value of 12.7 ppm [83]. The higher value of 7.2 ppm for $\Delta\delta_{C-M}$ for γ -indomethacin as compared to that for uracil corresponds to a stronger hydrogen bond, whereby the hydrogen bond parameters: $d(\text{X...Y})$, $d(\text{H...Y})$ and XHY angle for γ -indomethacin are 2.65 Å, 1.64 Å and 173.1°. In comparison to the hydrogen bond identified in uracil, this equates to a change of around

CHAPTER 10. TRENDS IN EXPERIMENTAL & CALCULATED NMR PARAMETERS FOR HYDROGEN BONDS

0.2 Å for $d(X...Y)$ and $d(H...Y)$, showing that the $d(X...Y)$ and $d(H...Y)$ distance is shorter in γ -indomethacin thus indicating a stronger hydrogen bonding interaction.

10.2.2 Difference in $\Delta\delta_{C-M}$ Values Between Salt and Cocrystal Forms

For the nicotinamide and bipyridine systems considered in chapters 7 and 8, in both the salt and cocrystal forms the value of $\Delta\delta_{C-M}$ is higher than the literature values referred to above (see table 10.1) with values in ppm of 12.8 (1-NH⁺:2-COO⁻) and 9.8 (1-N:3-COOH) for the nicotinamide system (see table 7.2) and 10.2 (4-NH⁺:5-SO₃⁻) and 8.9 (4-N:6-COOH) (see table 8.1). The greatest value of $\Delta\delta_{C-M}$ occurred in the salt forms of both systems (1-NH⁺:2-COO⁻ and 4-NH⁺:5-SO₃⁻) with a difference of 3 ppm and 1.3 ppm in the nicotinamide and bipyridine systems respectively between the salt and cocrystal forms. The hydrogen atom participating in the hydrogen bond is the same except, in the salt form, ionisation has taken place and the excipient has donated a hydrogen atom to the API while in the cocrystal the hydrogen atom remains part of the excipient molecule and ionisation has not occurred. The difference in $\Delta\delta_{C-M}$ value between the salt and cocrystal (in both systems) indicates the presence of a “stronger” intermolecular interaction in the salt forms (1-NH⁺:2-COO⁻ and 4-NH⁺:5-SO₃⁻). The stronger intermolecular interaction theory is supported by the value of the isotropic chemical shift of the hydrogen atom in question: H1 in the nicotinamide system and H4 in 4-NH⁺:5-SO₃⁻ and H17 in 4-N:6-COOH in the bipyridine system, with H1 having a $\Delta\delta_{iso}(\text{expt})$ of 1 ppm between the salt and cocrystal (17.6 ppm – 16.6 ppm) and where the $\Delta\delta_{iso}(\text{expt})$ is 2.2 ppm between the salt (H4) and cocrystal (H17) (17.8 ppm – 15.5 ppm). However, even though the salt forms possess a stronger intermolecular hydrogen bonding interaction, the hydrogen bond that is present in the cocrystal form is still strong with high isotropic ¹H chemical shift values for both systems of 16.6 and 15.5 ppm, respectively.

For the nicotinamide system in chapter 7, it is interesting to consider the hydrogen bond of O1-H1...N9 which has a lower $\Delta\delta_{C-M}$ than the hydrogen bond of N1-H1...O5. The shortest $d(H...Y)$, $d(X...Y)$ distances and angle closest to 180° position is 1.44 Å, 2.54 Å and 177.3° are for the O1-H1...N9 hydrogen bond in the cocrystal 1-N:3-COOH, with an experimental ¹H chemical shift of 16.6 ppm and a calculated value of 17.8 ppm. While $\Delta\delta_{C-M}$ has been shown to be useful in identifying intermolecular hydrogen bonding interactions, a limitation of this parameter is shown when the two hydrogen bonds in the nicotinamide system between the salt and cocrystal forms are compared. Even though as shown above the hydrogen bond parameters are more favourable for O1-H1...N9 (1-

N:3-COOH), it has a lower $\Delta\delta_{C-M}$ value of 9.8 ppm than the less favourable hydrogen bond of N1-H1...O5 (1-NH⁺:2-COO⁻) which has a $\Delta\delta_{C-M}$ of 12.8 ppm.

The explanation for this value can be seen in table 7.1 from $\delta_{iso}(\text{molc})$ which displays the calculated ^1H chemical shift value for all the hydrogen atoms in the isolated molecule calculation. As mentioned previously isolated molecule calculations effectively remove intermolecular interactions therefore the ^1H chemical shift values are expected to be lower due to lack of intermolecular hydrogen bonds. However, if intramolecular interactions are present this will cause a higher isolated molecule ^1H chemical shift. This is shown in the hydrogen atoms of H41 and H45 (1-NH⁺:2-COO⁻) and H1 and H5 (1-N:3-COOH) having higher than expected ^1H chemical shifts. This means that there are interactions which are intramolecular and cause the higher than expected isolated chemical shift value and thus making $\Delta\delta_{C-M}$ not as significant.

10.2.3 C-H...O Weak Hydrogen Bonding

Research conducted by Uldry et al [76] presents two hydrogen bonds of the form C-H...O where the $\Delta\delta_{C-M}$ value calculated was 2.0 and 2.2 ppm, corresponding to a ^1H experimental isotropic value of 7.5 and 6.0 ppm respectively. The hydrogen bond parameters are found in table 10.1, where it is seen that, in comparison to the other hydrogen bonds discussed, the bond angle of 161° is not as favourable (as it is further away from 180°) additionally the $d(\text{X...Y})$ is greater with values of over 3 Å for both bonds and values of over 2 Å for $d(\text{H...Y})$.

C-H...O bonds greater than those identified in this thesis. Four C-H...O hydrogen bonds were identified in 1-NH⁺:2-COO⁻ having $\Delta\delta_{C-M}$ values of 4.2, 3.3, 3.6 and 2.5 ppm, shown in figure 7.6 and table 8.1. Three C-H...O hydrogen bonds were identified in 4-NH⁺:5-SO₃⁻ having $\Delta\delta_{C-M}$ values of 2.6, 2.8 and 2.2 ppm, shown in figure 8.5 and table 7.2. All these cases have larger $\Delta\delta_{C-M}$ values than found in literature.

10.3 ^{14}N Quadrupolar Parameters

This thesis has shown that ^{14}N - ^1H HMQC solid-state NMR experiments have much potential for the characterisation of a pharmaceutical salt as compared to a cocrystal. ^{14}N shifts are a result of the isotropic chemical shift (which is the same for both ^{15}N and ^{14}N) and the isotropic second order quadrupolar shift. The ^{14}N shift was shown to change significantly upon protonation of the nitrogen site with changes in shift magnitude of hundreds of ppm being presented. Further evidence is provided by the variation of

CHAPTER 10. TRENDS IN EXPERIMENTAL & CALCULATED NMR PARAMETERS FOR HYDROGEN BONDS

the recoupling time to probe proximities of ^{14}N - ^1H distances approximately one bond length apart. Consequently, a hydrogen atom directly bonded to the nitrogen site (salt) will be visible in a ^{14}N - ^1H HMQC spectrum recorded with a short recoupling time. In the comparative cocrystal spectrum this peak will not be visible until a recoupling time which probes longer range correlations is used.

Evidence of the hydrogen bonding interactions at the nitrogen site are given by GIPAW calculated values (see Table 10.2) used in addition with one-dimensional ^1H MAS NMR and ^1H - ^1H DQ MAS NMR data. This further highlights the presence of a directly bound hydrogen atom to the nitrogen in a pharmaceutical salt and a longer range hydrogen bond where the hydrogen atom is not directly bound in the cocrystal form. This difference in hydrogen bonding interactions has shown that the ^{14}N shift is very sensitive to changes in the hydrogen bonding that takes place at the nitrogen site in the environments of a salt and cocrystal.

Table 10.2: GIPAW calculated ^{14}N quadrupolar parameters for nitrogen containing hydrogen bonds.

Compound	Hydrogen Bond Type	$ C_Q $ / MHz	η_Q	$ P_Q $ / MHz	X...Y	H...Y	$\angle\text{XHY}$ / $^\circ$	Reference
Nicotinamide	O-H...N	4.4	0.37	4.3	3.08	2.05	168.3	[171]
Nicotinamide-Palmitic acid cocrystal	O-H...N	4.0	0.36	4.0	2.70	1.67	176.2	[171]
G	N-H...O	3.8	0.39	3.9	2.92	1.95	156.9	[63]
	N2-H2b...O							
G	N-H...O	3.8	0.40	3.9	2.90	2.31	115.7	[63]
	N2-H2b...O							
G	N-H2a...O	3.8	0.36	3.9	2.88	1.91	153.3	[63]
G	N-H2a...O	3.8	0.36	3.9	3.07	2.40	122.5	[63]
1-N:3-COOH	OH...N	3.6	0.3	3.7	2.54	1.44	177.3	
4-N:6-COOH	OH...N	3.6	0.30	3.6	2.53	1.43	170.5	
4-N:6-COOH	NH...O	3.6	0.60	3.6	2.64	1.56	178.0	
Cimetidine	N3-H...N12	3.5	0.23	3.6	2.95	2.17	169.1	[82]
4-NH $^+$:5-SO $_3^-$	NH...O	3.4	0.30	3.4	2.59	1.53	174.0	
Cimetidine	N15-H...N1	3.3	0.17	3.3	2.88	2.06	158.4	[82]

Table 10.2: Continuation of Table 10.2.

Compound	Hydrogen Bond Type	$ C_Q $	η_Q	$ P_Q $ / MHz calc	X...Y	H...Y	$\angle XHY$ °	Reference
G(H1)A	N-H...N (N1-H1...N7)	3.2	0.24	3.2	2.85	1.79	178.6	[63]
G(H1)B	N-H...N N1-H1...N7	3.2	0.27	3.3	2.79	1.72	179.6	[63]
G	O-H...N3	3.2	0.24	3.2	2.80	1.83	162.0	[63]
G	N-H2...O	2.9	0.69	3.1	2.95	1.97	166.7	[63]
dG(C3) ₂	N6-H22...N4	2.9	0.6	3.0	2.87	1.81	178.7	[63]
dG(C3) ₂	N1-H1...N9	2.7	0.7	2.9	2.93	1.87	177.7	[63]
Gace B	N-H1...N7	2.7	0.7	2.9	2.80	1.74	170.4	[63]
Gace A	N-H1...N7	2.6	0.84	2.9	2.84	1.79	174.1	[63]
Sildenafil Citrate	NH...O	2.3	0.55	2.4	2.62	1.82	131.0	
Cimetidine	N10-H...N14	2.1	0.51	2.4	2.91	2.15	157.8	[82]
Sildenafil Citrate	NH...O	1.5	0.16	1.5	2.76	1.74	161.0	
1-NH ⁺ :2-COO ⁻	NH...O	1.3	0.3	1.3	2.64	1.57	170.3	
diethylcarbamazine citrate salt	N-H...O		0.07	1.3	2.76	1.79	150.7	[241]

10.4 Conclusion

This chapter collated hydrogen bonding interactions from literature and from this thesis where a DFT geometry optimisation of the crystal structure was performed followed by the calculation of NMR parameters by the GIPAW method. Specifically, ^1H chemical shifts and ^{14}N quadrupolar shifts were considered. It was noted that the greatest value of $\Delta\delta_{C-M}$ occurred in the salt forms of both systems indicating that this may be a possible trend. There is scope in future studies to investigate $\Delta\delta_{C-M}$ in relation to the strength of hydrogen bonds.

C-H...O weak hydrogen bonding was discussed and identified in this chapter. Not as much research on C-H...O has been conducted in solid-state NMR with calculations and this research has shown higher values of $\Delta\delta_{C-M}$ (2.2, 2.6 and 2.8 ppm) than have previously been identified in literature (2.0 and 2.2 ppm). It has been shown that the ^{14}N - ^1H HMQC solid-state NMR experiment has the potential for the characterisation of a pharmaceutical salt to a cocrystal. Future studies potentially could involve the use of a tertiary protonated nitrogen site in order to verify that this method can be used on a different type of molecule. One molecule of interest which was selected for this purpose was that of sildenafil and sildenafil citrate. This has the desired functional group and sildenafil citrate is also readily available, with only the need to reduce the sildenafil citrate down to the charged form of Sildenafil for experiments. Figure 9.21 shows that the ^{14}N - ^1H HMQC solid-state NMR experiment is viable for the compound of sildenafil citrate monohydrate, as is clearly shown by an N-H peak in the spectrum when a short recoupling time is used. As per the methodology used in chapters 7 and 8 a range of recoupling times would subsequently be conducted in order to compare the resulting salt spectra to the cocrystal spectra and the comparison should indicate a difference between the spectra and thus the salt and cocrystal forms.

If sildenafil and sildenafil citrate molecules showed the same results as was presented for the nicotinamide and bipyridine systems in this thesis the investigation could then be extended to include other pharmaceuticals.

It was highlighted during this chapter that there was a trend between the P_Q value and the nitrogen site (NH^+) becoming more symmetric upon protonation from the cocrystal to salt form. This has been identified for the salt and cocrystal systems of isonicotinamide and bipyridine whereby both systems showed an increase in the P_Q value in the salt form as can be seen in table 10.2. This trend could be further investigated with other pharmaceutical products with a quaternary nitrogen environment to add confidence to this statement with the addition of a larger sample size. This potentially could provide

CHAPTER 10. TRENDS IN EXPERIMENTAL & CALCULATED NMR PARAMETERS FOR HYDROGEN BONDS

another parameter which would be useful in identifying between a salt and cocrystal form.

It was also shown that the ^{14}N shift was very sensitive to protonation. It would be interesting to conduct further studies on pharmaceuticals where protonation occurs to gain an understanding or see there is a trend between the degree the ^{14}N chemical shift moves and the type of molecule under investigation: for example investigating whether there is there a difference in the sensitivity of the ^{14}N chemical shift between tertiary and quaternary nitrogen environments.

Thesis Summary

This chapter will provide a summary of the research findings of this thesis and will also provide an outlook for the future direction of NMR Crystallography.

11.1 Research Aim

The original aim of the research undertaken in this thesis was to use experimental NMR techniques with computational methods, under the umbrella of NMR Crystallography in order to characterise a pharmaceutical salt from a pharmaceutical cocrystal. The motivation for this research originated from GSK who were interested in using solid-state NMR to study cocrystals and in particular whether solid-state NMR could characterise a cocrystal from a salt product. Cocrystals are being researched by pharmaceutical companies as possible future drug products.

11.2 Key Findings

The development of pharmaceutical compounds is of significant interest to the community inside and outside of scientific research. Industry is working together with academic institutions in order to work together to further advance the technology of pharmaceutical projects. The aim of the project was to develop solid-state NMR techniques in order to characterise pharmaceutical compounds especially in the area of pharmaceutical cocrystals.

Cocrystals are currently being heavily researched by pharmaceutical companies as they could be an alternative to the most common solid-state delivery method of pharmaceutical salts. Pharmaceutical cocrystals may also have the potential for improvement over pharmaceutical salts, for example, the possibility of increased bioavailability, enhancement of the API (due to the increased number of coformers), and the availability of more coformers due to the API not having to be ionisable.

A core aim in the characterisation of pharmaceutical compounds is the determination of atomic positions. The difficulty with cocrystals and salts is that there may only be a subtle difference between them. As the difference between a pharmaceutical salt and a cocrystal may only be the position of a hydrogen atom (in terms of atomic position), a very sensitive probe of hydrogen atoms is required. Solid-state NMR is such a sensitive probe of the hydrogen atom which is why the project to use NMR crystallography to determine pharmaceutical salts and cocrystals was undertaken. NMR crystallography is the combination of a number of complementary techniques in order to solve crystal structures. The techniques that were chosen for the research undertaken in this thesis were that of solid-state NMR, calculations which used the GIPAW method and XRD.

Chapter 7 discussed the methodology undertaken to study the quaternary nitrogen site in an isonicotinamide salt and cocrystal system using NMR crystallography to identify when protonation had occurred. 1D one-pulse ^1H MAS NMR and ^1H - ^1H DQ MAS NMR solid-state NMR experiments were used alongside 2D ^{14}N - ^1H HMQC experiments to determine protonation. The ^{14}N shift in the 2D ^{14}N - ^1H HMQC experiment was shown to change significantly upon protonation of the nitrogen site, and changes in ^{14}N shift with magnitude of hundreds of ppm were observed. Further evidence of protonation was provided by the variation of the recoupling time in 2D ^{14}N - ^1H HMQC experiments to probe ^{14}N - ^1H proximities. The HMQC experiment along with chemical shielding data allows proximities between atoms to be viewed and are a good indicator of the strength of hydrogen bonding present. The experimental data complemented data obtained from GIPAW calculations of NMR chemical shielding and quadrupolar interactions which show that the combined experimental and calculation approach is viable in determining the presence of a salt or co-crystal form. Specifically, single crystal to full molecule GIPAW chemical shift calculations were also performed that give detailed information on hydrogen bonding strength within the molecules. This is compared with ^1H chemical shifts which are known to be sensitive to hydrogen bonding.

Chapter 8 introduced a further bipyridine salt and cocrystal to be studied, with the structures possessing greater amounts of symmetry than those considered in chapter chapter 7. The same process was applied to this system as was applied to the isonicotinamide

salt and cocrystal with experimental results of 1D ^1H one-pulse MAS NMR, ^1H - ^1H DQ MAS NMR and 2D ^{14}N - ^1H HMQC shown alongside NMR parameters calculated using the GIPAW method as implemented in the CASTEP software. The findings complemented those found in the isonicotinamide salt and cocrystal and the pharmaceutical salt was able to be identified from a cocrystal.

In chapter 9 research was presented which highlighted the effect citric acid had on the various APIs in terms of hydrogen bonding interactions inside a co-crystal, in particular for the carboxylic group. Furthermore, it discussed the proposed subsequent steps for the area of research undertaken in this thesis with an extension of the methodology to nitrogen sites which possess different chemical environments in pharmaceutical salts and cocrystals.

This lead onto the findings which were discussed in chapter 10 which collated hydrogen bonding information from the research presented in this thesis and from literature. The collation of the hydrogen bond data provided insights to be drawn into why particular hydrogen bonding interactions, for example had higher than expected ^1H chemical shifts.

11.3 The Future of NMR Crystallography

NMR crystallography, which uses complementary techniques, will become more pronounced in universities and industry. This is because the advantages of the individual techniques can be utilised and enable limitations to be overcome by working in unison. Not only will this be able to benefit the area of research in this thesis: pharmaceuticals but also, for example, the agrochemical industry (as detailed in Pöppler et al [79]).

Pöppler et al uses a range of complementary techniques including x-ray diffraction, solid-state NMR and GIPAW calculations to determine crystallographic information. The solid-state nmr approach employed by Pöppler et al used [79] ^1H - ^{13}C 2D correlation spectra enabling resolution and assignment of NH, aromatic CH and methyl resonances with intra and intermolecular distances able to be extracted from ^1H - ^1H DQ MAS spectra. Pöppler et al therefore shows that NMR crystallography would be applicable to a various chemical systems, not just pharmaceutical cocrystals and salts. Here, the advantages of using so-called "isolated molecule" calculations is shown with ^1H NMR chemical shift changes between the so-called isolated molecule and full crystal structure.

The applicability of so-called "isolated molecule" calculations is also shown in Martins et al [242]. The crystal structures of two novel protic gabapentin pharmaceutical salts prepared with the coformers methanesulfonic acid and ethanesulfonic acid were used in the study. Hydrogen bonding interactions were probed in order to gain a greater under-

standing of their role in supramolecular arrangements in crystalline solids. Where their effect on crystal packing arrangements is still not fully understood. The investigation used experimental and calculation techniques to analyse ^1H NMR chemical shifts. A focus of the study also assessed how ^1H NMR chemical shifts of protons engaged in particular hydrogen bonds are affected when other close hydrogen bonds involves bifurcated or geminal/vicinal hydrogen atoms are removed.

NMR crystallography involving GIPAW can involve a great computational cost especially when the sample is a powder. Thureau et al [243] writes about how the computational cost can be reduced and the method relies on using ^{13}C - ^{13}C couplings. The use of the ^{13}C - ^{13}C couplings were undertaken on powdered theophylline with dynamic nuclear polarisation. The hope is to maybe create a DFT-free, screening of a range of structures that have been predicted by *ab initio* random structure search. It is shown that the ^{13}C - ^{13}C couplings can identify structures which posses long range structural motifs and unit cell parameters which are close to that of the true structure. Future advances in reducing cost whether experimental, for example, reducing experiment time or computational will make NMR crystallography more attractive to businesses and researchers.

Tatton et al [78] have conducted research on a β -piroxicam compound, with a high R-factor, in order to showcase the possibilities of using NMR crystallography for structure determination of more challenging systems and thus more researchers may consider using the technique in their investigations. The research conducted confirmed NMR crystallography is an effective way to validate crystal structures which would be inconclusive using diffraction data alone. This research used the same NMR experiments contained in this thesis but the novelty is the comparison to PXRD with high R-factor, to verify the structures predicted.

Proton transfer is of importance in the pharmaceutical industry as exemplified by [155, 161, 244]. New APIs are constantly being developed and researched. APIs, however, maybe unsuitable for drug delivery in their current form. By combining an API with another molecule, via ionic bonding (salt) or via a hydrogen bond (cocrystal) may enable that API to be a viable drug product. Determining whether protonation has occurred is very important but also challenging. Research has been conducted on proton transfer in pharmaceutical salts and cocrystals. In Stevens et al [215, 245] photoelectron spectroscopy is used in conjunction with solid-state NMR, GIPAW calculations and XRD. The research utilised ^{15}N data to show proton transfer. The research conducted in this thesis used the nuclear isotope of ^{14}N whereas previous studies made use of the ^{15}N nuclear isotope. This can provide choice to researchers in the future as the two nuclear isotopes of nitrogen can now be utilised in research studies. ^{15}N data can be used to identify proton

11.3. THE FUTURE OF NMR CRYSTALLOGRAPHY

transfer, but due to its low isotropic abundance isotropic labelling is common. However, the quadrupolar nuclei of ^{14}N has a high isotropic abundance negating the need for costly isotropic labelling and providing a greater wealth of crystallographic information due to the presence of the second order quadrupolar shift.

Water in compounds is common and a greater understanding of the role of water can be gained by employing NMR crystallography as exemplified by the research by Abraham et al [239] in relation to the sildenafil citrate salt studied in chapter 9. Water was shown to be highly dynamic, with C_2 rotation and chemical exchange between different water molecules and the host structure.

Desiraju et al [244] explores salts and cocrystals and the position of the proton atom using NMR crystallography, specifically measuring N-H distances which vary with the length of hydrogen bond. The NMR crystallography method in exploring the proton position in salts and cocrystals is especially useful where the $\Delta\text{p}k_a$ rule breaks down in the range of $1 < \Delta\text{p}k_a < 3$. NMR can be also be used for ordered and disordered systems. Typically, a series of possible models are generated and NMR parameters predicted and compared to experimental measurements [246].

Dynamic behaviour was also at the heart of the research by Venâncio et al [247] who also investigated a citrate molecule, where variable temperature measurements were taken to reveal conformational changes. The approaches of dynamics using variable temperature solid-state NMR data could be utilised more in the future as it will provide greater crystallographic understanding of molecules under study.

For materials, however, where diffraction techniques are not possible NMR crystallography can still be used as shown by Brouwer et al [248] for zeolite structures. Here solid-state NMR is used solely to determine structures and provides a positive outlook for determining structures of similar materials which cannot be solved using diffraction.

Nitrogen is an important constituent of pharmaceutical products. ^{14}N and ^{15}N experiments are used in the area of pharmaceuticals and thus are also to be applied to other compounds, for example, solid APIs, and other biological and inorganic systems. ^{14}N quadrupolar solid-state NMR experiments were the main focus of my thesis to characterise a salt from a cocrystal but Veinburg et al [249] presents results which use a different type of ^{14}N NMR experiment with ^{15}N 2D experiments. ^{14}N ultra-wideline, ^1H - ^{15}N indirectly detected HETCOR and ^{15}N DNP solid-state NMR, with DFT calculations were shown to be effective at characterising a series of APIs which contain nitrogen. As with the research presented in this thesis all experiments were undertaken on samples which were at natural isotropic abundance. DNP increases the sensitivity of experiments by at least two orders of magnitude in biological systems. Current technology in DNP uses

the "cross-effect" whereby polarisation exchange occurs between three coupled spins, comprising two unpaired electrons and a nucleus. In low γ -nuclei such as ^{15}N [249] measurements involve an indirect route via protons, where DNP transfer occurs between the electron to ^1H then ^1H - ^{15}N transfer via CP. This shows the wide application DFT calculations which have been utilised in this thesis have in their ability to be applied to a wide range of compounds.

In summary, I believe NMR crystallography will have a positive impact in the future. Current possibilities of NMR crystallography have been shown which have a wide reach from using DNP, reducing computational cost of simulations, variable temperature measurements, the study of dynamics and understanding the role of water in compounds. It has also been shown that NMR crystallography is applicable to an ever increasing number of compounds ranging from biological and inorganic systems which include for example: disorder, hydrates and anhydrates. Knowledge and understanding in these current areas of research will grow and therefore provide researchers with ever increasing understanding of compounds at the atomic level.



Bibliography

- [1] S. Aitipamula, R. Banerjee, A. K. Bansal, K. Biradha, M. L. Cheney, A. R. Choudhury, G. R. Desiraju, A. G. Dikundwar, R. Dubey, N. Duggirala, P. P. Ghogale, S. Ghosh, P. K. Goswami, N. R. Goud, R. R. K. R. Jetti, P. Karpinski, P. Kaushik, D. Kumar, V. Kumar, B. Moulton, A. Mukherjee, G. Mukherjee, A. S. Myerson, V. Puri, A. Ramanan, T. Rajamannar, C. M. Reddy, N. Rodriguez-Hornedo, R. D. Rogers, T. N. G. Row, P. Sanphui, N. Shan, G. Shete, A. Singh, C. C. Sun, J. A. Swift, R. Thaimattam, T. S. Thakur, R. Kumar Thaper, S. P. Thomas, S. Tothadi, V. R. Vangala, N. Variankaval, P. Vishweshwar, D. R. Weyna and M. J. Zaworotko. Polymorphs, Salts, and Cocrystals: What's in a Name?, *Cryst. Growth Des.* **12** (2012), p. 2147.
- [2] J. F. Remenar, S. L. Morissette, M. L. Peterson, B. Moulton, J. M. MacPhee, H. R. Guzman and O. Almarsson. Crystal engineering of novel cocrystals of a triazole drug with 1,4-dicarboxylic acids, *J. Am. Chem. Soc.* **125** (2003), p. 8456.
- [3] D. P. McNamara, S. L. Childs, J. Giordano, A. Iarriccio, J. Cassidy, M. S. Shet, R. Mannion, E. O'Donnell and A. Park. Use of a glutaric acid cocrystal to improve oral bioavailability of a low solubility API, *Pharm. Res.* **23** (2006), p. 1888.
- [4] X-X. Li, Y. Wang, P-P. Xu, Q-Z. Zhang, K. Nie, X. Hu, B. Kong, L. Li and J. Chen. Effects of temperature and wavelength choice on in-situ dissolution test of Cimetidine tablets, *J. Pharm. Anal.* **3** (2012), p. 71.

BIBLIOGRAPHY

- [5] A. Trask, W. Motherwell and W. Jones. Physical stability enhancement of theophylline via cocrystallization, *Int. J. Pharm.* **320** (2006), p. 114.
- [6] C. A. Lipinski. Drug-like properties and the causes of poor solubility and poor permeability, *J. Pharmacol. Toxicol. Methods* **44** (2000), p. 235.
- [7] P. C. Vioglio, M. R. Chierotti and R. Gobetto. Pharmaceutical aspects of salt and cocrystal forms of APIs and characterization challenges, *Adv. Drug. Deliv. Rev.* **117** (2017), pp. 86–110.
- [8] A T M Serajuddin. Solid dispersion of poorly water-soluble drugs: Early promises, subsequent problems, and recent breakthroughs, *J. Pharm. Sci.* **88** (1999), p. 1058.
- [9] J. Desai, K. Alexander and A. Riga. Characterization of polymeric dispersions of dimenhydrinate in ethyl cellulose for controlled release, *Int. J. Pharmaceutics* **308** (2006), p. 115.
- [10] S. Janssens and G. Van den Mooter. Review: physical chemistry of solid dispersions, *J. Pharm. Pharmacol.* **61** (2009), p. 1571.
- [11] H. Grohgan, K. Löbmann, P. Priemel, K. Tarp Jensen, K. Graeser, C. Strachan and T. Rades. Amorphous drugs and dosage forms, *J. Drug. Deliv. Sci. Technol.* **23** (2013), pp. 403–408.
- [12] Lian Yu. Amorphous pharmaceutical solids: preparation, characterization and stabilization, *Adv. Drug Deliv. Rev.* **48** (2001), pp. 27–42.
- [13] M. Geppi, G. Mollica, S. Borsacchi and C. A. Veracini. Solid-state NMR studies of pharmaceutical systems, *Appl. Spectrosc. Rev.* **43** (2008), p. 202.
- [14] D. D. Gadade and S. S. Pekamwar. Pharmaceutical Cocrystals: Regulatory and Strategic Aspects, Design and Development, *Adv. Pharm. Bull.* **6** (2016), p. 479.
- [15] N. Blagden, M. de Matas, P. T. Gavan and P. York. Crystal engineering of active pharmaceutical ingredients to improve solubility and dissolution rates, *Adv. Drug. Deliv. Rev.* **59** (2007), p. 617.
- [16] B. Zhu, Q. Zhang, J-R. Wang and X. Mei. Cocrystals of Baicalein with Higher Solubility and Enhanced Bioavailability, *Cryst. Growth Des.* **17** (2017), p. 1893.
- [17] A. J. Smith, P. Kavuru, L. Wojtas, M.J. Zaworotko and R. D. Shytle. Cocrystals of Quercetin with Improved Solubility and Oral Bioavailability, *Mol. Pharm.* **8** (2011), p. 1867.
- [18] A. Newman, G. Knipp and G. Zografi. Assessing the performance of amorphous solid dispersions, *J. Pharm. Sci.* **101** (2012), p. 1355.

-
- [19] L. Kumar, A. Amin and A. K. Bansal. Salt Selection in Drug Development, *Pharmaceutical Technology* **32** (2008), p. 1.
- [20] Food Services, U.S. Department of Health and Human Administration, Drug (Center for Drug Evaluation, Research and CDER). *Guidance for Industry Regulatory Classification of Pharmaceutical Co-Crystals*, URL: <https://www.fda.gov/downloads/Drugs/Guidances/UCM281764.pdf> (visited on 2017-11-06).
- [21] R. K. Harris. Applications of solid-state NMR to pharmaceutical polymorphism and related matters, *J. Pharm. Pharmacol.* (2006), p. 225.
- [22] H. G. Brittain. Spectral methods for the characterization of polymorphs and solvates, *Journal of Pharmaceutical Sciences* **86** (1997), p. 405.
- [23] F. G. Vogt, J. Brum, L. M. Katrinic, A. Flach, J. M. Socha, R. M. Goodman and R. C. Haltiwanger. Physical, crystallographic, and spectroscopic characterization of a crystalline pharmaceutical hydrate: Understanding the role of water. *Cryst. Growth Des.* **6** (2006), p. 2333.
- [24] M. Geppi, S. Guccione, G. Mollica, R. Pignatello and C. A. Veracini. Molecular properties of ibuprofen and its solid dispersions with Eudragit RL100 studied by solid-state nuclear magnetic resonance. *Pharm. Res.* **22** (2005), p. 1544.
- [25] G. G. Z. Zhang, C. Gu, M. T. Zell, R. T. Burkhardt, E. J. Munson and D. J. W. Grant. Crystallization and transitions of sulfamerazine polymorphs. *J. Pharm. Sci.* **91** (2002), p. 1089.
- [26] R. Glaser, A. Novoselsky, D. Shiftan and M. Drouin. Eight-membered-ring solid-state conformational interconversion via the atom-flip mechanism, a CPMAS ^{13}C NMR and crystallographic stereochemical study. *J. Org. Chem.* **65** (2000), p. 6345.
- [27] L. Frydman, A. C. Olivieri, L. E. Diaz, B. Frydman, A. Schmidt and S. Vega. A ^{13}C solid-state NMR study of the structure and the dynamics of the polymorphs of sulphanilamide. *Mol. Phys.* **70** (1990), p. 563.
- [28] G. A. Stephenson, J. G. Stowell, P. H. Toma, D. E. Dorman, J. R. Green and S. R. Byrn. Solid-state analysis of polymorphic, isomorphic, and solvated forms of dirithromycin. *J. Am. Chem. Soc.* **116** (1994), p. 5766.
- [29] A. Portieri, R. K. Harris, R. A. Fletton, R. W. Lancaster and T. L. Threlfall. Effects of polymorphic differences for sulfanilamide, as seen through ^{13}C and ^{15}N solid-state NMR, together with shielding calculations. *Magn. Reson. Chem.* **42** (2004), p. 313.

BIBLIOGRAPHY

- [30] P. A. Tishmack, D. E. Bugay and S. R. Byrn. Solid-state nuclear magnetic resonance spectroscopy- Pharmaceutical applications. *J. Pharm. Sci.* **92** (2003), p. 441.
- [31] Gao P. Characterization of three crystalline forms (VIII, XI, and XII) and the amorphous form (V) of delavirdine mesylate using ^{13}C CP/MAS NMR, *Pharm. Res.* **15** (1998), p. 1425.
- [32] A. Forster, D. Apperley, J. Hempenstall, R. Lancaster and T. Rades. Investigation of the physical stability of amorphous drug and drug/polymer melts using variable temperature solid state NMR. *Pharmazie* **58** (2003), p. 761.
- [33] A. Koga, E. Yonemochi, M. Machida, Y. Aso, H. Ushio and K. Terada. Microscopic molecular mobility of amorphous AG-041 R measured by solid-state ^{13}C NMR. *Int. J. Pharm.* **275** (2004), p. 73.
- [34] K. Masuda, S. Tabata, Y. Sakata, T. Hayase, E. Yonemochi and K. Terada. Comparison of molecular mobility in the glassy state between amorphous indomethacin and salicin based on spin-lattice relaxation times. *Pharm. Res.* **22** (2005), p. 797.
- [35] S. Leung, B. E. Padden, E. J. Munson and D. J. W. Grant. Solid-state characterization of two polymorphs of aspartame hemihydrate. *J. Pharm. Sci.* **87** (1998), p. 501.
- [36] M. T. Zell, B. E. Padden, D. J. W. Grant, M.-C. Chapeau, I. Prakash and E. J. Munson. Two-dimensional high-speed CP/MAS NMR spectroscopy of polymorphs 1. Uniformly ^{13}C -labeled aspartame. *J. Am. Chem. Soc.* **121** (1999), p. 1372.
- [37] M. T. Zell, B. E. Padden, D. J. W. Grant, S. A. Schroeder, K. L. Wachholder, I. Prakash and E. J. Munson. Investigation of polymorphism in aspartame and neotame using solid-state NMR spectroscopy. *Tetrahedron* **56** (2000), p. 6603.
- [38] B. E. Padden, M. T. Zell, Z. Dong, S. A. Schroeder, D. J. W. Grant and E. J. Munson. Comparison of solid-state ^{13}C NMR spectroscopy and powder X-ray diffraction for analyzing mixtures of polymorphs of neotame. *Anal. Chem.* **71** (1999), p. 3325.
- [39] T. B. Grindley, M. S. McKinnon and R. E. Wasylshen. Towards understanding ^{13}C NMR chemical shifts of carbohydrates in the solid state. The spectra of D-mannitol polymorphs and DL-mannitol. *Carbohydr. Res.* **197** (1990), p. 41.
- [40] T. Yoshinari, R. T. Forbes, P. York and Y. Kawashima. Moisture induced polymorphic transition of mannitol and its morphological transformation. *Int. J. Pharm.* **247** (2002), p. 69.

-
- [41] G. A. Jeffrey. *An Introduction to Hydrogen Bonding*. New York: Oxford University Press, 1997, p. 298.
- [42] Y. Li, P. Chow and R. B. H. Tan. Quantification of polymorphic impurity in an enantiotropic polymorph system using differential scanning calorimetry, X-ray powder diffraction and Raman spectroscopy, *Int. J. Pharm.* **415** (2011), pp. 110–118.
- [43] A. Siddiqui, Z. Rahman, S. Bykadi and M. A. Khan. Chemometric Methods for the Quantification of Crystalline Tacrolimus in Solid Dispersion by Powder X-Ray Diffractometry, *J. Pharm. Sci.* **103** (2014), pp. 2819–2828.
- [44] P. Larkin. “Chapter 1 - Introduction: Infrared and Raman Spectroscopy”, ed. by Peter B T Infrared Larkin and Raman Spectroscopy. Oxford: Elsevier, 2011, pp. 1–5.
- [45] L. D. S. Yadav. “Infrared (IR) Spectroscopy - Organic Spectroscopy”, ed. by L. D. S. Yadav. Dordrecht: Springer Netherlands, 2005, pp. 52–106.
- [46] D.N. Sathyanarayana. *Vibrational Spectroscopy*. Second. New Delhi: New Age International Publishers, 2005.
- [47] J. R. Ferraro, K. Nakamoto and C. W. Brown. “Chapter 2 - Instrumentation and Experimental Techniques”, ed. by John R Ferraro, Kazuo Nakamoto and Chris W B T Introductory Raman Spectroscopy (Second Edition) Brown. San Diego: Academic Press, 2003, pp. 95–146.
- [48] M. J. Baker, C. S. Hughes and K. A. Hollywood. “Biophotonics: Vibrational Spectroscopic Diagnostics”, *Biophotonics: Vibrational Spectroscopic Diagnostics*. Morgan & Claypool Publishers, 2016. Chap. Raman spec, pp. 3–13.
- [49] I. Schnell, S. P. Brown, H. Y. Low, H. Ishida and H. W. Spiess. An Investigation of Hydrogen Bonding in Benzoxazine Dimers by Fast Magic-Angle Spinning and Double-Quantum ^1H NMR Spectroscopy, *J. Am. Chem. Soc.* **120** (1998), pp. 11784–11795.
- [50] G. E. Bacon and K. Lonsdale. Neutron diffraction, *Rep. Prog. Phys.* **16** (1953), pp. 1–61.
- [51] I. Khidirov. *Neutron diffraction. Principles, Instrumentation and application*. New York: Novinka, 2013, p. 80.

BIBLIOGRAPHY

- [52] P. M. B. Piccoli, T. F. Koetzle and A. J. Schultz. SINGLE CRYSTAL NEUTRON DIFFRACTION FOR THE INORGANIC CHEMIST - A PRACTICAL GUIDE, *Comment. Inorg. Chem.* **28** (2007), pp. 3–38.
- [53] S. P. Brown. Applications of high-resolution ^1H solid-state NMR, *Solid State Nuclear Magnetic Resonance* **41** (2012), p. 1.
- [54] J. R. Yates, T. N. Pham, C. J. Pickard, F. Mauri, A. M. Amado, A. M. Gil and S. P. Brown. A combined first principles computational and solid-state NMR study of a molecular crystal: flurbiprofen, *J. Am. Chem. Soc.* **127** (2005), p. 10216.
- [55] R. K. Harris. NMR crystallography: The use of chemical shifts, *Solid State Sci.* **6** (2004), p. 1025.
- [56] F. Taulelle. NMR crystallography: Crystallochemical formula and space group selection, *Solid State Sci.* **6** (2004), p. 1053.
- [57] R. K. Harris, R. Wasylishen and M. J. Duer, eds. *NMR Crystallography*. Chichester: Wiley, 2009.
- [58] Tremayne M., Kariuki B. M. and Harris K. D. M. Structure Determination of a Complex Organic Solid from X-Ray Powder Diffraction Data by a Generalized Monte Carlo Method: The Crystal Structure of Red Fluorescein, *Angew. Chem. Int. Ed.* **36** (1997), p. 770.
- [59] X. Filip, G. Borodi and C. Filip. Testing the limits of sensitivity in a solid-state structural investigation by combined X-ray powder diffraction, solid-state NMR, and molecular modelling, *Phys. Chem. Chem. Phys.* **13** (2011), p. 17978.
- [60] D. V. Dudenko, P. A. Williams, C. E. Hughes, O. N. Antzutkin, S. P. Velaga, S. P. Brown and K. D. M. Harris. Exploiting the Synergy of Powder X-ray Diffraction and Solid-State NMR Spectroscopy in Structure Determination of Organic Molecular Solids. *J. Phys. Chem. C.* **117** (2013), p. 12258.
- [61] X. Li, A. D. Bond, K. E. Johansson and J. Van de Streek. Distinguishing tautomerism in the crystal structure of (Z)-N-(5-ethyl-2,3-dihydro-1,3,4-thiadiazol-2-ylidene)-4-methylbenzenesulfonamide using DFT-D calculations and ^{13}C solid-state NMR, *Acta Crystallogr., Sect. C* **70** (2014), p. 784.
- [62] P. Li, Y. Chu, L. Wang, R. M. Wenslow, K. Yu, H. Zhang and Z. Deng. Structure determination of the theophylline–nicotinamide cocrystal: a combined powder XRD, 1D solid-state NMR, and theoretical calculation study, *CrystEngComm* **16** (2014), p. 3141.

-
- [63] G. N. M. Reddy, A. Marsh, J. T. Davis, S. Masiero and S. P. Brown. Interplay of Noncovalent Interactions in Ribbon-like Guanosine Self-Assembly: An NMR Crystallography Study, *Cryst. Growth Des.* **15** (2015), p. 5945.
- [64] A. E. Watts, K. Maruyoshi, C. E. Hughes, S. P. Brown and K. D. M. Harris. Combining the Advantages of Powder X-ray Diffraction and NMR Crystallography in Structure Determination of the Pharmaceutical Material Cimetidine Hydrochloride, *Cryst. Growth Des.* **16** (2016), p. 1798.
- [65] M. Sardo, S.M. Santos, A. A. Babaryk, C. López, I. Alkorta, J. Elguero, R. M. Claramunt and L. Mafra. Diazole-based powdered cocrystal featuring a helical hydrogen-bonded network: Structure determination from PXRD, solid-state NMR and computer modeling, *Solid-State Nucl. Magn. Reson* **65** (2015), p. 49.
- [66] C. E. Hughes, G. N. M. Reddy, S. Masiero, S. P. Brown, P. A. Williams and K. D. M. Harris. Determination of a complex crystal structure in the absence of single crystals: analysis of powder X-ray diffraction data, guided by solid-state NMR and periodic DFT calculations, reveals a new 2-deoxyguanosine structural motif, *Chem. Sci.* **8** (2017), p. 3971.
- [67] T. N. Pham, S. Masiero, G. Gottarelli and S. P. Brown. Identification by ^{15}N Refocused INADEQUATE MAS NMR of Intermolecular Hydrogen Bonding that Directs the Self-Assembly of Modified DNA Bases, *J. Am. Chem. Soc.* **127** (2005), p. 16018.
- [68] A. L. Webber, S. Masiero, S. Pieraccini, J. C. Burley, A. S. Tatton, D. Iuga, T. N. Pham, G. P. Spada and S. P. Brown. Identifying Guanosine Self Assembly at Natural Isotopic Abundance by High-Resolution ^1H and ^{13}C Solid-State NMR Spectroscopy, *J. Am. Chem. Soc.* **133** (2011), p. 19777.
- [69] C. Bonhomme, C. Gervais, C. Coelho, F. Pourpoint, T. Azaïs, L. Bonhomme-Courty, F. Babonneau, G. Jacob, M. Ferrari, D. Canet, J. R. Yates, C. J. Pickard, S. A. Joyce, F. Mauri and D. Massiot. New perspectives in the PAW/GIPAW approach: $\text{J}_{\text{P-O-Si}}$ coupling constants, antisymmetric parts of shift tensors and NQR predictions, *Magn. Reson. Chem.* **48** (2010), S86.
- [70] Harris R. K., Hodgkinson P., Pickard C. J., Yates J. R. and Z. Vadim. Chemical shift computations on a crystallographic basis: some reflections and comments, *Magn. Reson. Chem.* **45** (2007), S174.
- [71] C. J. Pickard and F. Mauri. All-electron magnetic response with pseudopotentials: NMR chemical shifts, *Phys. Rev. B* **63** (2001), p. 245101.

BIBLIOGRAPHY

- [72] J. R. Yates, C. J. Pickard and F. Mauri. Calculation of NMR chemical shifts for extended systems using ultrasoft pseudopotentials, *Phys. Rev. B* **76** (2007), p. 24401.
- [73] J. R. Yates, Tr. N. Pham, C. J. Pickard, F. Mauri, A. M. Amado, A. M. Gil and S. P. Brown. An Investigation of Weak CH...O Hydrogen Bonds in Maltose Anomers by a Combination of Calculation and Experimental Solid-State NMR Spectroscopy, *J. Am. Chem. Soc.* **127** (2005), p. 10216.
- [74] A. L. Webber, L. Emsley, R. M. Claramunt and S. P. Brown. NMR Crystallography of Campho [2,3 - c] pyrazole ($Z' = 6$): Combining High-Resolution ^1H - ^{13}C Solid-State MAS NMR Spectroscopy and GIPAW Chemical-Shift Calculations, *Society* (2010), p. 10435.
- [75] J. Schmidt, A. Hoffmann, H. W. Spiess and D. Sebastiani. Bulk Chemical Shifts in Hydrogen-Bonded Systems from First-Principles Calculations and Solid-State-NMR, *J. Phys. Chem. B.* **110** (2006), p. 23204.
- [76] A-C. Uldry, J. M. Griffin, J. R. Yates, M. Pérez-Torralba, M. D. S. María, Amy L Webber, M. L. L. Beaumont, A. Samoson, R.M. Claramunt, C. J. Pickard and S. P. Brown. Quantifying weak hydrogen bonding in uracil and 4-cyano-4'-ethynylbiphenyl: a combined computational and experimental investigation of NMR chemical shifts in the solid state. *J. Am. Chem. Soc.* **130** (2008), p. 945.
- [77] M. Zilka, S. Sturniolo, S. P. Brown and J. R. Yates. Visualising crystal packing interactions in solid-state NMR: Concepts and applications, *J. Chem. Phys.* **147** (2017), p. 144203.
- [78] A. S. Tatton, H. Blade, S. P. Brown, P. Hodgkinson, L. P. Hughes, S. O. N. Lill and J. R. Yates. Improving Confidence in Crystal Structure Solutions Using NMR Crystallography: The Case of β -Piroxicam, *Cryst. Growth Des.* **18** (2018), p. 3339.
- [79] A-C. Pöppler, E. K. Corlett, H. Pearce, M. P. Seymour, M. Reid, M. G. Montgomery and S. P. Brown. Single-crystal X-ray diffraction and NMR crystallography of a 1:1 cocrystal of dithianon and pyrimethanil, *Acta Crystallogr., Sect. C:* **73** (2017), p. 149.
- [80] C. Bonhomme, C. Gervais, F. Babonneau, C. Coelho, F. Pourpoint, T. Azaïs, S. E. Ashbrook, J. M. Griffin, J. R. Yates, F. Mauri and C.J. Pickard. First-Principles Calculation of NMR Parameters Using the Gauge Including Projector Augmented Wave Method: A Chemist's Point of View, *Chem. Rev.* **112** (2012), p. 5733.

-
- [81] S. E. Ashbrook and D. McKay. Combining solid-state NMR spectroscopy with first-principles calculations - a guide to NMR crystallography, *Chem. Commun.* **52** (2016), p. 7186.
- [82] A. S. Tatton, T. N. Pham, F.G. Vogt, D. Iuga, A. J. Edwards and S. P. Brown. Probing intermolecular interactions and nitrogen protonation in pharmaceuticals by novel ^{15}N -edited and 2D ^{14}N - ^1H solid-state NMR, *CrystEngComm* **14** (2012), p. 2654.
- [83] J. P. Bradley, S. P. Velaga, O. N. Antzutkin and S.P. Brown. Probing Intermolecular Crystal Packing in γ -Indomethacin by High-Resolution ^1H Solid-State NMR Spectroscopy, *Cryst. Growth Des.* **11** (2011), p. 3463.
- [84] A. L. Webber, B. Elena, J. M. Griffin, J. R. Yates, T. N. Pham, F. Mauri, C. J. Pickard, A. M. Fil, R. Stein, A. Lesage, L. Emsley and S. P. Brown. Complete ^1H resonance assignment of beta-maltose from ^1H - ^1H DQ-SQ CRAMPS and ^1H (DQ-DUMBO) - ^{13}C refocused INEPT 2D solid-state NMR spectra and first principles GIPAW calculations, *Phys. Chem. Chem. Phys.* **12** (2010), p. 6970.
- [85] T. Steiner and W. Saenger. Geometry of C-H...O Hydrogen Bonds in Carbohydrate Crystal Structures. Analysis of Neutron Diffraction Data. *J. Am. Chem. Soc.* **114** (1992), p. 10146.
- [86] Z. S. Derewenda, L. Lee and U. Derewenda. The Occurrence of C-H...O Hydrogen Bonds in Proteins, *J. Mol. Biol.* **252** (1995), p. 248.
- [87] C. Ochsenfeld, S.P. Brown, I. Schnell, J. Gauss and H. W. Spiess. Structure Assignment in the Solid State by the Coupling of Quantum Chemical Calculations with NMR Experiments: A Columnar Hexabenzocoronene Derivative, *J. Am. Chem. Soc.* **123** (2001), p. 2597.
- [88] S. P. Brown, Schaller T., Seelbach U. P., Koziol Felix, Ochsenfeld C., Klärner F.-G. and Spiess H. W. Structure and Dynamics of the Host-Guest Complex of a Molecular Tweezer: Coupling Synthesis, Solid-State NMR, and Quantum-Chemical Calculations, *Angew. Chem. Int. Ed.* **40** (2001), p. 717.
- [89] C. Ochsenfeld, F. Koziol, S.P. Brown, T. Schaller, U. P. Seelbach and F.-G. Klärner. A Study of a Molecular Tweezer Host-Guest System by a Combination of Quantum-Chemical Calculations and Solid-State NMR Experiments, *Solid State Nucl. Magn. Reson.* **22** (2002), p. 128.

BIBLIOGRAPHY

- [90] M. J. Potrzebowski, X. Assfeld, K. Ganicz, S. Olejniczak, A. Cartier, C. Gardienet and P. Tekely. An Experimental and Theoretical Study of the ^{13}C and ^{31}P Chemical Shielding Tensors in Solid O-Phosphorylated Amino Acids, *J. Am. Chem. Soc.* **125** (2003), p. 4223.
- [91] A. Hoffmann, D. Sebastiani, E. Sugiono, S. Yun, K.S. Kim, H.W. Spiess and I. Schnell. Solvent molecules trapped in supramolecular organic nanotubes: a combined solid-state NMR and DFT study, *Chem. Phys. Lett.* **388** (2004), p. 164.
- [92] J. R. Yates, S. E. Dobbins, C. J. Pickard, F. Mauri, P. Y. Ghi and R. K. Harris. A combined first principles computational and solid-state NMR study of a molecular crystal: flurbiprofen, *Phys. Chem. Chem. Phys.* **7** (2005), p. 1402.
- [93] S. J. Clark, M. D. Segall, C. J. Pickard, P. J. Hasnip, M. J. Probert, K. Refson and M. C. Payne. First principles methods using CASTEP, *Z. Kristallogr.* **220** (2005), p. 567.
- [94] P. Wentzcovitch, G. Baroni, S. Baroni, N. Bonini, M. Calandra, R. Car, C. Cavazzoni, D. Ceresoli, G. L. Chiarotti, M. Cococcioni, I. Dabo, A. D. Corso, S. de Gironcoli and S. Fabris. QUANTUM ESPRESSO: a modular and open-source software project for quantum simulations of materials, *J. Phys.: Condens. Matter* **21** (2009), p. 395502.
- [95] B. Berglund and R. W. Vaughan. Correlations between proton chemical shift tensors, deuterium quadrupole couplings, and bond distances for hydrogen bonds in solids, *J. Chem. Phys.* **73** (1980), p. 2037.
- [96] L. M. Ryan, R. E. Taylor, A. J. Paff and B. C. Gerstein. An experimental study of resolution of proton chemical shifts in solids: Combined multiple pulse NMR and magic-angle spinning, *J. Chem. Phys.* **72** (1980), p. 508.
- [97] S. P. Brown, A. Lesage, B. Elena and L. Emsley. Probing Proton-Proton Proximities in the Solid State: High-Resolution Two-Dimensional ^1H - ^1H Double-Quantum CRAMPS NMR Spectroscopy, *J. Am. Chem. Soc.* **126** (2004), p. 13230.
- [98] R. K. Harris, P. Jackson, L. H. Merwin, B. J. Say and G. Hagele. Perspectives in High-Resolution Solid-State Nuclear Magnetic-Resonance, with Emphasis on Combined Rotation and Multiple-Pulse Spectroscopy, *J. Chem. Soc., Faraday Trans. I.* **84** (1988), p. 3649.

-
- [99] I. de Boer, L. Bosman, J. Raap, H. Oschkinat and Huub J. M. de Groot. 2D ^{13}C - ^{13}C MAS NMR Correlation Spectroscopy with Mixing by True ^1H Spin Diffusion Reveals Long-Range Intermolecular Distance Restraints in Ultra High Magnetic Field, *J. Magn. Reson.* **157** (2002), p. 286.
- [100] B. Reif, B. J. van Rossum, F. Castellani, K. Rehbein, A. Diehl and H. Oschkinat. Characterization of ^1H - ^1H Distances in a Uniformly ^2H , ^{15}N -Labeled SH_3 Domain by MAS Solid-State NMR Spectroscopy. *J. Am. Chem. Soc.* **125** (2003), p. 1488.
- [101] L. Zheng, K. W. Fishbein, R.G. Griffin and J. Herzfeld. Two-dimensional solid-state proton NMR and proton exchange, *J. Am. Chem. Soc.* **115** (1993), p. 6254.
- [102] K. Seidel, M. Etzkorn, L. Sonnenberg, C. Griesinger, A. Sebald and M. Baldu. Studying Molecular 3D Structure and Dynamics by High-Resolution Solid-State NMR: Application to l-Tyrosine-Ethylester, *J. Phys. Chem. A.* **109** (2005), p. 2436.
- [103] H. Geen, J. J. Titman, J. Gottwald and H. W. Spiess. Solid-state proton multiple-quantum NMR spectroscopy with fast magic angle spinning, *Chem. Phys. Lett.* **227** (1994), p. 79.
- [104] S. P. Brown and H. W. Spiess. Advanced solid-state NMR methods for the elucidation of structure and dynamics of molecular, macromolecular and supramolecular systems, *Chem. Rev.* **101** (2001), p. 4125.
- [105] E. Vinogradov, P. K Madhu and S. Vega. Proton spectroscopy in solid state nuclear magnetic resonance with windowed phase modulated Lee-Goldburg decoupling sequences, *Chem. Phys. Lett.* **354** (2002), p. 193.
- [106] A. Lesage, D. Sakellariou, S. Hediger, B. Elena, P. Charmont, S. Steuernagel and L. Emsley. Experimental aspects of proton NMR spectroscopy in solids using phase-modulated homonuclear dipolar decoupling, *J. Magn. Reson.* **163** (2003), p. 105.
- [107] P. K. Madhu, E. Vinogradov and S. Vega. Multiple-pulse and magic-angle spinning aided double-quantum proton solid-state NMR spectroscopy, *Chem. Phys. Lett.* **394** (2004), p. 423.
- [108] B. Elena, G. Pintacuda, N. Mifsud and L. Emsley. Molecular Structure Determination in Powders by NMR Crystallography from Proton Spin Diffusion, *J. Am. Chem. Soc.* **128** (2006), p. 9555.
- [109] D. Suter and R. R. Ernst. Spin diffusion in resolved solid-state NMR spectra, *Phys. Rev. B* **32** (1985), p. 5608.

BIBLIOGRAPHY

- [110] T. Manolikas, T. Herrmann and B. H. Meier. Protein Structure Determination from ^{13}C Spin-Diffusion Solid-State NMR Spectroscopy, *J. Am. Chem. Soc.* **130** (2008), p. 3959.
- [111] Clauss J., Schmidt-Rohr K. and Spiess H W. Determination of domain sizes in heterogeneous polymers by solid-state NMR, *Acta Polymerica* **44** (1993), p. 1.
- [112] B. Elena and L. Emsley. Powder Crystallography by Proton Solid-State NMR Spectroscopy, *J. Am. Chem. Soc.* **127** (2005), p. 9140.
- [113] C. J. Pickard, E. Salager, G. Pintacuda, B. Elena and L. Emsley. Resolving Structures from Powders by NMR Crystallography Using Combined Proton Spin Diffusion and Plane Wave DFT Calculations, *J. Am. Chem. Soc.* **129** (2007), p. 8932.
- [114] E. Salager, R. S. Stein, C. J. Pickard, B. Elena and L. Emsley. Powder NMR crystallography of thymol, *Phys. Chem. Chem. Phys.* **11** (2009), p. 2610.
- [115] S. E. Bryn, R. R. Pfeiffer and J.G. Stowell. *Solid State Chemistry of Drugs*. West Lafayette: SSCI, 1999.
- [116] J. Bernstein and J. M. Bernstein. *Polymorphism in molecular crystals*. Vol. 14. Oxford University Press, 2002.
- [117] O. Abdullah, Evans J. S, I. Radosavljevic, R. K. Harris and P. Hodgkinson. Structural study of polymorphs and solvates of finasteride, *J. Pharm. Sci.* **96** (2007), p. 1380.
- [118] Schmidt A. C. Solid-state characterization of falicaine hydrochloride and isomorphous dyclonine hydrochloride. Part IV. Crystal polymorphism of local anaesthetic drugs, *Eur. J. Pharm. Sci.* **25** (2005), p. 407.
- [119] J. M. Rubin-Preminger, J. Bernstein, R. K. Harris, I. Radosavljevic Evans and P. Y. Ghi. Variable temperature studies of a polymorphic system comprising two pairs of enantiotropically related forms:[S,S]-Ethambutol dihydrochloride. *Cryst. Growth Des.* **4** (2004), p. 431.
- [120] Carss S. A., Harris R. K. and Fletton R. A. Carbon-13 NMR investigations of three fluorinated steroids, *Magn. Reson. Chem.* **33** (1995), p. 501.
- [121] S. M. Reutzel-Edens, J. K. Bush, P. A. Magee, G. A. Stephenson and S. R. Byrn. Anhydrides and hydrates of olanzapine: Crystallization, solid-state characterization and structural relationships. *Cryst. Growth Des.* **3** (2003), p. 897.

-
- [122] D. C. Apperley, R. A. Fletton, R. K. Harris, R. W. Lancaster, S. Tavener and T. L. Threlfall. Sulfathiazole polymorphism studied by magic-angle spinning NMR. *J. Pharm. Sci.* **88** (1999), p. 1275.
- [123] R. M. Wenslow, M. W. Baum, R. G. Ball, J. A. McCauley and R. J. Varsolona. A spectroscopic and crystallographic study of polymorphism in an aza-steroid. *J. Pharm. Sci.* **89** (2000), p. 1271.
- [124] F. G. Vogt, D. E. Cohen, J. D. Bowman, G. P. Spoor, G. E. Zuber, G. A. Trescher, P. C. Dell'Orco, L. M. Katrincic, C. W. Debrosse and R. C. Haltiwanger. Structural analysis of polymorphism and solvation in tranilast. *J. Pharm. Sci.* **94** (2005), p. 651.
- [125] A. R. Sheth, J.W. Lubach, E. J. Munson, F. X. Muller and D. J. W. Grant. Mechanochromism of piroxicam accompanied by intermolecular proton transfer probed by spectroscopic methods and solid-phase changes. *J. Am. Chem. Soc.* **127** (2005), p. 6641.
- [126] Z. J. Li, Y. Abramov, J. Bordner, J. Leonard, A. Medek and A. V. Trask. Solid-state acid-base interactions in complexes of heterocyclic bases with dicarboxylic acids: Crystallography, hydrogen bond analysis, and ^{15}N NMR spectroscopy, *J. Am. Chem. Soc.* **128** (2006), p. 8199.
- [127] D. C. Apperley, A. H. Forster, R. Fournier, R. K. Harris, P. Hodgkinson, R. W. Lancaster and T. Rades. Characterisation of indomethacin and nifedipine using variable-temperature solid-state NMR, *Magn. Reson. Chem.* **43** (2005), p. 881.
- [128] J. W. Steed. Should solid-state molecular packing have to obey the rules of crystallographic symmetry?, *CrystEngComm* **5** (2003), p. 169.
- [129] R. Saikat, B. Rahul, N. Ashwini and Kruger G. J. Conformational, Concomitant Polymorphs of 4,4-Diphenyl-2,5-cyclohexadienone: Conformation and Lattice Energy Compensation in the Kinetic and Thermodynamic Forms, *Chem. A-Eur. J.* **12** (2006), p. 3777.
- [130] J. Bernstein, J. D. Dunitz and A. Gavezzotti. Polymorphic Perversity: Crystal Structures with Many Symmetry-Independent Molecules in the Unit Cell, *Cryst. Growth Des.* **8** (2008), p. 2011.
- [131] G. E. Balimann, C. J. Groombridge, R. K. Harris, K. J. Packer, B. J. Say and S. F. Tanner. Chemical applications of high-resolution ^{13}C NMR spectra for solids, *Phil. Trans. R. Soc. Lond. A* **299** (1981), p. 643.

BIBLIOGRAPHY

- [132] A. C. Schmidt, U. J. Griesser, T. Brehmer, R. K. Harris and A. King. Conformational polymorphism of the local anaesthetic drug oxybuprocaine hydrochloride, *Acta Crystallogr. A* **58** (2002), p. 140.
- [133] R. K. Harris, A. M. Kenwright, B. J. Say, R. R. Yeung, R. A. Fletton, R.W. Lancaster and G. L. Hardgrove. Cross-polarization/magic-angle spinning NMR studies of polymorphism: Cortisone acetate, *Spectrochimica Acta, Part A* **46** (1990), p. 927.
- [134] E A Christopher, R K Harris and R A Fletton. No Title, *Solid State Nuclear Magnetic Resonance* **1** (1992), p. 93.
- [135] A. Lesage, D. Sakellariou, S. Steuernagel and L. Emsley. Carbon-Proton Chemical Shift Correlation in Solid-State NMR by Through-Bond Multiple-Quantum Spectroscopy, *J. Am. Chem. Soc.* **120** (1998), p. 13194.
- [136] P. K. Madhu. High-resolution solid-state NMR spectroscopy of protons with homonuclear dipolar decoupling schemes under magic-angle spinning, *Solid State Nucl. Magn. Reson.* **35** (2009), p. 2.
- [137] A. Bielecki, A. C. Kolbert and M. H. Levitt. Frequency-switched pulse sequences: Homonuclear decoupling and dilute spin NMR in solids, *Chem. Phys. Lett.* **155** (1989), p. 341.
- [138] E. Vinogradov, P. K. Madhu and S. Vega. High-resolution proton solid-state NMR spectroscopy by phase-modulated Lee- Goldburg experiment, *Chem. Phys. Lett.* **314** (1999), p. 443.
- [139] D. Sakellariou, A. Lesage, P. Hodgkinson and L. Emsley. Homonuclear dipolar decoupling in solid-state NMR using continuous phase modulation, *Chem. Phys. Lett.* **319** (2000), p. 253.
- [140] S P Brown. Recent Advances in Solid-State MAS NMR Methodology for Probing Structure and Dynamics in Polymeric and Supramolecular Systems. *Macromol. Rapid Commun.* **30** (2009), p. 688.
- [141] R. K. Harris, S. Cadars, L. Emsley, J. R. Yates, C. J. Pickard, R. K. R. Jetti and U. J. Griesser. NMR crystallography of oxybuprocaine hydrochloride, Modification II°, *Phys. Chem. Chem. Phys.* **9** (2007), p. 360.
- [142] B. Elena, A Lesage, S Steuernagel, A Bockmann and L Emsley. Proton to Carbon-13 INEPT in Solid-State NMR Spectroscopy, *J. Am. Chem. Soc.* **127** (2005), pp. 17296–17302.

-
- [143] R. K. Harris, P. Y. Ghi, R. B. Hammond, C. Y. Ma and K. J. Roberts. Refinement of hydrogen atomic position in a hydrogen bond using a combination of solid-state NMR and computation, *Chem. Commun.* (2003), p. 2834.
- [144] P. H. Stahl and C.G. Wermuth. *Pharmaceutical Salts: Properties, Selection, and Use*. Wiley-VCH, 2002.
- [145] E. D. L. Smith, R. B. Hammond, M. J. Jones, K. J. Roberts, J. B. O. Mitchell, S. L. Price, R. K. Harris, D. C. Apperley, J. C. Cherryman and R. Docherty. The Determination of the Crystal Structure of Anhydrous Theophylline by X-ray Powder Diffraction with a Systematic Search Algorithm, Lattice Energy Calculations, and ^{13}C and ^{15}N Solid-State NMR: A Question of Polymorphism in a Given Unit Cell, *J. Phys. Chem. B* **105** (2001), p. 5818.
- [146] E. J. MacLean, K. D. M. Harris, B. M. Kariuki, S. J. Kitchin, R. R. Tykwinski, I. P. Swainson and J. D. Dunitz. Ammonium Cyanate Shows N-H \cdots N Hydrogen Bonding, Not N-H \cdots O, *J. Am. Chem. Soc.* **125** (2003), p. 14449.
- [147] R. J. Abraham, C. J. Medforth and P. E. Smith. Conformational analysis. Part 16 Conformational free energies in substituted piperidines and piperidinium salts, *J. Comput. Aided Mol. Des.* **5** (1991), pp. 205–212.
- [148] W-Q. T. Tong and G. Whitesell. In situ salt screening-a useful technique for discovery support and preformulation studies, *Pharm. Dev. Technol.* **3** (1998), pp. 215–223.
- [149] P. H. Stahl and C. G. Wermuth. Handbook of pharmaceutical salts: properties, selection and use, *Chem. Int.* **24** (2002), p. 21.
- [150] N. Schultheiss and A. Newman. Pharmaceutical cocrystals and their physicochemical properties, *Cryst. Growth Des.* **9** (2009), p. 2950.
- [151] C. B. Aakeröy, M. E. Fasulo and J. Desper. Cocrystal or salt: does it really matter?, *Mol. Pharm.* **4** (2007), p. 317.
- [152] S. L. Childs, G. P. Stahly and A. Park. The Salt-Cocrystal Continuum: The Influence of Crystal Structure on Ionization State, *Mol. Pharm.* **4** (2007), p. 323.
- [153] R. Gobetto, C. Nervi, E. Valfré, M. R. Chierotti, D. Braga, L. Maini, F. Grepioni, R. K. Harris and P. Y. Ghi. ^1H MAS, ^{15}N CPMAS, and DFT investigation of hydrogen-bonded supramolecular adducts between the diamine 1, 4-diazabicyclo-(2.2. 2) octane and dicarboxylic acids of variable chain length, *Chem. Mater.* **17** (2005), p. 1457.

BIBLIOGRAPHY

- [154] C. G. Levy and R. L. Litcher. *Nitrogen-15 Nuclear Magnetic Resonance Spectroscopy*. Wiley, 1979.
- [155] J. S. Stevens, S.J. Byard, C. A. Muryn and S. L. M. Schroeder. Identification of protonation state by XPS, solid-state NMR, and DFT: Characterization of the nature of a new theophylline complex by experimental and computational methods, *J. Phys. Chem. B*. **114** (2010), p. 13961.
- [156] A. Taylor. *Practical surface analysis: Auger and X-ray photoelectron spectroscopy*. Ed. by D. Briggs & M. P. Seah. 2nd. Vol. I. New York: Wiley-Blackwell, p. 657.
- [157] J. S. Stevens, S. J. Byard and S. L. M. Schroeder. Characterization of Proton Transfer in Co-Crystals by X-ray Photoelectron Spectroscopy (XPS), *Cryst. Growth Des.* **10** (2010), p. 1435.
- [158] J. S. Stevens, S. J. Byard and S. L. M. Schroeder. Salt or Co-Crystal? Determination of Protonation State by X-Ray Photoelectron Spectroscopy (XPS), *J. Pharm. Sci.* **99** (2010), p. 4453.
- [159] R. Gobetto, C. Nervi, Chierotti M. R., D. Braga, L. Maini, F. Grepioni, R. K. Harris and P. Hodgkinson. Hydrogen Bonding and Dynamic Behaviour in Crystals and Polymorphs of Dicarboxylic-Diamine Adducts: A Comparison between NMR Parameters and X-ray Diffraction Studies, *Chem.-Eur. J.* **11** (2005), p. 7461.
- [160] F. G. Vogt, J. S. Clawson, M. Strohmeier, A. J. Edwards, T. N. Pham and S. A. Watson. Solid-State NMR Analysis of Organic Cocrystals and Complexes, *Cryst. Growth Des.* **9** (2009), p. 921.
- [161] J. S. Stevens, S. J. Byard, C. C. Seaton, G. Sadiq, R. J. Davey and S. L. M. Schroeder. Proton transfer and hydrogen bonding in the organic solid state: a combined XRD/ XPS/ssNMR study of 17 organic acid-base complexes, *Phys. Chem. Chem. Phys.* **16** (2014), p. 1150.
- [162] H. Hamaed, J. M. Pawlowski, B. F. T. Cooper, R. Fu, S. H. Eichhorn and R. W. Schurko. Application of Solid-State ^{35}Cl NMR to the Structural Characterization of Hydrochloride Pharmaceuticals and their Polymorphs, *J. Am. Chem. Soc.* **130** (2008), p. 11056.
- [163] A. S. Lipton, R. W. Heck, W. A. de Jong, A.R. Gao, X. Wu, A. Roehrich, G. S. Harbison and P.D. Ellis. Low Temperature ^{65}Cu NMR Spectroscopy of the Cu^+ Site in Azurin, *J. Am. Chem. Soc.* **131** (2009), p. 13992.

-
- [164] N. Redman-Furey, M. Dicks, A. Bigalow-Kern, R. T. Cambron, G. Lubey, C. Lester and D. Vaughn. Structural and analytical characterization of three hydrates and an anhydrate form of risedronate. *J. Pharm. Sci.* **94** (2005), p. 893.
- [165] C. Lester, G. Lubey, M. Dicks, G. Andol, D. Vaughn, R. T. Cambron, K. Poiesz and N. Redman-Furey. Dehydration of risedronate hemipentahydrate: analytical and physical characterization. *J. Pharm. Sci.* **95** (2006), p. 2631.
- [166] F. G. Vogt, P. C. Dell'Orco, A. M. Diederich, Q. Su, J. L. Wood, G. E. Zuber, L. M. Katrincic, R. L. Mueller, D. J. Busby and C. W. DeBrosse. A study of variable hydration states in topotecan hydrochloride. *J. Pharm. Biomed. Anal.* **40** (2006), p. 1080.
- [167] Z. Gan, J. P. Amoureux and J. Trébosc. Proton-detected ^{14}N MAS NMR using homonuclear decoupled rotary resonance, *Chem. Phys. Lett.* **435** (2007), p. 163.
- [168] L. A. O'Dell and R. W. Schurko. Fast and Simple Acquisition of Solid-State ^{14}N NMR Spectra with Signal Enhancement via Population Transfer, *J. Am. Chem. Soc.* **131** (2009), p. 6658.
- [169] S. Cavadini, S. Antonijevic, A. Lupulescu and G. Bodenhausen. Indirect detection of nitrogen-14 in solids via protons by nuclear magnetic resonance spectroscopy, *J. Magn. Reson.* **182** (2006), pp. 168–172.
- [170] S. Cavadini. Indirect detection of nitrogen-14 in solid-state NMR spectroscopy, *Prog. Nucl. Magn. Reson. Spectrosc.* **56** (2010), p. 46.
- [171] A. S. Tatton, T. N. Pham, F. G. Vogt, D. Iuga, A. J. Edwards and S. P. Brown. Probing Hydrogen Bonding in Cocrystals and Amorphous Dispersions Using ^{14}N - ^1H HMQC Solid-State NMR, *Mol. Pharm* **10** (2013), p. 999.
- [172] M. Khan, V. Enkelmann and G. Brunklaus. Crystal Engineering of Pharmaceutical Co-crystals: Application of Methyl Paraben as Molecular Hook, *J. Am. Chem. Soc.* **132** (2010), p. 5254.
- [173] M. Khan, V. Enkelmann and G. Brunklaus. Heterosynthon mediated tailored synthesis of pharmaceutical complexes: a solid-state NMR approach, *CrystEngComm* **13** (2011), p. 3213.
- [174] M. Bauer, R. K. Harris, R. C. Rao, D. C. Apperley and C. A. Rodger. NMR study of desmotropy in Irbesartan, a tetrazole-containing pharmaceutical compound, *J. Chem. Soc., Perkin Trans. 2* (1998), p. 475.

BIBLIOGRAPHY

- [175] G. V. Rubenacker and T. L. Brown. Nitrogen-14 nuclear quadrupole resonance spectra of coordinated pyridine. An extended evaluation of the coordinated nitrogen model, *Inorg. Chem.* **19** (1980), p. 392.
- [176] J. Seliger and V. Zagar. ^{14}N NQR Study of Polymorphism and Hydrogen Bonding in Molecular Complex Isonicotinamide-Oxalic Acid (2:1), *J. Phys. Chem. A.* **114** (2010), p. 12083.
- [177] L. A. O'Dell and R. W. Schurko. Static solid-state ^{14}N NMR and computational studies of nitrogen EFG tensors in some crystalline amino acids, *Phys. Chem. Chem. Phys.* **11** (2009), p. 7069.
- [178] D. C. Apperley, R. K. Harris and P. Hodgkinson. *Solid State NMR : Basic Principles & Practice*. New York: Momentum Press, 2012.
- [179] J. Keeler. *Understanding NMR Spectroscopy*. Chichester: Wiley, 2002.
- [180] M. H. Levitt. *Spin dynamics: Basics of Nuclear Magnetic Resonance*. 2nd Editio. Chichester: Wiley, 2012.
- [181] M. J. Duer. "Dipolar Coupling: Theory and Uses.", *Introduction to Solid-State NMR Spectroscopy*. Ed. by M J Duer. Oxford: Blackwell Publishing Ltd, 2004, p. 368.
- [182] P. J. Hore, J. A. Jones and S. Wimperis. *NMR: The Toolkit*. Ed. by Second. Oxford: Oxford University Press, 2000.
- [183] D. D. Laws, H. L. Bitter and A. Jerschow. Solid-State NMR Spectroscopic Methods in Chemistry, *Angew. Chem. Int. Ed.* (2002).
- [184] W. T. Dixon, J. Schaefer, M. D. Sefcik, E. O. Stejskal and R. A. McKay. Total suppression of sidebands in CPMAS C-13 NMR, *J. Magn. Reson. (1969)* **49** (1982), pp. 341–345.
- [185] A. Samoson, T. Tuherm and Z. Gan. High-field high-speed MAS resolution enhancement in ^1H NMR spectroscopy of solids, *Solid-State Nucl. Magn. Reson* **20** (2001), p. 130.
- [186] Y. Nishiyama, Y. Endo, T. Nemoto, H. Utsumi, K. Yamauchi, K. Hioka and T. Asakura. Very fast magic angle spinning ^1H - ^{14}N 2D solid-state NMR: Sub-microliter sample data collection in a few minutes, *J. Magn. Reson.* **208** (2011), p. 44.

-
- [187] T. Kobayashi, K. Mao, P. Paluch, A. Nowak-Król, J. Sniechowska, Y. Nishiyama, D. T. Gryko, M. J. Potrzebowski and M. Pruski. Study of Intermolecular Interactions in the Corrole Matrix by Solid-State NMR under 100 kHz MAS and Theoretical Calculations, *Angew. Chem. Int. Ed.* **125** (2013), p. 14358.
- [188] J. M. Lamley, D. Iuga, C. Öster, H.-J. Sass, M. Rogowski, A. Oss, J. Past, A. Reinhold, S. Grzesiek, A. Samoson and J. R. Lewandowski. Solid-State NMR of a Protein in a Precipitated Complex with a Full-Length Antibody, *J. Am. Chem. Soc.* **136** (2014), p. 16800.
- [189] V. Agarwal, S. Penzel, K. Szekely, R. Cadalbert, E. Testori, A. Oss, J. Past, A. Samoson, M. Ernst, A. Böckmann and Others. De Novo 3D Structure Determination from Sub-milligram Protein Samples by Solid-State 100 kHz MAS NMR Spectroscopy, *Angew. Chem., Int. Ed.* **53** (2014), p. 12253.
- [190] M. Geppi, G. Mollica, S. Borsacchi and C. A. Veracini. Solid-State NMR Studies of Pharmaceutical Systems, *Applied Spectroscopy Reviews* **43** (2008), p. 202.
- [191] Reddy G. N. M., Huqi A., Iuga D., Sakurai S., Marsh A., Davis J. T., Masiero S. and Brown S. P. Coexistence of Distinct Supramolecular Assemblies in Solution and in the Solid State, *Chem. A-Eur. J.* **23** (2017), p. 2235.
- [192] J.V. Hanna and M.E. Smith. Recent technique developments and applications of solid state NMR in characterising inorganic materials, *Solid State Nucl. Magn. Reson.* **38** (2010), p. 1.
- [193] S. Dusold and A. Sebald. Dipolar recoupling under magic-angle spinning conditions, *Annu. Rep. NMR. Spectro.* **41** (2000), p. 185.
- [194] P Hodgkinson. Heteronuclear decoupling in the NMR of solids, *Prog. Nucl. Magn. Reson.* **46** (2005), p. 197.
- [195] A. E. Bennett, C. M. Rienstra, M. Auger, K. V. Lakshmi and R. G. Griffin. Heteronuclear decoupling in rotating solids. *J. Chem. Phys.* **103** (1995), p. 6951.
- [196] B. M. Fung, A. K. Khitrin and K. Ermolaev. An improved broadband decoupling sequence for liquid crystals and solids. *J. Magn. Reson.* **142** (2000), p. 97.
- [197] S. R. Hartman and E. L. Hahn. Nuclear Double Resonance in the Rotating Frame. *Phys. Rev.* **128** (1962), p. 2042.
- [198] G. Metz, X. Wu and S. O. Smith. Ramped-Amplitude Cross Polarization in Magic-Angle Spinning NMR, *J. Magn. Reson.* **110** (1994), p. 219.

BIBLIOGRAPHY

- [199] J. S. Frye and G.E. Maciel. Setting the magic angle using a quadrupolar nuclide, *J. Magn. Reson.* **48** (1982), p. 125.
- [200] C. R. Morcombe and K. W. Zilm. Chemical shift referencing in MAS solid state NMR, *J. Magn. Reson.* **162** (2003), p. 479.
- [201] S. Hayashi and K. Hayamizu. Chemical shift standards in high-resolution solid-state NMR (^{13}C , ^{29}Si , and ^1H nuclei, *Bull. Chem. Soc. Jpn.* **64** (1991), p. 685.
- [202] I. Frantsuzov, S.K. Vasa, M. Ernst, S. P. Brown, V. Zorin, A. P. M. Kentgens and P. Hodgkinson. Rationalising Heteronuclear Decoupling in Refocussing Applications of Solid-State NMR Spectroscopy, *Chem. Phys. Chem* **18** (2017), p. 394.
- [203] D. J. States, R. A. Haberkorn and D. J. Ruben. A Two-Dimensional Nuclear Overhauser Experiment with Pure Absorption Phase in 4 Quadrants, *J. Magn. Reson.* **48** (1982), p. 286.
- [204] I. Schnell and H. W. Spiess. High-resolution ^1H NMR spectroscopy in the solid state: very fast sample rotation and multiple-quantum coherences. *J. Magn. Reson.* **151** (2001), p. 153.
- [205] W. Sommer, J. Gottwald, D. E. Demco and H. W. Spiess. Dipolar Heteronuclear Multiple-Quantum NMR Spectroscopy in Rotating Solids, *J. Magn. Reson.* **113** (1995), p. 131.
- [206] I. Schnell, A. Lupulescu, S. Hafner, D. E. Demco and H. W. W. Spiess. Resolution enhancement in multiple-quantum MAS NMR spectroscopy. *J. Magn. Reson.* **133** (1998), p. 61.
- [207] U. Friedrich, I. Schnell, S.P. Brown, A. Lupulescu, D. Demco and H. W. Spiess. Spinning-sideband patterns in multiple-quantum magic-angle spinning NMR spectroscopy, *Mol. Phys.* **95** (1998), p. 1209.
- [208] J. P. Bradley, C. Tripon, C. Philip and S. P. Brown. Determining relative proton-proton proximities from the build-up of two-dimensional correlation peaks in ^1H double-quantum MAS NMR: insight from multi-spin density-matrix simulations. *Phys. Chem. Chem. Phys.* **11** (2009), p. 6941.
- [209] R K Harris, E D Becker, S M de Menezes, P Granger, R E Hoffman and K W Zilm. No Title, *Pure Appl. Chem.* **80** (2008), p. 59.
- [210] G. E. Martin and C. E. Hadden. Long-Range ^1H - ^{15}N Heteronuclear Shift Correlation at Natural Abundance, *J. Nat. Prod.* **63** (2000), p. 543.

-
- [211] S. Sturniolo, T. F. G. Green, R. M. Hanson, M. Zilka, K. Refson, P. Hodgkinson, S. P. Brown and J. R. Yates. Visualization and processing of computed solid-state NMR parameters: MagresView and MagresPython, *Solid State Nucl. Magn. Reson.* **78** (2016), p. 64.
- [212] T. Charpentier. The PAW/GIPAW approach for computing NMR parameters: A new dimension added to NMR study of solids, *Solid State Nucl. Magn. Reson.* **40** (2011), p. 1.
- [213] C.G. Van de Walle and P. E. Blöchl. First-principles calculations of hyperfine parameters, *Phys. Rev. B* **47** (1993), p. 4244.
- [214] J. P. Perdew, K. Burke and M. Ernzerhof. Generalized gradient approximation made simple, *Phys. Rev. Lett.* **77** (1996), p. 3865.
- [215] J. S. Stevens, L. K. Newton, C. Jaye, C. A. Muryn, D.A. Fischer and S. L. M. Schroeder. Proton Transfer, Hydrogen Bonding, and Disorder: Nitrogen Near-Edge X-ray Absorption Fine Structure and X-ray Photoelectron Spectroscopy of Bipyridine-Acid Salts and Co-crystals, *Cryst. Growth. Des.* **15** (2015), p. 1776.
- [216] A. S. Tatton, J. P. Bradley, D. Iuga and S. P. Brown. ^{14}N - ^1H Heteronuclear Multiple-Quantum Correlation Magic-Angle Spinning NMR Spectroscopy of Organic Solids, *Z. Phys. Chem.* **226** (2012), p. 1187.
- [217] Harris R. K., Becker E. D., De Menezes S. M. C., Granger P., Hoffman R. E. and Zilm K. W. Further Conventions for NMR Shielding and Chemical Shifts (IUPAC Recommendations 2008), *Magn. Reson. Chem.* **46** (2008), p. 582.
- [218] K. Saalwächter, F. Lange, K. Matyjaszewski, C. F. Huang and R. Graf. BaBaxy16: Robust and broadband homonuclear DQ recoupling for applications in rigid and soft solids up to the highest MAS frequencies, *J. Magn. Reson.* **212** (2011), p. 204.
- [219] G. Roelofsen and J. A. Kanters. Citric acid monohydrate, *Cryst. Struct. Comm* **1** (1972), p. 23.
- [220] J. P. Glusker, J. A. Minkin and A. L. Patterson. X-ray crystal analysis of the substrates of aconitase. IX. A refinement of the structure of anhydrous citric acid, *Acta Crystallogr., Sect. B* **25** (1969), p. 1066.
- [221] A. V. Churakov. CCDC 635772: Experimental Crystal Structure Determination. *Cambridge Crystallographic Data Centre* (2007).

BIBLIOGRAPHY

- [222] M. D. King, E. A. Davis, T.M. Smith and T. M. Korter. Importance of Accurate Spectral Simulations for the Analysis of Terahertz Spectra: Citric Acid Anhydrate and Monohydrate, *J. Phys. Chem. A* **115** (2011), p. 11039.
- [223] A. Rammohan and J. A. Kaduk. Crystal structures of alkali metal (Group 1) citrate salts, *Acta Crystallogr., Sect. B* **74** (2018), p. 239.
- [224] M. Tomura and Y. Yamashita. One-Dimensional Zigzag Chain Structures with Intermolecular C-H... π and C-H...O Interactions Consisted of Phthalic Acid and Pyridine Derivatives, *Chem. Lett.* **30** (2001), pp. 532–533.
- [225] S. Karki, T. Frišćić, W. Jones and W. D. S. Motherwell. Screening for Pharmaceutical Cocrystal Hydrates via Neat and Liquid-Assisted Grinding, *Mol. Pharm.* **4** (2007), p. 347.
- [226] L. C. R; Almeida Andrade, M. M. R; Costa, J. A; Paixao, M. L; Santos, J. A; Moreira and M. R; Chaves. Crystal structure of trimethylglycine acid 2-hydroxy-1,2,3-propanetricarboxylic acid (1 : 1) adduct, C₆O₇H₈ . C₅NO₂H₁₁, *New Cryst. Struct.* **217** (2002), p. 77.
- [227] M. A. Elbagerma, H. G. M. Edwards, T. Munshi and I. J. Scowen. Identification of a new cocrystal of citric acid and paracetamol of pharmaceutical relevance, *CrystEngComm* **13** (2011), p. 1877.
- [228] A. Lemmerer and J. Bernstein. The co-crystal of two GRAS substances: (citric acid)·(nicotinamide). Formation of four hydrogen bonding heterosynthons in one co-crystal, *CrystEngComm* **12** (2010), p. 2029.
- [229] A. Alhalaweh, S. George, S. Basavoju, S. L. Childs, S. A. A. Rizvi and S. P. Velaga. Pharmaceutical cocrystals of nitrofurantoin: screening, characterization and crystal structure analysis, *CrystEngComm* **14** (2012), p. 5078.
- [230] M. Viertelhaus, R. Hilfiker, F. Blatter and M. Neuburger. Piracetam Co-Crystals with OH-Group Functionalized Carboxylic Acids, *Cryst. Growth Des.* **9** (2009), p. 2220.
- [231] D. Stepanovs and A. Mishnev. Molecular and crystal structure of sildenafil base, *Z. Naturforsch. B* **67** (2012), pp. 491–494.
- [232] F. M. Paruzzo, A. Hofstetter, F. Musil, S. De, M. Ceriotti and L. Emsley. Chemical shifts in molecular solids by machine learning, *Nature Communications* **9** (2018), p. 4501.

-
- [233] J. D. Hartman, R. A. Kudla, G. M. Day, L. J. Mueller and G. J. O. Beran. Benchmark fragment-based ^1H , ^{13}C , ^{15}N and ^{17}O chemical shift predictions in molecular crystals, *Phys. Chem. Chem. Phys.* **18** (2016), pp. 21686–21709.
- [234] J. M. Griffin, D. R. Martin and S. P. Brown. Distinguishing anhydrous and hydrous forms of an active pharmaceutical ingredient in a tablet formulation using solid-state NMR spectroscopy, *Angew. Chem., Int. Ed. Engl.* **46** (2007), p. 8036.
- [235] S. P. Brown. Probing proton-proton proximities in the solid state, *Prog. Nucl. Magn. Reson. Spectrosc.* **50** (2007), pp. 199–251.
- [236] Andrew S. Tatton, Tran N. Pham, Frederick G. Vogt, Dinu Iuga, Andrew J. Edwards and Steven P. Brown. Probing hydrogen bonding in cocrystals and amorphous dispersions using ^{14}N - ^1H HMQC solid-state NMR, *Molecular Pharmaceutics* **10** (2013), pp. 999–1007.
- [237] H. K. Miah, D. A. Bennett, D. Iuga and J. J. Titman. Measuring proton shift tensors with ultrafast MAS NMR, *J. Magn. Reson.* **235** (2013), pp. 1–5.
- [238] S. Sawatdee, C. Pakawatchai, K. Nitichai, T. Srichana and H. Phetmung. Why sildenafil and sildenafil citrate monohydrate crystals are not stable?, *Saudi Pharm J.* **23** (2015), p. 504.
- [239] A. Abraham, D. C. Apperley, S. J. Byard, A. J. Illott, A. J. Robbins, V. Zorin, R. K. Harris and P. Hodgkinson. Characterising the role of water in sildenafil citrate by NMR crystallography, *CrystEngComm* **18** (2016), p. 1054.
- [240] E. Carignani, S. Borsacchi, J. P. Bradley, S. P. Brown and M. Geppi. Strong Intermolecular Ring Current Influence on ^1H Chemical Shifts in Two Crystalline Forms of Naproxen: a Combined Solid-State NMR and DFT Study, *J. Phys. Chem. C* **117** (2013), p. 17731.
- [241] T. Venâncio, L. M. Oliveira, J. Ellena, N. Boechat and S. P. Brown. Probing intermolecular interactions in a diethylcarbamazine citrate salt by fast MAS ^1H solid-state NMR spectroscopy and GIPAW calculations, *Solid State Nucl. Magn. Reson.* **87** (2017), p. 73.
- [242] I. C. B. Martins, M. Sardo, T. Čendak, J.R. B. Gomes, J. Rocha, M. T. Duarte and L. Mafra. Hydrogen bonding networks in gabapentin protic pharmaceutical salts: NMR and in silico studies, *Magn. Reson. Chem.* **57** (2019), pp. 243–255.

BIBLIOGRAPHY

- [243] P. Thureau, S. Sturniolo, M. Zilka, F. Ziarelli, S. Viel, J. R. Yates and G. Mollica. Reducing the computational cost of NMR crystallography of organic powders at natural isotopic abundance with the help of ^{13}C - ^{13}C dipolar couplings, *Magn. Reson. Chem.* **57** (2019), pp. 256–264.
- [244] L. Rajput, M. Banik, J. R. Yarava, S. Joseph, M. K. Pandey, Y. Nishiyama and G. R. Desiraju. Exploring the salt–cocrystal continuum with solid-state NMR using natural-abundance samples: implications for crystal engineering, *IUCrJ* **4** (2017), pp. 466–475.
- [245] J. S. Stevens, M. Walczak, C. Jaye and D.A. Fischer. Frontispiece: In Situ Solid-State Reactions Monitored by X-ray Absorption Spectroscopy: Temperature-Induced Proton Transfer Leads to Chemical Shifts, *Chem. - Eur. J.* **22** (2016).
- [246] S. E. Ashbrook, J. M. Griffin and K. E. Johnston. Recent Advances in Solid-State Nuclear Magnetic Resonance Spectroscopy, *Annu. Rev. Anal. Chem.* **11** (2018), pp. 485–508.
- [247] T. Venâncio, L. M. Oliveira, T. Pawlak, J. Ellena, N. Boechat and S. P. Brown. The use of variable temperature ^{13}C solid-state MAS NMR and GIPAW DFT calculations to explore the dynamics of diethylcarbamazine citrate, *Magn. Reson. Chem.* **57** (2019), pp. 200–210.
- [248] D. H. Brouwer and J. Van Huizen. NMR crystallography of zeolites: How far can we go without diffraction data?, *Magn. Reson. Chem.* **57** (2019), pp. 167–175.
- [249] S. L. Veinberg, K. E. Johnston, M. J. Jaroszewicz, B. M. Kispal, C. R. Mireault, T. Kobayashi, M. Pruski and R. W. Schurko. Natural abundance ^{14}N and ^{15}N solid-state NMR of pharmaceuticals and their polymorphs, *Phys. Chem. Chem. Phys.* **18** (2016), pp. 17713–17730.